UAB

Universitat Autònoma de Barcelona

UAB

**Universitat Autònoma
de Barcelona**

Lab on a Chip Systems for Biochemical Analysis, Biology and Synthesis

Towards Simple, Scalable Microfabrication
Technologies Based on COC and LTCC

Miguel Berenguel Alonso

Tesi Doctoral
Programa de Doctorat en Química
Directors: Mar Puyol and Julián Alonso Chamarro

Departament de Química
Facultat de Ciències
2017

Memòria presentada per aspirar al Grau de Doctor per

Miguel Berenguel Alonso

Vist i plau

Mar Puyol   **Julián Alonso Chamarro**

Professora Agregada   Catedràtic
Departament de Química   Departament de Química

Bellaterra, 6 de Juny de 2017

The present dissertation was carried out with the following collaborations:

Universitat Autònoma de Barcelona Prof. Jordi Mas, Ferran Pujol-Vila, Núria Vigués-Frantzen and Núria Tomás, from the *Grup de Microbiologia Ambiental*. Dr. Joan Garcia and Javier Hellín, from the *Dept. of Electronic Engineering*. Prof. Manel López-Béjar, Dr. Maria Sabés-Alsina, Dr. Roser Morató, Dr. Oriol Talló-Parra and Laura Rodríguez-Vázquez, from the *Dept. of Animal Health and Anatomy*. Dr. Emma Rossinyol-Casals from the *Servei de Microscòpia*.

ICMAB-CSIC Dr. Jordi Faraudo, from the *Materials Simulation and Theory Group* and Dr. Xavier Granados, from the *Superconducting Materials and Large Scale Nanostructures* group.

ICN2 Prof. Laura M. Lechuga and Gerardo A. López-Muñoz from the *Nanobiosensors and Bioanalytical Applications* group.

Universidad de Granada Prof. Luis Fermín Capitán-Vallvey and Dr. Alfonso Salinas-Castillo, from the *ECSens* group.

To the women of my life . . .

my mother, Inma
my partner, Susanna
my daughter, Inma

Acknowledgements

Parecía que nunca iban a llegar este momento y estas líneas, pero el viaje está tocando a su fin. Aunque más que un final de trayecto, parece un salto entre dos trenes en marcha y a toda velocidad. Cuantos lugares y gentes descubriré allá donde aterrice, está por ver. Pero yo no sería el mismo sin este largo camino a mis espaldas en que se convirtió el doctorado. Por eso quiero dar las gracias a tantos que compartieron un trocito de camino y de sí mismos conmigo, de quienes tanto he aprendido.

En primer lugar, quiero agradecer la confianza y la libertad que me dieron mis directores, Mar y Julián. Habéis creado un espacio para aprender y crecer a todos los niveles (eso sí, con unos juguetes de 200.000 €!), y aunque quizás no os lo parezca, lo apreciamos mucho. Mar, gràcies per ser-hi sempre, tant en els moments bons com en els dolents, amb un somriure i sempre optimista. Gràcies pels teus consells i les nostres discussions, que sempre he tingut molt en compte tot i que de vegades no t'ho semblés. I gràcies també per les correccions de la tesi, que penso que han propiciat un salt qualitatiu molt important. Julián, gracias por ser un ejemplo y apostar por mí, ya que no era una jugada sencilla, por muchos motivos. Pero pienso que no ha salido nada mal, nos hemos sobrevivido y hemos hecho cosas muy interesantes. Gracias a ambos, esta tesis y todo lo que ha crecido a su alrededor os lo debo a vosotros.

Quiero también dar las gracias a Albert y Jealemy, mis mentores científicos en Enschede, sin los cuales posiblemente no hubiese escogido el tortuoso camino de la investigación. It was a pleasure to work with you (even in the sinking SMCT) and I learned a lot both scientifically and personally. I will never forget those days in the Laangezijds, the "nanobullshit", Albert's star roles in the goodbye movies, the ups and downs of the PhD life ... Thinking back, I've encountered many similar situations throughout my PhD. That year in the Netherlands turned my world upside down, and you were an important part of it. I would also like to thank Prof. Aldrik Velders and the SMCT for giving me the chance to spend a year in their lab, where I started my scientific career.

cousin Carlos for introducing me to this beautiful typesetting system. I would also like to thank the LaTeX community at StackExchange for having taken the time to stumble upon all the same problems I found.

During these last years I have been sharing home and much of my time with some amazing people, the Jovellaners. It certainly felt like we starred in Friends. You guys deserve a lot of credit for standing me, cheering me up on the bad moments and for celebrating the good ones. Gràcies també a tots els amics de Terrassa, que tot i que ens veiem molt menys del que m'agradaria, sé que sempre hi són. A més a més, vull agraïr a l'Adri el seu increïble talent amb la fotografia. Estic segur que qualsevol persona que fullegi la tesi sabrà quines fotos són meves. The amazing cover is not mine either, it was designed by Meike. Thanks a lot for making this thesis a beautiful book to show around.

Mi familia siempre ha sido un espejo en el que mirarme, ejemplos de que la vida merece ser celebrada por todo lo alto. Ejemplos todos, también, de que demasiado a menudo la vida es cruda y fría. Bien, un poco menos fría con vosotros cerca. Gracias a mi padre, mis hermanos, abuelos, tíos y primos, a todos, por todo, por estar ahí.

Por último, quiero dar las gracias a tres mujeres, por hacer que cada instante valga la pena, aunque duela. A mi madre, Inma, por regalarme la vida y diez años de amor. A veces, me da vértigo pensar cómo sería todo si no te hubieras ido. A mi pareja, Susanna, por devolverme la ilusión. Gracias por compartir tu increíble universo y tu amor conmigo. Y a mi hija, Inma, por ser la esencia de todo. Gracias por enseñarme el sentido de la vida: la luz que brilla en tus ojos.

Barcelona, Junio de 2017   **Miguel Berenguel Alonso**

Abstract

Lab on a Chip (LOC) technology has experienced a remarkable growth in the last two decades, owing to the development of novel microfabrication technologies and the better understanding of physical phenomena at the microscale. LOC systems present several advantages over conventional macroscopic systems: enhanced mass and energy transport, miniaturization, automation, integration and throughput, among others. These advantages have drawn the attention of a wide scientific and technological community, related to very different application areas such as chemistry, biology, medicine and nanotechnology.

However, the field is still in a development stage, as proven by the limited number of LOC products in the market. Different challenges need to be addressed to overcome this issue. On the one hand, the LOC system should integrate all the required operations for a given application, while keeping a simple interface for the end-users. Moreover, LOC systems should significantly outperform existing macroscopic analogues in order to justify the required investment in a new technology. On the other hand, materials and fabrication technologies need to provide the means to achieve that, both at a prototyping and mass production levels. Therefore, the scalability of the fabrication process should also be considered in order to bridge the gap between research prototyping and commercial production.

This dissertation is focused on the development of LOC devices using scalable processes based on multilayer fabrication approaches. These LOC systems are targeted at very different applications, examples of how different fields can benefit from this technology. The specific requirements of each application have driven the selection of the substrate and the integration of the necessary elements on the LOC systems.

The first case consists on the development of a LOC device using Cyclic Olefin Co-polymer (COC) as substrate and a simple magnetic actuator for the control and actuation of Magnetic Beads (MBs) *on-chip*. This analytical system was devoted to the detection of pathogenic E. coli O157:H7 whole cells, demonstrating an enhanced performance and simple operation. The second example is also based on a COC device, in this case, to trap and culture oocyte

cells. This LOC system demonstrated its suitability for Assisted Reproductive Technology (ART) applications. Moreover, the integration of transparent heaters lays the grounds for a fully independent culture/fertilization platform. In both cases, COC provides significant advantages such as high transparency, low autofluorescence and biocompatibility.

The last case consists on the development of Low Temperature Co-fired Ceramics (LTCC) microreactors for the synthetic process intensification of nanomaterials designed for analytical applications. This substrate and its associated fabrication technology enabled the monolithic integration of heaters, complex 3D-structures and optical windows. Magnetite nanoparticles and Carbon Dots (CDots) were synthesized under harsh reaction conditions, taking advantage of the chemical and structural stability of the LTCC substrate.

The results presented in this dissertation demonstrate the versatility of LOC technology and the advantages that it provides in a wide range of applications. Moreover, the fabrication methodologies developed could potentially be extrapolated to a mass production scale, which is of paramount importance for the technology transfer to commercial and industrial applications.

Resumen

La tecnología Lab on a Chip (LOC) ha experimentado un extraordinario crecimiento en las dos últimas décadas, gracias al desarrollo de nuevas tecnologías de microfabricación y al conocimiento más profundo de los fenómenos físicos dominantes a la microescala. Los sistemas LOC presentan diversas ventajas sobre los sistemas macroscópicos análogos: transporte de energía y materia más eficientes, miniaturización, automatización, integración y alta densidad de información, entra otras. Estas ventajas han llamado la atención de una amplia comunidad científica y tecnológica, relacionada con campos de aplicación tan distintos como la química, la biología, la medicina y la nanotecnología.

No obstante, el campo se encuentra todavía en una fase de desarrollo, tal como demuestra el limitado número de aplicacions LOC en el mercado. Es necesario afrontar diversos retos para superar esta barrera. Por un lado, los sistemas LOC deben integrar todas las operaciones necesarias para cada aplicación en cuestión, y al mismo tiempo, proporcionar una interfaz simple a los usuarios. Además, los sistemas LOC deben superar significativamente las prestaciones de sus análogos macroscópicos para justificar la inversión en una nueva tecnología. Por otro lado, los materiales y sus tecnologías de fabricación asociadas deben proporcionar la manera de producir tales dispositivos, tanto a nivel de prototipado como de fabricación en masa. Por tanto, al desarrollar sistemas LOC debe tenerse en cuenta la escalabilidad de los procesos de fabricación, y de esta manera, abordar el obstáculo que supone la transición a fabricación en masa.

Esta tesis se centra en el desarrollo de dispositivos LOC utilizando procesos de fabricación escalables basados en una aproximación multicapa. Estos sistemas LOC se han destinado a tres aplicaciones muy diferentes, ejemplo de como campos tan alejados pueden beneficiarse de esta tecnología. Los requerimientos específicos de cada aplicación han determinado la selección del material más adecuado y la integración de los elementos necesarios en el sistema LOC.

El primer caso consiste en el desarrollo de un dispositivo LOC fabricado con Co-polímero de Olefina Cíclica (COC), así como un actuador magnético para el control y la manipulación de partículas magnéticas dentro del dispositivo. Este sistema analítico fue utilizado para la detección de la bacteria patógena E. coli

O157:H7, demostrando una significativa mejora de la sensibilidad y una gran facilidad de operación. El segundo ejemplo también se basa en un dispositivo de COC, en este caso, para retener y madurar oocitos. Este sistema demostró su idoneidad para aplicaciones de reproducción asistida. Asimismo, la integración de calentadores transparentes en estos sistemas sienta la base para el desarrollo de plataformas de cultivo/fertilización totalmente independientes. En ambos ejemplos, el COC proporciona ventajas significativas como por ejemplo, una alta transparencia, baja autofluorescencia y biocompatibilidad.

El último caso consiste en el desarrollo de microreactores fabricado con cerámicas de sinterización a baja temperatura (LTCC, por sus siglas en inglés). Éstos se destinaron a la intensificación de procesos sintéticos de nanomateriales diseñados para aplicaciones analíticas. Este sustrato y su tecnología de fabricación asociada permiten la integración monolítica de calentadores, estructuras complejas 3D y ventanas ópticas. Nanopartículas de magnetita y Carbon Dots (CDots) fueron sintetizados bajo duras condiciones de reacción, aprovechando la estabilidad química y estructural del material LTCC.

Los resultados presentados en esta tesis demuestran la versatilidad de la tecnología LOC y las ventajas que proporciona a un amplio abanico de aplicaciones. Además, las metodologías de fabricación desarrolladas podrían ser potencialmente extrapoladas a procesos de fabricación en masa, hecho de gran importancia para la transferencia de tecnolgía hacia las aplicaciones comerciales e industriales.

Resum

La tecnologia Lab on a Chip (LOC) ha experimentat un extraordinari creixement en les dues últimes dècades, gràcies al desenvolupament de noves tecnologies de microfabricació i al coneixement més profund dels fenòmens físics dominants a la microescala. Els sistemes LOC presenten diversos avantatges sobre els sistemes macroscòpics anàlegs: transport d'energia i matèria més eficients, miniaturització, automatització, integració i alta densitat d'informació, entre d'altres. Aquests avantatges han cridat l'atenció d'una àmplia comunitat científica i tecnològica, relacionada amb camps d'aplicació tan diferents com la química, la biologia, la medicina i la nanotecnologia.

Tanmateix, el camp encara es troba en una fase de desenvolupament, tal com demostra el limitat nombre d'aplicacions LOC al mercat. És necessari encarar diferents reptes per a superar aquesta barrera. Per una banda, els sistemes LOC han d'integrar totes les operacions necessàries per a cada aplicació en qüestió, i al mateix temps, proporcionar una interfície simple per als usuaris. A més, els sistemes LOC han de superar significativament les prestacions dels seus anàlegs macroscòpics per a justificar la inversió en una nova tecnologia. Per altra banda, els materials i les tecnologies de fabricació han de proporcionar la manera de produir tals dispositius, tant a escala de prototipat com de fabricació en massa. Per tant, en desenvolupar sistemes LOC cal tenir en compte l'escalabilitat dels processos de fabricació, i així, abordar l'obstacle que suposa la transició a fabricació en massa.

Aquesta tesi se centra en el desenvolupament de dispositius LOC emprant processos de fabricació escalables basats en una aproximació multicapa. Aquests sistemes LOC han estat destinats a tres aplicacions ben diferents, exemples de com camps tan allunyats poden beneficiar-se d'aquesta tecnologia. Els requeriments específics de cada aplicació han determinat la selecció del material més adient i la integració dels elements necessaris al sistema LOC.

El primer cas consisteix en el desenvolupament d'un dispositiu LOC fabricat amb Co-polímer d'Olefina Cíclica (COC), així com un actuador magnètic per al control i la manipulació de partícules magnètiques dins el dispositiu. Aquest sistema analític va ésser emprat per a la detecció del bacteri patogen E. coli O157:H7, demostrant una significant millora de la sensibilitat i una

gran facilitat d'operació. El segon exemple també es basa en un dispositiu de COC, en aquest cas, per a retenir i madurar oòcits. Aquest sistema va demostrar la seva idoneïtat per a aplicacions de reproducció assistida. Així mateix, la integració d'escalfadors transparents en aquests sistemes assenta la base per al desenvolupament de plataformes de cultiu/fertilització totalment independents. En ambdós exemples, el COC proporciona avantages significatives com ara alta transparència, baixa autofluorescència i biocompatibilitat.

L'últim cas consisteix en el desenvolupament de microreactors fabricats amb ceràmiques de sinterització a baixa temperatura (LTCC, per les seves sigles en anglès). Aquests varen ser destinats a la intensificació de processos sintètics de nanomaterials dissenyats per a aplicacions analítiques. Aquest substrat i la seva tecnologia de fabricació associada permeten la integració monolítica d'escalfadors, estructures complexes 3D i finestres òptiques. Nanopartícules de magnetita i Carbon Dots (CDots) varen ésser sintetitzats sota dures condicions de reacció, aprofitant l'estabilitat química i estructural del material LTCC.

Els resultats presentats en aquesta tesi demostren la versatilitat de la tecnologia LOC i els avantatges que proporciona en un gran ventall d'aplicacions. A més, les metodologies de fabricació desenvolupades podrien ésser potencialment extrapolades a processos de fabricació en massa, fet de gran importància per a la transferència de tecnologia cap a aplicacions comercials i industrials.

Preface

LOC technology is a tool, not a final destination, but a way to get there. I consider LOC systems as an enabling technology, to enhance, miniaturize and automate chemical and biological processes. The downscaling provides several advantages over macroscopic systems, due to the enhanced transport phenomena and the possibility to mimic *in vivo* environments.

However, downscaling macroscopic systems also lays out several challenges, such as the control over "novel" physical phenomena at the microscale, the fabrication technologies or the lack of a "killer application". The first challenge is being actively tackled within the academic community, digging deeper into the novel phenomena observed at the microscale since the birth of the field. Fabrication technologies have greatly evolved, expanding the range of possible microstructures, improving resolution and bringing up new substrate materials with particular properties. Over the last years, there has been much discussion about the third challenge, the commercialization of LOC technology outside academia, as well as the further assimilation within scientists of different fields. This requires simple and low-cost fabrication approaches, as well as simple operation and low instrumental requirements.

This thesis is a little example of how diverse and rich are the potential applications of LOC systems. But besides that, it is an attempt to approach those applications with a scalable, simple fabrication technology. The substrate materials have been carefully selected to fulfill this premise, but also to suit each particular application —rather than the other way around. Finally, we attempted to create and use interfaces to control the liquids, particles and/or cells in a simple and intuitive way.

Miguel Berenguel Alonso

Contents

Glossary

μPAD	microfluidic Paper-based Analytical Devices
μTAS	micro Total Analysis Systems
4–MU	4-methylumbelliferone
4–MUP	4-methylumbelliferyl phosphate
AFM	Atomic-Force Microscope
AI	Artificial Insemination
AP	alkaline phosphatase
ART	Assisted Reproductive Technology
BPR	Back Pressure Regulator
BSA	bovine serum albumin
CA	citric acid
CAD	Computer-Aided Design
CASA	Computer-Assisted Sperm Analysis
CDots	Carbon Dots
CG	Cortical Granule
CNC	Computer Numeric Control
COC	Cyclic Olefin Co-polymer
COP	Cyclic Olefin Polymer
COP/COC	Cyclic Olefin (Co-)Polymers
DAPI	4',6-diamidino-2-phenylindole
DAQ	Data Acquisition Card
DEA	diethanolamine
DETA	diethylenetriamine
DMEM	Dulbecco's Modified Eagle's Medium
DNA	deoxyribonucleic acid
ED	ethylenediamine
FEM	Finite Element Modeling
FITC	fluorescein isothiocyanate

FITC-LCA	FITC-labeled Lens Culinaris Agglutinin
GND	ground
HEK293 cells	Human Embryonic Kidney cells 293
IPCA	5-oxo-1,2,3,5-tetrahydroimidazo[1,2-α]pyridine-7- carboxylic acid
IR	infrared
IVF	In Vitro Fertilization
LB	lysogeny broth
LED	Light Emitting Diode
LOC	Lab on a Chip
LOD	Limit of Detection
LOQ	Limit of Quantification
LTCC	Low Temperature Co-fired Ceramics
MBs	Magnetic Beads
MEMS	Microelectromechanical Systems
MII	Metaphase II
MTT	3-(4,5-dimethylthiazol-2-yl)-2,5-diphenyltetrazolium bromide
PBS	phosphate-buffered saline
PC	Polycarbonate
PCB	Printed Circuit Board
PDMS	Polydimethylsiloxane
PEI	polyethyleneimine
PID	Proportional-Integral-Derivative
PMMA	Poly(methyl methacrylate)
POC	Point of Care
PS	Polystyrene
PTFE	polytetrafluoroethylene
PVD	Physical Vapor Deposition
PWM	Pulse Width Modulated
QD	Quantum Dots
QY	Quantum Yield
RSD	Relative Standard Deviation
SAED	Selected Area Electron Diffraction
SD	Standard Deviation

SPION	superparamagnetic iron oxide nanoparticles
SQUID	Superconducting QUantum Interference Device
STM	Scanning Tunneling Microscope
T_g	Glass Transition Temperature
TBS	tris-buffered saline
TBST	tris-buffered saline-Tween 20
TCM-199	Tissue Culture Medium 199
TEM	Transmission Electron Microscopy
VAP	Velocity Average Path
XRD	X-Ray Diffraction

List of Figures

List of Tables

Chapter 1

General Introduction

Over the past 25 years, the field broadly known as Lab on a Chip (LOC) has experienced a dramatic growth due to the development of microfabrication techniques and novel materials, leading to important advancements in fields such as chemistry, biology and medicine (Whitesides 2006; Sackmann, Fulton and D. J. Beebe 2014; Castillo-León and Svendsen 2015). The realization of complex microfluidic structures and the possibility to integrate them together with actuators, sensors, power sources, etc., has attracted the attention of researchers, who see the potential of miniaturization and automation.

Different research fields can benefit of the advantages provided by LOCs, to name a few, analytical chemistry, synthetic chemistry or biology/biomedicine. Firstly, the need of monitoring a wide range of analytes —of environmental or biomedical importance— has fostered the development of micro Total Analysis Systems (μTAS) (Auroux et al. 2002; A. Arora et al. 2010; Kovarik et al. 2013), which may be used as Point of Care (POC). Secondly, microreactor technology has benefitted of the enhanced control over mass and heat transfer of LOC systems for the synthesis of organic and inorganic compounds and micro/-nanomaterials (DeMello 2006; Hartman and Jensen 2009; Marre and Jensen 2010; Elvira et al. 2013; Wirth 2013). Finally, the small features of LOC systems have also enabled the fabrication of devices mimicking *in vivo* structures (Ziółkowska, Kwapiszewski and Brzózka 2011; Huh et al. 2012; Swain, D. Lai, et al. 2013; Mehling and Tay 2014) and featuring high throughput (Dittrich and Manz 2006; Guo et al. 2012) for biological applications.

All of this research is driven by the need of society to attain autonomous and robust systems, that provide the required chemical or biological information in a cost-efficient way (both economically and environmentally) and on-site. However, much more effort is needed in order to transform all this research into commercial products and industrial applications. Researchers need to fill in several gaps regarding fabrication (materials, scalability, seal-

ing, interconnections, etc.), integration (pumping, electronics, detection, data transmission, etc.) and handling of reagents (liquids or solids), to name but a few.

In this dissertation we present our efforts to tackle some of these problems. Particularly, we develop novel LOC devices and instrumentation through scalable fabrication processes in Cyclic Olefin Co-polymer (COC) and Low Temperature Co-fired Ceramics (LTCC) —materials very well suited for particular applications— and also integrate simple actuators, for instance for particle handling *on-chip* or temperature and pressure control.

1.1 Miniaturization and Microfluidics

Miniaturization is considered to be the trend to downscale chemical and biological systems, offering certain advantages over the macroscopic analogous. This is schematically shown in Figure 1.1. Heat and mass transfer times are decreased in microfluidic channels due to the shorter distances. Furthermore, the higher surface-to-volume-ratio facilitates homogeneous heat distribution. Miniaturization of different functional units (reaction, separation, detection, etc.) enables the serial processing of samples as well as the parallelization of the process for high throughput. In this context, microfluidics can be defined as the study of behavior, precise control and manipulation of fluids which are constrained to the microscale. Microfluidics differs from conventional flow theory primarily due to the small characteristic scale of the system.

1.1.1 A Brief History

The strong and steady development of the microelectronic industry up from the 1960s —as predicted by Moore's law (Moore 1965)— established semiconductor fabrication technologies in order to increase the density of transistors in integrated circuits. This fabrication technologies led to the birth of the Microelectromechanical Systems (MEMS) in the 1980s. These are systems in the micrometer scale range envisioned as "small but movable machines" by Richard P. Feynman in his famous speech *There is plenty of room at the bottom* (Feynman 1960). Further refinement of the fabrication techniques of silicon-based MEMS made it straight forward to produce simple microfluidic systems (Madou 2002). The first example of microfluidic system is a miniaturized gas chromatographer, consisting of a 1.5 m long microchannel etched in silicon (Terry, Jerman and Angell 1979).

However, research on microfluidic systems did not pick up momentum until the early 1990s, when Manz first introduced the concept of miniaturized or micro Total Analysis System (µTAS) (Manz, Graber and Widmer 1990) and then fabricated an electrophoretic analytical system *on-chip* (Harrison et al.

Parameter	Macroscopic example	Factor change	Microscopic example
Length of edge	1 mm	d	1 μm
Surface	1 mm²	d²	1 μm²
Volume	1 μl	d³	1 fl
Number of molecules	10^9	d³	1
Diffusion time over d (D = 10^{-6} cm²s⁻¹)	15 min	d²	1 ms
Example: in flowing systems			
Linear flow rate	1 μm/s	d	1 mm/s
Separation time	10^5 s (>1 day)*	d²	100 ms
Example: in planar array			
Number of volumes per microwell plate	96	d²	10^8

*Typically, for example, high-performance liquid chromatography in packed column.

Figure 1.1: Scaling laws giving the dependence of reaction parameters on the size of the system, where d represents length of edge; n and m, numbers of reaction systems serial and parallel, respectively. Adapted from Dittrich and Manz 2006.

1993). These systems were envisioned to incorporate all the steps of the analytical process and outperform the existing technologies due to essentially two scale-dependent processes: mass and heat transfers. Furthermore, the development of micropumps, flow sensors and the implementation of the concepts for integrated fluid treatments in analytical systems brought the field to the forefront of research.

Researchers realized the potential of these systems in other areas besides analytical chemistry. The term Lab on a Chip (LOC) was then coined to refer to any kind of research with the goal of miniaturizing chemical and biological processes. In this sense, the materials inherited from the microelectronics technology (mainly silicon) had limitations derived from the fabrication process such as its complexity and cost, which hindered the adoption of this technology.

Therefore, Polydimethylsiloxane (PDMS) and soft lithography were introduced by the group of Whitesides (Duffy et al. 1998; Xia and Whitesides 1998), usually referred as one of the milestones on the field of microfluidics. PDMS is an optically transparent, biocompatible elastomer which can be used to replicate microstructures from a photolithographic master. PDMS-based

3

LOC systems enabled researchers to produce microfluidic systems for their applications, thanks to the simple, low-cost prototyping and the common laboratory equipment required for fabrication.

Other substrate materials gained traction due to their novel properties or fabrication technologies. For instance, thermoplastics emerged as an alternative due to their suitability to mass production using replication methods —like hot embossing or injection molding— very well established in the plastic industry (Heckele and Schomburg 2004; Becker and Gärtner 2008; Tsao and DeVoe 2009; Miserere et al. 2012). Paper-based LOCs emerged as a low cost POC alternative for resource-limited settings (Martinez et al. 2010; Yetisen, Akram and Lowe 2013; Xia, Si and Z. Li 2016). Other materials with interesting properties explored during the last decade include ceramics, such as the LTCC. This material also enables the simple integration of electronics and fluidics, and has outstanding chemical inertness (Ibáñez-García et al. 2008; Jiang, Haber, et al. 2015).

Over the last years, 3D printing technologies have emerged as a new solution for LOC fabrication. 3D printing provides a simple way to fabricate complex 3D microfluidic devices in an automated, assembly-free way (Au et al. 2016; Bhattacharjee et al. 2016). As this technology matures regarding improvements on resolution, throughput, development of new biocompatible resins and declining equipment costs, it is expected to expand its use within academia.

All these technology and material developments are yielding faster, simpler and cheaper LOC fabrication processes. This will hopefully spread the fabrication tools and know-how, not only to the academics, but to a wider community of scientists and makerspaces (Walsh et al. 2017). Makerspaces put together a diverse community of individuals, with technical and non-technical backgrounds, thus promoting development through collaboration and innovation. This hotbed may foster the success of microfluidics and LOC applications, which still lack a bridge between academic research and real world product commercialization.

1.1.2 Theoretical Aspects

This section does not pretend to be a comprehensive review of microfluidic theory, but to highlight a few interesting aspects.

Downscaling The surface-to-volume ratio plays an important role in microfluidic systems, for instance, when considering volume (gravity, inertia, etc.) and surface forces (surface tension, viscosity, etc.). Equations 1.1 imply that the surface forces become predominant in miniaturized LOC systems, where l represents their characteristic dimension (as the

size decreases, or l tends to 0).

$$\frac{Surface\ Forces}{Volume\ Forces} \propto \frac{l^2}{l^3} = l^{-1} \qquad \lim_{l \to 0} l^{-1} = \infty \qquad (1.1)$$

Laminar Flow In microfluidic devices, laminar flow (Figure 1.2a) is observed —as opposed to the turbulent flow (Figure 1.2b) in macroscopic flow systems. Laminar flow occurs when a fluid flows in parallel layers, with no disruption between the layers (Batchelor 2000).

(a) Laminar flow   (b) Turbulent flow
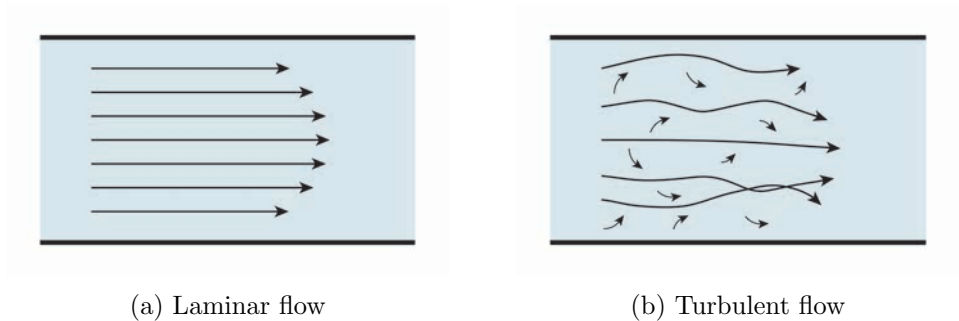
Figure 1.2: Schematic representation of turbulent and laminar flow regimes.

The Reynolds number (Re) is a dimensionless parameter that allows us to classify the behavior of a fluid. It accounts for characteristics of both the fluid (density ρ and dynamic viscosity μ) and the environment in which it is manipulated (characteristic dimension of the system d and fluid velocity v), as seen in Equation 1.2. The Reynolds number represents the ratio between inertial and viscous forces —volume and surface forces, respectively.

$$Re = \frac{Inertial\ Force}{Viscous\ Force} = \frac{\rho\,d\,v}{\mu} \qquad (1.2)$$

Figure 1.3a shows a microfluidic system in which laminar flow is attained and the different streams flow perfectly side by side. Laminar flow can be observed in LOC systems under a wide range of flow rates in channels of up to 1 mm, as seen in 1.3b. Generally, it is accepted that Reynolds numbers below 2000 indicate laminar flow (Folch 2012), although microfluidic systems usually are well below.

Pressure-Driven Flow There are two main strategies to actuate fluids in microfluidic channels, namely pressure-driven and electrokinetic flow (see Figure 1.4). Although other strategies exist (e.g. capillarity, magnetic, gravity-driven flow, etc.), they are not so well established and/or

(a) LOC system with laminar flow
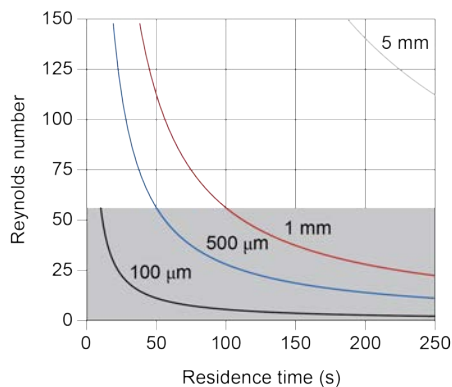
(b) *Re* for different channel sizes

Figure 1.3: Laminar flow photograph and Reynolds number in microfluidic systems. Adapted from Folch 2017 and Elvira et al. 2013, respectively.

limited to specific applications. Only pressure-driven flow has been used throughout this thesis.

Pressure-driven flow follows Pouseuille theory and is characterized by a smooth parabolic profile, with the maximum velocity in the center of the microchannel (see Figure 1.4a). This profile is based on the no-slip boundary condition, which establishes that the fluid velocity at a solid boundary (the walls of the microchannel) equals zero (Stone 2007).

Pressure-driven flow is well characterized, has a detailed fundamental understanding, it is simple to operate and can be generated with miniaturized instrumentation. On the other side, it has certain disadvantages such as the hydrodynamic dispersion of the samples (undesirable in separation processes), the need to use bulky macroscopic actuators (e.g. syringe pumps) due to the lower performance level of miniaturized actuators (Pennathur 2008; Badilescu and Packirisam 2011). Nevertheless, pressure-driven flow is widely used due to its versatility and straightforward operation for LOC end-users.

Diffusion Given the fact that fluids are in the laminar regime in microfluidic systems, diffusion is the only phenomenon for which mixing occurs. Diffusion is consequence of the Brownian motion, resulting from the collision with fast-moving solvent molecules. According to Fick's law, Equation 1.3 shows the diffusion time t_d for a molecule with diffusion coefficient D to move a distance l (valid for diffusion in one dimension).

(a) Pressure driven flow

(b) Electrokinetic flow
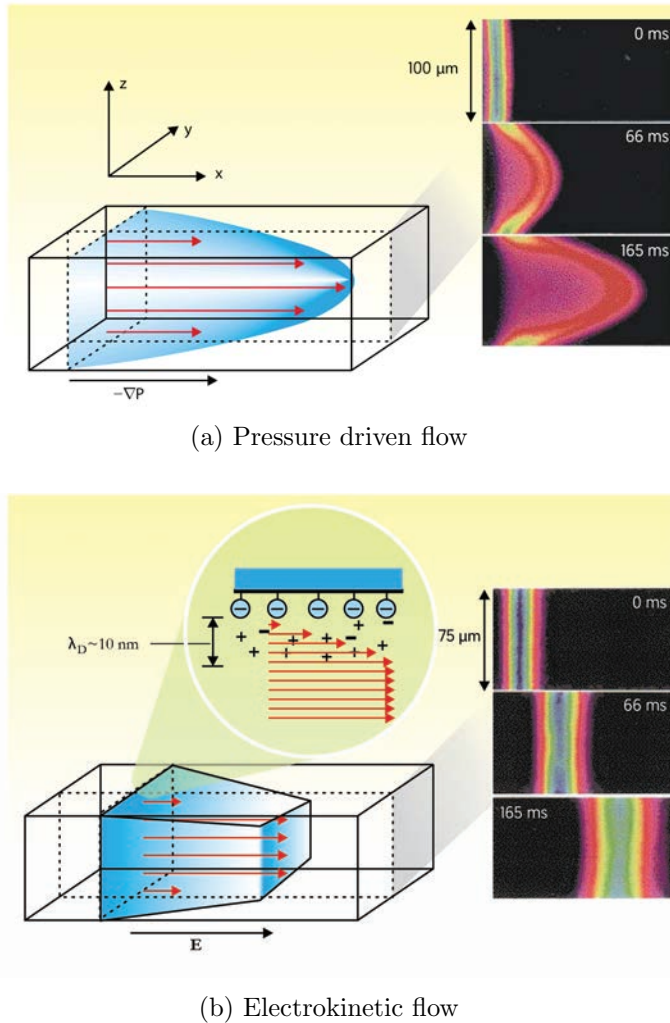
Figure 1.4: Schematic representation of pressure driven and electrokinetic flow profiles. On the right, experimental measurements of the flow distortion by monitoring the fluorescence of a molecule at different times. Adapted from Whitesides and Stroock 2001.

$$t_d = \frac{l^2}{2D} \tag{1.3}$$

Although mixing in microfluidic systems is limited only to diffusion, the reduced dimensions of the channels imply reduced diffusion times. Traditional laboratory methods such as microtiter plates may take longer times as compared to an analogous LOC (as seen in Equation 1.3, $t_d \propto l^2$).

Heat transfer The thermal Péclet number (Pe_L) is another dimensionless number, in this case indicating the ratio of advective to diffusive heat transport (see Equation 1.4). Like the Reynolds number, the thermal Péclet number accounts for characteristics of both the fluid (density ρ, thermal conductivity k and specific heat capacity C_p) and the environment in which it is manipulated (channel diameter d and fluid velocity v).

$$Pe_L = \frac{Advective}{Diffusive} = \frac{\rho \, d \, v \, C_p}{k} \tag{1.4}$$

This parameter is relevant because it describes the relative importance of heat transfer due to bulk fluid movement and heat conductivity. For instance, when heat is applied to a microchannel (e.g. in a microfluidic reactor), it can be transported by the moving fluid in the direction in which it travels (advective transport), or from the wall towards the center of the fluid flow (diffusive transport). The small dimensions of microfluidic channels enable a prevalent diffusive transport and consequently, a more homogeneous temperature distribution. Pe_L values for microfluidic systems are usually below 1000. In contrast, bulk systems usually have a more heterogeneous temperature distribution due to their much bigger characteristic dimension.

1.1.3   Potential Advantages & Challenges

The special behavior of fluids confined to the microscale, the integration potential and the enhanced mass and heat transfer confer LOC systems very interesting properties. Therefore several advantages over macroscopic or bulky systems are expected (Whitesides 2006), such as those listed below.

Portability The reduction in size enables the realization of portable (or even wearable) systems. This may have a great impact in biomedical diagnostics for POC applications, as well as in environmental analysis.

Automation LOC systems usually integrate several laboratory operations in an automated way, thus minimizing manual operation. In consequence, errors associated with manipulation are avoided. A lower degree of manual operation may also have positive effects in reducing manipulation stress in cells.

Small Volumes LOC systems require of much smaller volumes of sample and reagents. This has a positive impact on the cost of the process as well as in the sample requirements.

Throughput The reduced footprint of a LOC systems enables the parallelization or the serial processing of samples in a limited laboratory setting. This opens up new possibilities in drug discovery, proteomics, synthetic and analytical applications.

Biological Scale Microfabrication techniques enable the replication of environments that mimic in vivo conditions. This can have a great impact on biological applications for cell studies.

Mass and Energy Control Due to the smaller dimensions, mass and energy transfer processes can be more accurately controlled than in macroscopic systems. For instance, heating systems can be designed to achieve homogeneous temperature distribution in LOC systems for biological or synthetic applications.

Rapidity The small characteristic dimensions of microfluidic systems enable faster mass-transfer limited reactions (that is, reactions operating in the diffusive domain solely by diffusion).

Green Processes Processes carried out in LOC systems generate less waste due to the lower reagent consumption. Furthermore, these processes require a lower energy consumption (for operation and heating) than their bulk analogues.

Safety LOC systems are confined environments in which dangerous chemistry (involving toxic, very reactive or explosive intermediates) can be performed. Furthermore, the high surface to volume ratios enable fast heat dissipation in exothermic reactions.

Nevertheless, this is still an early-stage technology, and not all of the potential advantages described above can be fully realized or attributed to a single LOC system. Careful consideration of potential challenges and risks posed by the LOC technology needs to be assessed.

The reduced dimensions confer LOC systems many advantages, as previously discussed. However, the very same dimensions cause an important

problem. Surface adsorption in microchannels with such high surface to volume ratio may actually result in noticeable sample loss. Another facet of this problem is the nonspecific adsorption of proteins in enzymatic assays and its potential background noise. Different alternatives may be used to circumvent nonspecific adsorptions, such as surface passivation (Perez-Toralla et al. 2013) or physical separation of the unit operations (Herrmann, Veres and Tabrizian 2008), although more complexity is added to the system. Moreover, scaling down takes the conventional analytical techniques to the limit, and the reduction of sample volume involves that a lower number of molecules are to be found.

The development of certain components or processes also needs to be addressed. Issues like sample pre-treatment, matrix complexity, world-to-chip interfaces (Temiz et al. 2015), storage and stability of reagents, etc., are still hindering the development and commercialization of LOC systems (Chin, Linder and Sia 2012).

Furthermore, all the different steps of a process need to be integrated. As a technology in its early-stage, the LOC community has usually focused on the development of individual components. The lack of a holistic LOC development, or that of a standardized modular approach, is a major challenge in the future development of this technology. Finally, microfluidic applications require of specialized instrumentation and expertise, not available to all the potential end-users. Pumping, for instance, is usually performed with expensive, complex and non-miniaturized flow control systems, for convenience. Same occurs with detection instrumentation —generally due to lower performance of the miniaturized analogue— or other actuation systems. A balance must be found then, between convenience and performance on the one hand, and product vision and pragmatism on the other.

1.2 Microfabrication Technologies & Materials

Over the last two decades, microfabrication technologies significantly evolved and new materials emerged as substrates for LOC devices. The purpose of this section is to give a brief overview of the main technologies and materials available, their advantages and disadvantages in this field. However, the diversity of fabrication approaches is too wide to include them all, and therefore this is not a comprehensive review. The technologies of silicon/glass, PDMS, thermoplastics and LTCC ceramics are covered, as well as other trending materials, although not in such depth.

It is important to emphasize that there is no universal substrate ideally suited for every application. Each particular application should be thoroughly evaluated to define the required characteristics of the substrate, and in this

way, take advantage of the wide range of materials currently available.

Not only the final use of the LOC device should determine which substrate to use, other considerations need to be taken into account. In order to strengthen the establishment of LOC technology, it is important to carefully assess the fabrication processes required both at the prototyping and mass production scales.

For instance, two different substrate materials were used throughout this work: COC and LTCC. These two materials were selected because they fulfill the required characteristics demanded by each particular application. COC provides outstanding transparency, low autofluorescence and biocompatibility for applications in which optical detection was performed and live cells were involved. LTCC provides chemical inertness and the possibility to integrate electronic elements for synthetic applications requiring high temperature and/or pressure.

At the same time, these two materials enable simple and scalable fabrication processes. The fabrication is based on a multilayer approach, consisting on the individual manufacturing of several layers, which are then stacked, aligned and laminated together. This approach enables the realization of complex 3D structures by decomposing them in different layers (see Figure 1.5), which are easier to microstructure. The main disadvantage of this approach is the resolution, which is not as good as in the case of photolithographic/deposition processes. Nevertheless, the multilayer approach provides simple prototyping processes of LOC devices that can be easily scaled up to mass production without the need of special facilities such as cleanrooms.
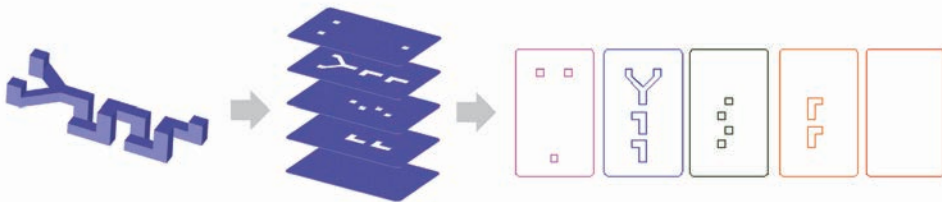
Figure 1.5: Design process using a multilayer approach. In this example, a 3D microfluidic mixer is broken down to individual layers. Adapted from Gómez-de Pedro 2014.

1.2.1 Silicon/Glass

Silicon and glass are the first materials used in LOC applications as their fabrication technology was inherited from the microelectronics industry. Therefore, the technology is well established, basically consisting of photolithography and

etching processes (see Figure 1.6). In general, photolithography involves the coating of a wafer with a photoresist and its selective irradiation with UV light through a photomask —which contains the desired patterns. The exposure to UV light chemically alters the photoresist modifying its solubility in a specific developer solution. Once the photoresist is patterned, the etching process removes either the exposed or unexposed substrate (depending on wether a positive or negative photoresist was used), thus creating the desired patterns in the wafer.

(a) Photolithography using a positive photoresist
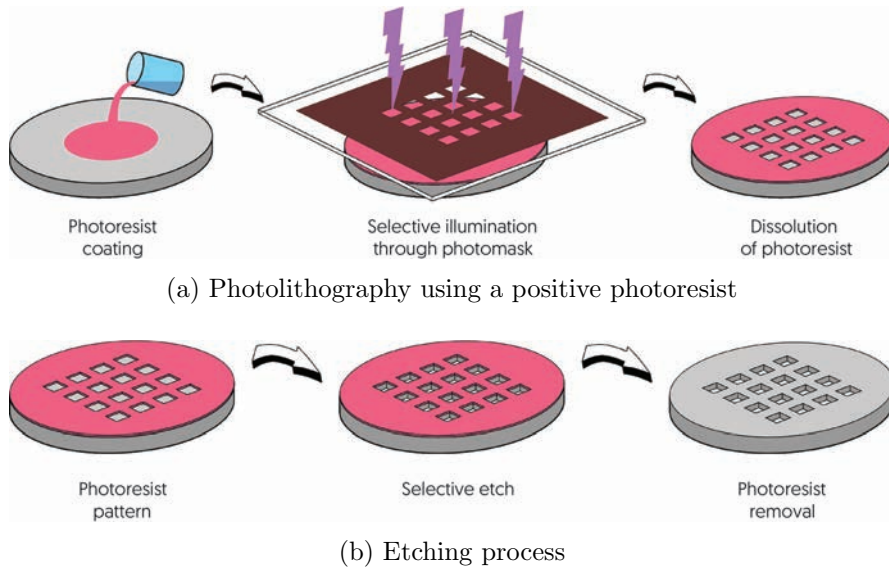
(b) Etching process

Figure 1.6: Schematic representation of basic photolithographic and etching processes. In this example, a positive photoresist was used, and therefore, the areas exposed to light were dissolved in the developer solution. On the contrary, using a negative photoresist would make the unexposed areas soluble in the developer solution. The etching process removes material only from the areas where the photoresist was removed. Adapted from Folch 2012.

The main advantages of this technology derive from the deep understanding and experience on photolithography and etching chemistries accumulated over the years. Microchannels can be precisely fabricated with a resolution down to ~ 0.5 μm and high aspect ratios, usually up to 20:1 (Iliescu et al. 2012). Silicon can withstand high temperatures and has a high thermal conductivity, very important characteristics when homogeneous temperature distribution is required (Pipper et al. 2007; Trachsel, Hutter and Von Rohr 2008). It also enables the integration of electrodes or even electronic circuits. On the other hand, fabrication processes need to be carried out in cleanroom facilities

and are not cost efficient at a prototyping level.

1.2.2 PDMS

This elastomer revolutionized the microfluidics and LOC communities thanks to the simple fabrication (at a prototyping level) and interesting properties for MEMS and microfluidic applications. The group of Whitesides developed a family of microfabrication techniques known as *Soft Lithography*, which have in common the use of a micro-molded PDMS piece (Xia and Whitesides 1998; Qin, Xia and Whitesides 2010). The fabrication of the PDMS piece requires a negative mold, usually produced by photolithography, although other techniques are also employed. Once the mold is produced, PDMS enables the rapid and simple replication of the microfluidic patterns by replica molding (see Figure 1.7). The PDMS positive replica can be bonded to itself (Eddings, Johnson and Gale 2008) as well as other materials such as glass or silicon (Duffy et al. 1998) to produce the final LOC device without the need of adhesive. The PDMS positive replica can also be used for fabrication purposes, i.e., as a tool for patterning.
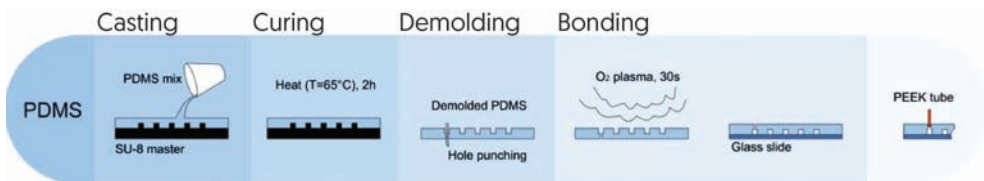
Figure 1.7: PDMS microfluidic device fabrication process. Adapted from Sollier et al. 2011.

PDMS-based LOC devices take advantage of the outstanding optical, surface and mechanical properties of PDMS. Together with its fabrication simplicity at a prototyping scale, these properties make of PDMS the material of choice for scientists in academia. The optical transparency enables visualization of the liquids as well as the integration of optical detection. PDMS is biocompatible and relatively inert although its surface can be functionalized (Zhou, Ellis and Voelcker 2010). The chemical structure of PDMS (see Figure 1.8) enables rotation of the Si——O bonds, thus originating its characteristic flexibility. This mechanical property is used for the fabrication of valves and pumps (Unger et al. 2000). However, PDMS suffers from certain drawbacks such as the adsorption of small molecules, solvent compatibility and permeability, uncross-linked polymer leaching and, most importantly, fabrication scalability (Toepke and D. J. Beebe 2006; Mukhopadhyay 2007; Berthier, Warrick, et al. 2008; Regehr et al. 2009; Becker 2009).

The PDMS positive replica can also be used for surface patterning. There
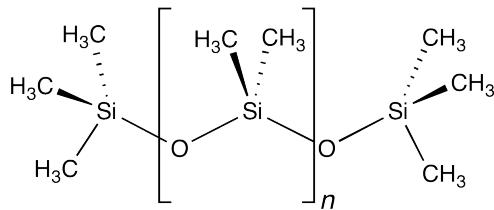
Figure 1.8: Chemical structure of PDMS. Some of the methyl groups are substituted by cross-linkers.

are two main soft lithographic patterning strategies, namely *Microcontact printing* and *Microfluidic patterning*. On the one hand, microcontact printing uses the PDMS as a "stamp" to pattern a surface by transferring the material of interest only on the contact areas (Perl, Reinhoudt and Huskens 2009). On the other hand, microfluidic patterning uses the channel network on the PDMS to deliver fluids onto selected areas of the substrate (Kane et al. 1999). This approach can be used both to deposit material on the substrate as well as to etch it.

1.2.3   Thermoplastics

The limitations of PDMS have hard-pressed the use of other materials in microfluidics, such as the thermoplastics, which are backed by the mass-production capabilities of the plastic industry. Thermoplastics are materials that become moldable above the Glass Transition Temperature (T_g) and regain their structural properties upon cooling (Becker and Gärtner 2008). Thanks to this behavior, thermoplastics are well-suited to mass-production techniques such as injection molding or hot embossing, and thus dramatically lower the cost per unit (Becker 2009). This is very important in µTAS applications, where single use devices are preferred to avoid contaminations, specially with biological samples. Furthermore, a wide variety of thermoplastics is available to choose from, making it possible to suit the needs of specific (bio)applications (Midwoud et al. 2012). The most common thermoplastics are Poly(methyl methacrylate) (PMMA), Polystyrene (PS), Polycarbonate (PC) and Cyclic Olefin (Co-)Polymers (COP/COC). Table 1.1 highlights some properties of these thermoplastic materials.

Many microstructuring methods exist for thermoplastics, both at the prototyping (direct structuring) and mass-production (replication) scales, offering different advantages and limitations (Becker and Locascio 2002). On the one hand, replication techniques, such as hot embossing or injection molding, are amenable for mass-production and well established in the plastic industry. However, they incur in high start-up costs, limiting their application to low-

Table 1.1: Qualitative properties of COP/COC compared to other thermoplastics. Information retrieved from Nunes et al. 2010 and Tsao 2016.

	Thermoplastics			
	COP/COC	PMMA	PC	PS
Thermal[1]	70–155 ℃	100–125 ℃	140–150 ℃	90–100 ℃
Solvent Resist.	+	∘	∘	−
Acid/Base Resist.	+	∘	∘	∘
Transmittance Vis	+	+	+	+
UV	+	∘	−	−
Biocompatibility	∘	∘	∘	∘
Cost[2]	20–25 $/kg	2–4 $/kg	<3 $/kg	<3 $/kg

[1] Thermal refers to the Glass Transition Temperature (T_g).
[2] Cost for the thermoplastic material in pellets.
 Legend: (+) Excellent, (∘) Good and (−) Poor.

volume production. On the other hand, direct structuring enables the rapid prototyping of microfluidic devices. Laser ablation (Gattass and Mazur 2008; Cai et al. 2017) and stereolithography (Au et al. 2016) offer very promising capabilities and are rapidly evolving, yet they still are not fully developed for thermoplastic manufacturing (Guckenberger et al. 2015). Laser ablation is not deeply studied in substrates like COC (Nunes et al. 2010) and may yield poorly defined structures (Ymbern 2016). Stereolithography may revolutionize the manufacturability of microfluidic devices in small to medium production numbers, although it still suffers from resin compatibility, resolution and throughput (Bhattacharjee et al. 2016).

Micromilling is an alternative for the rapid prototyping of microfluidic devices. It creates microscale features using cutting tools that remove bulk material from the substrate, as seen in Figure 1.9. Milling is a well-characterized machining process for other materials, such as aluminum or copper (for Printed Circuit Board (PCB) production), and therefore, there is in-depth technical knowledge about the process (Guckenberger et al. 2015). In the case of microfluidic systems, micromilling offers a key advantage: the short turnaround time from design to prototype. A comprehensive review on micromilling and its comparison to other methods (both from technical and economic perspectives) can be found in Guckenberger et al. 2015. This microstructuring method has been used throughout the thesis for the prototyping of thermoplastic microfluidic devices.
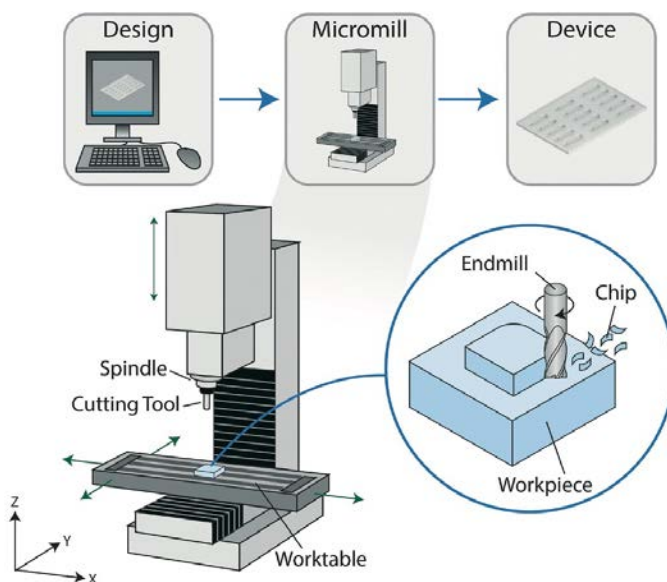
Figure 1.9: Schematic representation of the micromilling process and basic components of a CNC micromilling machine. Adapted from Guckenberger et al. 2015.

1.2.3.1 Cyclic Olefin (Co-)Polymers

COP/COC are a group of thermoplastics with very interesting properties for LOC applications (Nunes et al. 2010). COP/COC show excellent chemical resistance to acids, bases and solvents, low autofluorescence and an outstanding optical transparency, even in the UV range. Furthermore, they are biologically inert and therefore suitable for biological applications (Jeon et al. 2011; Midwoud et al. 2012; Berenguel-Alonso et al. 2017) and approved for use in medical devices through *USP Class VI* certification (Kuo and D. T. Chiu 2011). This assets put COP/COC in the spotlight for microfluidic applications.

Different materials are available under a handful of commercial suppliers, being TOPAS Advance Polymers (TOPAS) and Zeon Chemicals (Zeonex and Zeonor) the most commonly used in microfluidic applications. Two main approaches exist for the synthesis of these polymers (see Figure 1.10), namely *Chain polymerization* (used by TOPAS) and *Ring opening metathesis polymerization* (used by Zeon). Due to the fact that TOPAS is synthesized from two monomers (norbornene and ethylene), it is referred to as Cyclic Olefin Copolymer (COC), while Zeon products are generally referred as Cyclic Olefin Polymer (COP).

Another interesting characteristic of this group of polymers is their wide range of T_g (see Table 1.1). The T_g of COP/COC can be tuned without
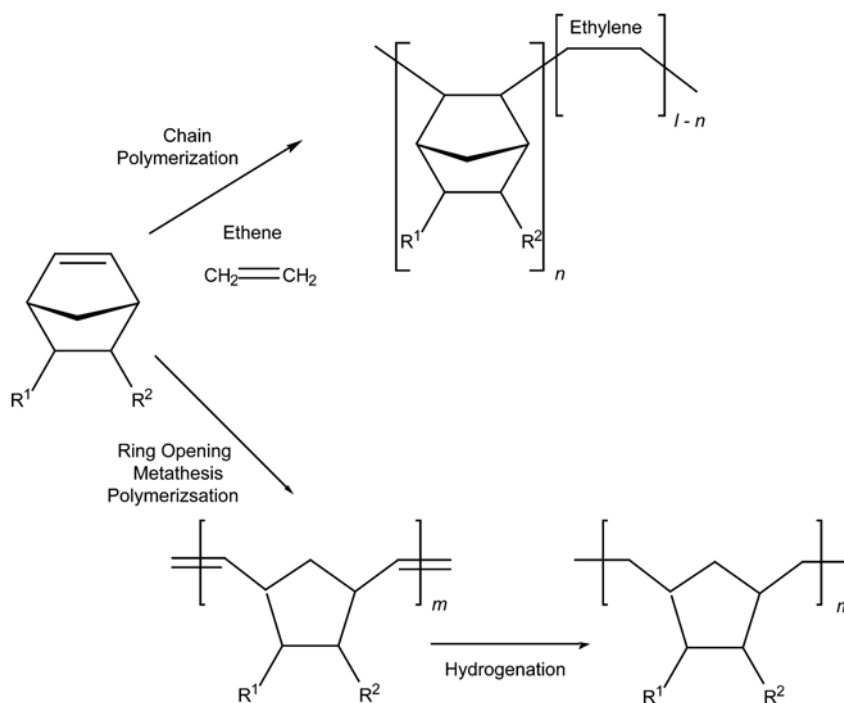
Figure 1.10: Typical polymerization scheme for a cyclic olefin polymer. Adapted from Shin et al. 2005.

altering the structural and optical properties of the material, by means of two different strategies. On the one hand, Zeon Chemicals tunes the T_g by changing the substituents of the norbornene (Yamazaki 2004). On the other hand, TOPAS tunes the T_g by varying the norbornene to ethylene ratio of the polymer (Błochowiak 2006). This simple fine-tuning of the polymer gives rise to a wide range of products commercially available, opening up new fabrication strategies, particularly regarding the bonding stage.

Bonding is one of the most challenging steps in the fabrication process of LOC devices. In thermoplastics, channel deformation restricts the experimental conditions of thermo-compression processes, while surface activation or solvent bonding may pose a threat for biology applications. COP/COC with different T_g enable a simple and effective sealing approach by thermal diffusion bonding. For instance, throughout this dissertation, a COC with higher T_g is used for the microfluidic structures, while a different grade with lower T_g is used as sealing or "gluing" layer. The strength of the bond is based on the interlink of the polymer chains when the surfaces are closely put together and locally heated above the T_g of the gluing layer, but below that of the

structural one (R. Jena, C. Yue and Anand 2011). In this way, the chemistry of the microchannels is not modified, the structural layer can easily maintain its integrity and a high strength bond can be achieved (Steigert et al. 2007). Furthermore, this technique can be easily scaled up for mass production.

In this thesis, COC (from TOPAS Advance Polymers) was used as substrate for the fabrication of LOC devices when optical detection and/or microchannel visualization were required. The choice was made according to the exceptional properties of the material, the simple prototyping process COC enables and its potential scalability.

1.2.4 LTCC

LTCC is a substrate originally devised for electronic multilayer packaging purposes. The two key features of this material are explicitly defined in its name. *Low Temperature* refers to the fact that these ceramics are sintered below 950 ℃, a relatively low temperature compared to that of classic ceramic substrates like α-Al$_2$O$_3$ (around 1650 ℃). But why is a lower sintering temperature necessary or an advantage? *Co-fired Ceramics* refers to the fact that LTCC are sintered together with other materials, usually metals (Ag, Au, Cu . . .), which act as conductors. These metals have melting temperatures around 1000 ℃, and therefore require sintering at lower temperatures in order to reliably produce high performing devices.

LTCC are polycrystalline solids containing alumina (Al$_2$O$_3$) and glass. They are commercially available as a tapes or layers of different thickness (50–400 μm). In its green state (i.e. before the sintering or firing process), LTCC are malleable and can be easily manipulated and microstructured; once fired, they become dense and hard (Strnad 1986). A sintering model is depicted in Figure 1.11. At sintering temperature, the glass is in liquid phase, while the alumina grains remain solid. The glass wets the alumina due to favorable surface free energies and capillary forces in the solid grains (Birol 2007). Upon temperature decrease, glass-ceramic vitrification is initiated (Gongora-Rubio et al. 2001).
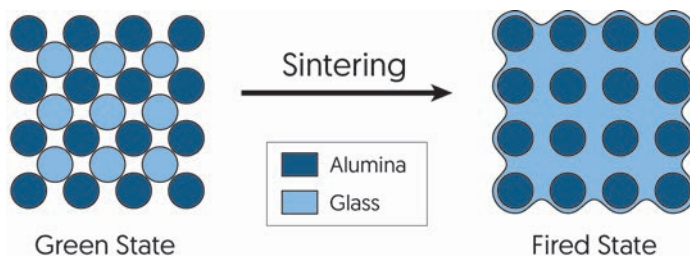
Figure 1.11: LTCC sintering model. Adapted from Gongora-Rubio et al. 2001.

Besides glass and alumina, the LTCC green tapes contain organic components where the amorphous and crystalline solids are dispersed. It consists of a polymeric binder, plasticizers and solvents, among others (X.-J. Luo et al. 2004). This organic medium gives very important properties to the green tapes, such as an appropriate viscosity, wettability, drying rate or chemical inertness towards the inorganic compounds present on the substrate and screen-printing pastes. The organic medium is removed in a burnout step at 350 ℃ before reaching the firing temperature.

The simple processing of LTCC devices, based on a multilayer approach (as mentioned in Section 1.2), enable the fabrication of microfluidic structures. Furthermore, these systems enable the monolithic integration of both fluidics and electronics in a simple way, for instance, for data acquisition or signal processing (see Figure 1.12). The fabrication process is based on three steps (Couceiro 2016): 1) individual machining (by laser processing) of each LTCC layer that constitutes the microfluidic system and (if required) application of conductive pastes, 2) stacking, alignment and lamination of all layers, and 3) sintering of the ceramic device. Another advantage of this technology is the fact that it does not require of cleanroom facilities for fabrication. The mechanical properties and chemical inertness of LTCC make this substrate an interesting candidate for both analytical (Ibáñez-García et al. 2008; Vasudev et al. 2013) and synthetic applications (Gómez-de Pedro, Puyol and Alonso-Chamarro 2010; Jiang, Maeder, et al. 2015). On the other hand, the main disadvantages of this substrate for LOC applications are its opacity, fragility and shrinkage upon firing (due to the removal of the organic components). However, the shrinkage is predictable and, therefore, dimension considerations can be assessed during the design stage.

In this thesis, LTCC was used as substrate for the fabrication of LOC devices when integration of electronics and fluidics, high chemical resistance and extreme conditions (pressure, temperature) were required. The choice was made not only according to the interesting properties of the material, but also taking into account the prototyping simplicity and its potential scalability.

1.2.5 Others

In the last years, new materials and technologies started to gain traction within the LOC community. These present certain key advantages over the more classic material approaches, previously described, in certain applications. However, further research must address the challenges posed by their early-stage technology.
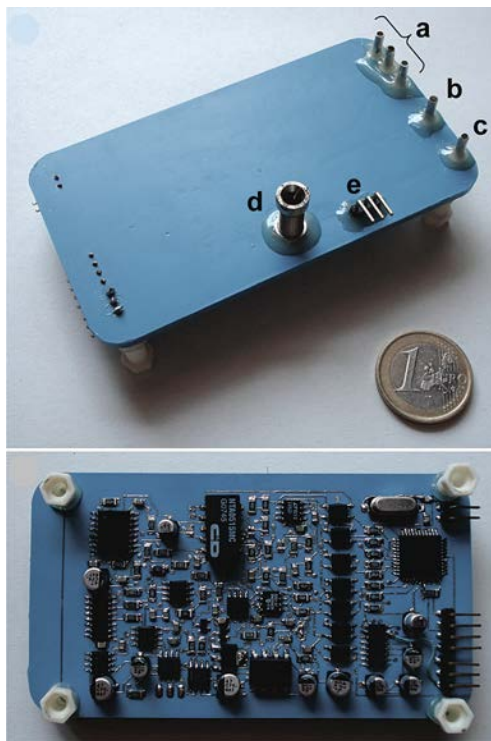
Figure 1.12: Monolithically integrated amperometric analyzer (top and bottom views, respectively). Adapted from Martínez-Cisneros, Rocha, et al. 2009.

1.2.5.1 Paper

Microfluidic Paper-based Analytical Devices (µPAD) have attracted notable interest within the µTAS community due to their low cost and operation requirements (Xia, Si and Z. Li 2016). These attributes enable the fabrication of disposable devices for POC applications, especially for limited resource settings. Paper is a highly porous cellulose matrix in which liquids are transported by capillary forces (see Figure 1.13).

Channels are defined by keeping their paths hydrophilic while modifying the rest of the surface hydrophobically. Fabrication approaches take advantage of simple surface modifications or more complex lithographic processes to render the desired surface character. Generally, these fabrication approaches are divided in two groups, namely photolithographic and printing techniques (Ren, Zhou and Wu 2013). Photolithography is the most complex and expensive approach, but has the best resolution. In contrast, printing methods require simpler equipment, are much cheaper and do not expose the microchannel area to chemicals. This approach can be further divided in printing, hand craft and cutting methods (Cate et al. 2015).

The simple fluid actuation in µPAD devices enables their application as POC analytical devices. Reagents are usually pre-stored along the microchan-
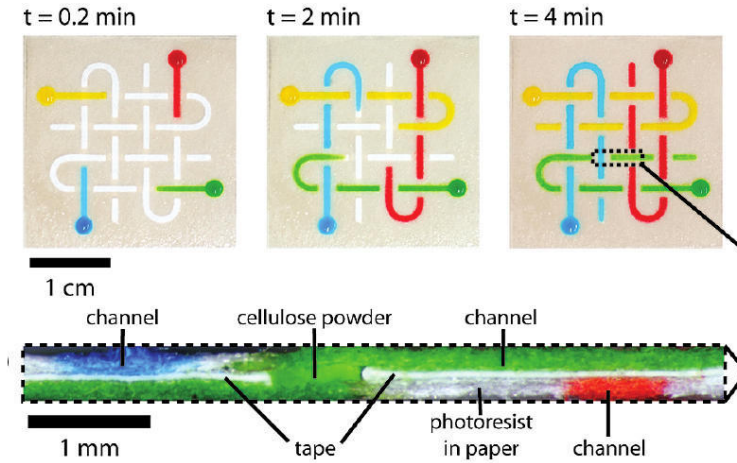
Figure 1.13: 3D microfluidic paper-based device. Top views at different times demonstrating good liquid transport, and cross-section view showing the 3D structure of the μPAD. Adapted from Martinez et al. 2010.

nel and detection methods are in most cases optical, due to their simpler implementation and readout (Mark et al. 2010; X. Li, Ballerini and Shen 2012). For instance, colorimetry enables naked eye readouts as well as the use of smartphones or cameras as detection systems (Ortiz-Gomez et al. 2016). Nevertheless, electrochemical detection strategies as well as integration of electronics have also been reported (Hamedi et al. 2016). In any case, smartphones open the possibility of telemedicine applications (Lopez-Ruiz et al. 2014).

1.2.5.2 Hydrogels

These materials are emerging as a promising alternative for cell-based studies in which the mimicking of biological conditions is an important factor. Hydrogels are 3D polymer networks in a water-based environment, resembling the extracellular environment (Geckil et al. 2010). Therefore, they are mainly used for cell culture or tissue engineering applications (Chung et al. 2012; Ghaemmaghami et al. 2012). They are highly porous, thus enabling transport of molecules and even particles, although diffusion is limited. Fabrication is still in an early development stage, and challenges arise from the complex necessities of functional tissues and cell environments (G. Y. Huang et al. 2011). The integration of microfluidic networks in hydrogels could greatly contribute to biological studies by mimicking *in vivo* conditions.

1.3 Applications of Microfluidic Systems

Microfluidics and LOC are *enabling* technologies. This means that as much fun as they can be on their own, they are simply tools. Therfore, the real value of LOC technology is the enhancement (or new possibilities) they provide in the myriad fields where they are applied. Possibilities are endless.

Chemistry can greatly benefit of LOC technology. In fact, analytical chemistry was the origin of the field, the birth of µTAS. These systems can potentially detect (bio)analytes of interest at a fraction of the cost, in an automated way, with little sample requirements, a small footprint and on-site. Synthetic chemistry can also take advantage of the possibilities of LOC technology. The enhanced mass and heat transfer, as well as the parallelization capabilities may bring synthetic chemists to a new paradigm.

Biology is the other main beneficiary of LOC technology. Proteomics can take advantage of the automation and high throughput of microfluidic devices. Cell biology studies can be taken to a whole new level by mimicking the *in vivo* conditions. This is possible due to the development of techniques that enable the fabrication of structures in the cell-scale range, and even smaller. Moreover, cells can be individually dealt with, by serial processing in flow cytometry or by trapping and culturing them. Not only can cells be alone in LOC systems, they can be studied in tissues resembling organs. LOC can simulate the necessary physiological and mechanical conditions in the so-called "organs-on-a-chip", which can even be combined into "humans-on-a-chip" to study interactions between organs.

1.4 Thesis Overview

This thesis reports on the development of novel LOC systems for analytical, biologic and synthetic applications. Advancements in the fabrication technologies of COC and LTCC enabled the development of fluidic structures for such varied applications. These substrate materials were carefully chosen according to their properties for each particular application. Moreover, the prototyping processes were designed to be as simple as possible and scalable to mass-production. Along the thesis, the fabrication processes become richer, building on previous development. Therefore, the basics will be explained in detail at first, to then focus on the particular features of the fabrication processes.

Chapter 2 describes the general objectives of the thesis. Chapter 3 reports on the design and fabrication of a magnetic actuator to control magnetic beads *on-chip*, together with its application to the detection of Escherichia coli O157:H7. Chapter 4 describes a novel fabrication process of a LOC system

for maturation of oocyte cells. Chapter 5 presents the development of microreactors for the synthesis of nanomaterials at high temperature and high pressure. Finally, Chapter 6 highlights the main conclusions and discusses future challenges and perspectives.

Chapter 2

Objectives

The Group of Sensors and Biosensors at the Universitat Autònoma de Barcelona has extensive experience in the development of Lab on a Chip (LOC) systems for water analysis and nanomaterial synthesis. This dissertation aims to keep strengthening these applications by developing devices with enhanced characteristics as well as novel analytical strategies. Furthermore, the use of LOC systems for biology applications is targeted for the first time in the group. The fabrication of LOC systems for such varied applications is based on the development of simple, scalable methodologies and the use of substrate materials particularly suitable for each application. The objectives can be summarized in more detail as follows:

- Development of a LOC system to perform Magnetic Beads (MBs)-based bioassays *on-chip*. Furthermore, the design and fabrication of a magnetic actuator is required, in order to capture and control the MBs.

- Development of a novel LOC system suitable for oocyte cells maturation *on-chip*.

- Development of novel microreactors for magnetite and Carbon Dots (CDots) synthesis.

Chapter 3

Magnetic actuator for the control of magnetic beads *on-chip*: mixing strategy for enhanced E. coli O157:H7 detection

3.1   Introduction

The development of micro Total Analysis Systems (μTAS) played an important role on the progress of analytical chemistry in the last 25 years due to their inherent advantages, as discussed in Section 1.1.3. Taking the lab to the sample (rather than the other way around) could fulfill the demand of society to attain simple, rapid, low-cost and *in situ* information of chemical or biological systems (Kovarik et al. 2013). The unfolding of the potential of μTAS has been fostered by the integration of (bio)sensor systems, which are usually suited for miniaturization due to the simple principles upon which they are based (Alegret 2003).

(Bio)Chemical sensors are self-contained analytical devices that provide real-time information about the composition of a test sample. A biosensor basically consists of a biorecognition element and a transducer, as seen in Figure 3.1. The biorecognition element (e.g. antibody, enzyme, nucleic acid, etc.) selectively interacts with the target analyte and generates a change in a physical parameter. On the other hand, the transducer converts the biorecognition event into a measurable signal (Bănică 2012).

The immobilization of the biorecognition element *on-chip* and the integra-
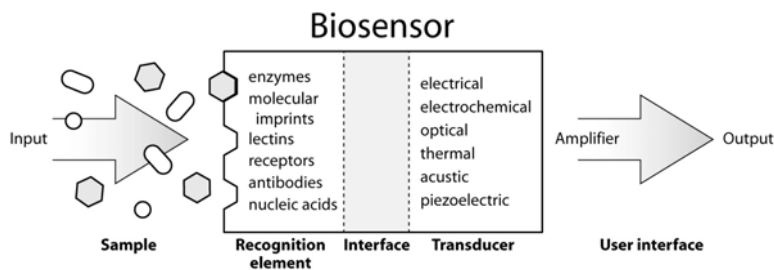
Figure 3.1: Working principle of a biosensor, showing biorecognition and transduction. Reproduced from Chambers et al. 2008.

tion of transducer systems enabled the development myriad analytic Lab on a Chip (LOC) systems (Chambers et al. 2008). The biorecognition element enables the retention of the target analyte and the removal of the sample matrix through washing steps. Immobilization strategies have been implemented for several types of biomolecules (Goddard and Erickson 2009), e.g. proteins such as antibodies or enzymes (D. Kim and Herr 2013), single stranded deoxyribonucleic acid (DNA) (Sabourin et al. 2010), etc. A different approach to immobilize the biorecognition element consists on the use of superparamagnetic microparticles —commonly known as Magnetic Beads (MBs).

MBs emerged in the 1980s as a suitable substrate to immobilize the biorecognition elements due to their high surface-to-volume ratio, surface tunability, easy control using an external magnetic field and facile redispersion in solution after removing it (Gehring and Tu 2011). Immunomagnetic separations, for instance, have been used for decades to isolate biomolecules and wash out the sample matrix using Eppendorf tubes (see Figure 3.2). Moreover, the easy control provided by external magnets also enables the strategic positioning of the MBs onto the surface of the transducer during the detection step (Liébana et al. 2009).

Superparamagnetism is observed in ferro- and ferrimagnetic materials (usually magnetite Fe_3O_4 or maghemite Fe_2O_3) below a critical dimension (*ca.* 5–100 nm). When the particle size is smaller than this dimension, the material exists as a single domain nanoparticle, i.e. the magnetic moments of all the atoms in the nanoparticle are aligned without applying an external magnetic field (Gijs 2004). This means that the nanoparticle has a net magnetic moment in one direction. However, the magnetization of these nanoparticles randomly flips due to thermal energy, and in consequence, their time-averaged magnetization is zero (Pankhurst et al. 2003).

When an external magnetic field is applied, the moments of the nanoparticles align, thus acquiring a net time-averaged magnetization. It is important to highlight that since the materials forming these nanoparticles are ferro- and
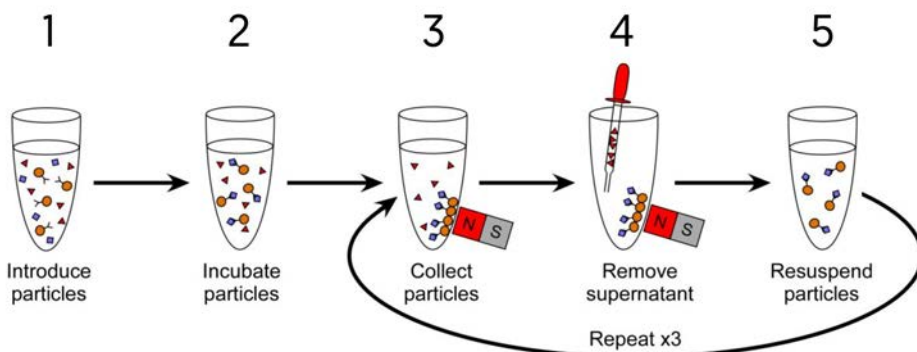
Figure 3.2: Typical procedure of separation using MBs. The sample is mixed (1) and incubated (2) with the MBs. Then, a magnet is used to collect the MBs (3), the supernatant is discarded (4) and MBs are resuspended with fresh buffer solution (5). To ensure a complete removal of unbound material, steps 3–5 are repeated 3 times. Adapted from Tarn 2011.

ferrimagnetic, they exhibit very high magnetic susceptibility. This magnetization triggers the migration of the nanoparticles towards the highest magnetic field region. Once the external magnetic field is removed, the thermal energy causes again the magnetic moments to randomly flip, the magnetic nanoparticles lose their net magnetization and therefore can be easily redispersed in solution. So how do micron-sized MBs exhibit superparamagnetic behavior? The answer is that they generally consist of a Polystyrene (PS) matrix with embedded superparamagnetic iron oxide nanoparticles (SPION).

The versatility and availability of MBs are promoting their use in LOC devices (Reenen et al. 2014), thus enabling the automation of the assays, the reduction of the equipment required and minimizing the consumption of reagents (Gijs, Lacharme and Lehmann 2010). Choi and co-workers pioneered in the development of a complete MB-based immunoassay in a microfluidic channel (Choi et al. 2002). They trapped the MBs with an electromagnet and sequentially performed all the reactions and washing steps involved, including the enzymatically generated electrochemical detection. Enzyme-linked bioassays are widely used in these systems because the amplification step allows achieving lower Limit of Detection (LOD). Other detection methods based on enzymatic signal generation have been applied in MB-based microfluidic assays, such as amperometry (Laczka et al. 2011), colorimetry (Shikida et al. 2006), fluorescence (Sen, Harvey and Clausen 2011) or chemiluminescence (Sista et al. 2008).

A key challenge in the development of LOC systems for MB-based bioassays is the limited interaction between the MBs and the reagents. On the one hand, diffusion is the only mixing mechanism in laminar flow. On the other hand, as a result of the external magnetic field MBs are aggregated, thus "hiding" the biorecognition elements from the reagents (Saville et al. 2013; Yeap et al. 2012). To overcome this issue, methods to control and mix MBs with the reagent *on-chip* have been proposed. In these approaches, MBs become not only the support of the bioassay, but also an active *on-chip* mixing and transport agent.

Continuous flow devices have been used as platforms for free-flow magnetophoresis, in which an external magnet deflects the MBs and separates them according to their size and amount of magnetic material. Pamme's group developed a system with co-flowing reagent streams and a permanent magnet on the side (see Figure 3.3a), demonstrating its suitability for both a sandwich immunoassay (Peyman, Iles and Pamme 2009) and DNA hybridization (Vojtíšek, Iles and Pamme 2010). The magnet deflects the trajectory of the MBs, making them cross the different streams, thus colliding and binding to sample/reagents. Other continuous-flow devices have been proposed, in which MBs are deflected by a magnet towards different streams in order to perform a reaction or to be washed (Karle et al. 2010; Sasso et al. 2012; J. J. Lai et al. 2009).

Another example is the magnetic trap developed by the group of Ligler (Verbarg et al. 2012) for a microflow cytometer, which consists of radially arranged magnets on a rotating support (see Figure 3.3b). Depending on the rotation direction, magnets trap —counteracting the liquid flow— or release the MBs. However, continuous flow systems may not be suitable for assays in which an amplification step is required, as they are limited by the flow rate. Furthermore, a continuous flow operation requires relatively high consumption of reagents.

More complex systems of magnets have been used to control the MBs in continuous flow. For instance, the actuator proposed by Ramadan and coworkers creates areas that sequentially trap and release MBs along a microfluidic channel (Ramadan and Gijs 2011). Despite being effective, this system is rather complex and requires a long microfluidic channel.

Unlike continuous flow systems, stop-flow approaches can tune the incubation time according to the assay needs, and the reaction volume is defined by the geometry of the device. Taking advantage of this, Herrmann et al. developed a magnetic actuator consisting of a mobile magnet (Herrmann, Veres and Tabrizian 2006), in order to move MBs from one end to the other end of a reaction chamber during the amplification step of an immunoassay. This movement enhanced the substrate exploitation rate and decreased the required reaction times. A further development of their Polydimethylsiloxane (PDMS) device
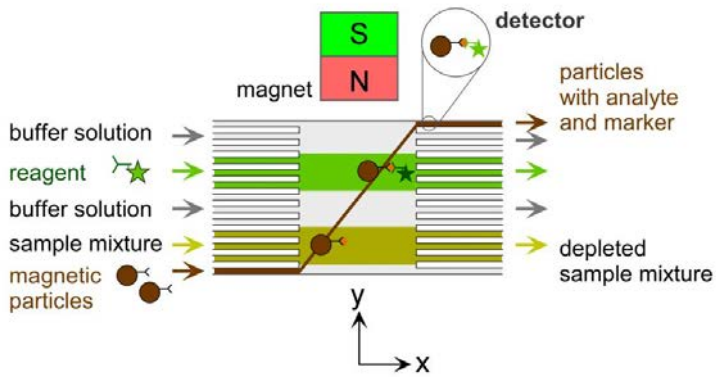
(a) Actuator proposed by Pamme's group
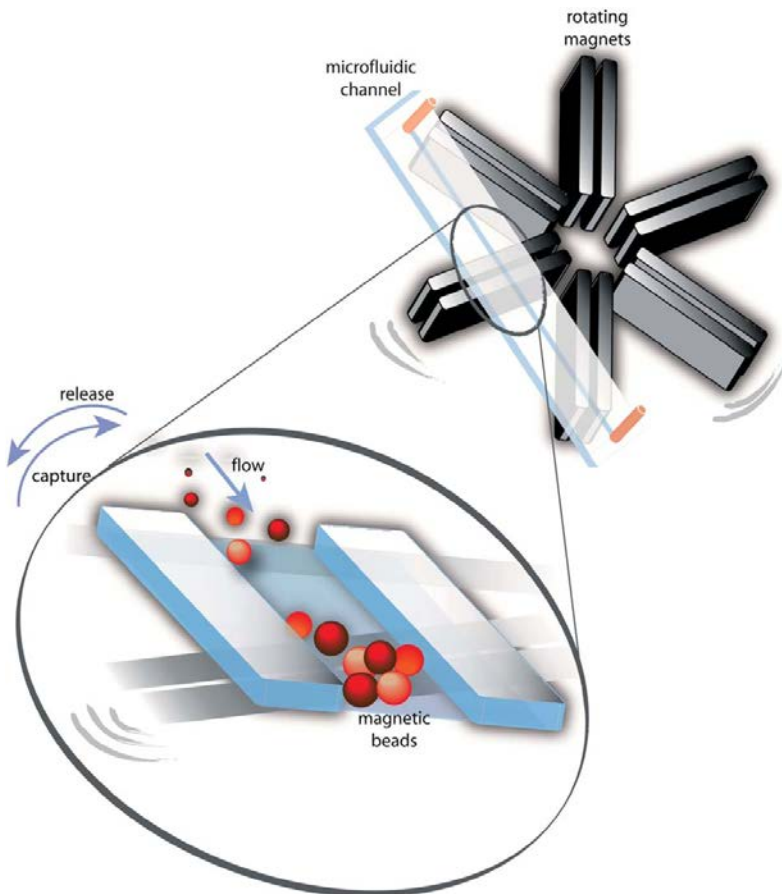
(b) Actuator proposed by Ligler's group

Figure 3.3: Magnetic actuators for the control of MBs *on-chip* found in the literature. Adapted from Vojtíšek, Iles and Pamme 2010 and Verbarg et al. 2012, respectively.

enabled both the formation of the immunocomplex and the enzymatic reaction to be carried out *on-chip* (Herrmann, Roy, et al. 2007; Herrmann, Veres and Tabrizian 2008). The problem of non-specific adsorption was avoided by means of a double network of chambers connected through pneumatic valves. However, difficulties to move the magnet linearly and at the desired velocity can be foreseen.

Based on the above considerations, in this Chapter we present a novel, compact and simple magnetic actuator that efficiently moves MBs within a microfluidic structure (microchannel or microchamber). It consists of a rotating unit (same size of a CD) containing a set of magnets, which is placed just under the LOC device. The rotation of the unit triggers the movement of the MBs within the microfluidic structure. Different arrangements of magnets are studied by means of the Finite Element Modeling (FEM) software COMSOL Multiphysics, in order to find the optimal movement of the MBs. The simplicity and the design of the actuator, consisting only of a rotating unit and a DC motor, together with its low cost, would enable its use in a portable platform. Furthermore, the design of the magnetic actuator takes its application to parallel or multiplex analyses and/or centrifugal microfluidics into consideration.

The actuator is used in a stop-flow enzyme-linked fluorescence immunoassay for the detection of *Escherichia coli* O157:H7 whole cells. Only the amplification step (enzymatic reaction and the fluorescence detection) is performed *on-chip*, in order to evaluate the improvement provided by the actuator. E. coli O157:H7 is a pathogenic strain, which may produce severe illness, and has caused several outbreaks not only in foodstuffs (Feng 1995; Centers for Disease Control and Prevention 2017), but also in water (Keene et al. 1994). The MBs used in this study are commercially available, and can be purchased with a great variety of antibody surface functionalizations, making the magnetic actuator useful for a wide range of assays with off-the-shelf reagents.

This actuator has become the basis for MBs handling *on-chip* for other researchers of our research group, further demonstrating its advantages and usability. For instance, it has been used in the development of a DNA hybridization assay (Gómez-de Pedro, Berenguel-Alonso, et al. 2017) for E. coli detection. Finally, the magnetic actuator is being applied to the capture and pre-concentration of pesticides using modified MBs.

3.2 Methods

3.2.1 Materials

Dynabeads anti-E. coli O157 (diameter 2.8 μm, 5 mg/mL, catalog no. 71003) were purchased from Dynal Biotech (Oslo, Norway). The fluorescein isothio-

cyanate (FITC)-labeled anti-E. coli antibody (ab30522) was purchased from Abcam (Cambridge, United Kingdom). The alkaline phosphatase (AP)-labeled anti-E. coli O157:H7 antibody (0.1 mg, lyophilized, catalog no. 05-95-90) was obtained from KPL (MD, USA). Chemicals used to prepare the different buffer solutions including tris-buffered saline (TBS) tablets, tris-buffered saline-Tween 20 (TBST), casein blocking buffer $10\times$ (B6429), potassium chloride (KCl), diethylamine, magnesium chloride hexahydrate ($MgCl_2 \cdot 6\,H_2O$), sodium chloride (NaCl) and 4-methylumbelliferyl phosphate (4–MUP) were purchased from Sigma-Aldrich (Barcelona, Spain). Tryptone and yeast extract were obtained from Pronadisa (Barcelona, Spain).

3.2.2 Magnetic Actuator

The Neodymium Iron Boron (NdFeB) block magnets (15 mm long, 2 mm wide and 8 mm thick) magnetized through thickness grade N50, and the cylinder magnet (radius 15 mm and 5 mm thick) grade N38 were purchased from Chen Yang Technologies GmbH (Finsing, Germany). Poly(methyl methacrylate) (PMMA) was purchased from Plásticos Ferplast (Terrassa, Spain).

The magnetic actuator consists of a set of permanent magnets embedded in a CD-shaped PMMA rotor (Figure 3.4), fabricated with a Computer Numeric Control (CNC) micromilling machine. The PMMA rotor containing the magnets was mounted on a stepper motor Maxon EC-I, which provided the rotation movement (from 1 to 20 rpm) with a digital positioning controller EPOS2 24/5 (Maxon, Sachseln, Switzerland). Magnets were positioned at different radii from the center of the rotor forming a circumference, and the microfluidic device was placed just above, attached to a fixed support structure. The rotation induces the movement of the MBs within the reaction chamber of the microfluidic device, as they follow the magnets.

3.2.3 Optical Detection System

Fluorescence was measured using an in-house built detection system developed in collaboration with the Photonics Technology Group at the University of Zaragoza (Gómez-de Pedro, Puyol, Izquierdo, et al. 2012). It basically consisted of a modulated Light Emitting Diode (LED) as light source and a photodiode (PIN Hamamatsu S1337-66BR large active area) as detector, integrated in a Printed Circuit Board (PCB) (see Figure 3.5). An emission bandpass filter MF460-60 from Thorlabs (Munich, Germany) was used to prevent any excitation light reaching the detector.

The LED XSL-365-5E from Roithner Lasertechnik (Vienna, Austria) had its emission peak at 365 nm, and was tilted 45° with respect to the plane of the microfluidic device, in order to reduce interferences of the light source in
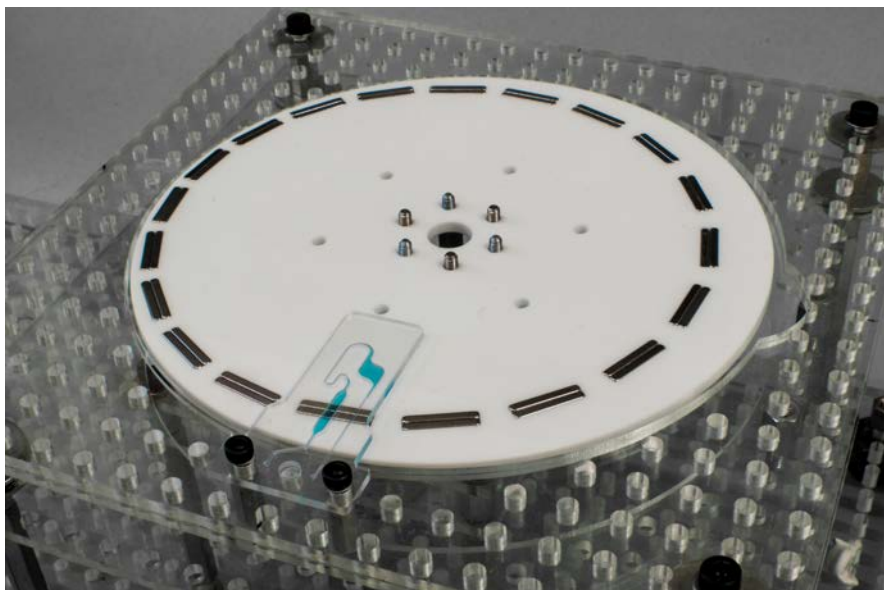
Figure 3.4: Photograph of the magnetic actuator. The white CD-shaped PMMA rotor containing the magnets is mounted on the stepper motor. The LOC device is mounted on a fixed support structure.
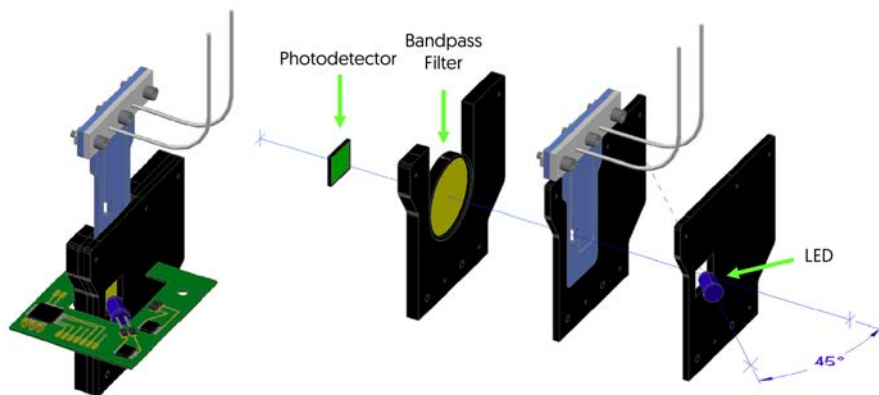
Figure 3.5: Schematic representation of the fluorescence detection system and breakdown of components. The green arrows highlight the main optical components, from left to right, photodetector, bandpass filter and LED, respectively. Adapted from Ymbern, Berenguel-Alonso, et al. 2015.

the detector. The LED was modulated and controlled by a Data Acquisition Card (DAQ) (NI USB-6211, National Instruments, Madrid, Spain), which also captured the detected signal and transferred it to a computer in order to process it. Both DAQ and PCB were powered by the computer through a USB connector. The PCB was embedded in an in-house built PMMA structure, which also accommodated the optical filter (see Figure 3.6). This structure features an insertion port for the microfluidic chip -as if it were a cartridge- with complementary shape (Ymbern, Berenguel-Alonso, et al. 2015). This insertion mechanism avoids alignment errors, and thus fluorescence readouts were performed rapid and reliably.
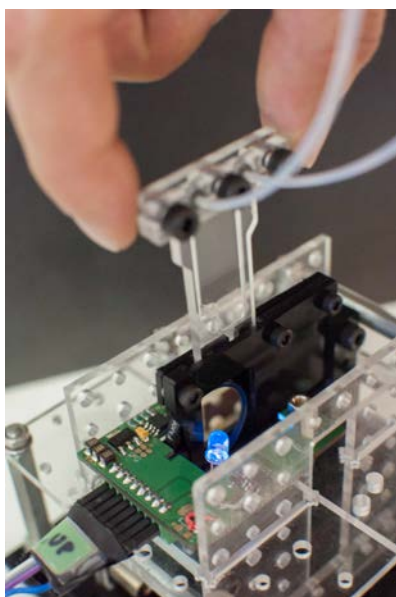
Figure 3.6: Photograph of the optical detection system while inserting a LOC device for readout.

3.2.4   E. coli culture

E. coli O157:H7 DSM number 17076 were obtained from DSMZ (German Collection of Microorganisms and Cell Cultures, Leibniz) and were cultured in lysogeny broth (LB) at 37 ℃ for 18 to 24 h with shaking at 160 rpm. Cells were pelleted by centrifugation (10,000 g, 8 min), washed twice with TBS and resuspended by gently vortexing in TBS. A portion of this bacterial solution was serially diluted and plated on LB agar in triplicate. The plates were incubated for 24 hours at 37 ℃ and the resultant colonies were enumerated in order to back calculate the bacterial culture concentration (see Figure 3.7). Only plates with 25–250 colonies were selected for enumeration.

The rest of the bacterial solution was divided in aliquots of 1 mL in Eppendorf tubes. The tubes were centrifuged in order to pellet the bacteria,

the supernatant was discarded and replaced by 50 μL of 33 % glycerol solution. Finally, the Eppendorf tubes were stored at –20 °C until needed. These ready-to-use samples enabled the daily preparation of fresh bacteria cultures by dilution with TBS (Baldrich et al. 2008).
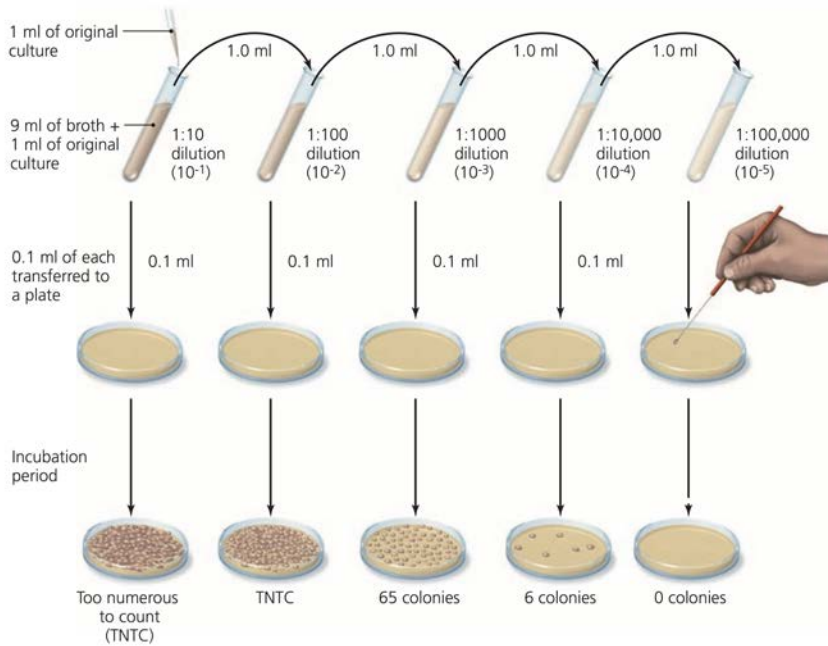
Figure 3.7: Serial dilution method for bacterial enumeration. Adapted from Bauman 2013.

3.2.5   Preparation of the Immunocomplex

10 μL of Dynabeads anti-E. coli O157 were placed in a 1.5 mL Eppendorf tube and rocked in TBST (TBST, in millimolar: 140 NaCl, 20 Tris, 0.1 % Tween 20, pH 7.6) with casein blocking buffer (diluted 1/10 in the TBST buffer) for 10 min (TBST-Casein), using a Thermomixer (Eppendorf, Hamburg, Germany) at 1,000 rpm. Then, the tubes were placed under the influence of a magnet for 2 min to trap the MBs, and the supernatant was discarded; 500 μL of the E. coli diluted sample was added and incubated for 10 min under the same rocking conditions as before. The supernatant was discarded, and the MBs were washed twice with TBST-Casein. Then, 200 μL of 1/100 diluted Phosphatase-labeled Anti-E. coli O157:H7 Antibody was added and incubated with rocking for 30 min. Finally, the MBs were washed twice with TBST-Casein and resuspended in 100 μL of diethanolamine (DEA) buffer (in

millimolar: 100 DEA, 50 KCl, 1 $MgCl_2$, pH 9.6). All reactions were carried out at room temperature.

3.3 LOC Device Fabrication

The fabrication of Cyclic Olefin Co-polymer (COC) devices consists of three main stages (Becker and Gärtner 2008), namely design, microstructuring and back-end processes (e.g. bonding, see Figure 3.8). Several microstructuring and bonding strategies are available for thermoplastics in general and COC in particular. Our fabrication approach is intended to enable simple and rapid prototyping, but taking into account the potential scalability of the process. The design consists of the 3D microfluidic structure breakdown in 2D layers (see Section 1.2). The microstructuring of the designed layers is carried out by CNC micromilling. Finally, the back-end processes correspond to the bonding of the different layers by thermal diffusion bonding. A simple strategy to upscale the fabrication would be a hot embossing process of the microfluidic structures.
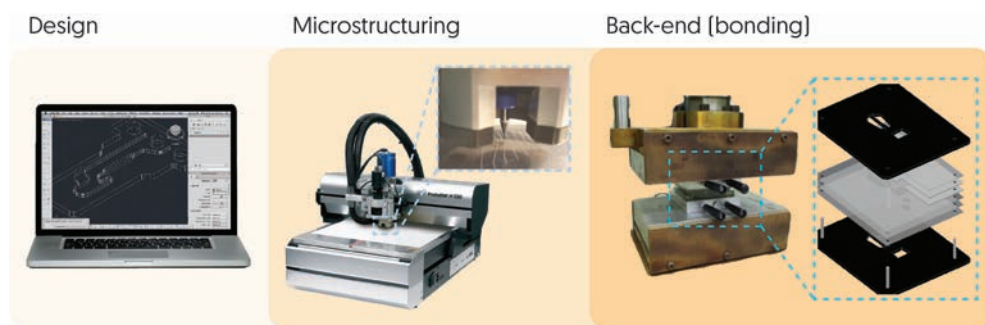
Figure 3.8: General fabrication of COC microfluidic devices, including design, microstructuring and back-end processes.

3.3.1 Design

The design of the LOC device was realized using Computer-Aided Design (CAD) software. The multilayer approach consists of the overlap of different layers to obtain the 3D structure of the device. Its design was rather simple and consisted of three layers (see Figure 3.9).

Top layer Contains inlet and outlet, as well as structural holes (blue circles) for the interconnection with the syringe pump.

(a) Top layer   (b) Middle layer   (c) Bottom layer
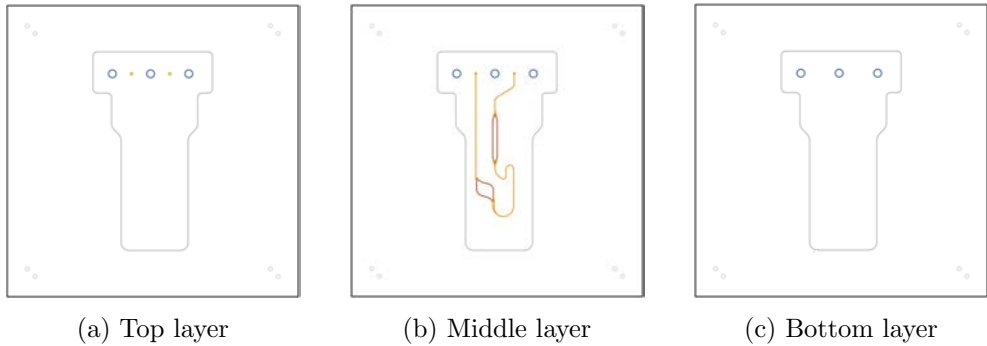
Figure 3.9: Layer breakdown of the LOC device for E. coli detection. The different colors indicate each pattern is designed for a different milling tool.

Middle layer Contains the main fluidic structures: microchannels, reaction chamber and detection chamber. Moreover, it contains the holes for interconnection with the pump.

Bottom layer Contains the structural holes for fluidic interconnection.

The same fluidic structures could be obtained using a two-layers design, i.e. a top layer with the inlet and outlet and a bottom layer with the fluidic structures. However, given our prototyping approach, this would require the micromilling of the fluidic elements in bas-relief. The surface roughness generated by the milling tool (Ymbern 2016) would, on the one hand, interfere with the optical detection and, on the other hand, hinder the movement of the MBs along the reaction chamber. Using instead a three-layers design, enables the through-cut of the fluidic structures in the middle layer, thus avoiding problems related to surface quality.

3.3.2 Microstructuring

The CAD microfluidic structures were machined using a CNC micromilling machine Protomat C100/HF (LPKF Laser & Electronics, Garbsen, Germany). Each layer was individually strapped with adhesive tape to a PMMA sacrificial layer attached on the milling worktable. The fluidic structures were micromilled by successive steps, each removing 250 μm more on the *z-axis*, until the desired depth was achieved. In this case, the fluidic structures were cut through in each layer, as stated above, to obtain surfaces with optical quality for detection purposes. Top, middle and bottom layers had thicknesses of 1 mm, 1 mm and 400 μm, respectively.

The CNC micromilling machine was originally intended for PCB machining, and therefore, the operational parameters were specially tailored for COC microstructuring in our group. Milling tools are available in different sizes, materials and shapes (see Figure 3.10). Carbide square-shaped endmills and drill bits were used throughout this thesis, in order to obtain good quality vertical channel walls.
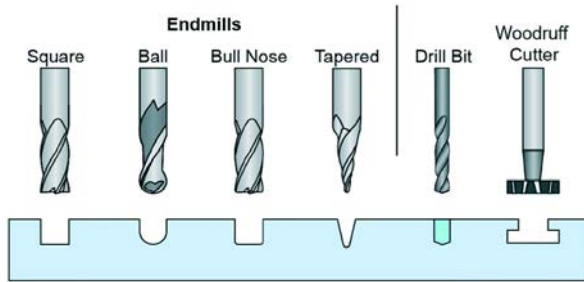
Figure 3.10: Different types of milling tools and their cutting profiles on a plastic substrate. Adapted from Guckenberger et al. 2015.

3.3.3 Back-end Processes

The main back-end process consisted of the thermal bonding of the three COC layers. In order to avoid channel occlusion and/or deformation, two different grades of TOPAS COC were used. As stated in the General Introduction chapter, several TOPAS COC grades —with varying Glass Transition Temperature (T_g) as a function of their norbornene content— are commercially available (see Table 3.1).

Table 3.1: Thermal properties of different grades of TOPAS COC. Information retrieved from Błochowiak 2006.

		TOPAS Grade				
		8007	5013	6013	6015	6017
Norbornene content	(mol %)	36	50	52	56	62
Glass Transition Temperature	(°C)	78	134	138	158	178
Heat Deflection Temperature[1]	(°C)	75	127	130	150	170

[1] Temperature at which a polymer or plastic sample deforms under a specified load. In this case, heat deflection temperature data under a load of 0.45MPa (HDT/B).

The device consisted of three layers of TOPAS 5013, which is recommended

for optical applications by the supplier. However, prior to microstructuring, the middle layer was thermo-laminated with two 25 μm thick films of TOPAS 8007 (see Figure 3.11). These films have a lower T_g than that of TOPAS 5013 (78 and 134 ℃, respectively). Then, the middle layer was microstructured under the same conditions as the others.

Figure 3.11: Schematic cross-section view of the layers of the device for E. coli detection. The middle layer is laminated with TOPAS 8007 prior to microstructuring in order to facilitate the bonding process. Not to scale.

Top, middle and bottom layers were sandwiched by two 2 mm silicone sheets (MVQ, Weinheim, Germany) and fixed in between two Aluminum plates with four pins for alignment. Then, they were pressed together using a uniaxial hydraulic press (Talleres Francisco Camp, Granollers, Spain) under a pressure of 6 bar and a temperature of 100 ℃. Therefore, $T_{bonding} = T_g(8007) + 22\,℃ = T_g(5013) - 34\,℃$, which means the bonding temperature was fairly above the T_g of TOPAS 8007, but below that of TOPAS 5013. The 5013 COC sheets were structurally stable under these conditions, while the 8007 films ensured a reliable bonding by interdiffusion of polymer chains into top and bottom layers. This bonding approach provides a strong bond while avoiding channel clogging and deformation of the microfluidic structures (Steigert et al. 2007).

Another aspect to take into account during the bonding process is the sagging of the cover layers (top and bottom) when the pressure load is applied. In this case, sagging of the bottom layer (400 μm thick) was observed in the area of the detection chamber (aspect ratio $\sim 1 : 5$). Therefore, lamination masks were fabricated in Delrin or Polycarbonate (PC) (both thermoplastics with T_g higher than the bonding temperature) using the CNC micromilling machine to produce holes of the same size and shape as the reaction and detection chambers. In this way, no pressure was applied in the areas with lower aspect ratios, avoiding sagging (D. S. Kim et al. 2007). A photograph of the LOC device is shown in Figure 3.12.
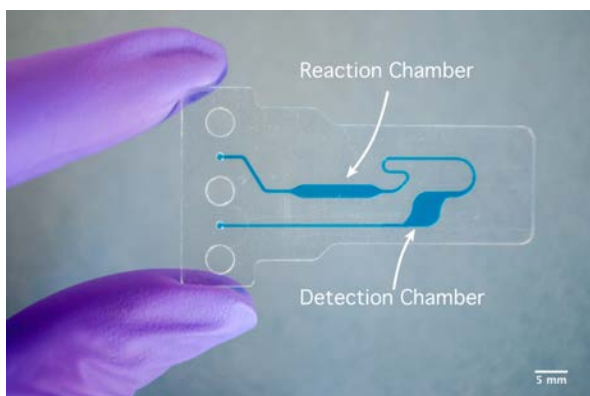
Figure 3.12: Photograph of the LOC device for E. coli O157:H7 detection. For clarity purposes, the channels are filled with blue dye.

3.4 Results & Discussion

3.4.1 Design of the Magnetic Actuator

The magnetic actuator is placed just under the microfluidic device, and consists of a rotating CD-shaped unit containing 20 slots for magnets (or magnet blocks) at different radii, forming an eccentric circumference (see Figure 3.13a). When rotating, the magnets pass sequentially under the reaction chamber (Figure 3.13b), where they trigger the movement of the MBs. The positions of the inner and outermost slots coincide with the two extremes of the reaction chamber, so that the MBs move back and forth on each revolution. A schematic representation of the MBs movement is shown in Figure 3.13b. The size and weight of the actuator is similar to that of a CD player, which makes it suitable for integration in a portable system. Its size and circular design would enable several reactions to be carried out in parallel —either in different microfluidic devices or in a single one with different microfluidic units—, as well as the use of centrifugal microfluidic devices. Furthermore, this actuator does not require relatively complex mechanical systems to work, as for instance other actuators consisting of magnets moving linearly (Herrmann, Veres and Tabrizian 2006), which would also have issues to control the movement of the MBs due to the deceleration and acceleration in the opposite direction to move the MBs back and forth.

Using this working principle (i.e. a rotating unit with embedded magnets) different types of magnets were tested (cylinders and blocks of different sizes). However, the movement of the MBs was difficult to attain, and it was effective only at very low speeds. Therefore, our researched group started a collaboration with Dr. Xavier Granados and Dr. Jordi Faraudo to perform a simulation
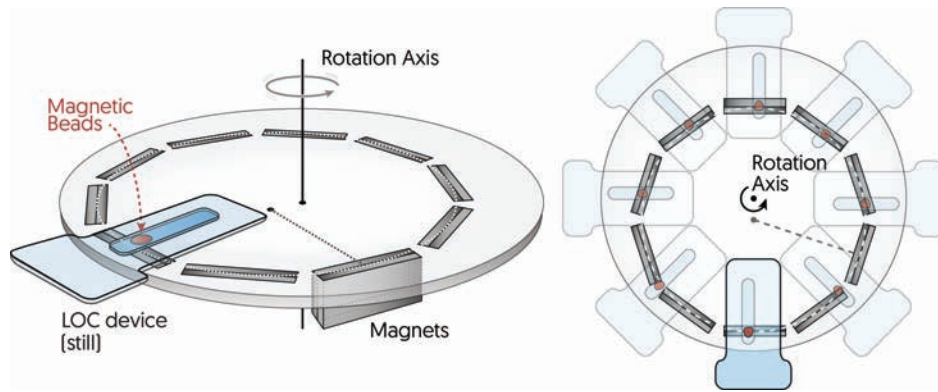
(a) Diagram of the magnetic actuator
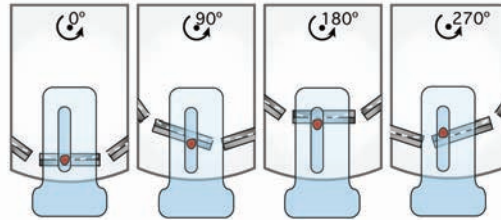
(b) Working principle

Figure 3.13: Diagram of the magnetic actuator and the LOC device with MBs, and its working principle. The magnets are arranged in a circumference eccentric to the rotation axis. The continuous rotation of the magnetic actuator causes a constant movement of the MBs back and forth in the reaction chamber. The actuator could be potentially used for parallel analyses. For clarity purposes, the different elements in the sketches are not to scale.

study of different magnet configurations.

3.4.1.1 Simulation Study

The magnetic properties of the MBs used in the simulations were retrieved from a previous detailed characterization study (Fonnum et al. 2005). The particles herein employed have a strong superparamagnetic response, with zero magnetization in absence of magnetic field (i.e. zero remanent magnetization). For moderate fields of 0.1 T, the magnetization is very high (about 8 Am^2/kg) and above 1 T, the magnetic response saturates at 10.8 Am^2/kg. Therefore, maximum magnetic response of the particles can be obtained with the fields generated by NdFeB magnets.

Due to the acquired magnetization, particles in suspension can interact with each other through anisotropic magnetic dipole-dipole interactions. If this interaction is strong enough, the magnetophoretic movement can become a cooperative motion involving a collective, concerted displacement of a large number of particles of the system (De Las Cuevas, Faraudo and Camacho 2008), which will improve the movement of the MBs and hence, the mixing process with the reagents inside the reaction chamber.

The strength of the particle-particle magnetic interaction is characterized by the magnetic coupling parameter Γ, which is dimensionless and involves the radius of a particle, its saturation magnetization and the thermal energy (Faraudo, Andreu and Camacho 2013). Typical values of Γ for composite superparamagnetic particles (including commercial beads) are between $10^2 - 10^3$. Using the diameter of the particles provided by the manufacturer, we estimate a value $\Gamma \sim 7 \cdot 10^4$ for the particles employed. Therefore, magnetic particle-particle interactions are predicted to be particularly strong between Dynabeads particles, provided that they are near saturation magnetization (with magnetic fields above 0.1 T). The possibility of a cooperative motion between particles also depends on the concentration of the suspension. In order to obtain cooperative motion, theory requires the aggregation number N^* to be much larger than 1, given by Equation 3.1, where ϕ is the volume fraction.

$$N^* = \sqrt{\phi \, exp \, (\Gamma - 1)} \qquad (3.1)$$

In general, the possibility of cooperative motion ($N^* > 1$) requires a concentration larger than a threshold, which depends on the value of Γ. According to Equation 3.1, and taking into account the large value of Γ obtained for our particles (note the exponential dependence in Γ), cooperative motion will always be achieved provided that the particles are under magnetic fields above 0.1 T. Therefore, a critical aspect in the design of the device is to ensure that all the particles are under the action of a large enough magnetic field. This

aspect becomes more important as one uses low concentrations or smaller particles. This is a known issue, for example, in the use of most commercial batch magnetic separators, in which significant regions of the sample are under low magnetic fields, with the subsequent loss of particles when working at low concentrations (Andreu et al. 2012).

At this point, it is important to recall that the magnetophoretic motion depends both on the magnetization of the particles and on the gradient of the magnetic field (De Las Cuevas, Faraudo and Camacho 2008). A uniform magnetic field does not generate any motion, it only magnetizes the particles or orients them along the field if some anisotropy is present. In non-uniform magnetic fields, the magnetization of the particles creates a force F_m over their dipolar magnetic moment m, as given by Equation 3.2:

$$\vec{F}_m = \vec{\nabla}\left(\vec{m} \cdot \vec{B}\right) \tag{3.2}$$

where B is the local value of the magnetic field and ∇ the gradient. Therefore, one has to design a system containing large enough magnetic fields (in the order of 0.1 T or larger) to maximize the magnetization of the particle (and consequently the magnetic dipole), but also large spatial magnetic gradient of the magnetic field in the adequate direction (at least of the order of $10 - 10^2$ T/m) to obtain the desired motion according to Equation 3.2.

Taking into account the above considerations three different magnet configurations were selected for the study on the basis of the following criteria: simplicity for their integration in the rotating unit; dimensions of the magnets for the accurate movement of the MBs; and expected magnetic field strength. Figure 3.14 shows the three configurations of magnets embedded in each slot: a) single magnet, b) magnet couple antiferromagnetic-like coupled —in order to enhance the magnetic gradient— and c) the same couple plus a static third magnet for creating a bias magnetizing field, which produces an out of plane magnetization.

For each configuration, we performed COMSOL simulations in which we calculated the profile of the magnetic field generated by the magnets and the resulting magnetic force over the MBs. For the calculations, we employed a constant magnetization of $9.6 \cdot 10^5$ A/m for the magnets (as usual for NdFeB magnets) and the bibliographic characterization data of the MBs (Fonnum et al. 2005). The simulation setup consisted of a single magnetic block (we neglected the interactions between magnets of different slots) and a set of 27 superparamagnetic particles homogeneously distributed in the channel —where the reaction should occur— in order to see the distribution of the forces generated upon them (see Figure 3.15). The distance between the microfluidic chamber and the magnet(s) is defined by the thickness of the COC sealing layers. The chamber channel is represented in the pictures as the two parallel,

(a) Single magnet (b) Magnet couple (c) Magnet couple + static
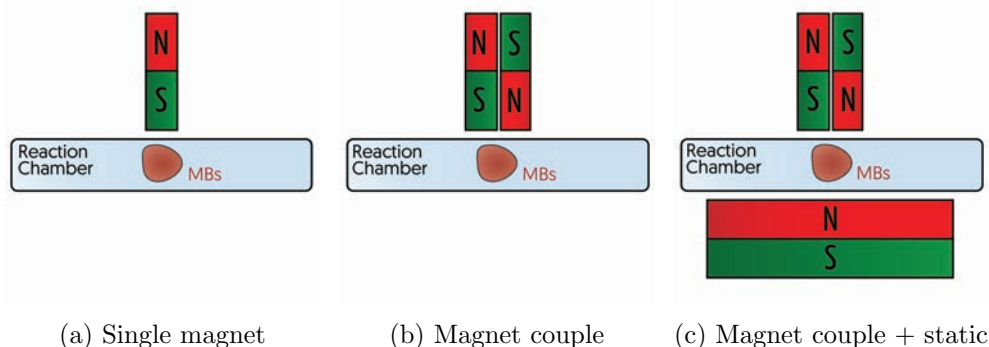
Figure 3.14: Schematic cross-section view of the different magnet configurations proposed for each slot of the rotating unit. For clarity purposes, the different elements are not to scale.

continuous lines confining the set of particles. Magnetization and force are represented by black and white arrows, respectively. It is worth noticing that magnetic flux density and magnetization are parallel.

As a general trend, we can observe in Figure 3.15 that the magnitude of the flux density of the field is larger for the couple of magnets (Figures 3.15b and 3.15c) than for the single magnet (Figures 3.15a). This is due to the overlapping of the stray field with the flux in the poles. More relevant, however, is the increase of the gradient of the magnetic field just in between both magnets, when they are coupled. These effects, namely the increase of the field and the increase of magnetic gradient, determine a substantial increase of the force over the MBs. Therefore, the single magnet configuration was discarded as it is outperformed by the configurations containing a magnet couple. This observation justifies the lack of movement in the preliminary tests (prior to the simulations), in which single magnets were used in order to trigger the movement of the MBs.

Increasing the magnetization of the MBs would also increase the magnetic force. For this reason, the arrangement of magnets in Figure 3.15c was proposed, since the static magnet was expected to create a larger and nearly homogeneous bias magnetic field, not disturbing the high gradient achieved with the magnet couple. Nevertheless, it is important to note that we could only take advantage of a larger bias field if the magnetization of the MBs did not saturate. In this respect, the magnetic configurations shown in Figures 3.15b and 3.15c show a magnetic field around the MBs larger than the saturation threshold of 0.1 T. Accordingly, configuration shown in Figure 3.15b was chosen as optimal because of its magnetic characteristics (saturation of the MBs magnetization and high magnetic gradient) and the simpler, more

(a) Single magnet   (b) Magnet couple   (c) Magnet couple + static
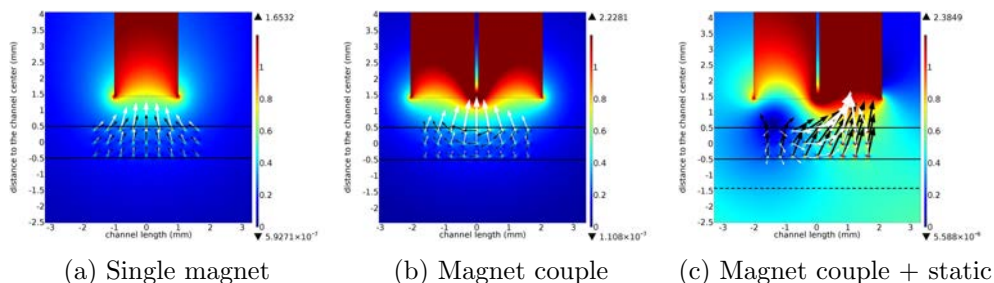
Figure 3.15: COMSOL simulations for the different magnet configurations proposed. The color map represents the local magnetic flux density for a stationary distribution of magnetizable particles, in Tesla. The magnetization of the particles and the acting force are represented by black and white arrows, respectively. In order to get a better image of the force and magnetization distributions, arrows in the different pictures are not in the same scale. The continuous horizontal lines confining the MBs represent the microfluidic chamber, and the dashed line represents the static magnet.

cost-effective setup (requires less magnets).

3.4.1.2   Movement of the Magnetic Beads

Using the magnet arrangement seen in Figure 3.14b, experiments performed at a concentration of 2 mg/mL (volume fraction $1.43 \cdot 10^{-3}$) clearly showed a collective, concerted motion of the particles along the reaction chamber (see Figure 3.16). This collective motion involves a very large number of particles, arranged in fibrous structures following the magnetic field. It could also be observed with naked eye, as in previous cooperative magnetophoresis experiments (De Las Cuevas, Faraudo and Camacho 2008). Adhesion of MBs to the walls of the device can be observed, but this issue could be addressed by modifying the surface of the microchannels to minimize adsorption (Perez-Toralla et al. 2013) and by optimizing the movement velocity of the magnets.

3.4.2   E. coli Detection

The detection strategy consisted of an enzyme-linked fluorescence sandwich immunoassay, using MBs with immobilized antibody (as biorecognition element) and primary antibody modified with AP (labelling antibody). Enzyme-linked immunoassays enhance the signal thanks to the amplification step, thus achieving lower detection limits.
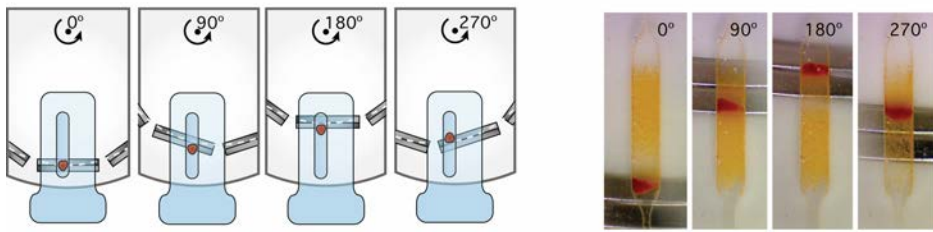
Figure 3.16: Schematic representation and photograph series of the MBs moving along the reaction chamber. The rotation of the magnetic actuator causes the movement of the MBs, which follow the magnets embedded in the actuator.

3.4.2.1 Fluorescence Immunoassay

However, prior to the enzymatic assay, a fluorescent label was used in order to determine wether the E. coli was effectively captured by the MBs. Due to the red autofluorescence of the MBs, FITC-labeled (green emission) anti-E. coli O157:H7 antibody was selected. Figure 3.17 shows two confocal microscope photographs of bacteria captured by the MBs. As clearly seen in Figure 3.17a, various MBs can capture the same E. coli cell. Larger aggregates are also observed (Figure 3.17b), probably due to remanent magnetization of the MBs.
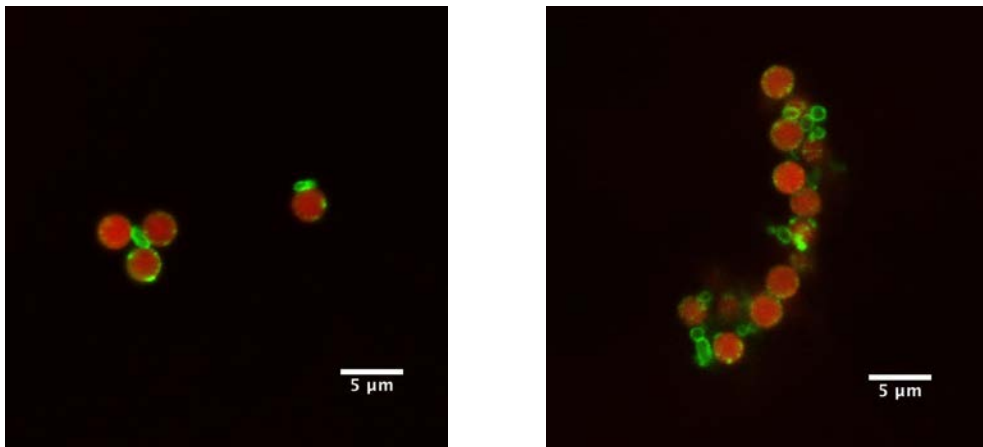
(a) Small groups of MBs

(b) Larger aggregate of MBs

Figure 3.17: Confocal images of immunocomplex aggregates. The red fluorescence comes from the MBs due to their autofluorescence. E. coli O157:H7 is labeled with FITC, producing green fluorescence.

3.4.2.2   Enzyme-linked Fluorescence Immunoassay

The formation of the immunocomplex was carried out *off-chip*, and subsequently injected into the LOC device to carry out the detection, i.e. the enzymatic reaction and the optical measurement. In this way, we focused on evaluating the enhancement provided by the magnetic actuator for a MB-based reaction *on-chip*, while avoiding optimization of several parameters of a microfluidic immunoassay. A typical sandwich immunoassay was performed using MBs as support material for the formation of the immunocomplex (see Figure 3.18). The reactions for the formation of the immunocomplex were carried out sequentially and washing twice between each reaction.
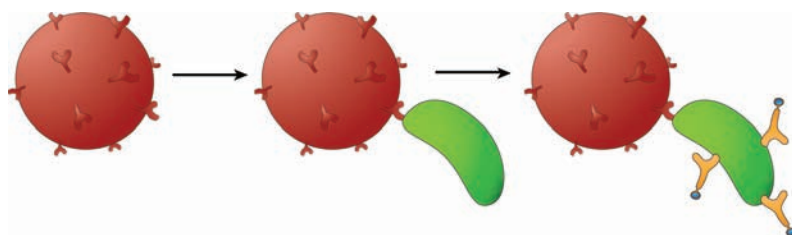
(a) *Off-chip* reactions
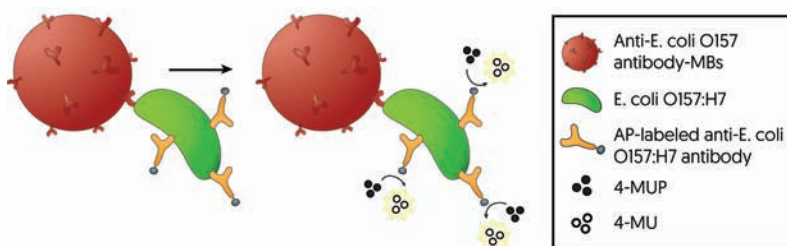
(b) *On-chip* reactions

Figure 3.18: Schematic representation of the enzyme-linked fluorescence immunoassay performed. The MBs are washed twice between each reaction.

The enzymatic reaction consisted of the dephosphorylation of 4–MUP catalyzed by AP, to obtain the fluorescent product 4-methylumbelliferone (4–MU). Considering the conversion rate of the reaction as constant and the time of incubation fixed, the signal intensity depends only on the amount of AP-labelled antibodies present, which is proportional to the number of E. coli O157:H7 captured by the MBs. The dilution factor of the labelling antibody was studied with actual assay conditions, in the range recommended by the manufacturer (see Figure 3.19). A dilution factor of 1/100 was chosen due to

the enhanced signal provided, with a comparable Relative Standard Deviation (RSD).
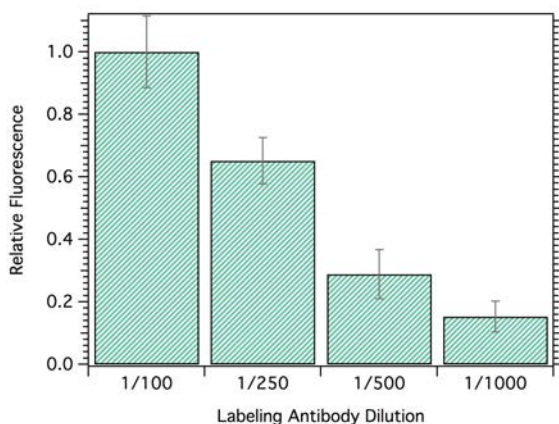
Figure 3.19: Alkaline phosphatase-labelled antibody dilution optimization.

The movement of the MBs can be tuned by increasing or decreasing the rotation speed of the magnetic actuator. One turn of the CD-shaped actuator is translated to one cycle of movement of the MBs, i.e. from one end to the other end of the reaction chamber, and back to the starting point. The movement increases the effective surface area of the MBs exposed to the substrate, because it creates a loose cloud of MBs following the magnets. Moreover, the movement of the MBs makes the substrate from all around the reaction chamber available to the enzyme (not only the substrate molecules directly next to the MBs capture spot), homogenizing the concentration of the enzymatic product throughout the reaction chamber. These two combined effects lead to a signal enhance. The optimal movement velocity was found to be 1.7 mm/s (see Figure 3.20). However, the signal enhancement decreased at higher velocities, due to the fact that MBs could not completely follow the magnets (i.e. the movement cycle was not completed) since they moved too fast, and therefore, MBs were not exposed to the whole of the substrate. It is also worth noticing that all the studied movement velocities provided a signal enhancement compared to the system that only captures the MBs (0 mm/s).

At the same time, the RSD of the signals decreased as the velocity increased (see Figure 3.20), even when the velocities were higher than 1.7 mm/s. The lower level of MBs aggregation achieved due to the magnetic actuation could cause this decrease. However, the RSD values are not in complete agreement with those found in Figure 3.21. Therefore, further reproducibility studies should be carried out in order to establish a relationship between RSD and linear movement velocity, because other factors must be also taken into ac-
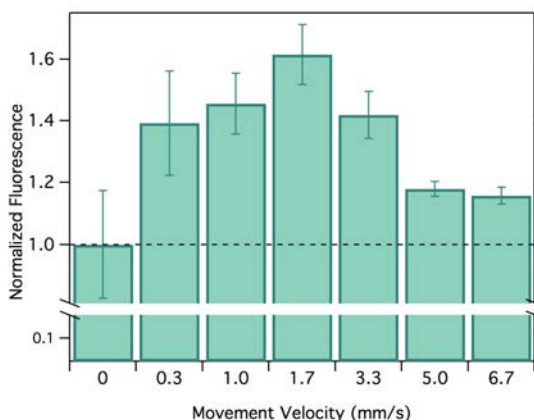
Figure 3.20: Signal obtained at different movement velocities of the MBs, which are tuned by increasing or decreasing the rotation speed of the magnetic actuator. The concentration of MBs was 2 mg/mL and the E. coli O157:H7 sample contained $2 \cdot 10^4$ CFU/mL (CFU per milliliter). The dashed line indicates the normalized signal obtained at 0 mm/s, for a better comparison with the other columns. The error bars show the RSD for $n = 3$.

count, as for instance the irreproducibility of the manual *off-chip* procedures (replicates were obtained from whole new assays).

To evaluate the performance of the magnetic actuator in comparison to systems that are only able to capture the MBs, three calibration experiments were performed: 1) at 0 mm/s, i.e. only capturing the MBs, 2) at 1.7 mm/s, the higher signal enhancement, and 3) at 3.3 mm/s (see Figure 3.21). The calibration curve obtained at 1.7 mm/s, the optimal velocity, showed a 2.7-fold enhancement of the sensitivity (defined as the slope of the calibration curve) with respect to the 0 mm/s curve. The sensitivity obtained at a velocity of 3.3 mm/s showed only 1.7-fold enhancement. These experimental results are in accordance to the previous optimization of the MBs movement velocity. The linearity of the three calibration curves over this concentration range was good, with values of 0.997, 0.996 and 0.998 for the curves 0, 1.7 and 3.3 mm/s respectively. The LOD for E. coli O157:H7 at 1.7 mm/s was calculated to be 603 CFU/mL (n=12), whereas it was higher, 2101 CFU/mL (n=3), for the system when no actuation was performed. The Limit of Quantification (LOQ) was 1470 CFU/mL (n=12) at 1.7 mm/s. LOD and LOQ were calculated as the concentration that yields a signal 3 or 10 times the standard deviation of the blank, respectively.

An even higher enhancement of the enzymatic reaction performance could
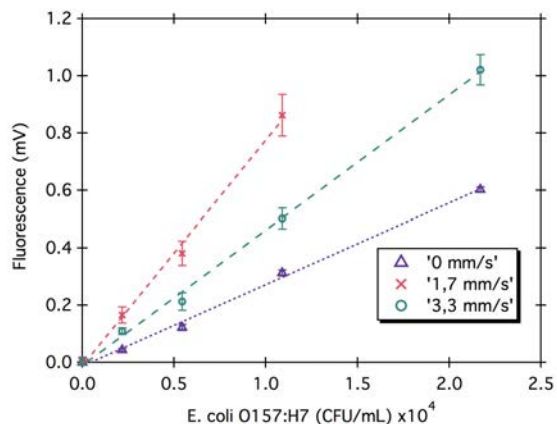
Figure 3.21: Calibration curves for the detection of E. coli O157:H7 at different movement velocities. The error bars show the standard deviation for $n = 3$.

be achieved by decreasing the height of the reaction chamber because we observed that MBs moved only on the lower section (i.e. as close as possible to the magnets) of the chamber (total height of 1 mm). The decrease of the chamber height would enable the particles to directly interact with the total volume of the solution in the reaction chamber. However, the height of the reaction chamber was chosen so that both reaction and detection chambers would have similar volumes, considering that the latter was previously optimized to have an optical path of 1 mm in order to be used with the optical detection system. This issue should be addressed in further studies.

This study demonstrates that the magnetic actuator herein proposed provides an enhancement of the reaction kinetics. Integrating all the reactions of the immunoassay *on-chip* as well as the washing steps would entail several challenges to be met, such as non-specific adsorption. However, the kinetics of each reaction would be enhanced with the actuator, in comparison to a system only able to trap the MBs. Reactions between the MBs and big entities, such as whole cells —less prone to diffusion—, would be expected to benefit even more from the mixing provided by the magnetic actuator.

3.4.3 Beyond Immunoassays

The magnetic actuator presented in this dissertation could potentially be applied to a wide variety of MB-based bioassays *on-chip*. In order to demonstrate this, an automatic DNA hybridization assay for the detection of an E. coli oligonucleotide was designed by another member of our research group and carried out with the magnetic actuator (Gómez-de Pedro, Berenguel-Alonso,

et al. 2017). A LOC device was developed, incorporating more inlets for the different reagents, but maintaining the same reaction and optical detection chambers. This study demonstrates the simple operation of the magnetic actuator in combination with LOC technology and the high degree of automation attainable.

E. coli oligonucleotides were detected after a MB-based multi-step DNA hybridization assay, with enzymatically generated colorimetric detection. An LOD of 1.1 nM was achieved in less than 30 min, thanks to the automation of the system and the enhancement provided by the magnetic actuator.

3.5   Conclusions

A novel magnetic mixing actuator for MB-based reactions in microfluidic systems has been developed. Its design is simple and compact (comparable to a CD player), featuring magnet couples embedded on a rotating structure, circularly arranged and eccentric to the rotation axis. The design of this magnetic actuator could enable its application to parallel analyses, centrifugal microfluidics, etc. We have also fabricated a COC microfluidic device to carry out the enzymatic reaction and detection of a MB-based immunoassay. The immunocomplex was formed *off-chip* and subsequently injected into the LOC device, where the MBs were used as an active agent to produce the mixing with the enzymatic substrate. In this way, we focused our efforts on the development of the actuator and its performance to improve an enzymatic reaction.

The use of the magnetic actuator demonstrated an enhancement of the enzymatic reaction at all the rotational speeds tested compared to a system only able to trap the MBs, which is the most common case scenario. The optimal movement velocity of MBs was found to be 1.7 mm/s. Calibration curves for E. coli O157:H7 whole cells were performed, showing a sensitivity enhancement of 2.7-fold at 1.7 mm/s with respect to the assay without mixing. The LOD achieved at this movement velocity was 603 CFU/mL, in contrast to the LOD obtained without actuation, 2101 CFU/mL, under the same conditions. The MBs used in this study are commercially available, and can be purchased already functionalized with a variety of antibodies, hence making the use of the magnetic actuator directly applicable to other reactions.

The use of the magnetic actuator would facilitate the handling of the MBs, thus enabling an easier transition from the *off-chip* manual procedures to automated *on-chip* protocols. This would entail the characteristic advantages of LOC systems such as automation, lower consumption of reagents, portability, etc.

The possible integration of all the reactions *on-chip* may highlight the enhancement provided by the magnetic actuator. This is consequence of the

type of interactions between MBs and whole cells, which are not controlled by diffusion —unlike interactions between small molecules— since their motion is very limited due to their large size (Gehring and Tu 2011). Therefore, the collisions and binding events in stop-flow strongly depend on the movement of the MBs. The design of the LOC device could also be adapted to perform parallel or multiplex assays with the same actuator, by simply replicating the current design in a circular microfluidic platform.

The automation of MB-based bioassays *on-chip* using the magnetic actuator presented in this dissertation was demonstrated in a parallel study led by another member of the research group. Particularly, a MB-based multi-step DNA hybridization assay was performed and applied to the detection of E. coli oligonucleotides.

Chapter 4

Rapid prototyping of a COC microfluidic device for oocyte trapping and culturing

4.1 Introduction

Assisted Reproductive Technology (ART) are becoming increasingly important in human reproduction, due to infertility issues (specially considering the increasing average age of mothers in western societies) as well as genetic conditions. Furthermore, the application of ART in animals, mainly by Artificial Insemination (AI), had a great impact in the efficiency enhancement of animal production. Reproductive biotechnologies intend to be used routinely to shorten generational intervals and to propagate genetic material among breeding animal populations. To achieve this goal, ART have been developed over the years, for instance AI, embryo transfer, In Vitro Fertilization (IVF), in vitro embryo production or multiplication techniques (cloning) for the application of transgenesis (Rodriguez-Martinez 2012).

Despite the remarkable progress made and the punctual relevance of some of the above-mentioned technologies, the efficiency of the processes is usually very low with the exception of AI in cattle. Furthermore, ART such as oocyte maturation or IVF require labor-intensive, time-consuming procedures (including frequent pipetting of oocytes to be washed, media changes, etc., which have not significantly evolved since their establishment) and some critical steps that only highly specialized personnel are able to perform.

Lab on a Chip (LOC) technology emerged as a new tool for ART, since it could potentially solve these problems by automating the handling and preparation procedures (Z. Luo et al. 2015), thus minimizing the errors associated to manual operation and reducing manipulation stress on the cells. Moreover,

LOC technology can also provide environments that mimic *in vivo* conditions. The current fabrication technologies enable the design of structures in the micrometer range, resembling biological environments (Ziółkowska, Kwapiszewski and Brzózka 2011; D. J. Beebe, Ingber and Toonder 2013; Rigat-Brugarolas et al. 2014; Auroux et al. 2002), including those relevant for ART applications (M. S. Kim et al. 2009). Furthermore, other inherent advantages of LOC technology, such as the low volumes required, the precise control of fluids or the miniaturization and integration of different elements in portable devices would also benefit ART.

The vast majority of microfluidic systems used in ART are made of Polydimethylsiloxane (PDMS), a transparent and gas-permeable elastomer. This responds to its widespread use in academia, which is due to several factors: cheap, rapid and easy prototyping, optical transparency, easy surface modification, elasticity, etc (Mukhopadhyay 2007). The latter also provides the grounds for the integration of actuation systems, such as pumping or valving. A key feature of PDMS is its gas permeability, which enables long term cell culture in incubators with controlled atmosphere (Mehling and Tay 2014). ART applications of PDMS devices range from sperm separation (Cho et al. 2003), to oocyte fertilization (Han et al. 2010; Ma et al. 2011) or embryo culture (Esteves et al. 2013), among others (see a comprehensive review in ART can be found in Swain, D. Lai, et al. 2013).

Particular interest has been devoted to the development of a LOC system capable of integrating oocyte maturation, fertilization and early stage embryo culture in a single device (see different examples of culture/fertilization systems in Figure 4.1). Such platform could potentially automate labour-intensive processes and increase success rates in the production of embryos, thanks to lower manipulation stress on the cells and the mimicking of *in vivo* environments.

However, PDMS presents certain limitations for cell-based techniques, which hinder the adoption of LOC technologies in biological and biomedical fields, as discussed in Section 1.2.2. For instance, PDMS is prone to absorb small hydrophobic molecules that diffuse towards the bulk of the material (Toepke and D. J. Beebe 2006). Another issue is the leaching of residual uncrosslinked polymer chains into the solution and their potential effects on the cultured cells (Regehr et al. 2009). Furthermore, the gas permeability of PDMS can lead to media evaporation, which can critically change concentrations or gradients (Berthier, Warrick, et al. 2008). All of these factors are critical to the cell's microenvironment, and therefore should be assessed to choose the most suitable material. Another issue related to the gas permeability of PDMS is the dependance on the outer atmosphere. Although generally considered an advantage due to necessary gas equilibria, or the buffering capacity of CO_2, this characteristic inevitably links PDMS devices to the use of
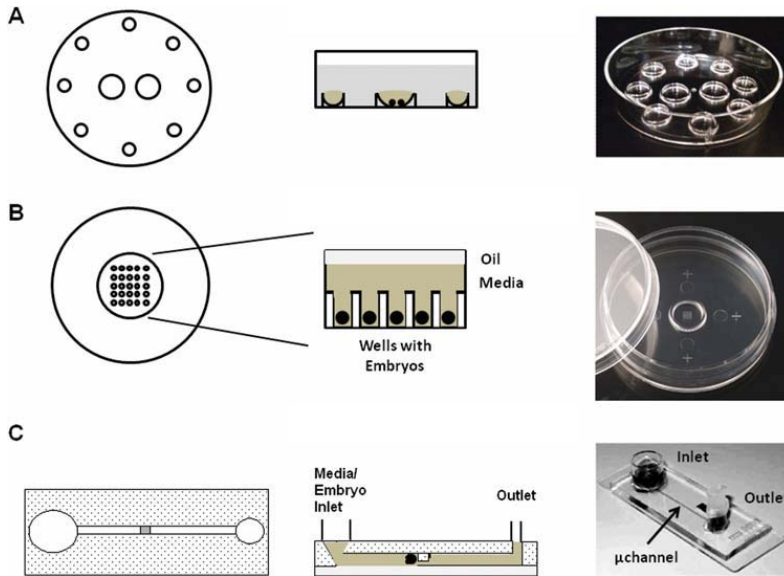
Figure 4.1: Diagrams and photopgraphs of different culture system approaches. A) Dishes for microdrop culture. B) Microwells for individual culture. C) Microchannel with a constriction. Adapted from Swain and Smith 2011.

expensive, bulky incubators with controlled atmosphere. Finally, manufacturing and packaging of PDMS is not easily scalable, and although small batches can be rapidly produced in a cost-effective way, production costs at a bigger scale are not competitive (Becker 2009).

These limitations have hard-pressed the use of other materials in microfluidics, such as the thermoplastics (Sackmann, Fulton and D. J. Beebe 2014). Among these, Polystyrene (PS) and Cyclic Olefin Co-polymer (COC) have emerged as alternatives for the production of microfluidic devices for biological applications, overcoming the limitations of PDMS. On the one hand, PS has been the choice material for disposable cell culture labware since the 1960s, and recently has been used as a substrate material to produce LOC devices (Young et al. 2011), thus bringing together state of the art microfluidics technology and a well known material for biologists. However, the fabrication process is still challenging, mostly due to bonding issues (Berthier, Young and D. Beebe 2012).

On the other hand, Cyclic Olefin (Co-)Polymers (COP/COC) are a group of polymers with very promising properties for LOC applications (Nunes et al. 2010), as discussed in Section 1.2.3.1. Particularly, cell-based applications *on-chip* could take advantage of COC's chemical resistance (higher than most thermoplastics), excellent optical transparency (even in the near UV region),

low water absorption and biological compatibility (Midwoud et al. 2012; Jeon et al. 2011). The biocompatibility has been demonstrated by the *USP Class VI* certification and its approval for use in medical devices (Kuo and D. T. Chiu 2011). However, to the best of the author's knowledge, COC monolithic LOC devices have not been used in ART applications.

As discussed throughout this dissertation, COC provides a very important fabrication advantage in comparison to other thermoplastic materials: easy bonding between different layers without channel deformation, achieved by using grades with low Glass Transition Temperature (T_g) as sealants (R. K. Jena, C. Y. Yue and Lam 2012). This bonding technique avoids processes like solvent bonding, which are not desired specially in biology applications, due to the potential harmful effects over the cells.

Herein, we studied for the first time the suitability of a COC monolithic LOC device for an ART application. Our main goal consisted on the development of an independent culture/fertilization platform. With this in mind, our research group started a collaboration with the Group of Animal Reproductive Biology and Embryology of Prof. Manel López-Béjar (Dept. of Animal Health and Anatomy, UAB). This synergy provided the required know-how both from the biologic and technological perspectives to realize the project. The group of Prof. Manel López-Béjar performed the required cell evaluation processes after the experiments and provided the statistical data for the discussion.

In order to evaluate the suitability and biocompatibility of COC, we independently studied sperm characteristics along time and bovine oocyte maturation. On the one hand, we fabricated a simple COC device consisting of a channel where sperm samples were stored. Sperm quality parameters were assessed after different periods of time and compared to control samples stored using conventional methods. On the other hand, we fabricated a COC microfluidic device able to trap and culture oocyte cells. Several oocyte maturation parameters and their ability to be fertilized were studied and compared to traditional maturation methods.

This latter LOC device is the basis for the development of an independent culture/fertilization platform. From a fabrication perspective, this LOC system posed two main challenges that needed to be addressed. On the one hand, the prototyping of microchannels containing a constriction to trap the cells, i.e. with dimensions smaller than the oocyte diameter ($\varnothing$ 100 µm). This issue was tackled through the development of a novel prototyping strategy based on hot embossing, with the particularity of using Low Temperature Co-fired Ceramics (LTCC) masters. This material enabled a rapid and low-cost master prototyping, compared to common substrates such as metals.

On the other hand, the optimal conditions for oocyte culture and fertilization require a thorough control of temperature (Cooke and Fleming 2009; Baak et al. 2016). LOC devices could outperform bulky instruments such as

incubators, due to the smaller dimensions and enhanced heat transfer observed in miniaturized systems (see Section 1.1.3). Therefore, we decided to integrate a transparent heater on the LOC device, in order to obtain an homogeneous temperature distribution while enabling the visualization of the cells. In this case, a thin gold layer was monolithically integrated in the LOC device to act as a Joule heater.

This is, to the best of our knowledge, the first COC monolithic LOC device dedicated to an ART application. The results obtained demonstrate the great potential of COC as a substrate material due to its biocompatibility and simple fabrication process at a prototyping level and its potential scalability to mass production. Furthermore, a transparent heater was monolithically integrated, laying the grounds for the development of an independent culture platform.

4.2 Methods

4.2.1 Materials

All reagents were purchased from Sigma-Aldrich (Barcelona, Spain) unless otherwise stated. Plastic dishes, four-well plates and tubes were obtained from Nunc (Roskilde, Denmark).

4.2.2 Biological Procedures

The classical biological procedures used to prepare the cells and to analyze their significant parameters after the different experiments are described in this section. Generally, these procedures were carried out by the group of Prof. M. López-Béjar.

4.2.2.1 Oocyte Collection and Maturation

Bovine ovaries were collected from recent culled dairy heifers at local slaughterhouses and immediately transported to the laboratory. They were then washed 3 times in warm saline solution (38 ℃). Subsequently, follicles with a diameter of 2–6 mm were aspirated using an 18-gauge needle. Only unexpanded cumulus oocyte complexes surrounded by five or more cumulus cell layers and with homogeneous cytoplasm were matured in vitro and cultured at 38.5 ℃ in a humidified atmosphere of 5 % of CO_2 for 24 h. The maturation medium contained Tissue Culture Medium 199 (TCM-199) supplemented with 10 % (v/v) fetal calf serum, 10 ng/mL epidermal growth factor and 50 µg/mL gentamycin (Rizos et al. 2001).

4.2.2.2 Oocyte Evaluation and Classification

After 24 h of in vitro maturation, oocytes were totally denuded of cumulus cells by gentle pipetting in phosphate-buffered saline (PBS). In order to evaluate nuclear stage and cortical granule distribution after in vitro maturation, oocyte samples were fixed in a solution of 4 % (w/v) of formaldehyde and PBS at 38.5 ℃ for 30 min and permeabilized in Triton X-100 2.5 % (v/v) in PBS for 15 min. Then, oocytes were immunostained for cortical granules detection with FITC-labeled Lens Culinaris Agglutinin (FITC-LCA). Fixed and stained oocytes were mounted on poly-L-lysine treated coverslips fitted with a self-adhesive reinforcement ring in a 3 μL drop of Vectashield containing 125 ng/mL of 4',6-diamidino-2-phenylindole (DAPI) (Vectorlabs, Burlingame, CA) for chromosome detection and flattened with a coverslip. The preparation was sealed with nail varnish and stored at 4 ℃ protected from light. Chromosomes and cortical granules status of each oocyte were assessed under an epifluorescence microscope (Nikon Eclipse TE 2000S) and a laser-confocal microscope (Leica TCS SP2). Oocyte images were recorded in a computer.

Cultured oocytes were checked to have reached the Metaphase II (MII) stage. In this stage, the chromosomes are aligned by the spindles in the center of the oocyte and are ready for fertilization (Clift and Schuh 2013). Oocytes that reached the MII stage after maturation were classified into two categories:

Normal MII Uniform alignment of the chromosomes on the spindle.

Anomalous MII Nuclear content changed into chromatin-like structure forming condensed aggregates, forming aberrantly distributed chromosomes or absence of chromosomes.

Translocation of cortical granules to the oolema was used as an indicator of cytoplasmic maturation (Damiani et al. 1996). The criteria used to define the cortical granules distribution of oocytes was also divided in two categories:

Normal cytoplasmic maturation Cortical granules were distributed adjacent to the plasma membrane and positioned such that they formed a continuous layer.

Anomalous cytoplasmic maturation Cortical granules appeared aggregated in clusters, or cortical granules were distributed in the cortical area (not limited to the vicinity of the plasma membrane), or absence of cortical granules.

4.2.2.3 Assessment of Sperm Parameters

Commercial frozen bull semen of proven fertility was used. Semen straws were thawed in a water bath at 38.5 ℃ for 30 s and then spermatozoa were

immediately centrifuged at room temperature in a top layer solution of a discontinuous gradient (BoviPure, Nidacon International AB, Göthenborg, Sweden) for 10 min and 100 g. The supernatant was removed, the pellet resuspended in 3 mL of BoviPure wash solution and centrifuged again for 5 min at 100 g. Sperm concentration of the pellet was determined using a haemocytometer chamber (Neubauer chamber) and adjusted to a final concentration of $1 \cdot 10^6$ spz/mL with fertilization medium (Tyrode's medium supplemented with 25 mM sodium bicarbonate, 22 mM sodium lactate, 1 mM sodium pyruvate, 6 mg/mL fatty acid-free bovine serum albumin (BSA) and 10 mg/mL heparin sodium salt [Calbiochem, Darmstadt, Germany]), and cultured at 38.5 ℃ in a humidified atmosphere of 5 % of CO_2 for 24 h.

The sperm cells viability and acrosome abnormalities were assessed by the nigrosine-eosin stain method (Bamba 1988). 10 μL of sperm sample and 10 μL of the dye solution were mixed and smeared onto a glass slide and allowed to air-dry. Then, the slide was covered with mounting medium and a cover glass. Slides were analyzed using an optical microscope (Motic BA210, Spain) at 1000x magnification under immersion oil. As many as 200 cells were counted on each slide and the percentage of sperm viability and spermatozoa with acrosome abnormalities were calculated.

The motility characteristics of the frozen-thawed spermatozoa were determined using a Computer-Assisted Sperm Analysis (CASA) system (Integrated Sperm Analysis System V1.2, Proiser SL, Valencia, Spain). The CASA system is based on the analysis of 25 consecutive digital images taken from a single field at 100x magnification in a dark background in a time lapse of 1s. A sample drop of 5 μL was placed on a pre-warmed slide and viewed in a phase contrast microscope equipped with a warmer stage at 37 ℃. At least five separate fields were taken of each sample and a minimum of 200 cells per sample were examined. The motility descriptors obtained after CASA were: progressive motility (percentage of spermatozoa that showed a Velocity Average Path (VAP) above 50 μm/s and 70 % of straightness coefficient) and total motility (percentage of spermatozoa that showed a VAP above 10 μm/s).

4.2.2.4   In vitro Fertilization

After maturation, the cumulus oocyte complexes were washed twice in PBS solution and then they were transferred to fertilization medium. Frozen-thawed bull spermatozoa were counted in a Neubauer chamber and diluted in an appropriate volume of fertilization medium to give a final concentration of 106 spermatozoa/mL. All cumulus oocyte complexes were co-incubated with spermatozoa for 20 h at 38.5 ℃ in fertilization medium in a humidified 5 % CO_2 incubator.

4.2.2.5 Evaluation of Sperm Penetration

At 20 h post-insemination, the presumptive zygotes were pipetted to remove excess sperm and cumulus cells, washed three times in PBS, fixed in 4 % (v/v) paraformaldehyde in PBS at 38.5 ℃ for 30 min, stained with Vectashield containing DAPI and mounted on glass slides. The number of pronucleus was assessed under an epifluorescence microscope (Axioscop 40FL, Carl Zeiss, Germany). Once stained, slides were examined and parameters including penetration, monospermic penetration, male pronucleus formation, and polyspermic penetration were recorded. Penetration was determined by the presence of one or more swollen sperm heads and/or male pronuclei. The presence of three or more pronuclei was designated as polyspermic.

4.2.2.6 Statistical Analysis

All statistical analyses were performed using R software (version 2.15.0, R development Core Team, 2009) by the group of Prof. M. López-Béjar. Data of *on-chip* oocyte maturation were analyzed using contingency tables and Pearson's Chi-squared statistical test. The analysis of differences among the different tested devices for sperm viability and motility parameters was carried out using the Kruskal-Wallis test. All data are expressed as mean $\pm$ Standard Deviation (SD). In all cases, differences between groups with $P < 0.05$ were considered significant.

4.2.3 Experimental Design & Setups

In order to evaluate the suitability and biocompatibility of COC as a substrate material for microfluidic devices used in ART, we designed two different microfluidic devices, one for sperm storage and another one for oocyte maturation. Three different sets of experiments were carried out.

Firstly, bovine oocytes were randomly distributed between the microfluidic device and a four-well culture dish, and matured for 24 h. Maturation rates were analyzed following nuclear and cytoplasmic maturation (chromosome and cortical granule distribution, respectively) by means of staining. Secondly, sperm viability, acrosome abnormalities and motility were assessed at 3, 6, 12 and 24 h in three different units, namely the sperm storage microfluidic device, a four-well culture dish and a 1.5 mL Eppendorf tube. Finally, bovine oocytes were matured either in the microfluidic device or in a four-well culture dish, and subsequently fertilized in vitro in four-well dishes to evaluate penetration rates. All the experiments were conducted in triplicate.

In order to carry out these sets of experiments, two different setups were designed. On the one hand, the experiments involving the sperm storage

microfluidic device were carried out by simply using a pipette to inject or retrieve the sperm samples into/from the device.

On the other hand, the experiments involving the oocyte-trapping LOC device were carried out in a setup schematically depicted in Figure 4.2. Inlet 1 was connected to a syringe pump (540060, TSE Systems, Bad Homburg, Germany) in combination with a 2.5 mL gas-tight glass syringe from Hamilton (Bonaduz, Switzerland) by means of polytetrafluoroethylene (PTFE) (i.d. 0.8 mm) tubing. This syringe (S1) contained the maturation medium to fill the microfluidic channels. Inlet 2 contained a short fragment of flexible Tygon tube, which was used as injection port for the polished glass capillary syringe (S2) containing the oocytes. Once the capillary was inserted in the injection port, the syringe was set on a pump in order to inject the oocytes into the microfluidic device. Port 3 was used as auxiliary waste outlet during the process of filling the device with media in order to remove any air bubbles, and then was capped with a stopper for the rest of the experiment. Port 4 was linked to a 3-way valve (161T031 NResearch, MA, USA) connecting the oocyte-trapping LOC device to either the waste (during oocytes loading) or a syringe (S4) with media (during oocyte collection after the experiment).
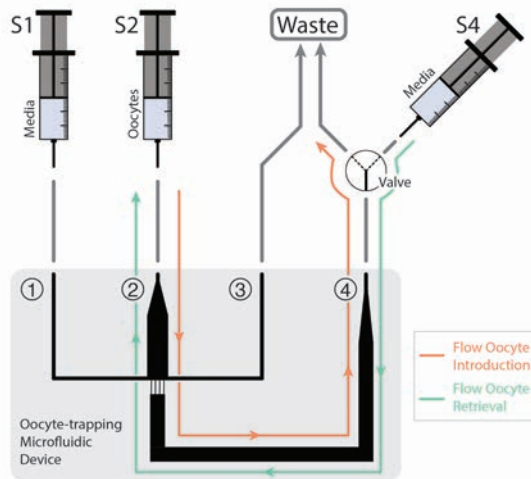
Figure 4.2: Schematic representation of the experimental setup for the oocyte maturation experiments *on-chip*. The oocyte-trapping microfluidic device consisted of four inlet/outlet ports. Ports 1 and 3 were simply used to fill the device with media and remove any air bubbles trapped next to the filter-like channels. Ports 2 and 4 were used for the oocyte injection/retrieval.

4.2.4   Oocyte and Sperm Handling *On-Chip*

The microfluidic devices were washed with 70 % ethanol and rinsed twice with Milli-Q water. After drying, they were exposed to UV light for 30 min for sterilization. Prior to introduction of either oocytes or sperm, the microfluidic devices were respectively filled in with maturation or fertilization medium equilibrated at 38.5 ℃ in a 5 % CO_2 incubator.

Oocytes were loaded into the microfluidic device through a flexible Tygon tube (Port 2, Figure 4.2), which acted as an injection port. The tip of the polished glass capillary syringe S2 was inserted in the flexible tube and then, the syringe was coupled to a pump. A flow rate of 50 µL/min was applied until the oocytes reached the maturation chamber. To achieve that, Port 3 was capped and therefore the flow was directed from Port 2 to Port 4 through the filter-like microchannels, and then into the waste (see Figure 4.2). The oocytes were thus retained in the filter-like structure since their size is bigger than the dimensions of the microchannels. In order to retrieve the oocytes after the maturation experiments, the flow direction was inverted: the syringe in Port 2 was unplugged —leaving only a small fragment of tube— and the valve in Port 4 was switched, connecting the device to the syringe S4. Then, a 50 µL/min flow rate was applied in the direction from Port 4 towards Port 2. Oocytes were thus collected in four-well plates.

Sperm samples were injected into the sperm storage microfluidic device directly with a pipette. Immediately after injection, both inlet and outlet were sealed using an adhesive film AB-1170 from Thermo Scientific (Schwerte, Germany), and the microfluidic device was incubated at 38.5 ℃ for the corresponding period of time. After the incubation, the film was removed and the sperm sample was collected with a pipette. The sperm samples were then analyzed to assess sperm quality parameters after different periods of time in contact with the COC.

4.2.5   Thermal Control System

Essentially, the thermal control system consisted of a temperature sensor and a gold heater embedded on the LOC device, and a Printed Circuit Board (PCB) with the control electronics (see Figure 4.3). The temperature sensor (PT100, Innovative Sensor Technology, Switzerland) provided the temperature input signal to the microcontroller. This input is converted to a digital signal and compared to a set value (target temperature). A Proportional-Integral-Derivative (PID) controller estimates the error (deviation from the target temperature) and tries to correct it by delivering a Pulse Width Modulated (PWM) signal. The PWM is amplified and the output current sent to the heating resistor to compensate the deviation from the target temperature.

The temperature control program is attached in Appendix B, while the design of the PCB can be found in Appendix C.

The thermal control system was previously prototyped in our research group using a breadboard, and was applied to microreactor syntheses (Martínez-Cisneros, Pedro, et al. 2012). During this project, the circuit was refined and redesigned to a PCB in collaboration with Dr. C.S. Martínez-Cisneros (Universidad Carlos III Madrid) and Prof. Joan Garcia and Javier Hellín (UAB, Dept. Electronic Engineering).

4.3 LOC Device Fabrication

Two different microfluidic devices were fabricated on COC to separately study the maturation of oocytes and sperm storage. TOPAS 5013 sheets (T_g 134 °C) were used in this study as substrate for the microchannels, while 25 μm thick TOPAS 8007 foils (T_g 78 °C) were used to ensure a reliable bond between layers using a temperature diffusion bonding technique (see Section 3.3.3 for a thorough explanation).

4.3.1 Sperm Storage Device

The microfluidic device for sperm storage consisted of a simple channel to store the sperm samples for different periods of time and then compare the quality of the samples with the control experiments. Four independent microfluidic units were fabricated on the same substrate to study the sperm samples at 3, 6, 12 and 24 h, respectively. The dimensions of the channel were chosen to provide the required volume for the motility and viability tests (total volume around 90 μL). Figure 4.4 shows the LOC device used in the study of the sperm samples.

The fabrication procedure of this device is very similar to that reported in Section 3.3. Briefly, the device consists of three layers of TOPAS 5013, 1 mm thick. In this case, top and bottom layers were laminated with a 25 μm TOPAS 8007 (which acted later as "glue" to seal the device) in a uniaxial hydraulic press. The COC layers were machined using a micromilling Computer Numeric Control (CNC) machine Protomat S63 (LPKF Laser & Electronics, Garbsen, Germany). The CNC micromilling machine used in this case is a new model recently acquired by the research group, and therefore the design approach was adapted to the new software (see Protomat S63 tutorial description in Appendix D). The previous software transformed a line into a microchannel with a width defined by the diameter of the milling tool (see Figure 3.9). With the new micromilling machine, the area of the channel is defined in the design, and the machine automatically selects the more suitable milling tool(s) to machine it (see Figure 4.5).
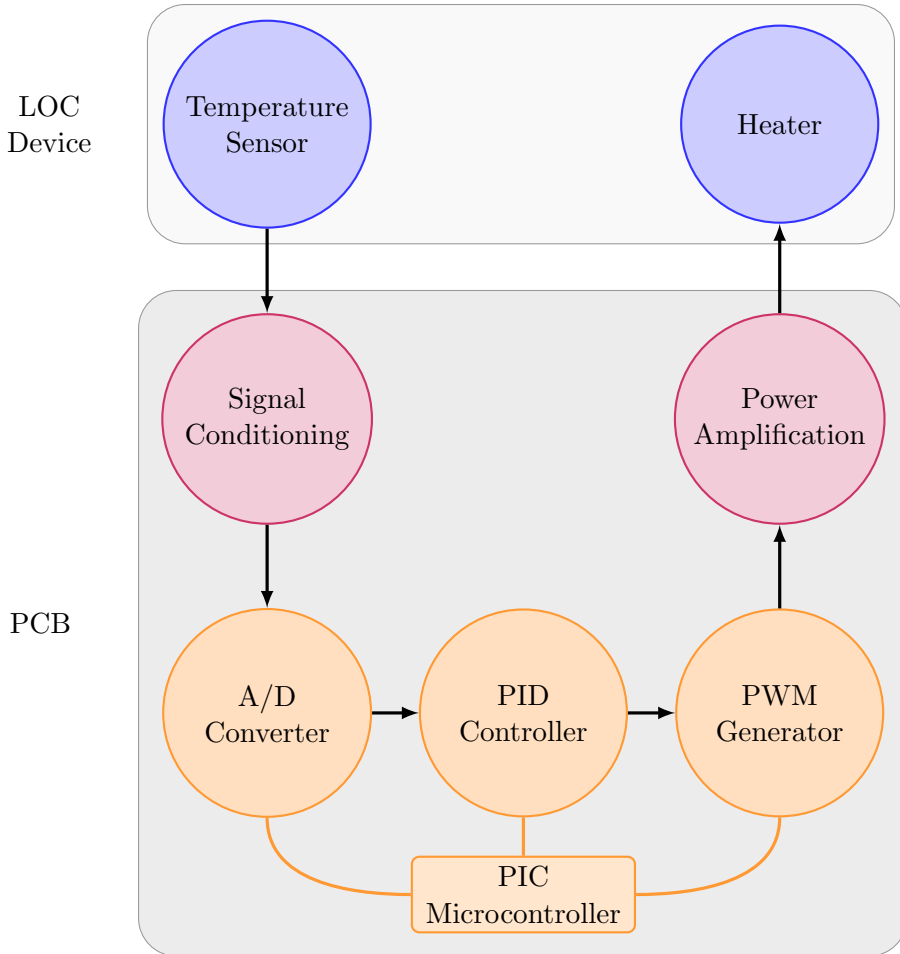
Figure 4.3: Block diagram of the thermal control system. The temperature input signal from the sensor is conditioned and sent to the PIC microcontroller. The analog signal is converted to digital and compared to the set value. A PWM wave is created to correct the difference between input and set values, which is then amplified and sent to the heater actuator to maintain the desired temperature.
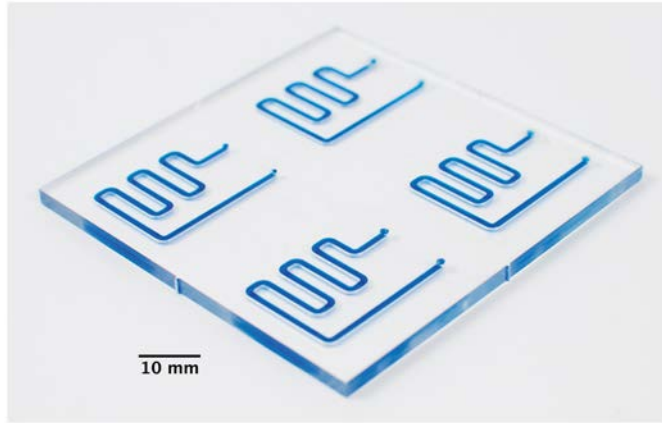
Figure 4.4: Microfluidic device for sperm storage. The device features four independent fluidic units to analyze a sample at different times. For clarity purposes, the channels were filled with blue dye.

(a) Top layer   (b) Middle layer   (c) Bottom layer
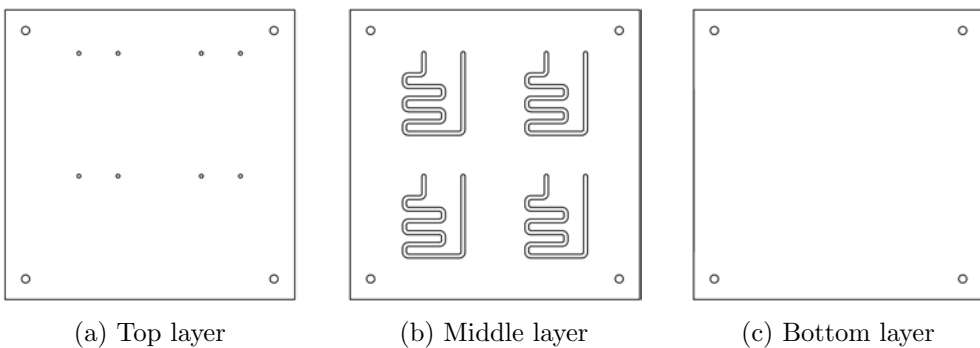
Figure 4.5: Layer breakdown of the LOC device for sperm storage.

67

The top layer was drilled to create the inlet and the outlet. The fluidic channel was milled in the middle layer, by cutting the COC through. The bottom layer did not include any fluidic feature. Then, the three layers were aligned and laminated at 100 ℃ under a pressure of 6 bar. This approach prevents any surface roughness created by the milling machine when creating a bas-relief channel.

4.3.2   Oocyte Maturation Device

The oocyte-trapping LOC device consisted of a maturation chamber with a filter-like structure to trap the oocytes and four inlet/outlet ports (see Figure 4.6). From a fabrication perspective, the microfluidic features were more challenging than those of the sperm device due to their reduced dimensions. Microfluidic channels with a smaller size than the oocyte diameter (around 100 μm) were required to trap them, and common micromilling equipment employed for thermoplastics is not able to achieve such dimensions (Guckenberger et al. 2015). Therefore, we developed a hybrid fabrication process consisting of a combination of hot embossing (for the smaller features) and micromilling.

(a) Oocyte trapping device   (b) Close-up of the trapping region
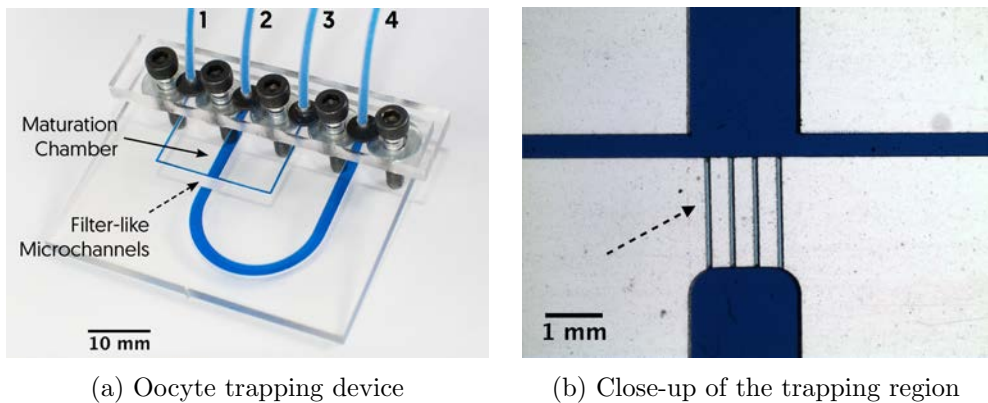
Figure 4.6: Oocyte-trapping LOC device and close-up of the oocyte-trapping region. The numbers 1–4 refer to the inlets/outlets, and the dashed arrow indicated the position of the filter-like microchannels. For clarity purposes, the channels were filled with blue dye.

On the one hand, the bigger channels and chambers were machined using the CNC micromilling machine. On the other hand, the smaller microchannels that retain the oocytes (microchannels highlighted with a dashed arrow in Figure 4.6) were fabricated by hot embossing using an LTCC master. These channels enable the liquid to flow but retain the oocyte cells, as seen in Figure 4.7. This type of microchannel constriction to trap the oocytes has been

used in studies with PDMS devices, showing an enhanced performance by mimicking the physical conditions *in-vivo* (Clark, Haubert, et al. 2005; Suh et al. 2006).
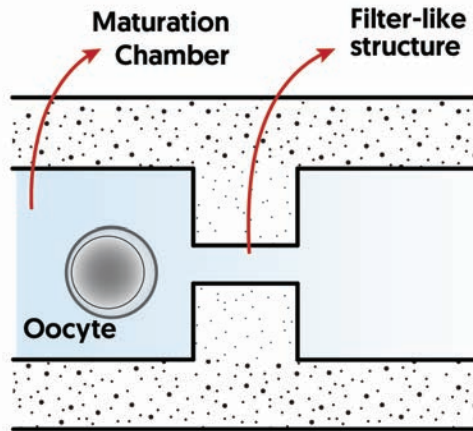
Figure 4.7: Cross section view of the device showcasing the oocyte-trapping principle. It is based on a channel constriction where the oocytes do not fit —the oocytes are trapped in a filter-like structure.

The use of LTCC enables a rapid and low-cost prototyping of the masters compared to metal molds. The fabrication process enabled the rapid iteration from design to prototype. Moreover, the LTCC masters did not require any demolding agents and showed good feature integrity after more than 30 uses. The synergy of hot embossing and micromilling provides a rapid fabrication method for multilayer LOC devices, combining the simplicity of milling with the smaller features achievable with hot embossing. The whole fabrication process is schematically depicted in Figure 4.8.

Firstly, the master was built using LTCC 951PX, 254 µm thick, from DuPont (Germany). 8 LTCC layers were thermo-laminated together in a uni-axial hydraulic press. Then, the ceramic block was etched by means of a Protolaser 200, from LPKF (Garbsen, Germany) and sintered in a programmable box furnace from Carbolite (CBCWF11/23P16, Afora, Spain). The master was designed to have four negative images of microchannels (Figure 4.8 Structure 4), in order to create a filter-like structure in the microfluidic device.

Secondly, the LTCC master was used to fabricate the trapping microchannels of the LOC device —the channels with smaller dimensions than the oocytes. A 500 µm thick layer of TOPAS 5013 was embossed with the LTCC master at 155 ℃ ($T_{embossing} = T_{\mathrm{g}}(5013) + 21\,℃$) and 6 bar, thus obtaining four microchannels in the COC substrate (Figure 4.8 Structure 6). Another
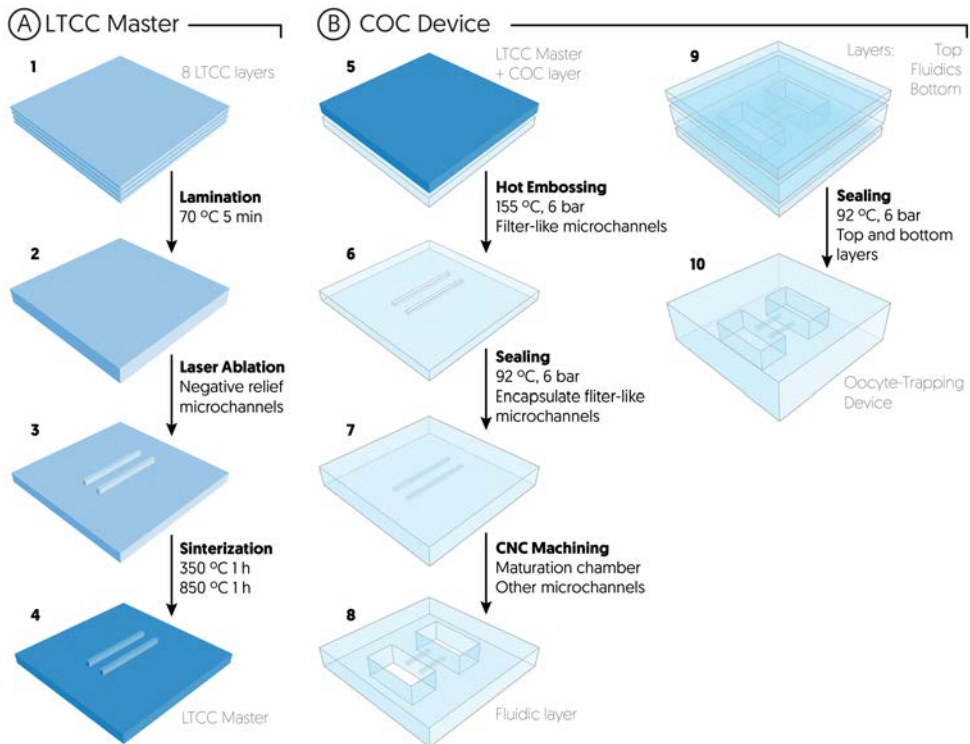
Figure 4.8: Schematic representation (not to scale) of the oocyte-trapping LOC device fabrication. A) Fabrication of the LTCC master. B) Fabrication of the COC oocyte-trapping LOC device, by means of hot embossing the smallest features (i.e. the filter-like microchannels) and micromilling the maturation chamber and the rest of the channels. The device is then sealed by means of a thermocompression process.

500 μm COC sheet (previously laminated with a 25 μm thick TOPAS 8007 foil) was used to seal the replica microchannels, at 92 ℃ and 6 bar. In this case, the lamination conditions were a bit softer than for prior devices (100 ℃ and 6 bar in the case of the sperm LOC device), in order to ensure the integrity of the smaller microchannels and avoid occlusion. After this lamination, the four trapping microchannels were completely sealed (Figure 4.8 Structure 7).

The rest of the fluidic structures, namely the maturation chamber and the inlet and outlet channels, were machined cutting through Structure 7 (replica and sealing layers) using the micromilling machine. The features microstructured with the CNC micromilling machine in this structure as well as in the top and bottom cover layers are shown in Figure 4.9). Then, the three COC layers were aligned and thermolaminated, thus obtaining the sealed LOC device. Both top and bottom layers had been pre-laminated with a film of TOPAS 8007, which acted as "gluing" layer, as described in Section 3.3.3. Inlet and outlet vias were drilled using the CNC micromilling machine.

(a) Top layer   (b) Middle layer   (c) Bottom layer
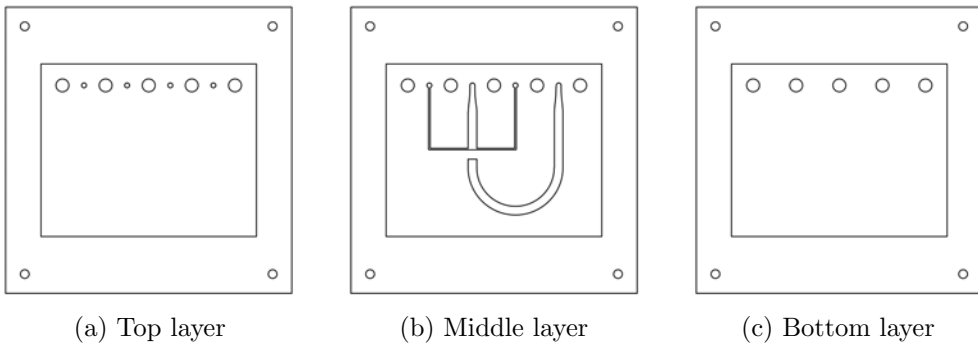
Figure 4.9: Layer breakdown of the LOC device for oocyte maturation. Only features microstructured with the CNC micromilling machine are included. Structural holes drilled in all layers are meant for interconnection purposes.

Figure 4.10 shows a cross section of the filter-like structure obtained. The channels had a trapezoidal shape, with dimensions of approximately 100 and 50 μm, respectively for the bases, and 55 μm high. This size was adequate to trap the oocytes ($\varnothing ca.$ 100 μm), while enabling a stable medium flow through them.

Figure 4.6 shows the oocyte maturation device with the tubing connected. As detailed in Section 4.2.3, Ports 1 and 3 served as auxiliary inlet and outlet, respectively, to fill up the device with medium. Ports 2 and 4 served to drive the flow during the oocyte injection and retrieval. The maturation chamber had a total approximate volume of 25 μL.
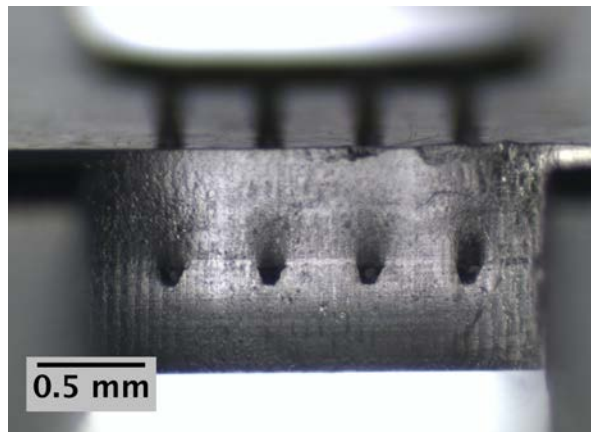
Figure 4.10: Cross section view of the oocyte-trapping microchannels embossed using the LTCC master, after lamination with another 500 μm layer.

4.3.3 Device with Integrated Heater

The fabrication of this LOC device was similar to that reported in Section 4.3.2 for the fabrication of the oocyte maturation device, with the addition of an integrated heater. The microchannels with smaller dimensions (the "filter-like" structure to trap the oocytes) were hot embossed with an LTCC master, while the rest of the fluidic elements were microstructured using the CNC micromilling machine (see layer breakdown in Figure 4.11). The main fluidic difference consisted on the modification of the channel corresponding to Port 1 (see the meandering channel in Figure 4.11b).

The meandering channel was conceived to store and deliver fresh media to the maturation chamber. This type of dynamic culture is intended to renew the factor availability in the vicinity of the oocytes, and thus improve the maturation process. In order to warm up the fresh buffer to the culture temperature, the channel was designed as a long meandering shape (100 mm) with a total volume of *ca.* 100 μL.

The main innovation of this LOC device consisted on the monolithic integration of a transparent heater. This heater provides the grounds for the development of an independent culture/fertilization platform by avoiding the need for an incubator, and furthermore, enabling the continuous visualization of the oocytes under a microscope. The actuator consisted of a thin layer of Au (in the tens of nanometers range) that acted as a Joule heater. The low thickness enabled enough light transmission to see the cells.

The gold was deposited in collaboration with Gerardo López, from the group of Prof. Laura M. Lechuga at *Institut Català de Nanociència i Nanotec-*

(a) Top layer

(b) Fluidics block

(c) Bottom layer

(d) Heater cover

(e) Deposition mask
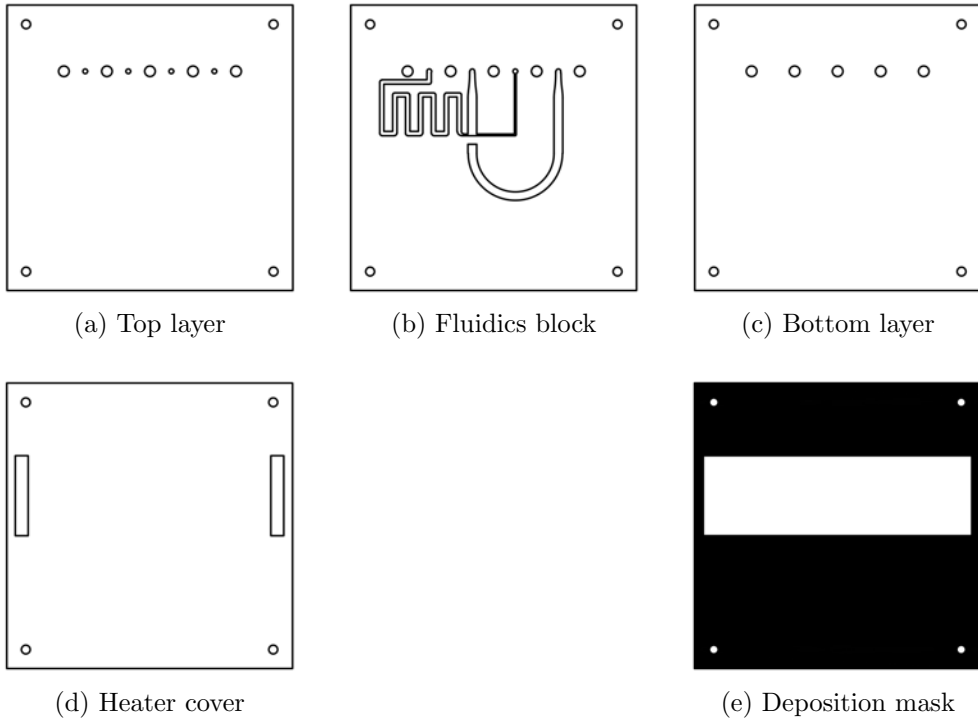
Figure 4.11: Layer breakdown of the LOC device for independent oocyte maturation. Only features microstructured with the CNC micromilling machine are included. Structural holes drilled in all layers are meant for interconnection purposes. The deposition mask was attached to the heater cover layer during the gold sputtering process in order to pattern only the white rectangle area.

nolgoa. The deposition was performed by Physical Vapor Deposition (PVD) on a TOPAS 5013 COC layer 500 μm thick (the bottom layer, see Figure 4.11c) using a deposition mask to cover a selected area (see Figure 4.11e). The COC sheet was exposed to the Au for different times, thus obtaining thicknesses ranging from 10 to 60 nm. The Au layers showed good adhesion to the COC surface by withstanding a scotch tape test, where a strip of tape is placed over the pattern, rubbed, and then removed (Madou 2002). Another TOPAS 5013 COC sheet 500 μm thick was used as cover for the deposited gold heater. It contained two rectangular through-cuts for the electrical connection of the gold resistor (see Figure 4.11d).

All the different layers making up the LOC device were aligned and laminated at 92 °C and 6 bar (see Figure 4.12). Bonding between the Au-sputtered area and the COC cover was performed under normal conditions, yielding devices with perfect structural integrity. No bonding issues such as delamination were observed. Then, the two rectangular through-cuts of the cover layer were filled with silver conductive epoxy paste (Circuitworks 2400, Chemtronics, GA) to create electrical contacts —bus bars for current power distribution. A PT100 temperature sensor (Innovative Sensor Technology, Switzerland) was glued to the microreactor using Epoxi paste EPO-TEK H20E (Billerica, MA, USA). The LOC device was placed in an oven in order to cure the epoxi pastes overnight at 50 °C.

4.4   Results & Discussion

In order to assess the viability of an independent COC culture and fertilization platform, several factors needed to be studied. First, the functionality of the LOC device to effectively trap the oocyte cells had to be determined. Second, the suitability of the COC as substrate material was evaluated from a biocompatibility perspective. Different experiments were devised to separately study the biocompatibility of the COC with oocytes and spermatozoa cells, and results were compared to traditional culture methods. On the one hand, the oocytes were matured *on-chip* and different parameters were evaluated, such as cytoplasmic maturation and their ability to be fertilized. On the other hand, spermatozoa were stored in a LOC device and then common sperm quality parameters were assessed. Finally, the LOC device with integrated heater and its thermal behavior were evaluated.

4.4.1   Oocyte Trapping

The oocytes were trapped in the vicinity of the filter-like microchannels of the maturation chamber, as seen in Figure 4.13. The oocytes were injected at a flow rate of 50 μL/min. This flow rate was experimentally optimized taking

(a) Cross-section diagram before lamination

(b) Cross-section diagram after lamination
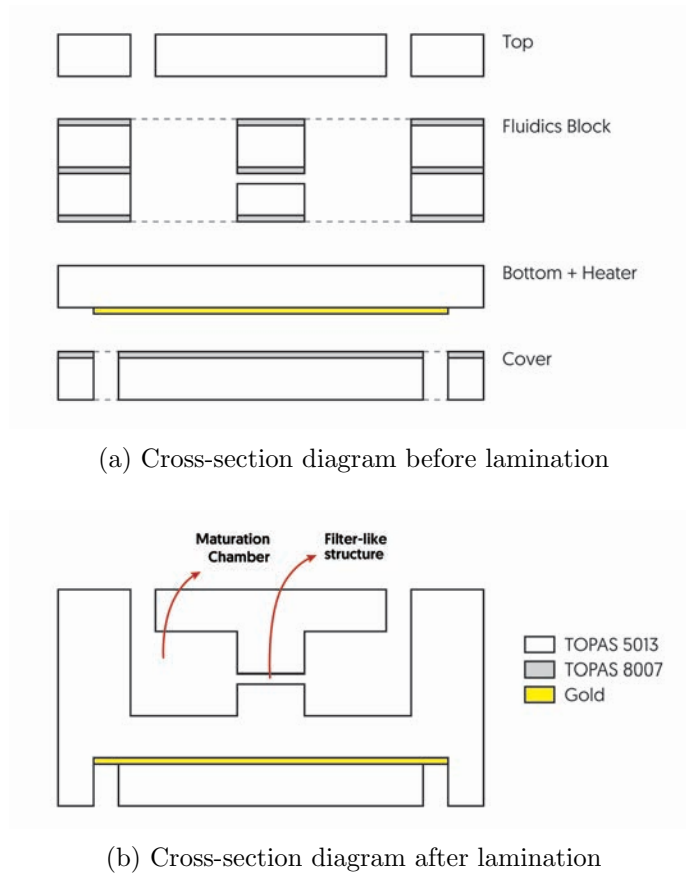
Figure 4.12: Schematic cross-section view of the device with integrated heater, before and after lamination. For clarity purposes, the different elements are not to scale.

two factors into account: oocyte integrity and required time. On the one hand, using smaller flow rates would involve longer times for oocyte loading/retrieval. On the other hand, no oocyte deformation was observed using this condition. Higher flow rates caused the deformation and/or denudation of the oocytes in the filter-like channels (channel constriction).
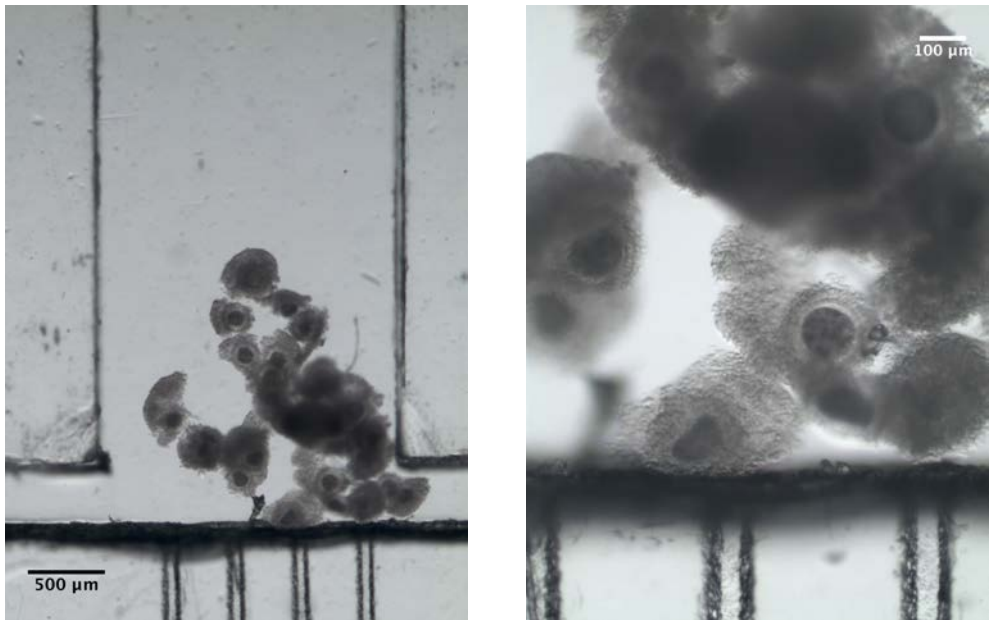
(a) Oocytes trapped in the LOC device   (b) Close-up of the trapping region

Figure 4.13: Microscope pictures of the oocytes trapped in the LOC device. (a) General view of the maturation chamber and (b) close-up of the oocytes near the capillary channels. The shadowed areas of the capillary channel correspond to its walls, as it has a trapezoidal shape.

Other studies in the literature take advantage of this phenomenon for cumulus removal (Zeringue, D. J. Beebe and Wheeler 2001), an essential process prior to fertilization. However, at this stage we were not interested in that due to the important role of cumulus cells in oocyte maturation (L. Zhang et al. 1995) and the fact that fertilization was not performed *on-chip*. Nevertheless, the possibility to perform oocyte denudation by simply applying a certain flow pattern strengthens our vision of an independent COC culture/fertilization platform.

4.4.2 *On-chip* Oocyte Maturation

Figure 4.14 shows the results obtained from the oocytes *in vitro* matured into the LOC device compared with the four-well culture dish. Figure 4.15 shows examples of oocytes correctly matured, i.e. correct nuclear maturation (Figure 4.15a) and Cortical Granule (CG) migration (Figure 4.15b). Although oocytes matured in the LOC device showed a low-grade cumulus cell expansion, no significant differences ($P > 0.05$) were found in the percentage of oocytes progressing to normal MII and cytoplasmic maturation between both devices. These results are in agreement with others found in the literature (Walters, D. J. Beebe and Wheeler 2001), in which pig oocytes matured in PDMS microchannels did not show significant differences ($P > 0.05$) in the percentage of maturation rates compared with oocytes matured in conventional 500 µL drops or in 8 µL drops (volume control). In addition, Walters, D. J. Beebe and Wheeler 2001 also observed a low grade of cumulus cell expansion of the cumulus-oocyte complexes matured in the PDMS device. The molecular processes involved in cumulus cell expansion need to be evaluated to check presumptive implications on processes related to fertilization and embryo development.
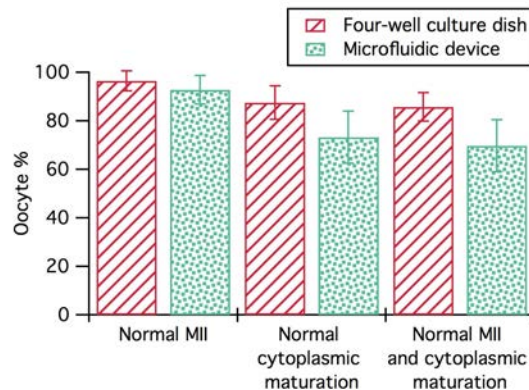
Figure 4.14: Effect of different culture devices on nuclear and cytoplasmic maturation of bovine oocytes. No significant differences were detected ($P > 0.05$).

The small volumes used in microfluidic systems may lead to a rapid depletion of factors and/or a pH shift in the surroundings of the oocytes. The pH in the LOC device is not buffered with the CO_2 atmosphere of the incubator because it is airtight —unlike the four-well dish— and this could cause the lower cumulus cell expansion. This could happen because oocytes appear to

(a) Correct nuclear maturation

(b) Nuclear maturation & CG migration
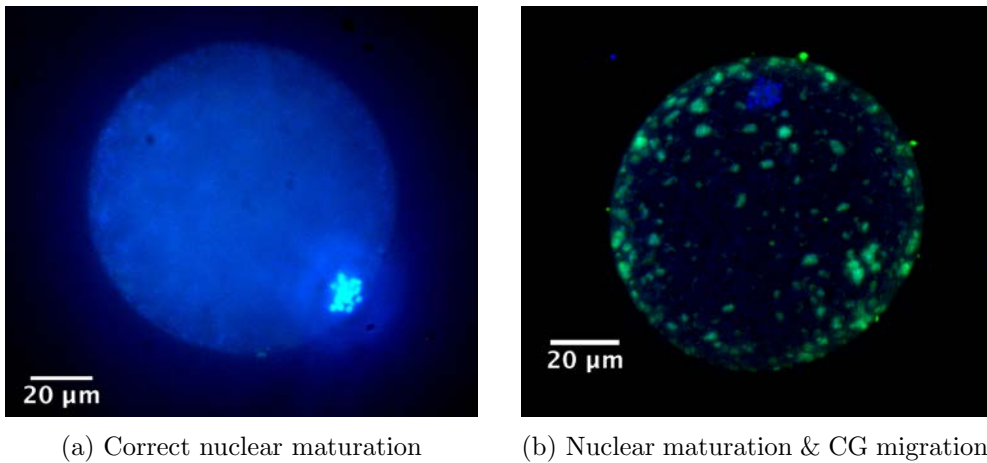
Figure 4.15: Microscope images of correctly matured oocytes. 4.15 Oocyte correctly matured in vitro to the MII nuclear stage. Image obtained under an epifluorescence microscope after DAPI staining. Oocyte diameter is close to 100 µm. Oocyte correctly matured in terms of nuclear maturation (MII stage) and cortical granule (CG) migration. Image merged from nuclear (blue fluorescence) and CG (green fluorescence) staining under confocal laser microscopy.

lack porters to regulate their intracellular pH (FitzHarris 2006; K. P. Phillips 2002), which is greatly affected by CO_2 and O_2 concentrations (Pinyopummintr and Bavister 1995). Although this could be overcome by employing dynamic culture —for instance by imparting flow and thus renewing the media— in this study we evaluated the static culture, as it can be more easily compared with the traditional four-well dish method.

4.4.3   In Vitro Fertilization After *On-Chip* Maturation

Table 4.1 shows the significantly higher percentages of sperm penetration observed in the four-well culture dish when compared with the LOC device at 18 h after IVF (61.44 % vs. 35.63 %, respectively; $P < 0.05$). However, in terms of normal fertilization with male pronuclear formation, no significant differences were observed between both devices ($P > 0.05$). These data suggest that when an oocyte is penetrated by a sperm cell, fertilization is comparable and efficient in both maturation systems. Thus, the detected reduction in the fertilization rate after *on-chip* oocyte maturation seems to be a consequence of the quality of the matured oocyte rather than due to deficiencies in the process of fertilization.

Table 4.1: Effect of culture systems on the fertilization rates of *in vitro* matured oocytes.

System	Oocytes (n)	Total Penetration (%)	Normal Male Pronucleus Formation (%)	Abnormal Polyspermic Penetration (%)
Four-well	153	61.4[*]	82.9	17.0
LOC device	87	36.8[*]	78.8	21.9

[*] Values within a column differing significantly, $p < 0.05$.

The oocyte maturation system adequately supported nuclear maturation but probably failed to produce oocytes with a complete cytoplasmic competency, additionally to correct CG migration and maturation. Cytoplasmic maturation encompasses a wide array of metabolic and structural modifications, including events that ensure the occurrence of normal fertilization, meiotic-to-mitotic cell cycle progression, and activation of pathways required for genetic and epigenetic programs of preimplantation embryonic development (Combelles 2002). Additionally, it is known that cumulus cell expansion is an important marker for oocyte maturation (Chen et al. 1990). Indeed, in cattle, inhibition of cumulus cell expansion was shown to be independent from nuclear maturation, but essential for fertilization and subsequent cleav-

age and blastocyst development (Gutnisky et al. 2007). Thus, it might be thought that the low grade of cumulus cell expansion observed after *on-chip* maturation could also be related to a poorer maturation of the zona pellucida, necessary for a proper fertilization of the oocyte. However, and as stated before, employing a dynamic culture with the *on-chip* oocyte maturation system could help to improve the overall oocyte maturation.

4.4.4 Time-Dependent Sperm Evaluation

Sperm samples were distributed between the sperm LOC device, a four-well culture dish and an Eppendorf tube. After certain periods of time, the samples were retrieved and their quality parameters assessed. Results obtained are shown in Table 4.2. The data show the expected decrease of the percentage of viability and motility, and an increase of the percentage of acrosome abnormalities over time, with no significant differences among the three devices ($P > 0.05$). This suggests that COC is an innocuous and biocompatible material regarding sperm quality parameters, and it could be used for the development of LOC systems for ART applications. Previous studies have tested the biocompatibility of materials such as PS (standard petri dish material), polyimides, silicons and PDMS, assessing mice embryo development and pig sperm motility parameters (Chan, Raty, et al. 2001; Clark, Davis, et al. 2001; Chan, Lyman, et al. 1999). However, to the authors' best knowledge, this is the first study that has tested the biocompatibility and absence of COC toxicity on bovine gametes.

4.4.5 Towards an Independent Maturation Device

The differences observed between the LOC device and the four-well culture dish presented throughout this chapter can also be explained by the fact that the COC LOC device is airtight and does not allow the gas exchange, thus impeding the buffering of the media by the CO_2 contained inside the incubator. Similar maturation studies in PDMS devices (gas permeable) show a significantly higher percentage of porcine embryo cleavage rates (67 % vs. 49 %; $P < 0.05$) (Hester et al. 2002).

Although the gas permeability is generally accounted as an advantage, it has a negative side. Due to this intrinsic property, PDMS devices require a controlled atmosphere, usually attained in an incubator. Moreover, the problem of the depletion of factors around the oocytes and the media buffering could be overcome by using a dynamic culture —renewing the media by pumping fresh one into the maturation chamber. The issue of the necessary gas exchange could also be overcome by designing a LOC consisting of independent liquid and gas systems, interconnected by a gas permeable membrane. The integra-

Table 4.2: Sperm quality parameters (viability, acrosome abnormalities and motility characteristics) after the storage in three different devices (LOC device, four-well culture dish and 1.5 mL Eppendorf tube) for 3, 6, 12, and 24 h.

	Time (h)	LOC device	Four-well dish	Eppendorf tube
Cell	3	48.3 ± 3.0	52.8 ± 3.6	50.2 ± 4.5
Viability	6	34.7 ± 5.5	37.7 ± 10.9	39.6 ± 8.5
(%)	12	20.5 ± 0.5	29.1 ± 5.3	27.8 ± 6.1
	24	20.0 ± 8.2	27.0 ± 4.8	22.5 ± 3.1
Acrosome	3	44.8 ± 11.6	43.5 ± 19.8	37.2 ± 2.5
Abnormalities	6	46.3 ± 9.8	38.2 ± 7.7	48.0 ± 6.1
(%)	12	70.5 ± 12.2	46.2 ± 17.4	52.5 ± 4.6
	24	70.5 ± 17.8	67.5 ± 9.9	66.7 ± 2.8
Progressive	3	18.1 ± 0.5	15.9 ± 4.9	18.2 ± 0.6
Motility	6	17.9 ± 5.0	19.4 ± 3.2	22.4 ± 7.6
(%)	12	6.1 ± 4.8	12.5 ± 3.1	12.8 ± 7.2
	24	1.7 ± 0.5	5.7 ± 5.8	3.0 ± 1.3
Total	3	28.9 ± 3.4	22.3 ± 3.9	24.0 ± 2.4
Motility	6	27.2 ± 5.0	24.1 ± 3.9	27.2 ± 6.4
(%)	12	11.1 ± 2.8	16.0 ± 3.2	16.7 ± 8.9
	24	4.1 ± 3.1	7.2 ± 6.4	4.2 ± 1.1

tion of gas permeable membranes in COC devices has been demonstrated in previous studies in our research group (Ymbern, Sández, et al. 2014; Calvo-López, Ymbern, Puyol, et al. 2015; Calvo-López, Ymbern, Izquierdo, et al. 2016).

Another aspect that needs to be addressed is the heating and temperature control of the device (Miralles et al. 2013). Furthermore, the heater should be transparent in order to study the development of the gametes with optical microscopy techniques. Therefore, very thin layers of gold were used as resistors to dissipate heat when a current was applied (Joule effect). The temperature was controlled with a PID implemented on a PIC18F4553 microcontroller (find the temperature control program attached in Appendix B).

Au deposition thicknesses ranging from 10 to 60 nm were studied. The 10 nm thick gold layer was directly discarded due to current discontinuities, attributed to discrete Au islands (clusters) present on the substrate surface (Siegel et al. 2011). The rest of the Au layers behaved as continuous elec-

trical layers when evaluated with a multimeter. Although transmittance of the sputtered layers decreased with thickness, all the studied Au layers were transparent to a certain degree (see Figure 4.16). Due to the higher transparency and more adequate resistance value, the 20 nm Au layer was selected for integration in the LOC device.

(a) 20 nm Au   (b) 30 nm Au   (c) 40 nm Au

(d) 50 nm Au   (e) 60 nm Au
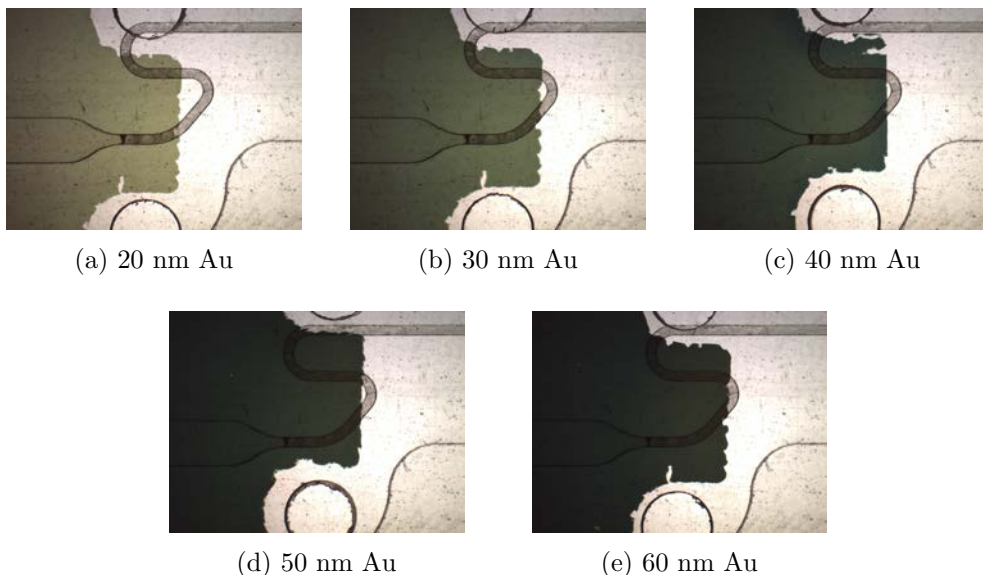
Figure 4.16: Photographs of COC sheets with different thicknesses (20–60 nm) of sputtered Au. For a better notion of the transparency, the sputtered COC sheets were placed on top of a LOC device.

The device with integrated heater was very similar to the oocyte maturation device presented in Section 4.3.2, regarding the fluidic elements (see Figure 4.17). The only significant difference in the fluidics is the extension of the auxiliary inlet channel (Port 1, compare compare Figures 4.6a and 4.17). The purpose of that longer channel is to serve as media inlet in dynamic cultures, i.e. to renew the medium of the maturation chamber periodically. In order to warm up the media and avoid temperature drops in the maturation chamber, the channel was enlarged and designed to accommodate *ca.* 100 µL.

In order to obtain the temperature distribution and study the heating capability of the Au heater, an infrared (IR) camera (Fluke Ti200) was used to take thermal photographs of the device. Figure 4.18a shows the temperature distribution over the LOC device. The area inside the rectangle —where maturation chamber and auxiliary inlet are located— has an average temperature of 37.9 °C. Figure 4.18b shows the temperature profile along the dashed line crossing the rectangle. The average temperature is in this case very close
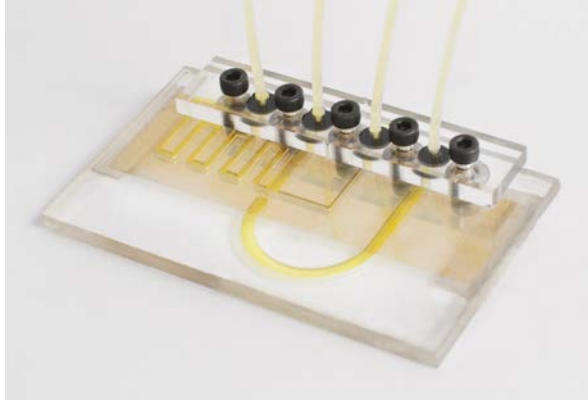
Figure 4.17: Oocyte maturation device with integrated heater. The temperature sensor does not appear in the photograph. For clarity purposes, the channels were filled with a yellow food dye solution.

to the adequate value for oocyte maturation (38.5 ℃), although it shows a variation of nearly ± 1 ℃.

The LOC system with integrated heater is currently prepared for evaluation with oocyte maturation experiments, and ultimately for IVF. This studies will be conducted in the near future within our research group, again in collaboration with the group of Prof. Manel López-Béjar.

4.5   Conclusions

This chapter describes a novel rapid prototyping process for LOC devices made of COC. It combines a hot embossing step for the smaller features required —using an LTCC master— and a micromilling step for the rest of the fluidic structures. The LOC device allows trapping the oocytes by means of a filter-like structure as well as their maturation. We have demonstrated that the COC device enables the functional and automated maturation of oocytes, and that it is nontoxic for gametes. No significant differences were observed in oocytes reaching normal MII and cytoplasmic maturation in terms of CG migration, compared with the control experiments. Lower penetration rates were observed for oocytes matured in the LOC device, which could be related to the lower grade of cumulus cell expansion of the cumulus–oocyte complexes or an incomplete cytoplasmic maturation of the oocytes. However, this issue could be addressed by improving the factor availability and pH buffering capacity in the surroundings of the oocytes, for instance, by dynamic culture.

A LOC device with integrated Au heater was also developed. Gold layers of different thickness were sputtered over the COC substrate showing good

(a) IR thermal photograph

(b) Temperature profile plot
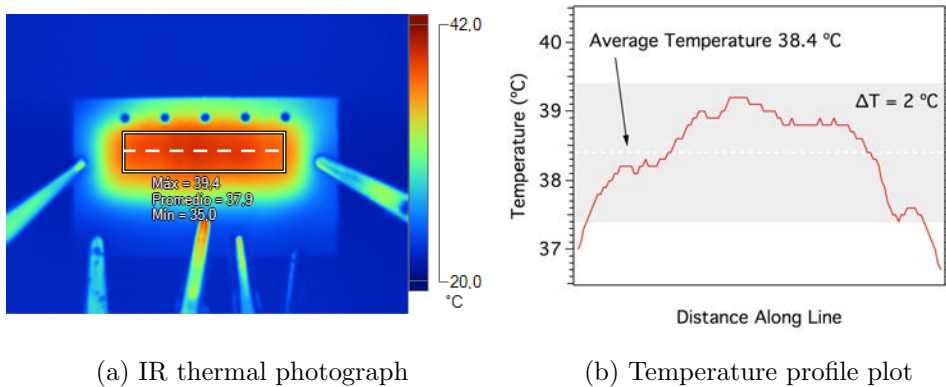
Figure 4.18: IR thermal photograph of the LOC device with integrated Au heater and temperature profile of the dashed line. The temperature control system was programed to maintain a temperature of 38.5 ℃, the same value as used for oocyte maturation in the incubator.

adhesion to the surface. Thermal images ware taken from the system, showing a good temperature distribution over the area where maturation chamber and inlet channels are located. However, the integrated heater should be further improved in order to obtain a better temperature homogeneity in the area of interest. A possible step towards that end is the design of a bigger heater area. However, a simulation study would greatly advance the development of the device to obtain the most homogeneous temperature distribution.

The properties of COC open new possible applications for LOC systems in ART due to the simple fabrication processes at both the prototyping and mass production scales, taking advantage of the different material grades commercially available. COC is not hindered by mass production limitations, absorption of molecules, or gas permeability, thus avoiding a strict control of the exterior atmosphere conditions, and provides simpler fabrication methods than other thermoplastics, especially regarding bonding. Therefore, we believe this material has great potential for the development of an independent culture and fertilization platform.

Chapter 5

LTCC microreactors for the synthesis of nanoparticles

5.1 Introduction

Nanotechnology is defined as the manipulation of matter with at least one dimension in the range 1–100 nm (National Nanotechnology Innitiative 2017). Therefore, this multidisciplinary field deals with extremely small things (see a scale comparison in Figure 5.1) that can be used in countless applications covering all scientific-technic areas, such as chemistry, biology, physics, engineering, etc. Nanotechnology examples abound in nature, taking advantage of the special properties conferred by their small size and large relative surface areas. Two common examples are the adhesion of gecko's feet to smooth surfaces (Autumn and Gravish 2008) or the hydrophobicity of lotus leaves (Karthick and Maheshwari 2008).

Feynman's visionary talk *There is plenty of room at the bottom* (Feynman 1960) is generally considered to have set the origins of nanotechnology, and more broadly, of miniaturization (as mentioned in Section 1.1.1). However, it was not until two decades later that his words started to receive significant attention (Toumey 2009), due to several breakthrough events between 1981 and 1991. The development of the Scanning Tunneling Microscope (STM) and the Atomic-Force Microscope (AFM) empowered scientists with higher resolution to study the nanoworld. The term nanotechnology was popularized by K. Eric Drexler in his book *Engines of Creation: The Coming Era of Nanotechnology* (Drexler 1986) and further spread within the scientific community with the foundation of the journal *Nanotechnology*, in 1989. The manipulation of individual Xe atoms to spell out IBM (Eigler and Schweizer 1990) and the *Science* special issue on nanotechnology (Brauman 1991) were other milestones that led to the coalescence of a novel, distinct field: Nanotechnology.
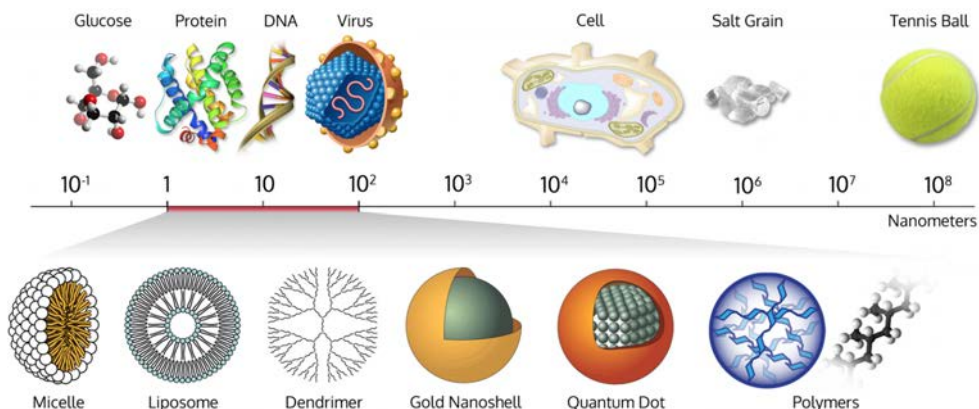
Figure 5.1: Scale comparison: from nano to macro. Adapted from Wich Lab 2017.

The immense potential of nanotechnology arises from the fact that properties of nanoscale objects are dominated by quantum effects. This means that material properties may dramatically change —compared to the bulk material— when a critical dimension is reached, due to the spatial confinement. One of the most typical examples of this behavior is observed when metal particles are downsized. For instance, the typical yellow color of gold disappears at about 50 nm to become purple, and further reduction of the colloid size results in red color, at *ca.* 15–20 nm. This color change is due to a sharp and intense absorption band in the visible range caused by a collective resonant oscillation (plasmon resonance) of the free electrons in the conduction band of the metal (Eustis and El-Sayed 2006). Depending on the particle size, the wavelength of the plasmon resonance absorption changes, giving rise to the color range of gold nanoparticle solutions.

Over the last years, a wide range of engineered nanomaterials have been developed. Particles with very different chemistries are synthesized and tailored to applications such as medical diagnostics and therapeutics, energy harvesting and storage, textiles, construction materials, electronics, chemical synthesis and purification, etc. Particularly, analytical chemistry has taken great advantage of the novel and enhanced properties of nanomaterials (Ligler and White 2013). For instance, nanomaterials used as labels can enhance the sensitivity of analytical methods compared to molecular labels (Zeng et al. 2014). Another example is the use of magnetic nanomaterials to separate and pre-concentrate an analyte, thus avoiding matrix effects and enhancing the sensitivity (Beveridge, Stephens and Williams 2011). Nanomaterials have also been extensively used in micro Total Analysis Systems (μTAS), thus bringing together the advantages of both technologies (Pumera 2011; Medina-Sánchez,

Miserere and Merkoçi 2012).

There are many different approaches for the synthesis of nanomaterials. These can be divided in top-down (breaking down a substrate) and bottom-up approaches (building up from molecules). In this dissertation, we used a bottom-up approach based on the nucleation and growth of nanoparticles in supersaturated solutions. This process is generally described using the theory developed by La Mer (LaMer and Dinegar 1950), schematically described in the La Mer diagram (Figure 5.2). As the concentration of monomer reaches a certain concentration (C_{min}), a rapid nucleation of the nanoparticles takes place. These nuclei or seeds will then undergo a slower process of growth.
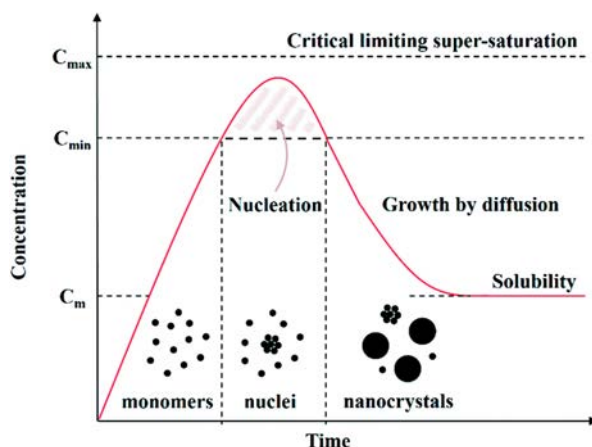
Figure 5.2: La Mer diagram describing the processes of nucleation and growth of nanocrystals in solution. Upon reaction of the reagents, product monomers are formed and their concentration steadily increases until the nucleation begins (C_{min}). Then, the concentration in solution drops and the colloids start growing by diffusion. Adapted from Nguyen and Do 2011.

Although there has been a great progress in the last two decades, the synthesis of nanomaterials still presents certain challenges, such as product homogeneity and batch-to-batch reproducibility. These issues originate from the difficulty to locally control reagent mixing and temperature. These small changes lead to size inhomogeneity of the product and, in consequence, to varying properties.

In this regard, microfluidic reactor technology emerged as a solution for the synthesis of nanomaterials and process intensification (Stankiewicz and Moulijn 2000). This technology is capable of improving the synthetic processes not only by better controlling shape and size distribution (Marre and Jensen 2010), but also by minimizing energy consumption, reagent volumes and waste

production (Elvira et al. 2013). The smaller reactor size contributes to more efficient and controlled heat and mass transfer due to the lower diffusion times, and thus, to a more homogeneous particle distribution (Gómez-de Pedro 2014).

Microreactor syntheses are easily automated by programming the flow impulsion systems, thus contributing to their reproducibility. Several strategies can be implemented to control the diffusion of the reagents, the nucleation of the nanoparticles and their growth. For instance, Figure 5.3 schematically depicts continuous (Marre, Park, et al. 2008; Gómez-de Pedro, Puyol and Alonso-Chamarro 2010; Makgwane and Ray 2014), segmented (Sebastian Cabeza et al. 2012; Nightingale and Demello 2013; Larrea et al. 2015) and droplet (Frenz et al. 2008; Erdem et al. 2014; Lignos et al. 2015) flow profiles, usually employed in microreactor syntheses.

(a) Continuous flow   (b) Segmented flow   (c) Droplet flow
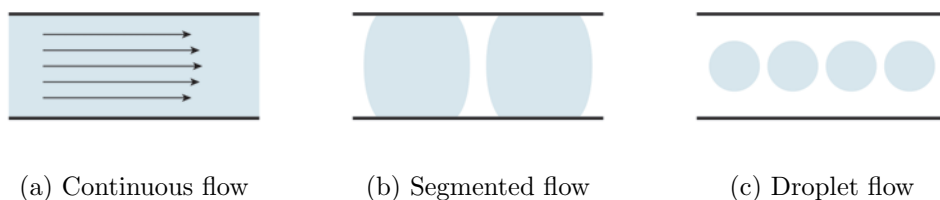
Figure 5.3: Schematic representation of different flow patterns in a microreactor. The two straight lines represent the walls of the microchannel. (a) Single phase continuous flow. (b) In segmented flow, the reaction mixture is divided into discrete units by an immiscible fluid (either gas or liquid). (c) Droplet flow is achieved when the reaction mixture is completely isolated from the channel walls. Adapted from T. W. Phillips et al. 2014.

Each flow profile has its advantages and disadvantages. For instance, segmented and droplet flows confine the reagents into discrete amounts (slugs or droplets), thus eliminating velocity dispersion and reducing the chances of channel fouling (Nightingale and Demello 2013). On the other hand, this approaches require of complex microreactor geometries and/or flow setups.

In this work, continuous flow was used owing to its simplicity of design and operation. Moreover, certain hydrodynamic strategies can be applied to better control the diffusion and mixing of the reagents. Hydrodynamic flow focusing provides a major control over reagent diffusion, and therefore, over shape and size distribution of the nanomaterials, when compared to single fluid stream configurations (Puigmartí-Luis 2014).

Planar channel configurations generally lead to 2D hydrodynamic flow focusing. In this type of flow profile, the middle reagent stream is sandwiched between two or more sheath streams (Figure 5.4a). The confinement of the

reagents to a plane minimizes the probability of channel clogging. 3D hydro-dynamic flow focusing goes one step further and confines the flow of reagents to a cylindrical stream at the center of the microchannel, thus avoiding contact to any of its walls (Figure 5.4b).

(a) 2D hydrodynamic flow focusing   (b) 3D hydrodynamic flow focusing
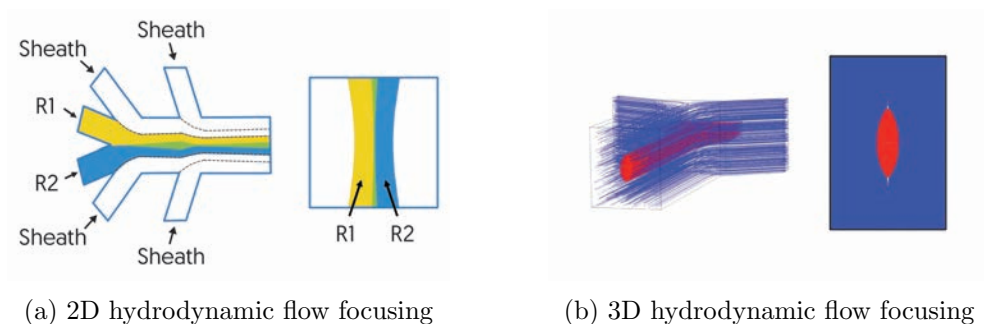
Figure 5.4: Schematic representation of 2D and 3D hydrodynamic flow focus-ing. Adapted from Puigmartí-Luis 2014 and Y.-J. Chiu et al. 2013, respectively.

3D hydrodynamic flow focusing can be achieved using planar (i.e. single-layer) or three-dimensional microfluidic designs. Planar designs take advan-tage of their geometry to create 3D flow focusing, owing to the generation of Dean vortices (Mao, Waldeisen and T. J. Huang 2007; Ha et al. 2014). Other planar designs use several sheath flows to sequentially focus the reagent stream, first vertically and then horizontally (Rhee et al. 2011).

Three-dimensional microfluidic designs have also been employed to achieve this reagent confinement. The simplest approach consists on using coaxial flows, which consists on a capillary inside a channel or tube of bigger diam-eter (Abou Hassan et al. 2008). More complex designs translate this same concept into a monolithic device (Y.-J. Chiu et al. 2013), in which the mid-dle inlet has a smaller height than the two sheath channels (see Figure 5.5). This channel geometry is relatively complex to fabricate with replica mold-ing processes commonly employ for Polydimethylsiloxane (PDMS) devices. In contrast, fabrication processes based on a multilayer approach (see Section 1.2) could produce this type of channel geometries using materials such as thermo-plastics or Low Temperature Co-fired Ceramics (LTCC) in a straightforward manner.

A wide range of materials for microreactor fabrication can be found in the literature (Marre and Jensen 2010). The most common are described next:

PDMS or other rubber-based materials share the advantages of a sim-ple, rapid prototyping (Abou Hassan et al. 2008; Cabrera, Souza, et al. 2014; Cabrera, Melo, et al. 2015). However, they show poor chemical stability to-

89
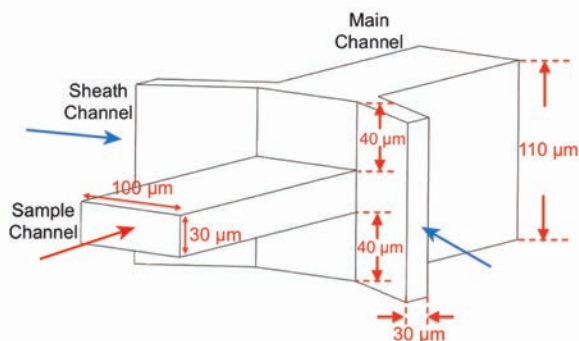
Figure 5.5: Three-dimensional microfluidic design for 3D hydrodynamic flow
focusing. Adapted from Y.-J. Chiu et al. 2013

.

wards solvents and strong acids or bases, and moreover, they usually cannot
withstand harsh reaction conditions, such as high temperature or pressure.

Fluoropolymers have also been used in the development of microreactors,
exhibiting a better chemical compatibility. However, they require complex fab-
rication strategies such as photolithographic processes in cleanroom facilities
(J.-O. Kim et al. 2014), or coating with fluoropolymer of silicon microchan-
nels (Kuhn et al. 2011). Furthermore, these materials possess low bonding
strength.

Silicon & Glass microreactors (or a hybrid combination of both materi-
als) have an excellent chemical stability (Sebastian Cabeza et al. 2012), and
enable working at high temperature and pressure (Benito-Lopez et al. 2007;
Trachsel, Hutter and Von Rohr 2008; Marre, Park, et al. 2008). Furthermore,
glass grants optical transparency and consequently permits the integration of
characterization techniques, while silicon has a better thermal conductivity.
On the downside, these materials require of complex fabrication processes in
cleanroom facilities.

Metal based microreactors (usually stainless steel) do not require of clean-
room facilities for fabrication, and have a good chemical stability except for
strong acids (Iglesia et al. 2007; Clifford et al. 2014). On the other hand,
metal-based microreactors are not transparent, and 3D complex fluidic struc-
tures remain difficult to fabricate.

LTCC are proposed in this work as substrate for the fabrication of mi-
crofluidic reactors. LTCC microreactors have demonstrated great potential
in the synthesis of nanomaterials due to their chemical inertness, the wide
working temperature range and the possibility to fabricate complex multi-
layer structures (Gómez-de Pedro, Puyol and Alonso-Chamarro 2010; Gómez-

de Pedro, Martínez-Cisneros, et al. 2012; Jiang, Haber, et al. 2015). LTCC are compatible with screen-printing techniques (Ibáñez-García et al. 2008), which enable the integration of electronic elements such as heaters (Jiang, Haber, et al. 2015; Martínez-Cisneros, Pedro, et al. 2012) or electrochemical detection systems (Martínez-Cisneros, Rocha, et al. 2009). Furthermore, LTCC technology does not require cleanroom facilities, which decreases the fabrication costs.

However, opacity is one of the main drawbacks for the further application of LTCC devices —not only in microreactor applications, but also in µTAS (Vasudev et al. 2013). Particularly in microreactor synthesis, the opacity of the material prevents the visualization of the reaction progress, which is of paramount importance to understand the behavior of the fluid streams, specially in the case of complex flow patterns (such as droplets) or harsh reaction conditions (for instance, reactions above the boiling point of the solvent).

To overcome this limitation, hybrid devices incorporating transparent materials have been developed using, for instance, glass (Suarez et al. 2010; Bembnowicz and Golonka 2010) or PDMS (Malecha, Gancarz and Tylus 2010; Malecha 2016). However, these approaches require of complex, time-consuming post-fabrication processes in order to seal the microfluidic device or the optical path. Furthermore, the different properties of the sealing material (thermal expansion coefficient, chemical stability) may limit the application of these devices, specially in synthetic applications in which harsh environments and high temperatures are often required. Previous work in our research group demonstrated the integration of thin ceramic layers as optical windows for absorbance detection (Couceiro, Gómez-de Pedro and Alonso-Chamarro 2015).

In this chapter, LTCC microreactors incorporating 3D complex structures and an optical window along the whole microchannel are developed. On the one hand, a 3D hydrodynamic flow focusing inlet system is developed in order to enhance the flow pattern and the mixing of reagents. On the other hand, the monolithic optical window fulfills the purpose of monitoring the formation of a photoluminescent product and the flow pattern inside the device. The microreactors were applied to the synthesis of superparamagnetic iron oxide nanoparticles (SPION) and Carbon Dots (CDots) under harsh reaction conditions.

5.1.1 Superparamagnetic Iron Oxide Nanoparticles

Downsizing iron oxides has remarkable effects on the properties of the resulting nanoparticles. Below a critical dimension, magnetite (Fe_3O_4) and maghemite (γ-Fe_2O_3) are superparamagnetic, while their bulk analogues are ferrimagnetic (Tartaj et al. 2006). In sufficiently small nanoparticles, thermal energy overwhelms the magnetic anisotropy energy per particle, which is responsible

for holding the magnetic moments along a certain direction (A.-H. Lu, Salabas and Schüth 2007). This means that magnetization can randomly flip direction under the influence of temperature. Therefore in absence of an external magnetic field the magnetization of iron oxide nanoparticles appears to be in average zero. However, when an external magnetic field is applied, their magnetic moments tend to align along the applied field, leading to a net magnetization.

SPION have attracted great interest due to their superparamagnetic behavior as well as their large surface area. These attributes make SPION ideal candidates specially for biomedical applications —hyperthermia (Ito, Honda and Kobayashi 2006; Laurent, Dutz, et al. 2011), drug delivery (Yu et al. 2008; Xing et al. 2011; Wahajuddin and Arora 2012), magnetic resonance imaging (L. Li et al. 2013; Jin et al. 2014), etc. However, SPION have great potential in analytical applications as well (A.-H. Lu, Salabas and Schüth 2007). The surface functionalization together with the possibility to manipulate the particles with external magnetic fields enables the separation of analytes from their matrixes (Liébana et al. 2009; Lee et al. 2014), as seen in Chapter 3 with commercial Magnetic Beads (MBs) for the detection of E. coli O157:H7. For this type of application, a stronger magnetization saturation is desirable in order to better control the magnetic particles. This is achieved by synthesizing big clusters of nanoparticles (Cheng et al. 2010; Xing et al. 2011), or by embedding the SPION in a polymeric matrix (Philippova et al. 2011), since they remain superparamagnetic but with higher saturation magnetization.

Magnetite has a higher saturation magnetization than maghemite (Fu and Ravindra 2012), and therefore the former are usually preferred. There are many strategies for the synthesis of magnetite (Majewski and Thierry 2008), including co-precipitation, thermal decomposition and hydrothermal methods. Herein, magnetite nanoparticles were synthesized by means of co-precipitation of ferric and ferrous salts upon pH basification (Massart and Cabouil 1987; Laurent, Forge, et al. 2008). The size, shape and composition of the nanoparticles can be tuned by modifying parameters such as temperature, pH, ionic strength, the Fe^{2+}/Fe^{3+} ratio or the iron salts selected (Vayssieres et al. 1998). Oxidation of Fe(II) to Fe(III) —i.e. the oxidation of magnetite to maghemite— can be avoided by using an inert atmosphere or increasing the Fe(II) to Fe(III) ratio (Karaagac et al. 2010).

SPION co-precipitation syntheses using microreactors were first performed by Salazar-Álvarez and co-workers using a flow injection setup and Teflon tubing ⌀ 0.5 mm submerged in a thermostat (Salazar-Alvarez, Muhammed and Zagorodni 2006). A PDMS device with a glass capillary to generate a coaxial flow was developed shortly after for the continuous flow synthesis of maghemite nanoparticles (Abou Hassan et al. 2008). This type of flow configuration enabled a 3D hydrodynamic flow focusing, thus avoiding adsorption

of the precipitate onto the walls. Simmons and co-workers used a commercial glass microreactor to co-precipitate SPION (with a composition of 70 % maghemite and 30 % magnetite) using a 2D flow focusing inlet system at room temperature (Simmons et al. 2013). Droplet flow techniques have also been used for the synthesis of SPION using a glass capillary droplet generator in a polytetrafluoroethylene (PTFE) tube (Kumar et al. 2012).

All of these approaches point towards the synthesis of SPION either in microreactors at room temperature or in PTFE tubing submerged in hot baths. Furthermore, these works higlhlight the difficulty to handle the precipitate in microchannels and tackle the problem in different ways —i.e. with flow focusing techniques or droplet generation. Our approach consisted on the development of an LTCC microreactor with integrated heater for high temperature synthesis and a 3D flow focusing system to avoid channel occlusion and enhance the mixing of reagents.

5.1.2   Photoluminescent Carbon Dots

Photoluminescent nanoparticles have drawn great attention over the last years due to their potential applications in (bio)sensing, bioimaging or photovoltaic cells. For instance, Quantum Dots (QD) have been thoroughly researched due to their outstanding optical properties —such as high Quantum Yield (QY) and photostability— and great potential in sensing, medical and bioimaging applications (Michalet 2005; Drummen 2010). However, this type of nanoparticle suffers from some drawbacks such as toxicity (due to their heavy metal content), that hinder their further application. Over the last years, CDots have emerged as a suitable alternative to QD due to their comparable optical properties and the added benefits of biocompatibility, low toxicity, chemical stability, well-known carbon chemistry and low cost (H. Li et al. 2012; Y. Wang and A. Hu 2014; Baptista et al. 2015; Lim, Shen and Gao 2015).

Depending on their structure, CDots can be further divided in different types (see Figure 5.6), although no actual consensus has been reached within the academic community regarding their nomenclature (Cayuela et al. 2016). Herein, we will generally refer to them as CDots.

CDots can be synthesized using top-down —breaking down carbon structures, such as C_{60} in J. Lu et al. 2011— and bottom-up approaches —building up from small organic molecules, such as citric acid (CA) in Zhu, Meng, et al. 2013. In this work, CDots were synthesized by means of a bottom-up synthesis, using a hydrothermal method (Zhu, Meng, et al. 2013). This synthesis was chosen due to the high QY of the CDots obtained and its water-based nature, to avoid biocompatibility issues caused by solvents. It consisted of the hydrothermal reaction of CA and ethylenediamine (ED) as Carbon and Nitrogen sources, respectively. Other reaction conditions, such as microwaves, have also
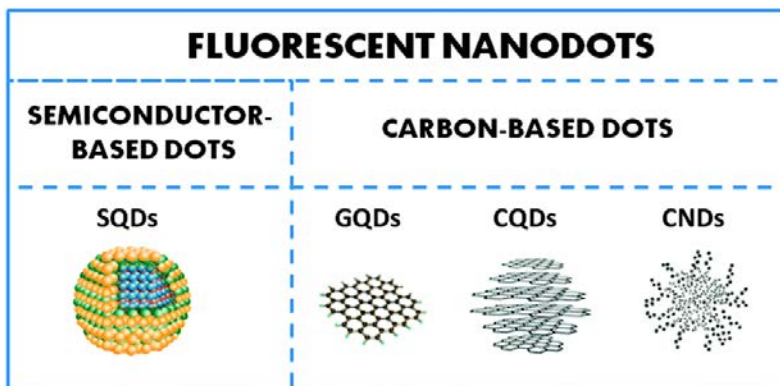
(a) Types of Carbon Dots according to Cayuela et al. 2016
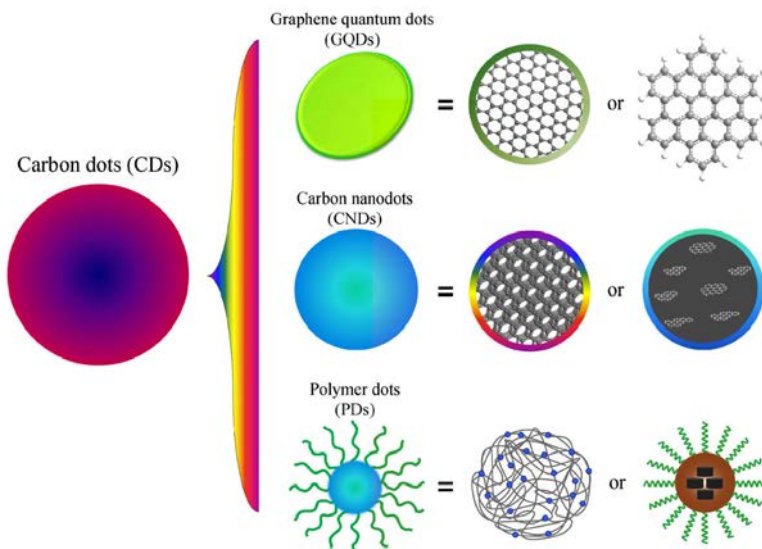
(b) Types of Carbon Dots according to Zhu, Song, et al. 2015

Figure 5.6: Classification and different nomenclature of photoluminescent Carbon Dots. Notice the different names for a given structure —CNDs in (a) vs. PDs in (b)— or the different structures for a given name —see CNDs in both examples. Reproduced from Cayuela et al. 2016 and Zhu, Song, et al. 2015.

been applied elsewhere (Xiao et al. 2017) to produce similar CDots. The introduction of heteroatom(s) in the CDots structure —in this case, Nitrogen— modifies the electronic environment and effectively enhances the photoluminescence properties (Q. Xu et al. 2016).

Photoluminescent mechanism studies of these particular CDots point towards nanoparticles with two contributions to their emission: on the one hand, the Carbon core and on the other hand, molecular like fluorophores (presumably the fluorophore 5-oxo-1,2,3,5-tetrahydroimidazo[1,2-α]pyridine-7- carboxylic acid (IPCA)) present on the surface of the carbon cores and/or embedded on polymer-like structures (Song et al. 2015; J. Wang et al. 2015). Several parameters have an important role on the composition of the final product, such as precursor ratio, initial pH and temperature. Specially, synthesis temperature plays a key role on the CDots composition and the origin of their photoluminescence, because it controls the degree of carbonization of the product (see Figure 5.7).
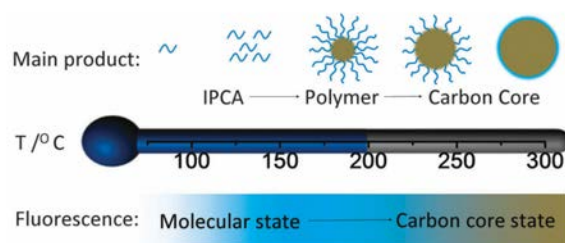
Figure 5.7: Structure and photoluminescence mechanism of the Carbon Dots according to the temperature of hydrothermal synthesis. Reproduced from Song et al. 2015.

To the author's best knowledge, only two previous studies deal with the synthesis of CDots in microreactors. On the one hand, Lu and co-workers synthesized CDots using various Carbon precursors and solvents using a ⌀ 1 mm Teflon tube submerged in an oil bath (Y. Lu, L. Zhang and Lin 2014). This simple setup enabled a rapid screening of reaction conditions to obtain CDots with QY of up to 0.37. On the other hand, our research group reported a modular LTCC microreactor consisting of two separate units: a microfluidic platform and a heating module (Gómez-de Pedro, Salinas-Castillo, et al. 2014). The CDots obtained exhibited blue photoluminescence and a low QYs of up to 0.03 due to the type of reaction. Nevertheless, the synthesis demonstrated to be highly reproducible owing to the temperature control and the CDots were investigated as pH sensor and bioimaging contrast agents.

To improve the properties of the synthesized CDots, different strategies have been addressed in this dissertation. In this regard, the precursors were

changed and the reaction performed at high temperature and pressure conditions. The microfluidic platform and the heating module were integrated in a monolithic device. Additionally, an optical window was developed to enable monitoring of the photoluminescent reaction product and the flow pattern inside the entire microchannel. The obtained CDots are highly luminescent and preliminary studies show promising results for their application as nanoprobes for metal detection and bioimaging contrast agents.

5.2 Methods

5.2.1 Materials

Iron (III) chloride anhydrous ($FeCl_3$, 99 %) and polyethyleneimine (PEI), branched MW 10,000, 99 % (Alfa Aesar) were purchased from Fisher Scientific. Iron (II) chloride tetrahydrate ($FeCl_2 \cdot 4\,H_2O$, 99 %), hydrochloric acid (HCl, 35 %), sodium hydroxide (NaOH, 98 %), sodium citrate tribasic dihydrate (99 %), CA (99 %), ED absolute (99.5 %), diethylenetriamine (DETA) (99 %) and copper (II) sulfate pentahydrate ($CuSO_4 \cdot 5\,H_2O$, 98 %) were purchased from Sigma-Aldrich. Mercury standard solution (1.000 ± 0.002 g/L) was obtained from Panreac (Barcelona, Spain). All reagents were used as received, without any further purification, unless otherwise stated.

5.2.2 Preparation of Precursors

5.2.2.1 Magnetite Synthesis

Two different precursor solutions were used in this synthesis. On the one hand, an Iron aqueous precursor containing both Fe^{2+} and Fe^{3+} in a 1:2 ratio (the same proportion of Fe(II) and Fe(III) atoms found in magnetite). Different concentrations of this precursor mixture were prepared by weight in acidic media (HCl 1.1 M), in order to avoid the precipitation of hydroxides. For convenience, the concentration is always given as the sum of both iron ions, ranging from 30 to 360 mM. On the other hand, a solution of NaOH 1 M was prepared by dissolving 20 g in 500 mL of deionized water. Additionally, the citrate solution was prepared by dissolving 4.456 g in 25 mL of deionized water and the pH was adjusted to 12 by adding NaOH 1 M.

5.2.2.2 Carbon Dots Synthesis

The CA solution was prepared by dissolving 0.5764 g in 15 mL of water. The ED solution was prepared by dissolving 200 µL in water, to a total volume of 15 mL. DETA solution was prepared by dissolving 325 µL in water to a total volume of 15 mL. Finally, the PEI solution consisted of 0.144 g dissolved

in water to a total volume of 15 mL. The solutions were loaded into 0.5 mL gas-tight glass syringes (Hamilton, Bonaduz, Switzerland).

5.2.3 Experimental Procedure

All precursor solutions were degassed for 15 min in a vacuum chamber and then kept in glass gastight syringes prior to their injection into the microreactor. The solutions were pumped using syringe pumps (540060, TSE Systems, Bad Homburg, Germany) coupled to the microreactor with PTFE ($\varnothing$ 0.8 mm) tubing.

Figure 5.8 schematically represents the microreactor with its inlets, downstream microreactor channel and outlet. The main precursor solution (i.e. the iron salts or the CA solutions, for the synthesis of magnetite nanoparticles and CDots, respectively) was injected into the microreactor through Inlet 2 (the purple inlet in the figure). The other precursor (NaOH or Nitrogen source, for the synthesis of magnetite nanoparticles and CDots, respectively) was injected through Inlets 1 and 3. These two inlets generate a sheath flow for the 3D hydrodynamic flow focusing. Additionally, a stabilizer solution was pumped when required (certain experiments of the magnetite synthesis) into the microreactor through Inlet 4, which joined the main channel at the middle of its length.
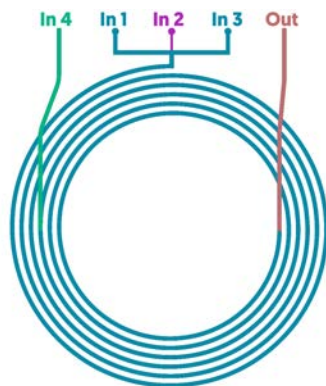
Figure 5.8: Schematic representation of the microreactor and its inlets and outlet.

Once the flows were stabilized, the integrated heater was switched on and, when required, a Back Pressure Regulator (BPR) (IDEX Health & Science, WA, USA) was connected to the outlet of the microreactor thus providing the required pressure (only in the syntheses of CDots). Once the system reached the working temperature, the reaction was allowed a period of 45 min to stabilize. Only then, nanoparticles were collected using eppendorf tubes.

5.2.4 Characterization

5.2.4.1 Magnetite Nanoparticles

The magnetic properties of the nanoparticles synthesized were determined using a Superconducting QUantum Interference Device (SQUID) magnetometer at 300 K. This characterization provided evidence regarding the type of magnetic behavior and the magnetic strength of the nanoparticles. On the one hand, the magnetic behavior is correlated to the remanent magnetization, i.e. the magnetic field generated by the nanoparticles in absence of an external magnet. On the other hand, the magnetic strength is correlated to the saturation magnetization, i.e. the maximum magnetic moment induced in the nanoparticles when an external magnetic field is applied (Moskowitz 1991).

Transmission Electron Microscopy (TEM) images were obtained with a JEOL 1400 (Tokyo, Japan) in order to determine the size and morphology of the nanoparticles. The obtained images were processed to obtain their sizes using ImageJ, a public domain image processing program. At least 100 particles were counted to produce the size histogram and a Gaussian-like curve fitting was performed. Moreover, TEM measurements also provided the Selected Area Electron Diffraction (SAED) pattern of the sample, indicative of its crystal structure. X-Ray Diffraction (XRD) spectra were obtained with an X'Pert Powder diffractometer (PANalytical) in order to further study the crystallinity of the nanoparticles.

5.2.4.2 Carbon Dots

UV/Vis absorption spectra were obtained using a double beam scanning spectrophotometer Shimadzu UV-310PC UV-Vis-NIR (Kyoto, Japan). Photoluminescence spectra were obtained with a Fluorolog 1 Modular spectrofluorometer (Horiba Jobin Yvon, France). Absorption and emission spectra also provide an idea of the size dispersion of the sample, which is correlated to the width of the bands.

The QY was calculated with the optically dilute measurements method (Crosby and Demas 1971), using quinine sulphate in 0.1 M sulphuric acid as a standard and applying the following equation,

$$\phi_x = \phi_{st} \cdot \frac{I_x}{I_{st}} \cdot \frac{A_{st}}{A_x} \cdot \frac{\eta_x^2}{\eta_{st}^2} \qquad (5.1)$$

where ϕ is the photoluminescence QY, I the integrated area of the corrected emission spectrum, A the absorbance at the maximum of the absorption band, and η the refractive index of the solvent. The subindexes x and st refer to sample and reference standard, respectively. Given the fact that both standard and sample were dissolved in water, the last term of the equation can

be ignored. QY measurements provide the efficiency of the CDots as photo-luminophores.

TEM images were obtained with a JEOL 2011 (high resolution) or a JEOL 1400 (Tokyo, Japan) in order to determine the size and morphology of the nanoparticles.

5.2.5 Photoluminescence Quenching Measurements

The synthesized CDots were evaluated as nanoprobes for metal ion detection. For that, a fluorescence cuvette was filled with 2.5 mL of blank/sample and 0.5 mL of CDots. The concentration of CDots was previously adjusted to obtain an absorption of *ca.* 0.05 a.u. after mixing with the sample, and thus avoid undesired autoabsorption. The blank simply consisted of phosphate buffer. The metal ion samples were prepared by weighting the metal salt and dissolving it in the same buffer. Different metal ion concentrations were obtained by diluting the stock solution with phosphate buffer. The cuvette was gently shaken by hand to ensure a complete mixing of components. Then, it was placed in the sample chamber of the spectrofluorometer and the photoluminescence spectrum was registered.

5.2.6 Cell Culture and Cytotoxicity Assay

Human Embryonic Kidney cells 293 (HEK293 cells) were cultured in Dulbecco's Modified Eagle's Medium (DMEM) supplemented with 10 % fetal bovine serum, 2 mM L-glutamine and 1 % penicillin-streptomycin solution, at 37 ℃ in a humidified atmosphere with 5 % of CO_2. The cells were plated at a concentration of $2 \cdot 10^4$ cells/well onto glass bottom well plates, previously coated with 10 g/mL poly-L-lysine. After 24 h in culture, the cells were incubated for 24 or 48 h at 37 ℃ with different concentrations of CDots-ED (0.1, 0.5, 1 and 2 mg/mL) dispersed in the culture medium mentioned above.

In order to determine the cell viability, an 3-(4,5-dimethylthiazol-2-yl)-2,5-diphenyltetrazolium bromide (MTT) assay was performed (Berridge, Herst and Tan 2005). This assay is based on a colorimetric reaction (the reduction of the MTT to purple formazan) catalyzed by certain enzymes of the cells. Under defined conditions, the MTT assay reflects the cell viability of the sample. 10 μL of MTT (5 mg/mL) reagent was added to each well and incubated for 4 h at 37 ℃. Thereafter, 150 μL of 100 % DMSO were added per well, mixed thoroughly to dissolve the dark purple crystals and the wells were subsequently read on an ELISA plate reader at a wavelength of 570 nm.

5.3 Microfluidic Device Fabrication

The fabrication process of LTCC microreactors is based on a multilayer approach, as described in Sections 1.2 and 3.3. Therefore, the same processing steps apply, namely design, microstructuring and back-end operations. Although the fabrication of LTCC and Cyclic Olefin Co-polymer (COC) devices is conceptually similar, the differing properties of these materials set aside the processes. The general LTCC fabrication process is schematically depicted in Figure 5.9.
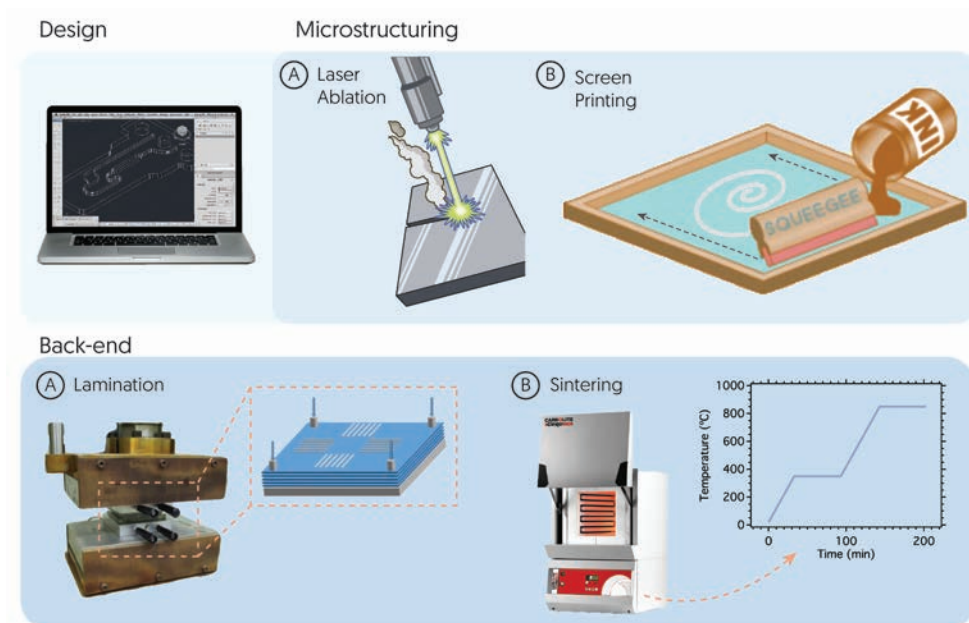
Figure 5.9: General fabrication of LTCC microfluidic devices, including design, microstructuring and back-end processes.

The microreactor can be conceptually separated in two units, namely the fluidics and the electronics. The fluidic elements were microstructured on LTCC 951 Green Tape ceramics (DuPont, Germany) using a Protolaser 200 (LPKF, Garbsen, Germany), a Nd:YAG (neodymium-doped yttrium aluminum garnet) laser type, working in the infrared region at 1064 nm. The electronics integrated in the device consisted on the heater (actuator), while the control system was located in a separated Printed Circuit Board (PCB) to avoid the high temperatures of the microreactor.

The LTCC layers were individually ablated using the laser and depending on their thickness, different mark speeds were used in order to microstructure through-cuts. 254, 114 and 50 µm thick green tape LTCC layers were through-

cut with mark speeds of 25, 50 and 150 mm/s, respectively.

Once the different layers were microstructured, they were placed in between two aluminum plates with four alignment pins and laminated at 70 ℃ and 25 bar. In order to avoid adhesion of the ceramic layers to the aluminum plates, mylar films (provided with the LTCC) were used as a separation. After lamination, the fluidic LTCC block was fastened to the working table of a screen-printer (DEK248, Asflex Internacional, Spain) and a gold conductive paste (DuPont 5742) was applied to create the resistor pattern on the reverse side. This step could have also been performed on an individual layer after the laser ablation, although in this case the order was reversed for convenience. The paste was allowed to dry for 10 min at 80 ℃. A block of three LTCC layers was laminated on top of the resistor to encapsulate it, and another screen-printing step was performed (using silver paste DuPont 6141) in order to fill the vias and create connection pads.

Finally, the LTCC device was sintered in a programmable box furnace (Carbolite CBCWF11/23P16, Afora, Spain) in air atmosphere, following the temperature profile recommended by the ceramics provider. The LTCC — as other ceramic materials— suffer shrinkage upon firing. In the case of 951 Green Tapes, the shrinkage is well characterized, and found to be 12.7 ± 0.3 % in X and Y, and 15 ± 0.5 % in Z (data provided by the manufacturer). The screen printed pastes have the same thermal expansion coefficient as the LTCC substrate and therefore no structural problems were observed after firing.

Two different microreactors were developed for the syntheses of magnetite and CDots. Both consist of a monolithic LTCC block integrating fluidics and the screen-printed heating resistor. In order to avoid channel occlusion and to enhance the contact area between the reagent streams, a 3D hydrodynamic flow focusing inlet system was developed. This was a significant improvement compared to other microreactors previously developed in our research group, based on 2D flow focusing (Gómez-de Pedro, Puyol and Alonso-Chamarro 2010; Gómez-de Pedro, Puyol, Izquierdo, et al. 2012).

The main difference between both microreactors laid on the thickness of the top LTCC cover layer, used as optical window in the case of the CDots synthesis. Since CDots are photoluminescent, the optical window enabled the monitoring of the reaction over the entire microchannel. Furthermore, the optical window enabled the study of the flow pattern inside the microreactor, which is, in this case, of paramount importance given the fact that the reaction temperature was above the boiling point of the solvent. The fabrication processes are described in more detail in the following subsections.

5.3.1 SPION Microreactor

Figure 5.10 schematically shows the elements of the microreactor. The fluidics consisted basically of three main inlets for reagent injection (to create a 3D hydrodynamic flow focusing), a spiral-shaped microreactor channel and an outlet. Additionally, another inlet was added for reagents such as stabilizers, joining the main microreactor channel approximately at the middle of its length (see Figure 5.10a). The screen-printed heating resistor was located beneath the microreactor channel. It was designed to occupy approximately the same area in order to obtain a temperature distribution within the microreactor channel as homogeneous as possible (Martínez-Cisneros, Pedro, et al. 2012).

The microreactor had an inlet of smaller height and two sheath flow channels of bigger height (see Figure 5.10b). These three inlets merged into the downstream main microreactor channel, thus creating the necessary structure to generate the 3D hydrodynamic flow focusing, and therefore, the reagent pumped into the middle stream was confined at the centre of the microchannel. In this way, the contact area between the reagents was enhanced and the chance of precipitation of solid reaction products on the walls was reduced, thus minimizing the chances of channel clogging (Puigmartí-Luis 2014).

It is important to notice that this inlet configuration can be fabricated owing to the multilayer approach (see Figure 5.11). Three layers of DuPont 951PT Green Tape (114 μm thick, prior to firing) were individually ablated with the laser and laminated together, creating a short encapsulated channel (see Figure 5.11 Steps 1–3 for the processing steps and Figure 5.12 a–c for the laser ablation pattern of each individual layer). This ceramic block was then aligned in the laser working table using the built-in fiducial recognition camera. The sheath flow inlets, the downstream main microchannel, the stabilizer inlet, and the outlet were microstructured cutting through the ceramic block (Figure 5.12 d–e). In order to do that, the laser was configured to a much higher mark speed (1000 mm/s) and the microstructuring pattern (see Figure 5.12e) was repeated 20 times. Furthermore, the whole area of the microchannels was ablated, instead of only the edges, in order to avoid problems (structural stability) while removing the remaining material.

This lower energy configuration of the laser enabled the through-cut of the core microfluidic block (5.11 Step 4), while meeting two more requirements. First, the lower energy density produced a cleaner cut due to a lower heating of the substrate near the ablated areas. This was important in order to obtain a well-defined middle inlet to generate the 3D hydrodynamic flow focusing. Second, this configuration enabled the precise control of the cutting process, to the point of avoiding the ablation of a support mylar placed beneath the LTCC block. Due to the length of the microreactor channel and its geometry,
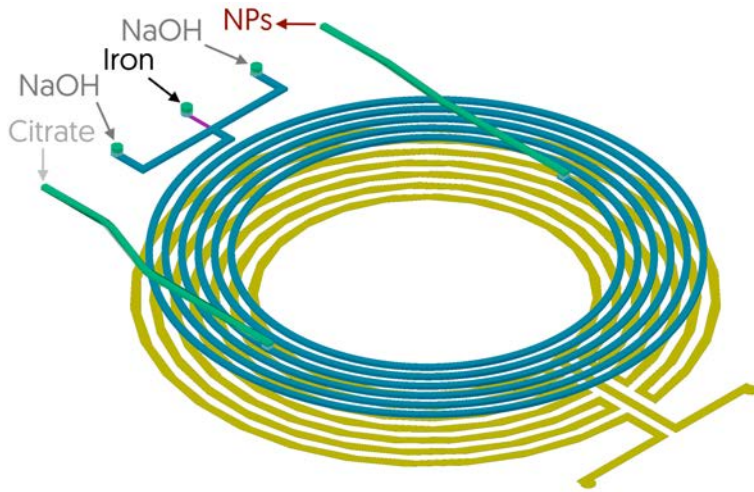
(a) Microreactor for magnetite synthesis
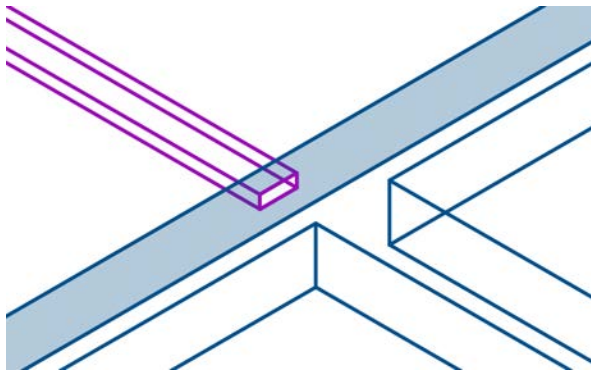
(b) Close-up of the inlet area

Figure 5.10: 3D representation of the inlets, outlet and microreactor channel (blue colors), and heating resistor (yellow). Close-up of the inlet area that enables 3D hydrodynamic flow focusing.
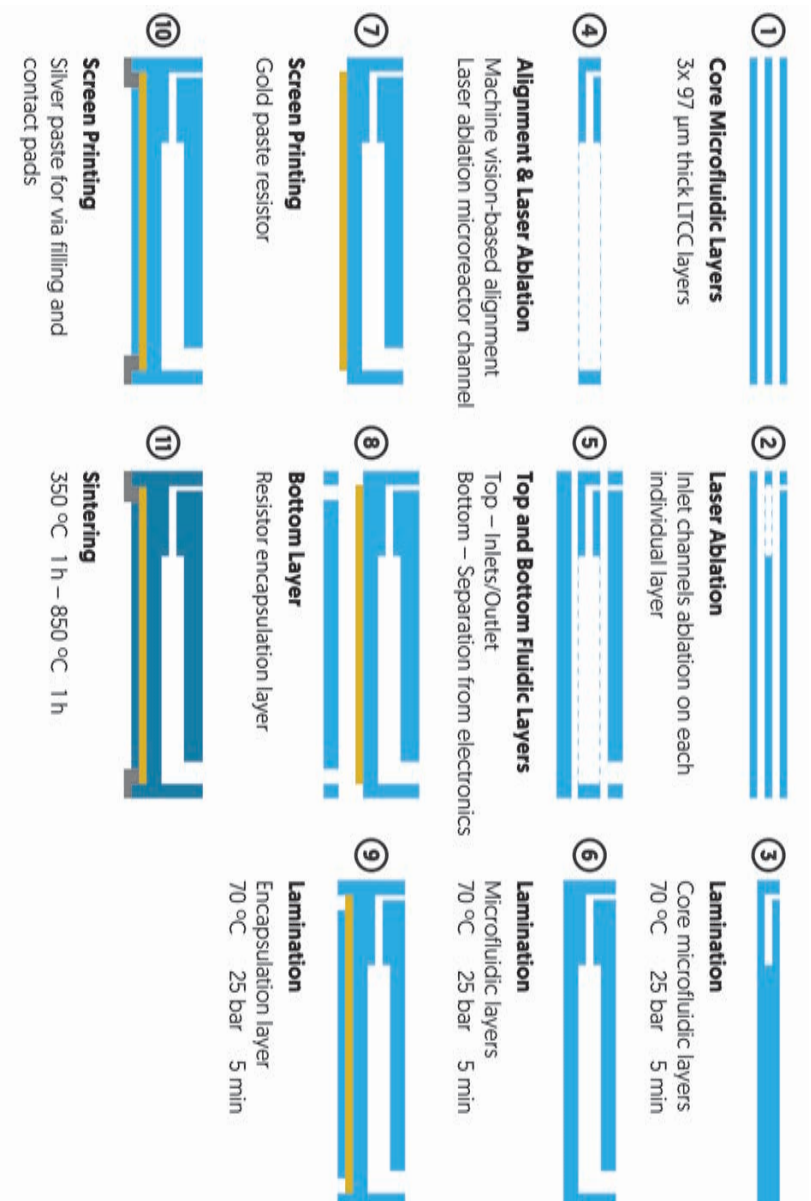
Figure 5.11: Schematic representation of the LTCC microreactor fabrication process. This process enables the fabrication of a monolithic device integrating the fluidics and the heating resistor.

(a) Top core layer

(b) Middle core layer

(c) Bottom core layer

(d) Core fluidics block

(e) Close-up laser profile
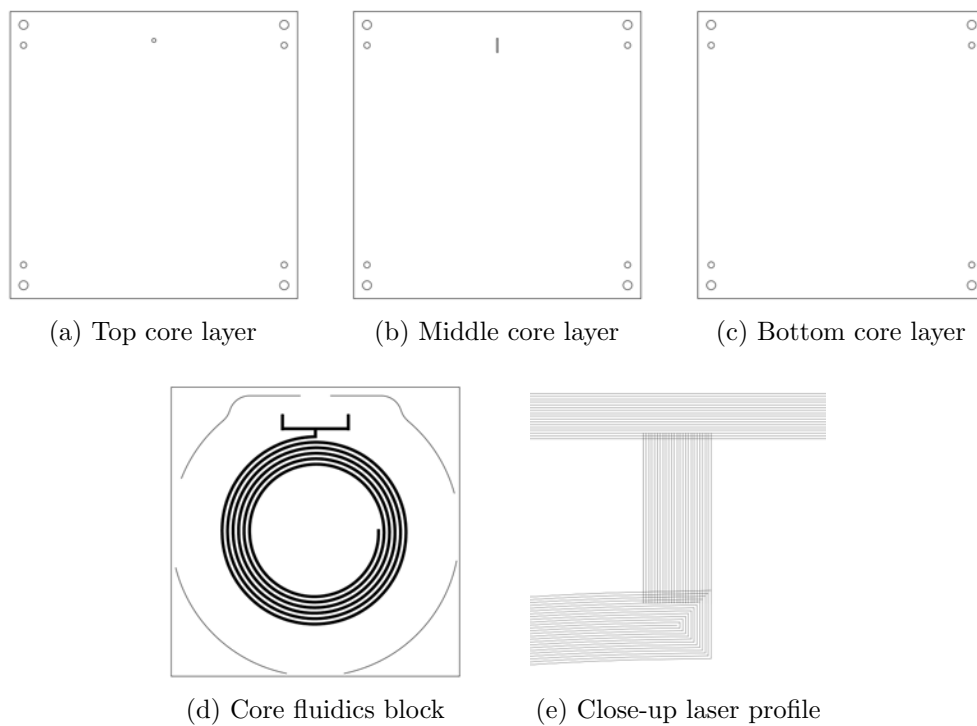
Figure 5.12: Layer breakdown of the LOC core microfluidic layers of the device for magnetite synthesis. The first row of the figure corresponds to the laser cuts on each of the three 114 μm thick LTCC layers. The second row corresponds to the laser cut performed on the LTCC block obtained after lamination of the three layers, including a close-up of the laser microstructuring pattern.

the mylar enabled the subsequent manipulation of the ceramic block without deformation or movement of the microfluidic structure.

Figure 5.13 presents two images of the inlet area, with open channels for inspection. The close-up photograph clearly shows the two sheath flow channels and the middle inlet in the center of the channels' wall.

(a) Open microchannels   (b) Close-up of the inlet area
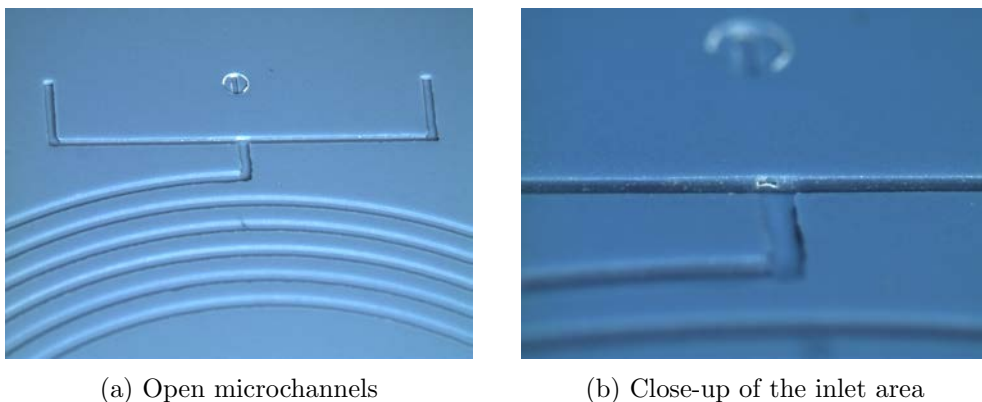
Figure 5.13: Photographs of the open microchannels of the device for magnetite synthesis and close-up of the middle inlet and the two sheath flow channels.

The microreactor was then sealed with top and bottom layers (steps 5–6 in Figure 5.11) using DuPont 951PX Green Tape (254 µm thick, prior to firing). The total volume of the microreactor channel was *ca.* 100 µL, with a length of 630 mm and cross-section dimensions of 525 µm wide times 290 µm high (dimensions after firing).

The heating resistor was then screen-printed (see the mask design in Figure 5.14a) on the reverse of the fluidic LTCC block and it was allowed to dry for 10 min at 80 °C (Step 7 in Figure 5.11). Three LTCC layers were then laminated on top of the resistor in order to encapsulate it (Steps 8–9). A new screen-printing step (see the mask in Figure 5.14b) was performed to fill the vias and create pads for electrical connection, allowing to dry at 80 °C for 30 min, due to the higher depth of the vias (Step 10 in Figure 5.11). A photograph of the screen-printed gold resistor (without encapsulation, for inspection purposes) is shown in Figure 5.14c. Finally, the device was sintered in a programmable furnace, with a temperature profile consisting of 1 h organic burnout at 350 °C and 1 h firing at 850 °C.

The temperature of the microreactor was set using the same temperature control system described in Section 4.2.5, for the oocyte culture device with integrated heater. Therefore, a PT100 temperature sensor (Innovative Sensor Technology, Switzerland) was glued to the microreactor using Epoxi paste

(a) Heating resistor mask   (b) Electrical pads mask   (c) Gold resistor
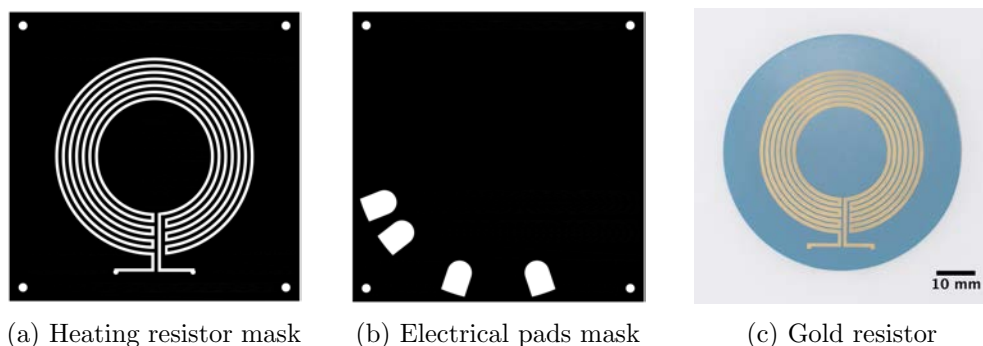
Figure 5.14: Design of the masks for screen printing the gold resistor and the pads for electrical connection. The resulting gold resistor is also shown after sintering (not encapsulated, for inspection purposes only).

EPO-TEK H20E (Billerica, MA, USA), which was cured overnight at 80 ℃. The final microreactor for SPION synthesis is shown in Figure 5.15.

5.3.2   CDots Microreactor

The microreactor for the synthesis of CDots is very similar to that presented for the synthesis of magnetite nanoparticles in Section 5.3.1, in order to take advantage of the 3D hydrodynamic flow focusing inlet system. A schematic representation of the device is shown in Figure 5.16. The main difference consisted on the lower thickness of the top ceramic layer —in order to maximize light transmittance. It was used as optical window, thus enabling the monitoring of photoluminescent CDots formation in the monolithic microreactor. The optical window permitted the study of the flow pattern inside the microreactor, at temperatures above the boiling point of the solvent. Consequently, an optimal pressure could be determined for the synthesis of CDots.

The distribution channels were redesigned to accommodate the downstream main microreactor channel just below the top cover layer, and thus use that layer as optical window for photoluminescence observation. The difference is noticeable comparing Figures 5.10a and 5.16. Another change from the previous design is the absence of the additional inlet joining the main microreactor channel at the middle of its length, since it was not needed in this synthesis. Nevertheless, the rest of the fluidic elements as well as the heating resistor remained the same. Consequently, the fabrication process was analogous to that presented in Figure 5.11, with slight design modifications.

Different top cover layers of varying thickness were evaluated on the basis of structural stability and light transmittance. On the one hand, the top
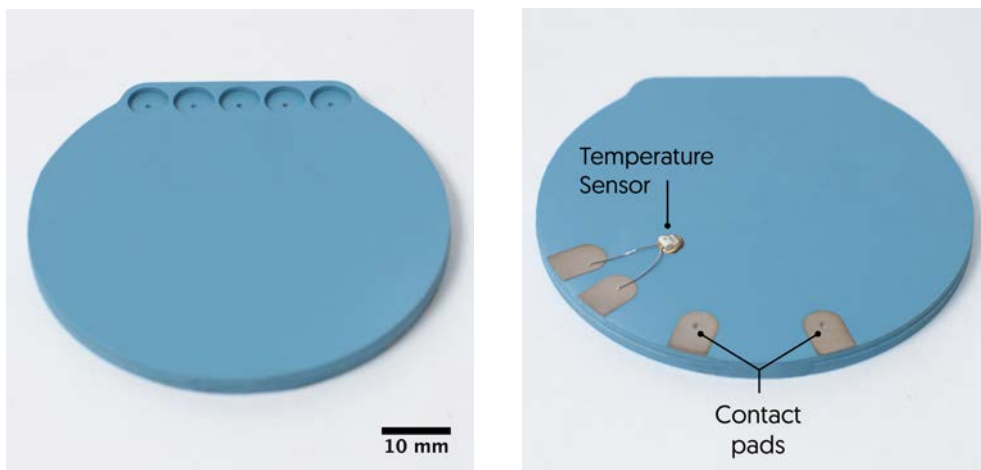
(a) SPION microreactor top view

(b) SPION microreactor bottom view

Figure 5.15: Top and bottom photographs of the microreactor for the synthesis of SPION. The top side includes the fluidic inlets/outlet while the bottom side contains the PT100 temperature sensor and the contact pads of the gold resistor.

cover layer had to be thick enough to withstand harsh reaction conditions, e.g. pressures of up to 17 bar and temperatures of 190 ℃. On the other hand, it had to be thin enough to enable sufficient light transmittance to excite the CDots with a UV lamp and detect their photoluminescence.

A first prototype was fabricated with a top cover consisting of three 951PX LTCC layers, each 254 µm thick (prior to firing). A cross-section view of the microreactor is shown in Figure 5.17. Although no photoluminescence could be detected with such thick cover, the microreactor was able to withstand the harsh reaction conditions.

Once the functionality of the microreactor was proved under the operation conditions (up to 17 bar and 190 ℃), other prototypes were fabricated using thinner cover layers. Single LTCC layers DuPont 951C2, 951PT and 951PX (50, 114 and 254 µm thick, respectively, prior to firing) were employed as top cover layers. As expected, light transmittance decreased with the increasing window thickness, and it was found that the thicker window (951PX, 254 µm thick, prior to firing) did not have noticeable transmittance. The two thinner LTCC layers enabled the monitoring of forming photoluminescent CDots, and therefore were suitable to be employed as optical windows.

As expected, the microreactor with the thinner 951C2 cover layer exhibited higher transmittance. A photograph taken during the synthesis of CDots (upon irradiation with a UV lamp at 365 nm) is shown in Figure 5.18. As the
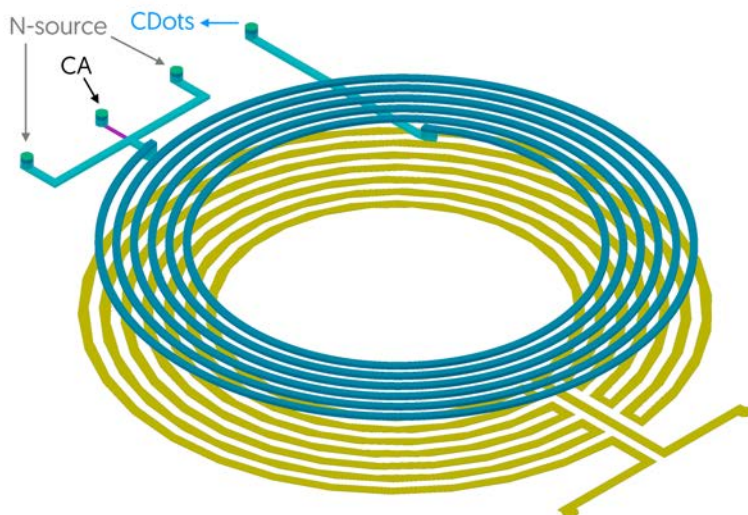
Figure 5.16: 3D representation of the microreactor channel and heating resistor for Carbon Dot synthesis. The fluidic elements are represented in different shades of blue, green and purple. The screen-printed heating resistor is shown in yellow.

reaction progresses inside the microreactor channel (towards the center of the spiral), the photoluminescence increases due to the formation of the reaction product.

However, the 951C2 optical window was prone to bursting after a few syntheses runs, due to the high pressure and temperature conditions of the synthesis. Although the 951PT optical window did not match the transmittance of the thinner 951C2 layer, it proved to be structurally robust while enabling photoluminescence monitoring of the reaction progress. Therefore it was chosen as the optimal optical window for the fabrication of high pressure and high temperature synthesis microreactors. A cross-section view of the prototype is shown in Figure 5.19. Finally, Figure 5.20 shows two photographs of the final microreactor for CDots synthesis.

5.4   Results & Discussion

5.4.1   Synthesis of Magnetite Nanoparticles

The synthesis of magnetite nanoparticles is based on a co-precipitation reaction upon addition of a strong base (A.-H. Lu, Salabas and Schüth 2007), as seen in Equation 5.2. The synthesis of magnetite is preferred over other
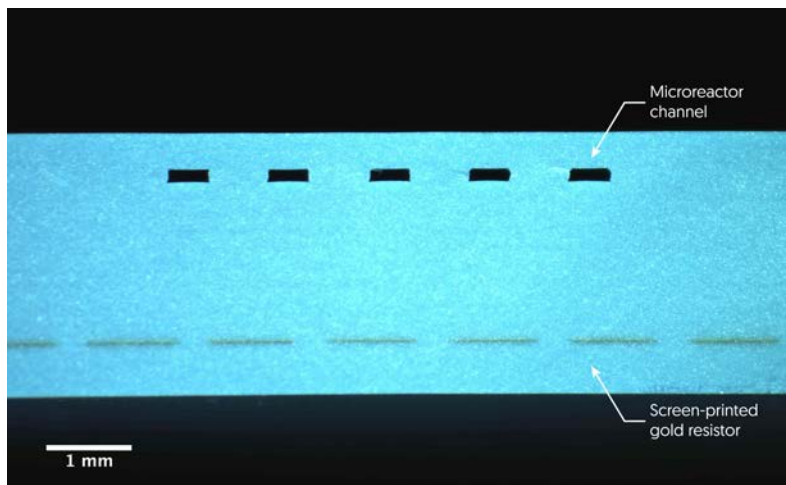
Figure 5.17: Cross-section microscope photograph of the LTCC microreactor, showing the microchannel (five spiral turns) and the screen-printed gold resistor. The top cover consisted of three 951PX layers, each 254 μm thick (prior to firing).
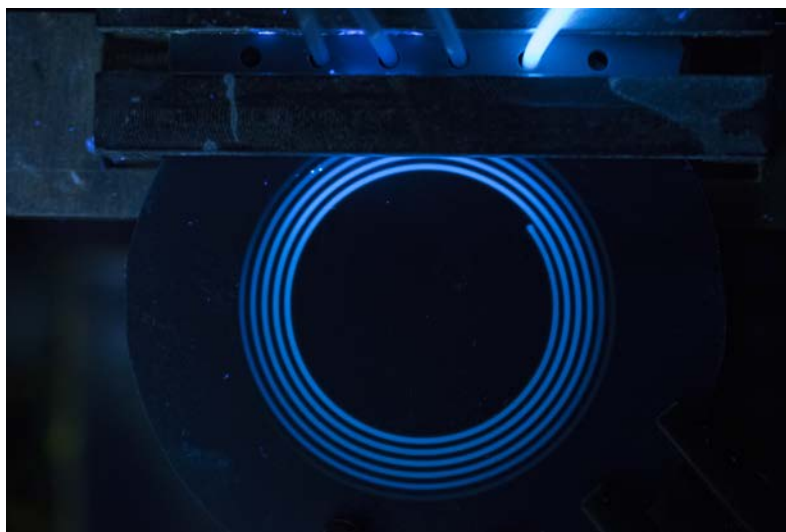
Figure 5.18: Photoluminescence of Carbon Dots during the synthesis in the microreactor. The top cover layer consists of a 951C2 LTCC layer (50 μm thick, prior to firing) acting as an optical window. The tree tubes on the left hand side are reagent inlets, and the tube on the right is the product outlet. As the reaction progresses inside the microchannel (towards the center of the spiral), the photoluminescence intensity increases.
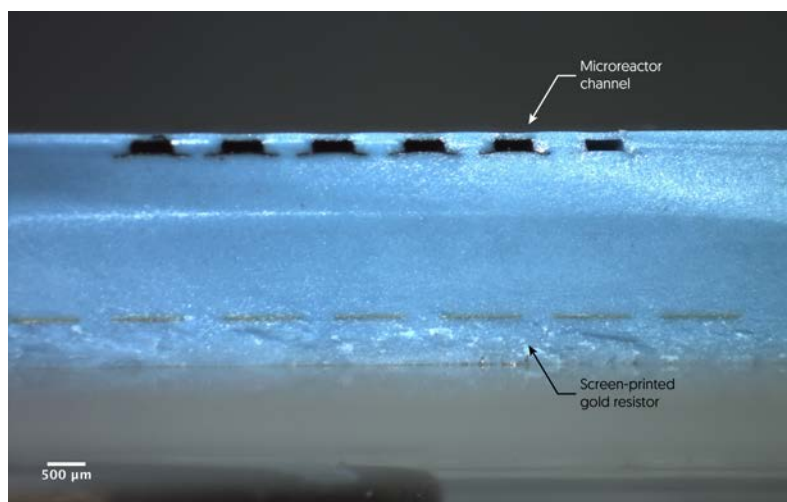
Figure 5.19: Cross-section microscope photograph of the LTCC microreactor, showing the microchannel (five spiral turns) and the screen-printed gold resistor. The top layer consisted of a single 951PT layer, 114 μm thick prior to firing.

(a) CDots microreactor top view
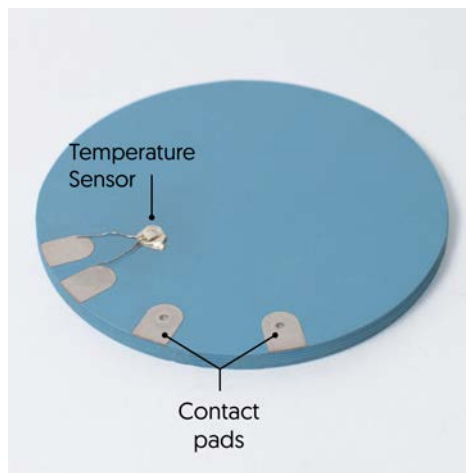
(b) CDots microreactor bottom view

Figure 5.20: Top and bottom view photographs of the microreactor for the synthesis of CDots. The top side image includes the tubing connected to the microreactor through an aluminum interconnect. The bottom side contains the PT100 temperature sensor and the contact pads of the gold resistor.

iron oxides such as maghemite γ-Fe_2O_3, since the former has the highest magnetic saturation and susceptibility (Cullity and Graham 2011), making it more desirable for a myriad applications.

$$Fe^{2+}_{(aq)} + 2\,Fe^{3+}_{(aq)} + 8\,OH^{-}_{(aq)} \longrightarrow Fe_3O_4 \downarrow + 4\,H_2O_{(l)} \qquad (5.2)$$
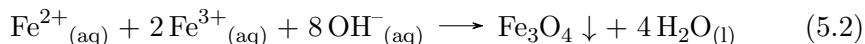
The reaction product is influenced by several parameters such as the final pH, the iron ions ratio and total concentration, as it can be deduced from Equation 5.2. Other parameters that have influence are the temperature and the residence time in the microreactor.

The iron precursor, containing both Fe^{2+} and Fe^{3+}, was introduced through Inlet 2, while the sodium hydroxide solution was introduced through Inlets 1 and 3 (see Figure 5.8), thus creating a 3D sheath flow. In some experiments, Inlet 4 was used to inject a stabilizer into the microreactor downstream channel and evaluate its effect on the formation of the nanoparticles. The ratio Fe^{2+}/Fe^{3+} was set to $1/2$, just as the stoichiometry of the reaction. The reagents were degassed and directly introduced in the gastight syringes, thus preventing oxidation of Fe(II). Oxidation of Fe(II) to Fe(III) would prevent the obtention of magnetite —which contains an Fe(II) in its structure $Fe^{II}Fe_2^{III}O_4$— in favor of other oxides such as maghemite. The confined microreactor environment avoids the need of a controlled atmosphere or the increase of the Fe^{2+}/Fe^{3+} ratio, as seen in batch synthesis (Karaagac et al. 2010).

The hydrodynamic parameters were optimized on an experimental basis, in order to obtain an enhanced mixing and avoid channel clogging due to the formation of the nanoparticles. In this way, several flow rate ratios $Q_1(NaOH) : Q_2(Fe) : Q_3(NaOH)$ were evaluated, prioritizing a stable flow pattern and avoiding channel occlusion. A ratio $3 : 1 : 3$ was determined as optimal for this synthesis —considering the iron concentration range employed— since it enabled a stable flow while producing the required pH shift. Experiments using an analogous microreactor with a 2D flow focusing inlet channel system —rather than the 3D system herein developed— were not able to reliably perform under the same experimental conditions, often clogging and exhibiting irregular flow patterns. These experimental observations demonstrate the enhancement provided by the 3D hydrodynamic flow focusing inlet system.

Other important parameters such as the total iron concentration, reaction temperature and residence time were studied. Table 5.1 shows the reaction conditions employed and the nanoparticle average size determined by analysis of the TEM images. The conditions selected as optimal were an iron concentration of 300 mM and a temperature of 90 °C (Sample B in Table 5.1). These experimental conditions produced nanoparticles with an average size of

5.5 nm. On the one hand, lower iron concentrations produced very small particles, while higher concentrations could sometimes occlude the microreactor channel. On the other hand, room temperature conditions produced a dark-orange/red precipitate —usually indicative of maghemite (Fu and Ravindra 2012)— of smaller particles, in contrast to the black precipitate —indicative of magnetite— obtained at higher temperature. A residence time of 5 minutes was selected as it enabled a stable flow and reasonable time to obtain the product.

Table 5.1: Reaction conditions of the magnetite synthesis and average nanoparticle size.

		Sample				
		A	B	C	D	E
$[Fe]_{tot}$	(mM)	30	300	360	300	300
T	(℃)	90	90	90	25	90
t_R	(min)	5	5	5	5	1.5
Size	(nm)	2.7	5.5	7.5	2.3	6.0

As expected (Karaagac et al. 2010), the size of the nanoparticles increased with the total concentration of iron (2.7, 5.5 and 7.5 nm for total iron concentrations of 30, 300 and 360 mM, respectively). The reaction temperature also had a great impact on the size of the SPION. The reaction at room temperature produced a dark-orange/red precipitate with an average particle size of only 2.31 nm, while the analogous reaction at 90 ℃ produced a black precipitate with an average of 5.5 nm.

The larger size found at higher reaction temperature may arise from Ostwald ripening theory, which is based on the dissolution of small crystals and the redeposition of the dissolved species on the surfaces of larger crystals. This is caused by the higher total Gibbs energy of smaller nanoparticles (they are less stable). On the other hand, larger crystals are more energetically stable and temperature can favor their growth through its effect on interfacial energy, growth rate coefficients, and equilibrium solubility (Madras and McCoy 2004). However, other studies suggest that at high pH, size and dispersion are mainly dominated by nucleation rather than ripening (Vayssieres et al. 1998). The increasing particle size at higher temperature could then be originated on the thermal activation of chemical reactions involved in the precipitation.

The residence time was modified by changing the total flow rate (not the ratio). Given the microreactor volume (*ca.* 100 µL), total flow rates of 21 and 70 µ/min corresponded to residence times of approximately 5 and 1.5 min, respectively. The reduction of the residence time produced a slight increase

in the particle size, however negligible. As previously stated, certain studies suggest that at high pH values, the size and polydispersity are mainly dominated by nucleation rather than ripening (Vayssieres et al. 1998), and therefore residence time has no significant effect (Salazar-Alvarez, Muhammed and Zagorodni 2006).

Finally, preliminary experiments were performed using Inlet 4 to introduce a surface stabilizer, in this case citrate. Surface functionalization determines the interaction of the nanoparticles with the environment, affecting the colloidal stability (Sperling and Parak 2010) and providing accessible surface chemistries for routine conjugation of other (bio)molecules, specially in biomedical applications (Nigam, Barick and Bahadur 2011). Citrate-stabilized magnetite nanoparticles are very appealing due to their dispersibility in water and simple conjugation strategies using the uncoordinated carboxylic groups (Liu et al. 2009).

The citrate was introduced at the middle of the downstream microreactor channel, that is when the nanoparticles were at a growing stage. The ratio $Fe : Citrate$ was set at 1:2, as seen in Nigam, Barick and Bahadur 2011. With the addition of the new reagent, the residence time was slightly decreased, because of the increase in total flow rate. Nevertheless, as seen in Table 5.1, the residence time had little effect on the size of the nanoparticles obtained in this range of experimental conditions. The flow was stable under this conditions and the obtained precipitate was black, as expected, showing a good magnetic susceptibility when probed with a magnet.

5.4.1.1 Characterization of Magnetite Nanoparticles

The obtained nanoparticles were optically characterized by means of TEM to determine their size and morphology. Figure 5.21 shows a TEM image and the size distribution of the nanoparticles synthesized using the optimal experimental conditions. The nanoparticles have a roughly spherical shape and appear in big aggregates, which is expected as seen in similar synthesis (Karaagac et al. 2010; Simmons et al. 2013; Abboud et al. 2015). The average size was calculated to be 5.5 nm.

The SAED pattern of the nanoparticles indicates their crystalline structure (see Figure 5.22). As it can be observed from inside to outside, the diffraction rings can be assigned to the (110), (220), (311), (400), (511) and (440) lattice planes of the Fe_3O_4 spinel structure (Haavik et al. 2000). This confirms the presence of magnetite as the predominant phase in the product using the optimized reaction conditions.

The powder XRD spectrum (see Figure 5.23) further demonstrates the crystallinity of the sample. Moreover, it shows a cubic structure with the characteristic peaks of magnetite, confirming the assignment in the SAED

(a) TEM image

(b) Nanoparticle size histogram
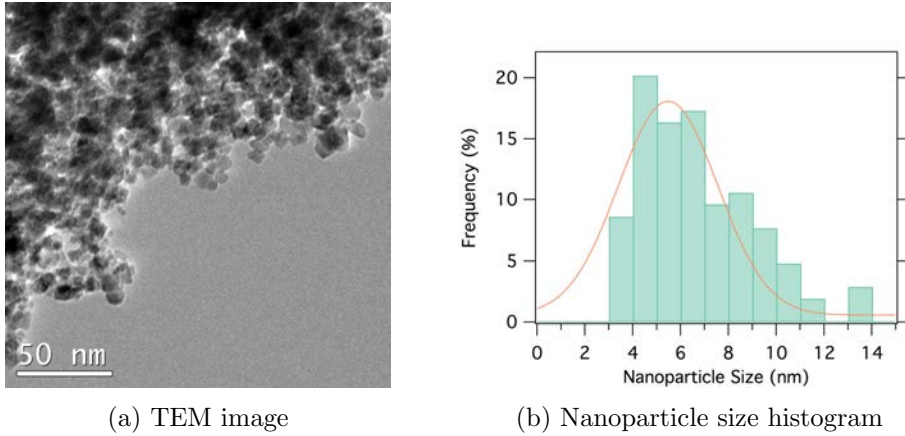
Figure 5.21: TEM image and size histogram of the magnetite nanoparticles obtained under the optimal synthesis conditions.
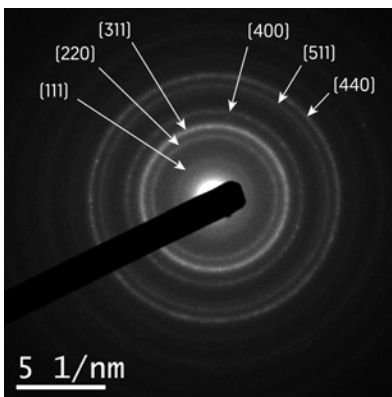
Figure 5.22: SAED pattern of the synthesized magnetite sample, with indexing of the main diffraction rings for Fe_3O_4

pattern. However, the resolution is not good enough to clearly differentiate from maghemite (γ-Fe$_2$O$_3$, see blue bars in Figure 5.23), which also has a cubic structure. Although characteristic peaks of maghemite such as those at 23.8° and 26.2° do not show in the spectrum, they could be hidden by the noise due to their low relative intensity (<5 %). No peaks from other oxide phases (e.g. hematite γ-Fe$_2$O$_3$ or wüstite FeO) were observed.
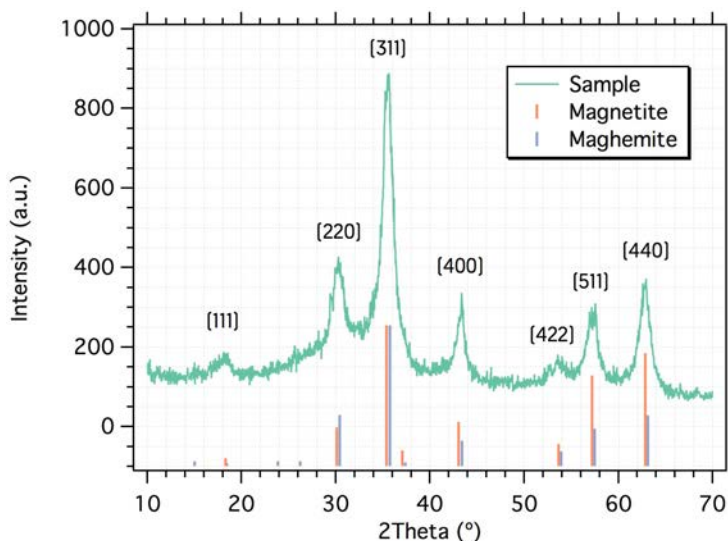
Figure 5.23: Powder XRD spectrum of the magnetic sample. For comparison, the reference spectra of magnetite (red, JCPDS 001-1111) and maghemite (blue, JCPDS 004-0755) are represented with bar graphs.

With this information, the actual composition of the synthesized SPION cannot be determined. The SAED pattern and the XRD indicate that the sample consists of a cubic spinel structure, attributable to magnetite. Nevertheless, both magnetite and maghemite phases possess the same spinel structure and almost identical lattice parameters, and therefore their identification is rather intricate. There are methods to assess the exact composition of the SPION sample, such as XRD deconvolution of the peak corresponding to the plane (511) (W. Kim et al. 2012), Mössbauer spectroscopy (Gorski and Scherer 2010), etc. A more in-depth study on the exact composition of the samples will be undergone by our research group, in order to have a better characterization in later studies using these SPION for analytical applications. Nevertheless, the black color of the product seems to point towards the predominance of the magnetite phase (Fu and Ravindra 2012). In any case, both magnetite and maghemite exhibit superparamagnetic behavior at this nanoparticle size

range.

The magnetic properties of the SPION sample were determined by means of a SQUID magnetometer at 300 K. The hysteresis curves (see Figure 5.24) demonstrate the superparamagnetic behavior of the nanoparticles, with a remanent magnetization of only 0.7 emu/g. The SPION had a saturation magnetization slightly above 30 emu/g, which is within the experimental range of 30–50 emu/g found in the literature for magnetite nanoparticles (A.-H. Lu, Salabas and Schüth 2007). The relatively low saturation magnetization may be caused by the small size of the nanoparticles. Furthermore, it could be indicative of the presence of a certain proportion of maghemite, since γ-Fe_2O_3 has a lower saturation magnetization when compared to magnetite (Kemp et al. 2016).

(a) Hysteresis loop   (b) Low field region
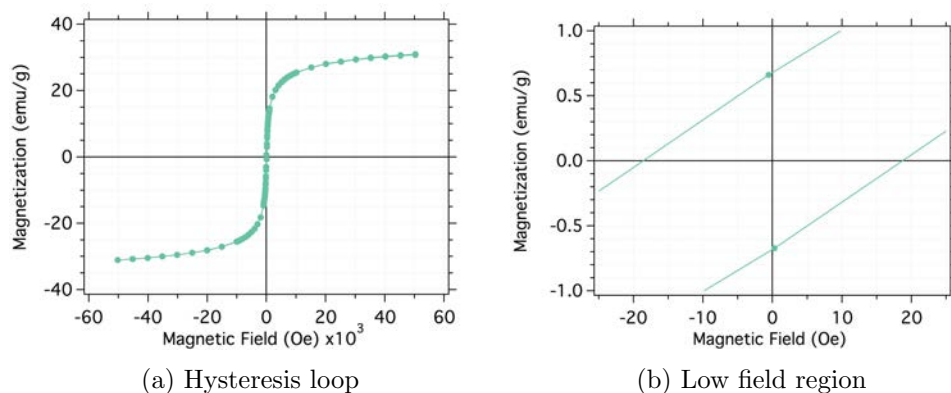
Figure 5.24: Magnetic hysteresis loop of the SPION and close-up of the low field region, recorded at 300 K.

A preliminary TEM study of the citrate-modified SPION shows a slightly better dispersion of the particles. The SPION do not tend to aggregate as much or in such big clusters as the non-stabilized or naked particles (see Figure 5.25). However, a more detailed study is required in order to determine a representative size distribution. Furthermore, zeta potential measurements could help determine the surface differences between the coated and the uncoated SPION. The carboxylic groups from the citrate are expected to create a highly negative surface charge on the citrate-modified nanoparticles.

5.4.2 Synthesis of Carbon Dots

The synthesis of CDots herein presented is based on that proposed in Zhu, Meng, et al. 2013. CA and ED were dissolved in water and a hydrothermal method was applied to first condense and then carbonize the reagents, thus producing N-doped CDots with high QY. The authors used a Teflon-lined
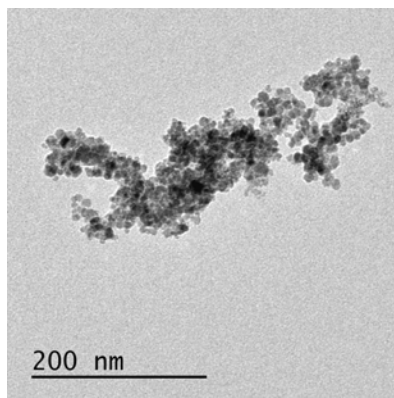
Figure 5.25: TEM image of the citrate-stabilized magnetite nanoparticles.

autoclave and temperatures of up to 300 °C, which generated high pressures. Therefore, our microreactor system was intended to function at high temperatures —by means of the integrated heater— and high pressures —using a BPR, as seen elsewhere (Faustini et al. 2013).

CA was pumped into the microreactor through Inlet 2, while ED was pumped through Inlets 1 and 3 (see Figure 5.8), thus confining the CA to a cylindrical fluid stream in the centre of the ED. The outlet was connected to the BPR, where different cartridges could be used to set the desired pressure in the microreactor.

The concentration of the two reagents initially employed were those found in Zhu, Meng, et al. 2013. However, the viscosity of the solutions was too high, leading to occlusion of the microreactor after a certain period at high temperature. The dilution of the precursor solutions by a factor 1/10 enabled the reaction to be carried out without channel clogging. The reagents were pumped at a total flow rate of 10 μL/min (3.33 μL/min each inlet) in order to achieve a relatively long residence time inside the microreactor. Considering a microreactor approximate total volume of 100 μL (same volume as the downstream main microchannel of the magnetite microreactor), the residence time was *ca.* 10 min. These parameters were used throughout the rest of the experiments, in order to focus our attention on the optimization of temperature and pressure.

The optimal reaction conditions were studied by comparing the QY of the CDots and studying the flow pattern inside the microreactor channel. Figure 5.26 shows the QY of the CDots obtained at different temperature and pressure conditions. On the one hand, pressure does not have a significant effect on the QY of the nanoparticles obtained, except for a slight decrease at 190 °C and pressures of 1 and 7 bar, compared to the increase at 17 bar (see Figure 5.26). On the other hand, there is a dramatic effect of temperature on the QY of the CDots obtained, with a maximum at 190 °C.
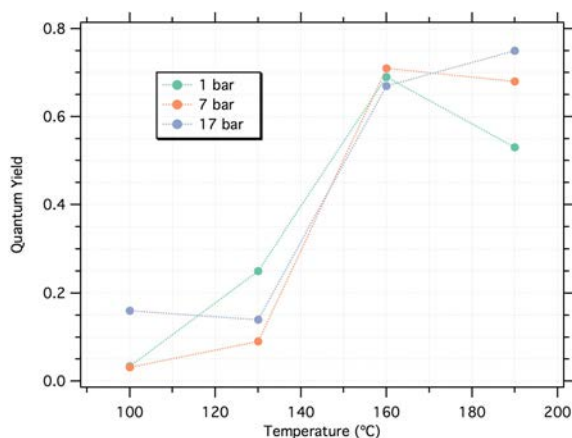
Figure 5.26: Quantum Yield of the Carbon Dots obtained under different re-action conditions.

Figure 5.27 shows photographs taken under UV lamp excitation during the syntheses at different conditions. The high temperatures (up to 190 ℃) achieved in the microreactor are above the boiling point of water at the two lower pressures evaluated (Chaplin 2017). In consequence, a discontinued flow was observed in the microreactor channel due to the formation of gas bubbles at these two pressures (see Figure 5.27a). This phenomenon could lead to channel occlusion —due to the deposition of solid particles on the walls— and a less homogeneous reaction product —due to the flow fluctuations created. However, a continuous and stable flow was observed at 17 bar indicating no water evaporation (see the water phase diagram in Chaplin 2017). Therefore, 17 bar was selected as the optimal pressure for the rest of the experiments. No cartridges of higher back pressure were evaluated because of the working range limitations of the syringe pumps. Nevertheless, high-pressure equipment would allow working at more extreme conditions. Figure 5.27b shows the expected increasing photoluminescence dependence with reaction temperature.

Nitrogen sources other than ED were used to produce a pool of differ-ent CDots under the optimized pressure and temperature conditions. The structural differences on the CDots induced by the use of different N-sources produced varying optical properties, as seen elsewhere (J. Wang et al. 2015). Moreover, different interactions to potential photoluminescence quenchers were observed, as will be discussed later in this chapter. The N-sources selected were DETA, a longer linear analog of ED, and PEI, a branched polymer formed by ED units and tertiary amines.

(a) Varying pressure

(b) Varying temperature
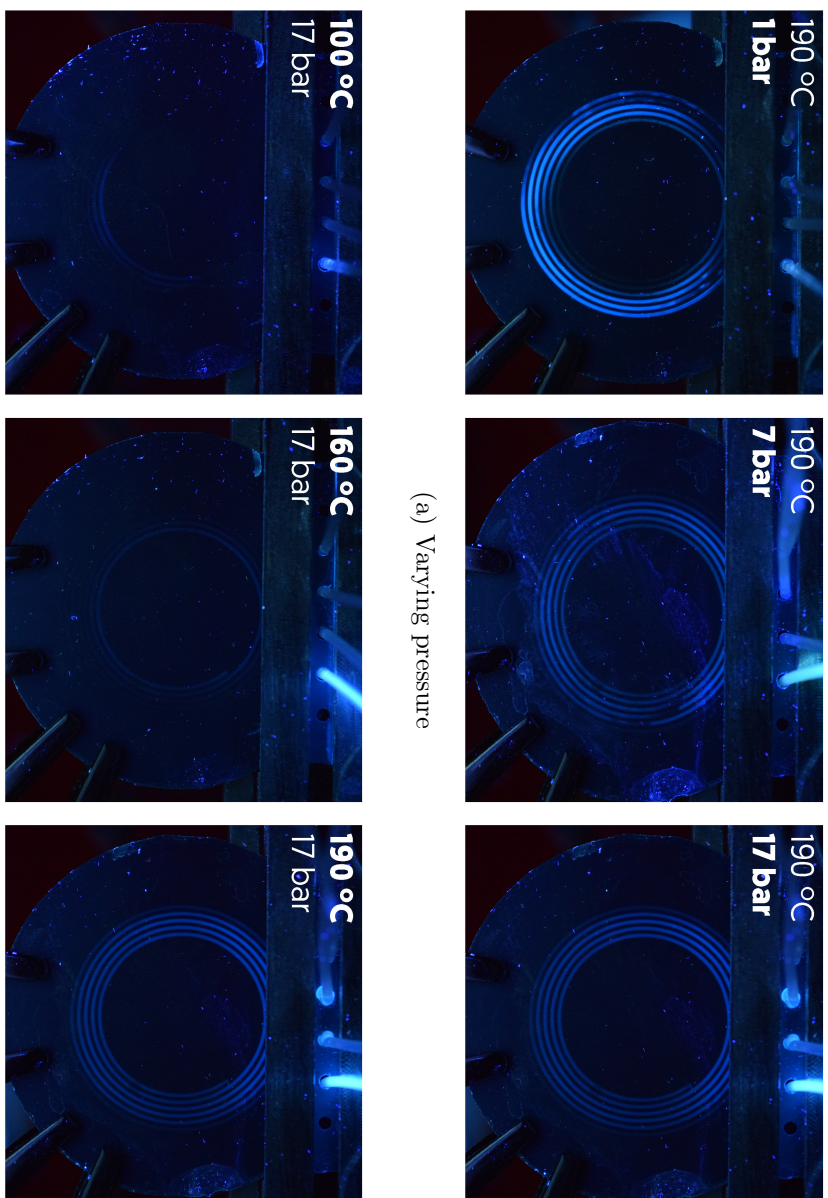
Figure 5.27: Photographs taken during the synthesis of Carbon Dots at different conditions and under UV light excitation. (a) Varying pressure at a constant temperature of 190 °C. (b) varying temperature at a constant pressure of 17 bar.

5.4.2.1 Characterization of CDots

All the obtained CDots (i.e. CDots-ED, CDots-DETA and CDots-PEI) exhibited a bright, blue photoluminescence upon irradiation with a UV lamp. They presented similar absorbance and photoluminescence spectra, with bands located at around 350 and 450 nm, respectively, as seen in Figure 5.28. However, depending on the Nitrogen source employed, namely ED, DETA and PEI, the CDots exhibited QY values of 0.77, 0.76 and 0.17, respectively. These results demonstrate the relationship between the emission properties and the Nitrogen source. The QY values and the absorbance and photoluminescence spectra are comparable to those of other CDots reported in the literature synthesized in batch under similar conditions (Zhu, Meng, et al. 2013; J. Wang et al. 2015; C. Wang, Z. Xu and C. Zhang 2015).

(a) Absorption spectra (b) Photoluminescence spectra
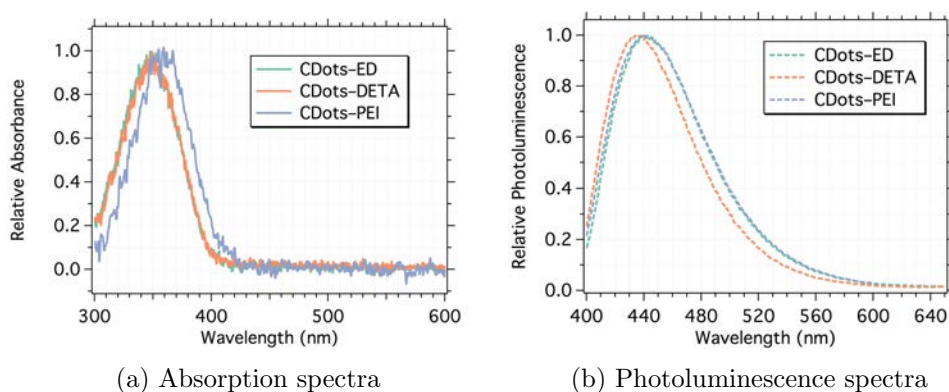
Figure 5.28: Normalized absorption (continuous) and photoluminescence (dashed lines) spectra of the obtained Carbon Dots.

The size of the CDots ranges from 2.2 to 4.3 nm, although the population was not big enough to extract a representative value (see Figure 5.29). TEM images of the CDots were difficult to obtain for a number of reasons, as in other similar syntheses (Dong et al. 2012). They showed a low contrast on the carbon-coated copper grids. This could be partly caused by the low crystallinity of the nanoparticles obtained, as observed in Figure 5.29. The lack of crystallinity is indicative of the incomplete carbonization of the precursors.

Recent studies by different groups on the formation of CDots from CA and ED may explain this (Y. Hu et al. 2015; Zhu, Song, et al. 2015; Song et al. 2015; J. Wang et al. 2015; Schneider et al. 2017). They propose a synthetic mechanism consisting on first, the polymerization of the CA and ED and second, the subsequent carbonization, thus yielding the CDots. However, the product usually consists of a mixture of polymer clusters (specially at lower temperatures, when carbonization does not have enough energy to pro-
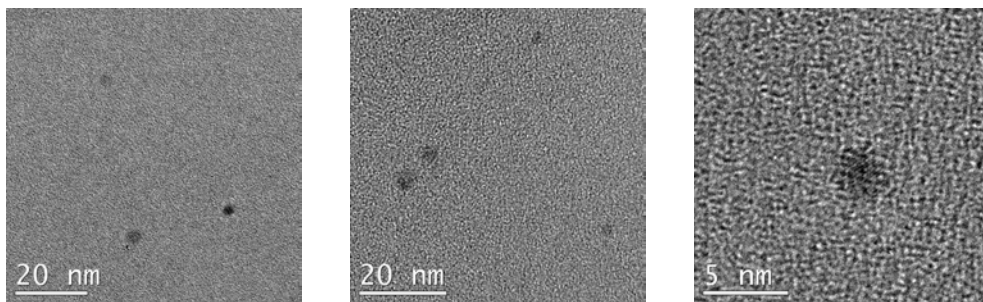
Figure 5.29: TEM images of CDots-ED.

ceed) and carbon-core nanoparticles, both bearing molecular-like fluorophores embedded on their surfaces (Song et al. 2015).

This type of CDots can exhibit photoluminescence generated in two different emission centers (Song et al. 2015; Schneider et al. 2017). On the one hand, the molecular-like fluorophores embedded on the surface of the particles produce a "molecular state" photoluminescence. The use of ED favors the formation of the fluorophore IPCA, while other Nitrogen sources seem to favor the formation of other fluorophore structures (Schneider et al. 2017). On the other hand, the carbon core also exhibits photoluminescence, although with lower QY (Schneider et al. 2017).

The composition of the final product depends on several experimental parameters (as stated in Section 5.4.2), such as starting material ratio, initial pH and temperature (Song et al. 2015). Particularly in this case, temperature appears to have a central role on the actual composition of the product, since the reaction time is dramatically decreased compared to batch syntheses: from several hours to just a few minutes (residence time in the microreactor was 10 min). Therefore, the composition of the CDots herein obtained may be shifted towards the polymer clusters, also referred to as "polymer dots" (Zhu, Song, et al. 2015) or "carbon nanodots" (Cayuela et al. 2016) depending on the source. The amorphous nature of these structures explains the difficulty to find more particles in the TEM images. Higher temperatures could not be employed in the synthesis due to the formation of gas bubbles in the microreactor, which eventually led to channel clogging. As previously stated, the use of high pressure pumping systems would enable the use of a higher pressure, thus widening the range of operational temperature.

5.4.2.2 Screening Applications for Carbon Dots

CDots have unique properties that make them suitable for several applications, such as chemical sensing, imaging, catalysis or drug delivery (H. Li et al. 2012; Lim, Shen and Gao 2015). We evaluated the synthesized CDots as nanoprobes

for metal ion detection and as bioimaging agents.

Metal Sensing   The synthesized CDots were evaluated as metal sensors by monitoring the induced photoluminescence quenching. The different surface chemistries of the CDots triggered different behaviors in presence of certain metals ions, such as Cu(II) and Hg(II), in the µM range. For instance, Cu(II) produced photoluminescence quenching only in CDots-PEI, as seen in Figure 5.30.

(a) CDots-ED Cu^{2+} quenching

(b) CDots-DETA Cu^{2+} quenching

(c) CDots-PEI Cu^{2+} quenching
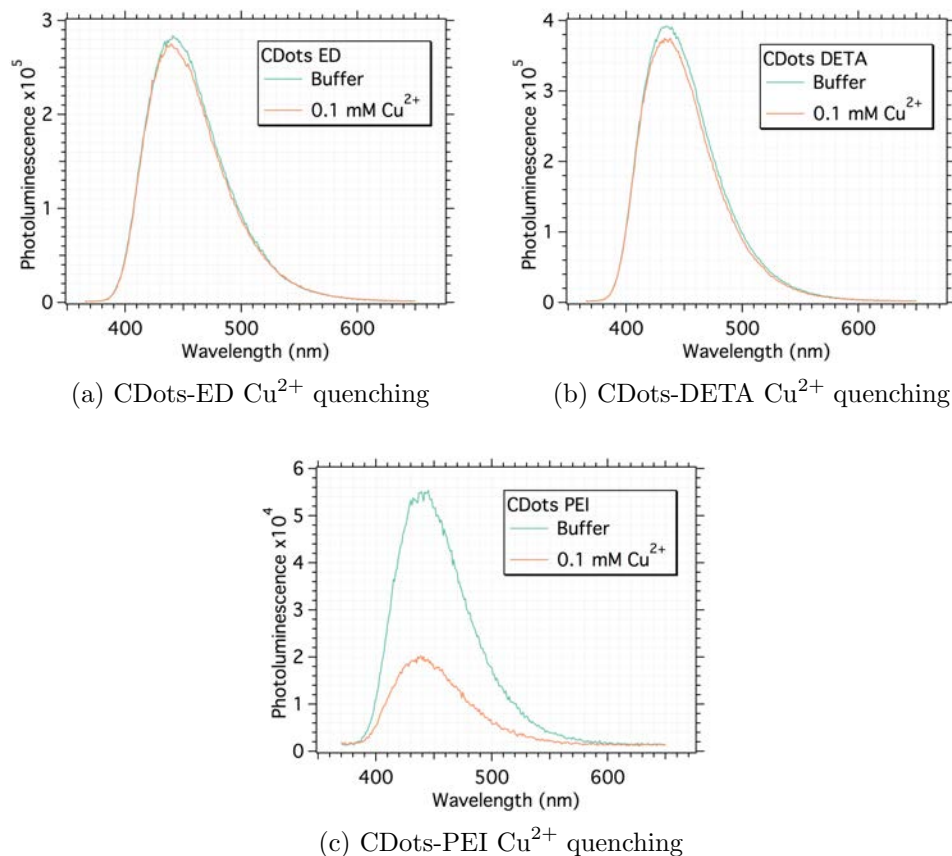
Figure 5.30: Photoluminescence spectra of the Carbon Dots in absence/presence of Cu^{2+} ions. Only in the case of CDots-PEI the photoluminescence is substantially quenched.

The CDots-PEI photoluminescence quenching was further studied in the range 0.5–100 µM. Figures 5.31a and 5.31b show the intensity decrease in the photoluminescence spectra as the copper concentration increases. The resulting Stern-Volmer plot (Figure 5.31c) shows a relatively good linearity in this

Cu^{2+} concentration range. These results demonstrate the applicability of the CDots-PEI as Cu(II). Further studies need to address the optimization of the experimental parameters as well as the selectivity of the nanoprobe.
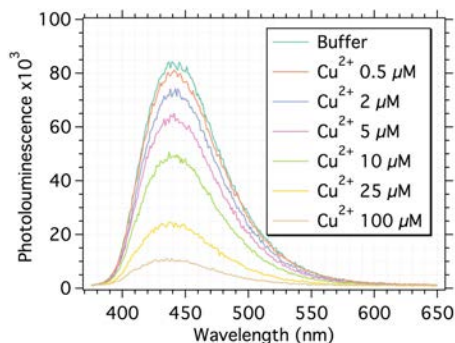
(a) CDots-PEI Cu^{2+} quenching spectra
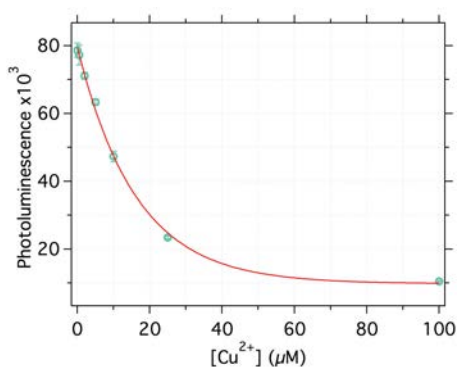
(b) Quenching curve
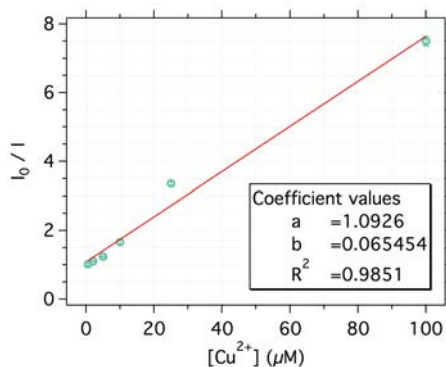
(c) Stern-Volmer plot

Figure 5.31: Cu^{2+} sensing using CDots-PEI. Photoluminescence emission spectra in presence of different Cu^{2+} concentrations and Stern-Volmer plot of the Cu^{2+} quenching.

Similarly, preliminary results show the quenching effect of Hg^{2+} ions on the CDots-ED, as seen in Figure 5.32. These first results indicate a relationship between the concentration of mercuric ion and the photoluminescence of the CDots-ED. The mercuric ion solution of higher concentration (500 µM) presented a significant absorption at the emission wavelength of the CDots-ED. Therefore, it was discarded from the Stern-Volmer plot.

Bioimaging This is one of the most cited applications of CDots. The outstanding optical properties of these nanoparticles, the well-know carbon chemistry for surface functionalization and their stability make them a suitable can-
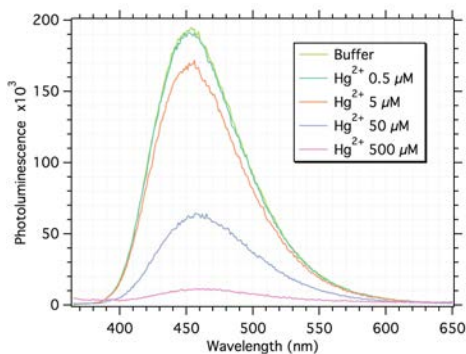
(a) CDots-PEI Cu^{2+} quenching spectra
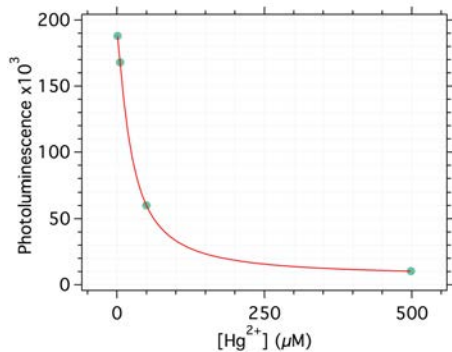
(b) Quenching curve
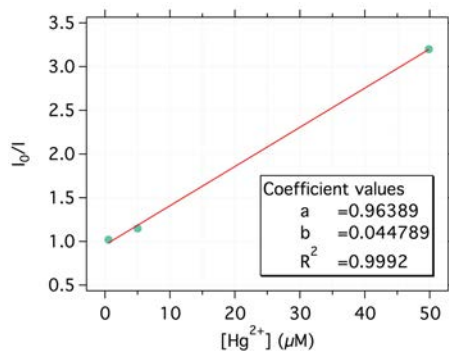
(c) Stern-Volmer plot

Figure 5.32: Hg^{2+} sensing using CDots-ED. Photoluminescence emission spectra in presence of different Hg^{2+} concentrations and Stern-Volmer plot of the Hg^{2+} quenching.

didate for *in vivo* imaging applications. Although other nanoparticles extensively investigated —such as QD— share similar characteristics, CDots offer higher biocompatibility and lower cost. Herein, we investigated the suitability of the synthesized CDots-ED as cell markers, since they exhibited the higher QY of the different CDots synthesized. Figure 5.33 shows different confocal microscope images of HEK293 cells. The confocal images prove the cellular uptake of the CDots.

(a) Bright-field image   (b) Fluorescence image   (c) Overlapped images
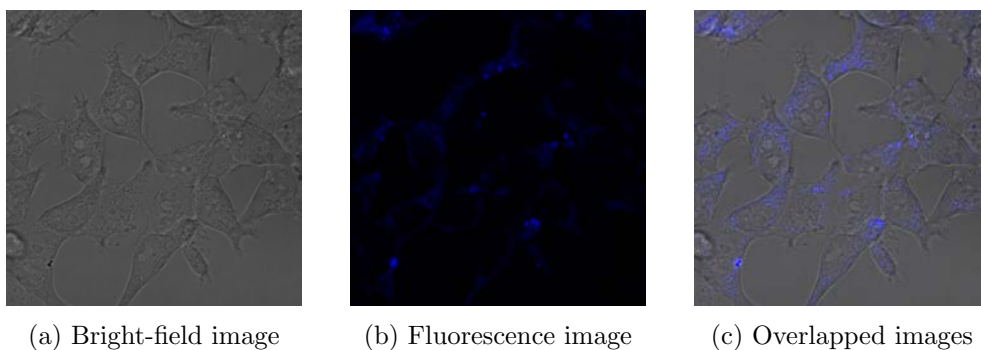
Figure 5.33: Confocal bright-field and fluorescence images of HEK293 cells with CDots-ED.

The cell viability was studied by means of an MTT test, a cell metabolic activity experiment. These study was performed in the group of Prof. L.F. Capitán-Vallvey and Dr. A. Salinas-Castillo, at the University of Granada. The results, given in Figure 5.34, show a slight decrease of cell viability compared to the control sample. However, viability remains above 80 % in all studied concentrations after 24 h. Even after 48 h, viability remains above that threshold at relatively high CDots concentrations of up to 1 mg/mL. These results demonstrate a comparable or better biocompatibility to similar CDots (J. Wang et al. 2015) as well as graphene quantum dots (Yuan et al. 2014).

5.5 Conclusions

Microreactor technology brings several advantages to the synthesis of nanomaterials, arising from the inherent characteristics of these miniaturized systems. Microfluidic reactor technology enables the automation of synthetic processes and provides the grounds for an enhanced control over temperature and mass gradients. These factors have a key impact on the homogeneity of the product and a higher reproducibility of the syntheses. In the case of nanomaterials, this enhanced control is of paramount importance to obtain homogeneous properties.
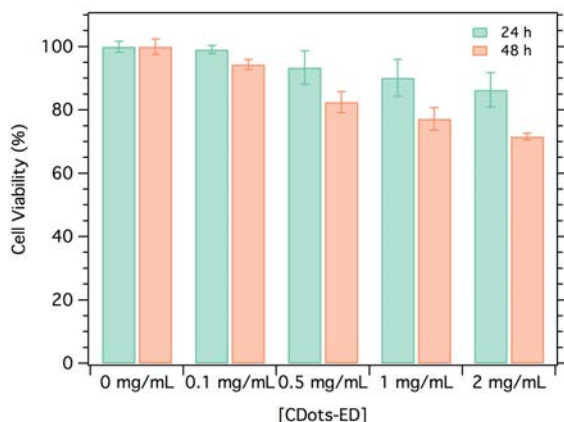
Figure 5.34: MTT viability study with CDots-ED on HEK293 cells.

It is important to highlight the experimental possibilities provided by the LTCC microreactors developed in this work, enabling the synthesis of nanoparticles in a wide range of conditions. First, LTCC microreactors take advantage of the inherent properties of the material, such as inertness and mechanical robustness. In synthetic applications, chemical inertness is essential, specially in harsh environments (e.g. organic solvents, strong acids, strong bases, etc.). Furthermore, LTCC can easily withstand extreme temperature and pressure conditions, which are often required for synthesis. Second, the multilayer fabrication approach enables the development of complex 3D structures, such as the inlet system for sheath flow. This structure is essential to obtain an enhanced flow pattern and a controlled reaction interface between the different reagents, and therefore, to the reproducibility of the syntheses. Third, the compatibility of LTCC with other materials enables the simple fabrication of integrated electronic elements and actuators, such as the heaters used in this work. This could facilitate adoption of the microreactor technology by simplifying the manipulation and widening the possibilities of application. Finally, the integration of optical windows for photoluminescence monitoring has been demonstrated and used for flow inspection, thus overcoming the limitations of the bulk material opacity.

The use of LTCC microreactors enabled the synthesis of different types of nanoparticles, namely SPION and CDots. On the one hand, superparamagnetic iron oxide nanoparticles were synthesized by co-precipitation of ferric and ferrous salts upon pH basification. Although the synthesis was performed at high temperature (90 ℃) and with relatively high total iron concentrations (up to 360 mM), the microreactor was able to maintain a stable flow pattern and avoid channel occlusion. The nanoparticles obtained under op-

timized conditions had a spherical shape and a diameter of 5.5 nm. Their crystallinity was confirmed by the SAED pattern and the XRD diffractogram. XRD data shows the presence of a cubic spinel structure, and the peaks can be assigned to magnetite. However, the presence of maghemite cannot be discarded since it has the same spinel structure and almost identical lattice parameters. The magnetization study shows a superparamagnetic behavior of the nanoparticles, with a remanent magnetization of only 0.7 emu/g and a saturation magnetization slightly above 30 emu/g.

On the other hand, a pool of CDots were synthesized at high temperature and pressure using different Nitrogen sources. The formation of the photoluminescent CDots was monitored through a thin top cover LTCC layer, which acted as a monolithic optical windows. The CDots exhibited blue photoluminescence under UV light excitation, with QY of up to 0.77. Preliminary studies show the potential applicability of the CDots as nanoprobes for heavy metal detection and, due to their low cytotoxicity, as bioimaging contrast agents.

Chapter 6

Concluding Remarks and Future Challenges

6.1   Remarks

This dissertation presents three different applications of Lab on a Chip (LOC) systems based on simple, scalable fabrication methodologies. The use of Cyclic Olefin Co-polymer (COC) and Low Temperature Co-fired Ceramics (LTCC) as substrate materials provided several advantages over other materials in these specific applications, such as simple bonding techniques, biological compatibility or chemical stability. Although the fabrication of the LOC systems was performed on a prototyping level, the methodologies were intended to easily scale-up. The fabrication approaches developed were devised to bridge the gap that separates the development of LOC systems in academia from the "real world" applications, usually hindered by scalability issues.

On the one hand, the fabrication of COC devices could be scaled-up using injection molding techniques, readily available from the thermoplastic industry. On the other hand, LTCC devices could be mass-produced by high throughput multilayer fabrication, using laser ablation or hot embossing, together with functional printing techniques such as roll-to-roll.

During this work, the developed LOC systems were applied in such different fields as biochemical analysis, biology and synthesis. The development of these fluidic systems was central to this dissertation, but their real value consisted on the advantages and new possibilities they opened up in each application. They enabled the enhanced analysis of bacteria, the potential development of an independent platform for automated oocyte maturation and fertilization, or contributed to the process intensification in the synthesis of nanomaterials with a significant added value. Therefore, LOC technology proved to be an incredibly versatile toolset that can contribute to a myriad

chemical and biological processes.

The first application consisted on the development of a LOC device and a magnetic actuator for the control of Magnetic Beads (MBs) *on-chip*. The simplicity of the actuator makes it suitable for integration in a compact analytical system, thus combining the advantages of magnetic separation and those of LOC systems. The control over the movement of the MBs —not only the ability to trap them— provided a substantial sensitivity enhancement on the enzymatic reaction of an immunoassay for the detection of enterohemorrhagic E. coli O157:H7. Furthermore, the same actuator was applied to a fully automated bioassay for the detection of an oligonucleotide specific to E. coli, as part of the thesis of another member of the group.

The second application consisted on the development of a LOC for oocyte trapping and culturing. Biology applications *on-chip* exploit the possibility to mimic *in vivo* structures and the automation of traditionally labour-intensive processes. In this case, we developed a prototyping methodology combining hot embossing (with an LTCC master) and micromilling in order to achieve the required channel dimensions to trap the cells. The use of COC as substrate material proved to be successful for this Assisted Reproductive Technology (ART) application due to its biocompatibility. Furthermore, an Au transparent heater was integrated in the LOC device, providing the grounds for an independent culture system with temperature control.

Finally, we developed LTCC microreactors with integrated heaters for the synthesis of nanoparticles under harsh reaction conditions. Process intensification in the production of nanomaterials could benefit of the inherent advantages of microfluidic systems (enhanced transport phenomena) and those provided by LTCC microreactors (integration, chemical and mechanical stability, fabrication possibilities and scalability, etc.). The microreactors developed incorporate a complex microfluidic structure that enables a 3D sheath flow, thus avoiding channel clogging and enhancing the mixing of reagents. Furthermore, a thin ceramic layer used as cover enabled enough light transmission to monitor the formation of the photoluminescent product, thus avoiding one of the main limitations of LTCC microfluidic systems. In this way, superparamagnetic iron oxide nanoparticles (SPION) and Carbon Dots (CDots) were synthesized under high temperature and pressure conditions.

6.2 Future Directions

In order to realize the whole potential of LOC technologies, I believe that academia needs to take a step towards the development of systems that can be applied in the "real world". Of course, basic research is always required to achieve new advancements, as in any field. But the most convenient solution

for academic studies may not be the most suitable for real applications. Therefore, the development of LOC systems should be application-specific, specially regarding the choice of substrate material and fabrication technology, taking into account the constraints each challenge poses. In this way, LOC technology will be empowered to leave the lab and find viable commercial and industrial applications.

6.2.1 Magnetic Separation On-Chip

Chapter 3 describes the development of a simple, low cost magnetic actuator to trap and control the movement of MBs *on-chip*, and thus enhance the kinetics of reactions. To validate this concept, the enzymatic reaction of a sandwich immunoassay for the detection of E. coli O157:H7 was performed in a LOC with integrated fluorescence detection.

However, the reactions to form the immunocomplex were performed *off-chip*, in order to focus on the performance of the actuator and avoid non-specific adsorption related problems. The integration of all the reactions *on-chip* and the study of COC surface blocking strategies —to avoid non-specific adsorptions— would be a necessary step towards the development of a portable, simple-to-use platform for enhanced E. coli O157:H7 detection. Moreover, the commercial availability of MBs functionalized with different antibodies enables the development of a screening platform for the most common pathogenic bacteria, such as E. coli O157, Salmonella, Listeria, etc.

The combination of magnetic separation and LOC technologies brings together important advantages, such as the miniaturization of the analytic system and the separation of the analyte from its sample matrix. This advantages are not limited to the use of antibodies as recognition elements. The wide range of possible MBs surface functionalizations widens the possible applications of these systems. For instance, functionalized MBs could enable the accumulation of certain heavy metals or pesticides, usually difficult to detect due to their low concentrations and strict environmental regulations.

6.2.2 Independent Oocyte Fertilization Platform

Chapter 4 describes a novel fabrication process for the rapid prototyping of a LOC device for oocyte maturation. We demonstrated the functional and automated maturation of oocytes, as well as the nontoxic nature of COC for gametes. Therefore, the next step would be the study of the fertilization process *on-chip*. Although this process has already been studied in LOC systems made of other materials (such as Polydimethylsiloxane (PDMS)), COC could be an interesting alternative.

COC provides some key advantages, such as simple bonding process, integration of transparent gold heaters and potential fabrication scalability. Furthermore, COC is gas impermeable, and therefore, an independent fertilization platform could be developed avoiding a strict control of the exterior atmosphere conditions, currently performed in incubators. To achieve that, a thorough study of factor availability and pH buffering capacity should be performed, in order to maintain the optimal conditions for the cells. Dynamic culture (i.e. continuous or periodic infusion of media) could potentially solve this issue, although the optimal conditions need to be determined to avoid shear stress on the oocytes. This fertilization platform could avoid the use of big, expensive apparatus such as incubators, while enabling continuous optical monitoring of the biological processes due to the transparency of the COC and gold heaters.

6.2.3 Microreactor Synthesis of Nanomaterials

Chapter 5 deals with the development of LTCC microreactors with integrated heaters, a 3D hydrodynamic flow focusing inlet system or monolithic optical windows. These microreactors were applied to the continuous flow synthesis of SPION and CDots under harsh reaction conditions, taking advantage of the chemical and mechanical stability of the ceramic substrate. However, the experimental conditions were restricted to a maximum pressure of $\sim$17 bar due to the pump operational range. Therefore, the use of a high-pressure pumping system would enable the exploration of a much wider experimental range.

The LTCC microreactors offer many other possibilities not explored within this dissertation. For instance, they could be applied to droplet-based syntheses. The 3D inlet system for sheath flow could produce the droplet-based flow, while the monolithic optical window would enable their visualization. Two possible strategies could be implemented for that purpose. On the one hand, the formation of a photoluminescent product inside the droplets could be monitored. On the other hand, droplets could also be observed as dark spots in a carrier phase containing a fluorophore.

The nanomaterials synthesized in this work could be further studied due to their potential application in different fields. On the one hand, further characterization of the magnetite should be addressed in order to determine the exact composition of the product. Moreover, functionalization of the SPION could open the possibility to use them in biomedical or analytical applications. On the other hand, preliminary results showed the potential of the synthesized CDots for both bioimaging and heavy metal detection purposes. A more detailed study of the analytical parameters (Limit of Detection (LOD), selectivity, linear range, etc.) should be performed to determine the actual applicability of the CDots as metal nanoprobes.

References

Abboud, M. et al. (2015). "Superparamagnetic Fe3O4 nanoparticles, synthesis and surface modification". In: *Mater. Sci. Semicond. Process.* 39, pp. 641–648.

Abou Hassan, A. et al. (2008). "Synthesis of iron oxide nanoparticles in a microfluidic device: preliminary results in a coaxial flow millichannel." In: *Chem. Commun. (Camb).* (15), pp. 1783–5.

Alegret, S. (2003). *Integrated Analytical Systems.* Comprehensive Analytical Chemistry Comprehensive Analytical Vol. 39. Elsevier.

Andreu, J. S. et al. (2012). "Simulation of Magnetophoretic Separation Processes in Dispersions of Superparamagnetic Nanoparticles in the Noncooperative Regime". In: *J. Nanomater.* 2012, pp. 1–10.

Arora, A. et al. (2010). "Latest Developments in Micro Total Analysis Systems". In: *Anal. Chem.* 82 (12), pp. 4830–4847.

Au, A. K. et al. (2016). "3D-Printed Microfluidics". In: *Angew. Chemie Int. Ed.* 55 (12), pp. 3862–3881.

Auroux, P.-A. et al. (2002). "Micro Total Analysis Systems. 2. Analytical Standard Operations and Applications". In: *Anal. Chem.* 74 (12), pp. 2637–2652.

Autumn, K. and N. Gravish (2008). "Gecko adhesion: evolutionary nanotechnology". In: *Philos. Trans. R. Soc. A Math. Phys. Eng. Sci.* 366 (1870), pp. 1575–1590.

Baak, N. A. et al. (2016). "Temperature of embryo culture for assisted reproduction". In: *Cochrane Database Syst. Rev.* Ed. by N. A. Baak. Chichester, UK: John Wiley & Sons, Ltd.

Badilescu, S. and M. Packirisam (2011). *BioMEMS: Science and Engineering Perspectives.* Boca Raton: CRC Press.

Baldrich, E. et al. (2008). "Self-assembled monolayers as a base for immunofunctionalisation: unequal performance for protein and bacteria detection." In: *Anal. Bioanal. Chem.* 390 (6), pp. 1557–62.

Bamba, K. (1988). "Evaluation of acrosomal integrity of boar spermatozoa by bright field microscopy using an eosin-nigrosin stain". In: *Theriogenology* 29 (6), pp. 1245–1251.

Bănică, F.-G. (2012). *Chemical Sensors and Biosensors.* Chichester, UK: John Wiley & Sons, Ltd.

Baptista, F. R. et al. (2015). "Recent developments in carbon nanomaterial sensors". In: *Chem. Soc. Rev.* 44 (13), pp. 4433–4453.

Batchelor, G. K. (2000). *An Introduction to Fluid Dynamics.* Cambridge: Cambridge University Press.

Bauman, R. W. (2013). *Microbiology with Diseases by Taxonomy.* 4th Editio. Pearson.

Becker, H. and L. E. Locascio (2002). "Polymer microfluidic devices". In: *Talanta* 56 (2), pp. 267–287.

Becker, H. (2009). "It's the economy..." In: *Lab Chip* 9 (19), pp. 2759–62.

Becker, H. and C. Gärtner (2008). "Polymer microfabrication technologies for microfluidic systems." In: *Anal. Bioanal. Chem.* 390 (1), pp. 89–111.

Beebe, D. J., D. E. Ingber and J. den Toonder (2013). "Organs on Chips 2013". In: *Lab Chip* 13 (18), p. 3447.

Bembnowicz, P. and L. J. Golonka (2010). "Integration of transparent glass window with LTCC technology for μTAS application". In: *J. Eur. Ceram. Soc.* 30 (3), pp. 743–749.

Benito-Lopez, F. et al. (2007). "Substantial rate enhancements of the esterification reaction of phthalic anhydride with methanol at high pressure and using supercritical CO2 as a co-solvent in a glass microreactor". In: *Lab Chip* 7 (10), p. 1345.

Berenguel-Alonso, M. et al. (2017). "Rapid Prototyping of a Cyclic Olefin Copolymer Microfluidic Device for Automated Oocyte Culturing". In: *SLAS Technol.* P. 247263031668462.

Berridge, M. V., P. M. Herst and A. S. Tan (2005). "Tetrazolium dyes as tools in cell biology: New insights into their cellular reduction". In: pp. 127–152.

Berthier, E., J. Warrick, et al. (2008). "Managing evaporation for more robust microscale assays. Part 1. Volume loss in high throughput assays." In: *Lab Chip* 8 (6), pp. 852–9.

Berthier, E., E. W. K. Young and D. Beebe (2012). "Engineers are from PDMS-land, Biologists are from Polystyrenia." In: *Lab Chip* 12 (7), pp. 1224–37.

Beveridge, J. S., J. R. Stephens and M. E. Williams (2011). "The Use of Magnetic Nanoparticles in Analytical Chemistry". In: *Annu. Rev. Anal. Chem.* 4 (1), pp. 251–273.

Bhattacharjee, N. et al. (2016). "The upcoming 3D-printing revolution in microfluidics". In: *Lab Chip* 16 (10), pp. 1720–1742.

Birol, H. (2007). "Fabrication of Low Temperature Co-fired Ceramic (LTCC)-based sensor and microfluidic structures". PhD Thesis. École Polytechnique Fédérale de Lausanne.

Błochowiak, M. (2006). "Structure and properties of norbornene-ethylene copolymers". PhD Thesis. Max Planck Institute for Polymer Research.

Brauman, J. I. (1991). "Room at the Bottom". In: *Science* 254 (5036), pp. 1277–1277.

Cabrera, F. C., A. F. Melo, et al. (2015). "A flexible lab-on-a-chip for the synthesis and magnetic separation of magnetite decorated with gold nanoparticles". In: *Lab Chip*.

Cabrera, F. C., J. C. P. de Souza, et al. (2014). "Natural-rubber-based flexible microfluidic device". In: *RSC Adv.* 4 (67), p. 35467.

Cai, J. et al. (2017). "Rapid prototyping of cyclic olefin copolymer based microfluidic system with CO2 laser ablation". In: *Microsyst. Technol.*

Calvo-López, A., O. Ymbern, D. Izquierdo, et al. (2016). "Low cost and compact analytical microsystem for carbon dioxide determination in production processes of wine and beer". In: *Anal. Chim. Acta* 931, pp. 64–69.

Calvo-López, A., O. Ymbern, M. Puyol, et al. (2015). "Potentiometric analytical microsystem based on the integration of a gas-diffusion step for on-line ammonium determination in water recycling processes in manned space missions". In: *Anal. Chim. Acta* 874, pp. 26–32.

Castillo-León, J. and W. E. Svendsen, eds. (2015). *Lab-on-a-Chip Devices and Micro-Total Analysis Systems*. Cham: Springer International Publishing.

Cate, D. M. et al. (2015). "Recent Developments in Paper-Based Microfluidic Devices". In: *Anal. Chem.* 87 (1), pp. 19–41.

Cayuela, A. et al. (2016). "Semiconductor and carbon-based fluorescent nanodots: the need for consistency". In: *Chem. Commun.* 52 (7), pp. 1311–1326.

Centers for Disease Control and Prevention (2017). *Reports of Selected E. coli Outbreak Investigations*. http://www.cdc.gov/ecoli/outbreaks.html, last accessed March 8th 2017.

Chambers, J. P. et al. (2008). "Biosensor Recognition Elements". In: *Curr. Issues Mol. Biol.* 10 (1-2), pp. 1–12.

Chan, N., J. Lyman, et al. (1999). "Development of an embryo transport and analysis system: Material biocompatablity". In: *Theriogenology* 51 (1), p. 234.

Chan, N., S. Raty, et al. (2001). "Development of Microfabricated Devices for Embryo Production: Embryo Biocompatibility". In: *Theriogenology* 55 (1), pp. 237–535.

Chaplin, M. (2017). *Water Structure and Science - Water phase diagram*. http://www1.lsbu.ac.uk/water/water_phase_diagram.html, last accessed April 3rd 2017.

Chen, L. et al. (1990). "Hyaluronic acid synthesis and gap junction endocytosis are necessary for normal expansion of the cumulus mass". In: *Mol. Reprod. Dev.* 26 (3), pp. 236–247.

Cheng, W. et al. (2010). "One-step synthesis of superparamagnetic monodisperse porous Fe3O4 hollow and core-shell spheres". In: *J. Mater. Chem.* 20 (9), p. 1799.

Chin, C. D., V. Linder and S. K. Sia (2012). "Commercialization of microfluidic point-of-care diagnostic devices". In: *Lab Chip* 12 (12), p. 2118.

Chiu, Y.-J. et al. (2013). "Universally applicable three-dimensional hydrodynamic microfluidic flow focusing". In: *Lab Chip* 13 (9), p. 1803.

Cho, B. S. et al. (2003). "Passively Driven Integrated Microfluidic System for Separation of Motile Sperm". In: *Anal. Chem.* 75 (7), pp. 1671–1675.

Choi, J.-W. et al. (2002). "An integrated microfluidic biochemical detection system for protein analysis with magnetic bead-based sampling capabilities". In: *Lab Chip* 2 (1), p. 27.

Chung, B. G. et al. (2012). "Microfluidic fabrication of microengineered hydrogels and their application in tissue engineering". In: *Lab Chip* 12 (1), pp. 45–59.

Clark, S. G., J. Davis, et al. (2001). "Biocompatibility of porcine sperm cells in polydimethylsioloxane (PDMS)". In: *Theriogenology* 55 (1), p. 421.

Clark, S. G., K. Haubert, et al. (2005). "Reduction of polyspermic penetration using biomimetic microfluidic technology during in vitro fertilization." In: *Lab Chip* 5 (11), pp. 1229–32.

Clifford, D. M. et al. (2014). "Room Temperature Synthesis of Highly Magnetic Cobalt Nanoparticles by Continuous Flow in a Microfluidic Reactor". In: *J. Flow Chem.* 4 (3), pp. 148–152.

Clift, D. and M. Schuh (2013). "Restarting life: fertilization and the transition from meiosis to mitosis". In: *Nat. Rev. Mol. Cell Biol.* 14 (9), pp. 549–562.

Combelles, C. (2002). "Assessment of nuclear and cytoplasmic maturation in in-vitro matured human oocytes". In: *Hum. Reprod.* 17 (4), pp. 1006–1016.

Cooke, S. and S. D. Fleming (2009). *Textbook of Assisted Reproduction for Scientists in Reproductive Technology.* Vivid Publishing.

Couceiro, P. (2016). "Microfabrication processes based on low temperature co-fired ceramics technology for the fabrication of a microfluidic free flow electrophoresis device". PhD thesis. Universitat Autònoma de Barcelona.

Couceiro, P., S. Gómez-de Pedro and J. Alonso-Chamarro (2015). "All-ceramic analytical microsystems with monolithically integrated optical detection microflow cells". In: *Microfluid. Nanofluidics* 18 (4), pp. 649–656.

Crosby, G. A. and J. N. Demas (1971). "Measurement of photoluminescence quantum yields. Review". In: *J. Phys. Chem.* 75 (8), pp. 991–1024.

Cullity, B. D. and C. D. Graham (2011). *Introduction to Magnetic Materials.* Wiley.

Damiani, P. et al. (1996). "Evaluation of developmental competence, nuclear and ooplasmic maturation of calf oocytes". In: *Mol. Reprod. Dev.* 45 (4), pp. 521–534.

De Las Cuevas, G., J. Faraudo and J. Camacho (2008). "Low-Gradient Magnetophoresis through Field-Induced Reversible Aggregation". In: *J. Phys. Chem. C* 112 (4), pp. 945–950.

DeMello, A. J. (2006). "Control and detection of chemical reactions in microfluidic systems". In: *Nature* 442 (7101), pp. 394–402.

Dittrich, P. S. and A. Manz (2006). "Lab-on-a-chip: microfluidics in drug discovery". In: *Nat. Rev. Drug Discov.* 5 (3), pp. 210–218.

Dong, Y. et al. (2012). "Blue luminescent graphene quantum dots and graphene oxide prepared by tuning the carbonization degree of citric acid". In: *Carbon N. Y.* 50 (12), pp. 4738–4743.

Drexler, K. E. (1986). *Engines of Creation.* Science, technical. Anchor Press/-Doubleday.

Drummen, G. P. (2010). "Quantum Dots—From Synthesis to Applications in Biomedicine and Life Sciences". In: *Int. J. Mol. Sci.* 11 (1), pp. 154–163.

Duffy, D. C. et al. (1998). "Rapid Prototyping of Microfluidic Systems in Poly(dimethylsiloxane)". In: *Anal. Chem.* 70 (23), pp. 4974–4984.

Eddings, M. A., M. A. Johnson and B. K. Gale (2008). "Determining the optimal PDMS–PDMS bonding technique for microfluidic devices". In: *J. Micromechanics Microengineering* 18 (6), p. 067001.

Eigler, D. M. and E. K. Schweizer (1990). "Positioning single atoms with a scanning tunnelling microscope". In: *Nature* 344 (6266), pp. 524–526.

Elvira, K. S. et al. (2013). "The past, present and potential for microfluidic reactor technology in chemical synthesis". In: *Nat. Chem.* 5 (11), pp. 905–915.

Erdem, E. Y. et al. (2014). "Multi-temperature zone, droplet-based microreactor for increased temperature control in nanoparticle synthesis". In: *Small* 10, pp. 1076–1080.

Esteves, T. C. et al. (2013). "A microfluidic system supports single mouse embryo culture leading to full-term development". In: *RSC Adv.* 3 (48), p. 26451.

Eustis, S. and M. A. El-Sayed (2006). "Why gold nanoparticles are more precious than pretty gold: Noble metal surface plasmon resonance and its enhancement of the radiative and nonradiative properties of nanocrystals of different shapes". In: *Chem. Soc. Rev.* 35 (3), pp. 209–217.

Faraudo, J., J. S. Andreu and J. Camacho (2013). "Understanding diluted dispersions of superparamagnetic particles under strong magnetic fields: a review of concepts, theory and simulations". In: *Soft Matter* 9 (29), p. 6654.

Faustini, M. et al. (2013). "Microfluidic approach toward continuous and ultrafast synthesis of metal-organic framework crystals and hetero structures in confined microdroplets". In: *J. Am. Chem. Soc.* 135, pp. 14619–14626.

Feng, P. (1995). "Escherichia coli serotype O157:H7: novel vehicles of infection and emergence of phenotypic variants." eng. In: *Emerg. Infect. Dis.* 1 (2), pp. 47–52.

Feynman, R. P. (1960). "There's Plenty of Room at the Bottom". In: *Eng. Sci.* 23 (5), pp. 22–36.

FitzHarris, G. (2006). "Granulosa cells regulate intracellular pH of the murine growing oocyte via gap junctions: development of independent homeostasis during oocyte growth". In: *Development* 133 (4), pp. 591–599.

Folch, A. (2012). *Introduction to BioMEMS*. Boca Raton: CRC Press, p. 528.

— (2017). *Folch Lab Gallery*.

Fonnum, G. et al. (2005). "Characterisation of Dynabeads® by magnetization measurements and Mössbauer spectroscopy". In: *J. Magn. Magn. Mater.* 293 (1), pp. 41–47.

Frenz, L. et al. (2008). "Droplet-based microreactors for the synthesis of magnetic iron oxide nanoparticles." In: *Angew. Chem. Int. Ed. Engl.* 47 (36), pp. 6817–20.

Fu, C. and N. M. Ravindra (2012). "Magnetic iron oxide nanoparticles: synthesis and applications". In: *Bioinspired, Biomim. Nanobiomaterials* 1 (4), pp. 229–244.

Gattass, R. R. and E. Mazur (2008). "Femtosecond laser micromachining in transparent materials". In: *Nat. Photonics* 2 (4), pp. 219–225.

Geckil, H. et al. (2010). "Engineering hydrogels as extracellular matrix mimics". In: *Nanomedicine* 5 (3), pp. 469–484.

Gehring, A. G. and S.-I. Tu (2011). "High-Throughput Biosensors for Multiplexed Food-Borne Pathogen Detection". In: *Annu. Rev. Anal. Chem.* 4 (1), pp. 151–172.

Ghaemmaghami, A. M. et al. (2012). "Biomimetic tissues on a chip for drug discovery". In: *Drug Discov. Today* 17 (3-4), pp. 173–181.

Gijs, M. (2004). "Magnetic bead handling on-chip: new opportunities for analytical applications". In: *Microfluid. Nanofluidics*, pp. 22–40.

Gijs, M., F. Lacharme and U. Lehmann (2010). "Microfluidic Applications of Magnetic Particles for Biological Analysis and Catalysis". In: *Chem. Rev.* 110 (3), pp. 1518–1563.

Goddard, J. M. and D. Erickson (2009). "Bioconjugation techniques for microfluidic biosensors". In: *Anal. Bioanal. Chem.* 394 (2), pp. 469–479.

Gómez-de Pedro, S., M. Berenguel-Alonso, et al. (2017). "Automatic microfluidic system to perform multi-step magneto-biochemical assays". In: *Sensors Actuators B Chem.* 245, pp. 477–483.

Gómez-de Pedro, S., A. Salinas-Castillo, et al. (2014). "Microsystem-assisted synthesis of carbon dots with fluorescent and colorimetric properties for pH detection." In: *Nanoscale* 6 (11), pp. 6018–24.

Gómez-de Pedro, S. (2014). "(Bio)Analytical microsystems based on the use of nanoparticles." PhD thesis. Universitat Autònoma de Barcelona.

Gómez-de Pedro, S., C. S. Martínez-Cisneros, et al. (2012). "Microreactor with integrated temperature control for the synthesis of CdSe nanocrystals". In: *Lab Chip* 12 (11), p. 1979.

Gómez-de Pedro, S., M. Puyol and J. Alonso-Chamarro (2010). "Continuous flow synthesis of nanoparticles using ceramic microfluidic devices". In: *Nanotechnology* 21 (41), p. 415603.

Gómez-de Pedro, S., M. Puyol, D. Izquierdo, et al. (2012). "A ceramic microreactor for the synthesis of water soluble CdS and CdS/ZnS nanocrystals with on-line optical characterization". In: *Nanoscale* 4 (4), p. 1328.

Gongora-Rubio, M. et al. (2001). "Overview of low temperature co-fired ceramics tape technology for meso-system technology (MsST)". In: *Sensors Actuators A Phys.* 89 (3), pp. 222–241.

Gorski, C. A. and M. M. Scherer (2010). "Determination of nanoparticulate magnetite stoichiometry by Mossbauer spectroscopy, acidic dissolution, and powder X-ray diffraction: A critical review". In: *Am. Mineral.* 95 (7), pp. 1017–1026.

Guckenberger, D. J. et al. (2015). "Micromilling: A method for ultra-rapid prototyping of plastic microfluidic devices". In: *Lab Chip.*

Guo, M. T. et al. (2012). "Droplet microfluidics for high-throughput biological assays". In: *Lab Chip* 12 (12), p. 2146.

Gutnisky, C. et al. (2007). "Influence of hyaluronic acid synthesis and cumulus mucification on bovine oocyte in vitro maturation, fertilisation and embryo development". In: *Reprod. Fertil. Dev.* 19 (3), p. 488.

Ha, B. H. et al. (2014). "Three-dimensional hydrodynamic flow and particle focusing using four vortices Dean flow". In: *Microfluid. Nanofluidics* 17 (4), pp. 647–655.

Haavik, C. et al. (2000). "Equation of state of magnetite and its high pressure modification: Thermodynamics of the Fe-O system at high pressure". In: *Am. Mineral.* 85 (3-4), pp. 514–523.

Hamedi, M. M. et al. (2016). "Integrating Electronics and Microfluidics on Paper". In: *Adv. Mater.* 28 (25), pp. 5054–5063.

Han, C. et al. (2010). "Integration of single oocyte trapping, in vitro fertilization and embryo culture in a microwell-structured microfluidic device." In: *Lab Chip* 10 (21), pp. 2848–54.

Harrison, D. J. et al. (1993). "Micromachining a Miniaturized Capillary Electrophoresis-Based Chemical Analysis System on a Chip". In: *Science* 261 (5123), pp. 895–897.

Hartman, R. L. and K. F. Jensen (2009). "Microchemical systems for continuous-flow synthesis." In: *Lab Chip* 9 (17), pp. 2495–507.

Heckele, M. and W. K. Schomburg (2004). "Review on micro molding of thermoplastic polymers". In: *J. Micromechanics Microengineering* 14 (3), R1–R14.

Herrmann, M., T. Veres and M. Tabrizian (2006). "Enzymatically-generated fluorescent detection in micro-channels with internal magnetic mixing for the development of parallel microfluidic ELISA". In: *Lab Chip* 6 (4), p. 555.

Herrmann, M., E. Roy, et al. (2007). "Microfluidic ELISA on non-passivated PDMS chip using magnetic bead transfer inside dual networks of channels". In: *Lab Chip* 7 (11), p. 1546.

Herrmann, M., T. Veres and M. Tabrizian (2008). "Quantification of Low-Picomolar Concentrations of TNF-α in Serum Using the Dual-Network Microfluidic ELISA Platform". In: *Anal. Chem.* 80 (13), pp. 5160–5167.

Hester, P. et al. (2002). "Enhanced cleavage rates following in vitro maturation of pig oocytes within polydimethylsiloxane-borosilicate microchannels". In: *Theriogenology* 57 (1), p. 723.

Hu, Y. et al. (2015). "How do nitrogen-doped carbon dots generate from molecular precursors? An investigation of the formation mechanism and a solution-based large-scale synthesis". In: *J. Mater. Chem. B* 3 (27), pp. 5608–5614.

Huang, G. Y. et al. (2011). "Microfluidic hydrogels for tissue engineering". In: *Biofabrication* 3 (1), p. 012001.

Huh, D. et al. (2012). "Microengineered physiological biomimicry: Organs-on-Chips". In: *Lab Chip* 12 (12), p. 2156.

Ibáñez-García, N. et al. (2008). "Green-tape ceramics. New technological approach for integrating electronics and fluidics in microsystems". In: *TrAC Trends Anal. Chem.* 27 (1), pp. 24–33.

Iglesia, O. de la et al. (2007). "Preparation of Pt/ZSM-5 films on stainless steel microreactors". In: *Catal. Today* 125 (1-2), pp. 2–10.

Iliescu, C. et al. (2012). "A practical guide for the fabrication of microfluidic devices using glass and silicon". In: *Biomicrofluidics* 6 (1), p. 016505.

Ito, A., H. Honda and T. Kobayashi (2006). "Cancer immunotherapy based on intracellular hyperthermia using magnetite nanoparticles: a novel concept of "heat-controlled necrosis" with heat shock protein expression". In: *Cancer Immunol. Immunother.* 55 (3), pp. 320–328.

Jena, R. K., C. Y. Yue and Y. C. Lam (2012). "Micro fabrication of cyclic olefin copolymer (COC) based microfluidic devices". In: *Microsyst. Technol.* 18 (2), pp. 159–166.

Jena, R., C. Yue and L. Anand (2011). "Improvement of thermal bond strength and surface properties of Cyclic Olefin Copolymer (COC) based microfluidic device using the photo-grafting technique". In: *Sensors Actuators B Chem.* 157 (2), pp. 518–526.

Jeon, J. S. et al. (2011). "Hot embossing for fabrication of a microfluidic 3D cell culture platform". In: *Biomed. Microdevices* 13 (2), pp. 325–333.

Jiang, B., J. Haber, et al. (2015). "Fine structuration of low-temperature co-fired ceramic (LTCC) microreactors". In: *Lab Chip* 15 (2), pp. 563–574.

Jiang, B., T. Maeder, et al. (2015). "A low-temperature co-fired ceramic micro-reactor system for high-efficiency on-site hydrogen production". In: *J. Power Sources* 273, pp. 1202–1217.

Jin, R. et al. (2014). "Superparamagnetic iron oxide nanoparticles for MR imaging and therapy: design considerations and clinical applications". In: *Curr. Opin. Pharmacol.* 18, pp. 18–27.

Kane, R. S. et al. (1999). "Patterning proteins and cells using soft lithography". In: *Biomaterials* 20 (23-24), pp. 2363–2376.

Karaagac, O. et al. (2010). "A Simple Way to Synthesize Superparamagnetic Iron Oxide Nanoparticles in Air Atmosphere: Iron Ion Concentration Effect". In: *IEEE Trans. Magn.* 46 (12), pp. 3978–3983.

Karle, M. et al. (2010). "Continuous microfluidic DNA extraction using phase-transfer magnetophoresis". In: *Lab Chip* 10 (23), p. 3284.

Karthick, B. and R. Maheshwari (2008). "Lotus-inspired nanotechnology applications". In: *Resonance* 13 (12), pp. 1141–1145.

Keene, W. E. et al. (1994). "A Swimming-Associated Outbreak of Hemorrhagic Colitis Caused by Escherichia coli O157:H7 and Shigella Sonnei". In: *N. Engl. J. Med.* 331 (9), pp. 579–584.

Kemp, S. J. et al. (2016). "Monodisperse magnetite nanoparticles with nearly ideal saturation magnetization". In: *RSC Adv.* 6 (81), pp. 77452–77464.

Kim, D. and A. E. Herr (2013). "Protein immobilization techniques for microfluidic assays". In: *Biomicrofluidics* 7 (4), p. 041501.

Kim, D. S. et al. (2007). "Collapse-free thermal bonding technique for large area microchambers in plastic lab-on-a-chip applications". In: *Microsyst. Technol.* 14 (2), pp. 179–184.

Kim, J.-O. et al. (2014). "A monolithic and flexible fluoropolymer film microreactor for organic synthesis applications". In: *Lab Chip* 14 (21), pp. 4270–4276.

Kim, M. S. et al. (2009). "A microfluidic in vitro cultivation system for mechanical stimulation of bovine embryos." In: *Electrophoresis* 30 (18), pp. 3276–82.

Kim, W. et al. (2012). "A new method for the identification and quantification of magnetite–maghemite mixture using conventional X-ray diffraction technique". In: *Talanta* 94, pp. 348–352.

Kovarik, M. L. et al. (2013). "Micro Total Analysis Systems: Fundamental Advances and Applications in the Laboratory, Clinic, and Field". In: *Anal. Chem.* 85 (2), pp. 451–472.

Kuhn, S. et al. (2011). "Teflon-Coated Silicon Microreactors. Impact on Segmented Liquid-Liquid Multiphase Flows". In: *Langmuir* 27 (10), pp. 6519–6527.

Kumar, K. et al. (2012). "Direct synthesis of dextran-coated superparamagnetic iron oxide nanoparticles in a capillary-based droplet reactor". In: *J. Mater. Chem.* 22 (11), p. 4704.

Kuo, J. S. and D. T. Chiu (2011). "Disposable microfluidic substrates: Transitioning from the research laboratory into the clinic". In: *Lab Chip* 11 (16), p. 2656.

Laczka, O. et al. (2011). "Improved bacteria detection by coupling magneto-immunocapture and amperometry at flow-channel microband electrodes". In: *Biosens. Bioelectron.* 26 (8), pp. 3633–3640.

Lai, J. J. et al. (2009). "Dynamic bioprocessing and microfluidic transport control with smart magnetic nanoparticles in laminar-flow devices." In: *Lab Chip* 9 (14), pp. 1997–2002.

LaMer, V. K. and R. H. Dinegar (1950). "Theory, Production and Mechanism of Formation of Monodispersed Hydrosols". In: *J. Am. Chem. Soc.* 72 (11), pp. 4847–4854.

Larrea, A. et al. (2015). "Gas Slug Microfluidics: A Unique Tool for Ultrafast, Highly Controlled Growth of Iron Oxide Nanostructures". In: *Chem. Mater.* 27 (12), pp. 4254–4260.

Laurent, S., S. Dutz, et al. (2011). "Magnetic fluid hyperthermia: Focus on superparamagnetic iron oxide nanoparticles". In: *Adv. Colloid Interface Sci.* 166 (1-2), pp. 8–23.

Laurent, S., D. Forge, et al. (2008). "Magnetic Iron Oxide Nanoparticles: Synthesis, Stabilization, Vectorization, Physicochemical Characterizations, and Biological Applications". In: *Chem. Rev.* 108 (6), pp. 2064–2110.

Lee, W. et al. (2014). "Ultra-rapid Detection of Pathogenic Bacteria Using a 3D Immunomagnetic Flow Assay." In: *Anal. Chem.*

Li, H. et al. (2012). "Carbon nanodots: synthesis, properties and applications". In: *J. Mater. Chem.* 22 (46), p. 24230.

Li, L. et al. (2013). "Superparamagnetic Iron Oxide Nanoparticles as MRI contrast agents for Non-invasive Stem Cell Labeling and Tracking". In: *Theranostics* 3 (8), pp. 595–615.

Li, X., D. R. Ballerini and W. Shen (2012). "A perspective on paper-based microfluidics: Current status and future trends". In: *Biomicrofluidics* 6 (1), p. 011301.

Liébana, S. et al. (2009). "Rapid detection of Salmonella in milk by electrochemical magneto-immunosensing." In: *Biosens. Bioelectron.* 25 (2), pp. 510–3.

Ligler, F. S. and H. S. White (2013). "Nanomaterials in Analytical Chemistry". In: *Anal. Chem.* 85 (23), pp. 11161–11162.

142

Lignos, I. et al. (2015). "Millisecond-Timescale Monitoring of PbS Nanoparticle Nucleation and Growth Using Droplet-Based Microfluidics". In: *Small* 11 (32), pp. 4009–4017.

Lim, S. Y., W. Shen and Z. Gao (2015). "Carbon quantum dots and their applications". In: *Chem. Soc. Rev.* 44 (1), pp. 362–381.

Liu, J. et al. (2009). "Highly Water-Dispersible Biocompatible Magnetite Particles with Low Cytotoxicity Stabilized by Citrate Groups". In: *Angew. Chemie Int. Ed.* 48 (32), pp. 5875–5879.

Lopez-Ruiz, N. et al. (2014). "Smartphone-Based Simultaneous pH and Nitrite Colorimetric Determination for Paper Microfluidic Devices". In: *Anal. Chem.* 86 (19), pp. 9554–9562.

Lu, A.-H., E. L. Salabas and F. Schüth (2007). "Magnetic nanoparticles: synthesis, protection, functionalization, and application." In: *Angew. Chem. Int. Ed. Engl.* 46 (8), pp. 1222–44.

Lu, J. et al. (2011). "Transforming C60 molecules into graphene quantum dots". In: *Nat. Nanotechnol.* 6 (4), pp. 247–252.

Lu, Y., L. Zhang and H. Lin (2014). "The Use of a Microreactor for Rapid Screening of the Reaction Conditions and Investigation of the Photoluminescence Mechanism of Carbon Dots". In: *Chem. - A Eur. J.* 20 (15), pp. 4246–4250.

Luo, X.-J. et al. (2004). "Effects of organic additives and glass on the properties of AlN/glass tape-casting slurries and green tapes". In: *J. Mater. Sci.* 39 (13), pp. 4387–4389.

Luo, Z. et al. (2015). "Deformation of a single mouse oocyte in a constricted microfluidic channel". In: *Microfluid. Nanofluidics* 19 (4), pp. 883–890.

Ma, R. et al. (2011). "In vitro fertilization on a single-oocyte positioning system integrated with motile sperm selection and early embryo development." In: *Anal. Chem.* 83 (8), pp. 2964–70.

Madou, M. J. (2002). *Fundamentals of Microfabrication: The Science of Miniaturization.* 2nd Editio. Taylor & Francis.

Madras, G. and B. J. McCoy (2004). "Temperature effects on the transition from nucleation and growth to Ostwald ripening". In: *Chem. Eng. Sci.* 59 (13), pp. 2753–2765.

Majewski, P. and B. Thierry (2008). "Functionalized Magnetite Nanoparticles. Synthesis, Properties, and Bioapplications". In: *Part. Syst. Nano- Biotechnol.* CRC Press, pp. 331–352.

Makgwane, P. R. and S. S. Ray (2014). "Synthesis of Nanomaterials by Continuous-Flow Microfluidics: A Review". In: *J. Nanosci. Nanotechnol.* 14 (2), pp. 1338–1363.

Malecha, K. (2016). "The utilization of LTCC-PDMS bonding technology for microfluidic system applications – a simple fluorescent sensor". In: *Microelectron. Int.* 33 (3), pp. 141–148.

Malecha, K., I. Gancarz and W. Tylus (2010). "Argon plasma-assisted PDMS–LTCC bonding technique for microsystem applications". In: *J. Micromechanics Microengineering* 20 (11), p. 115006.

Manz, A., N. Graber and H. Widmer (1990). "Miniaturized total chemical analysis systems: A novel concept for chemical sensing". In: *Sensors Actuators B Chem.* 1 (1-6), pp. 244–248.

Mao, X., J. R. Waldeisen and T. J. Huang (2007). ""Microfluidic drifting"– implementing three-dimensional hydrodynamic focusing with a single-layer planar microfluidic device." In: *Lab Chip* 7 (10), pp. 1260–1262.

Mark, D. et al. (2010). "Microfluidic lab-on-a-chip platforms: requirements, characteristics and applications." In: *Chem. Soc. Rev.* 39 (3), pp. 1153–82.

Marre, S. and K. F. Jensen (2010). "Synthesis of micro and nanostructures in microfluidic systems." In: *Chem. Soc. Rev.* 39 (3), pp. 1183–202.

Marre, S., J. Park, et al. (2008). "Supercritical Continuous-Microflow Synthesis of Narrow Size Distribution Quantum Dots". In: *Adv. Mater.* 20 (24), pp. 4830–4834.

Martinez, A. W. et al. (2010). "Diagnostics for the Developing World: Microfluidic Paper-Based Analytical Devices". In: *Anal. Chem.* 82 (1), pp. 3–10.

Martínez-Cisneros, C. S., S. G.-d. Pedro, et al. (2012). "Design, fabrication and characterization of microreactors for high temperature syntheses". In: *Chem. Eng. J.* 211-212, pp. 432–441.

Martínez-Cisneros, C. S., Z. da Rocha, et al. (2009). "A Monolithic Continuous-Flow Microanalyzer with Amperometric Detection Based on the Green Tape Technology". In: *Anal. Chem.* 81 (17), pp. 7448–7453.

Massart, R. and V. Cabouil (1987). "Effect of some parameters on the formation of colloidal magnetite in alkaline medium. Yield and particle-size control." In: *J. Chim. Phys. Physico-Chimie Biol.* 84, pp. 967–973.

Medina-Sánchez, M., S. Miserere and A. Merkoçi (2012). "Nanomaterials and lab-on-a-chip technologies". In: *Lab Chip* 12 (11), p. 1932.

Mehling, M. and S. Tay (2014). "Microfluidic cell culture". In: *Curr. Opin. Biotechnol.* 25, pp. 95–102.

Michalet, X. (2005). "Quantum Dots for Live Cells, in Vivo Imaging, and Diagnostics". In: *Science* 307 (5709), pp. 538–544.

Midwoud, P. M. van et al. (2012). "Comparison of Biocompatibility and Adsorption Properties of Different Plastics for Advanced Microfluidic Cell and Tissue Culture Models". In: *Anal. Chem.* 84 (9), pp. 3938–3944.

Miralles, V. et al. (2013). "A Review of Heating and Temperature Control in Microfluidic Systems: Techniques and Applications". In: *Diagnostics* 3 (1), pp. 33–67.

Miserere, S. et al. (2012). "Fabrication of thermoplastics chips through lamination based techniques". In: *Lab Chip* 12 (10), p. 1849.

Moore, G. E. (1965). "Cramming more components onto integrated circuits (Reprinted from Electronics, pg 114-117, April 19, 1965)". In: *Proc. Ieee* 86 (1), pp. 82–85.

Moskowitz, B. M. (1991). *Hitchhiker's Guide to Magnetism*. Tech. rep.

Mukhopadhyay, R. (2007). "When PDMS isn't the best". In: *Anal. Chem.* 79 (9), pp. 3248–3253.

National Nanotechnology Innitiative (2017). *What is Nanotechnology?* https://www.nano.gov/nanotech-101/what/definition, last accessed April 16th 2017.

Nguyen, T.-D. and T.-O. Do (2011). "Size- and Shape-Controlled Synthesis of Monodisperse Metal Oxide and Mixed Oxide Nanocrystals". In: *Nanocrystal*. Ed. by Y. Masuda. InTech.

Nigam, S., K. Barick and D. Bahadur (2011). "Development of citrate-stabilized Fe3O4 nanoparticles: Conjugation and release of doxorubicin for therapeutic applications". In: *J. Magn. Magn. Mater.* 323 (2), pp. 237–243.

Nightingale, A. M. and J. C. Demello (2013). *Segmented flow reactors for nanocrystal synthesis.*

Nunes, P. S. et al. (2010). "Cyclic olefin polymers: emerging materials for lab-on-a-chip applications". In: *Microfluid. Nanofluidics* 9 (2), pp. 145–161.

Ortiz-Gomez, I. et al. (2016). "Tetrazine-based chemistry for nitrite determination in a paper microfluidic device". In: *Talanta* 160, pp. 721–728.

Pankhurst, Q. A. et al. (2003). "Applications of magnetic nanoparticles in biomedicine". In: *J. Phys. D. Appl. Phys.* 36 (13), R167–R181.

Pennathur, S. (2008). "Flow control in microfluidics: are the workhorse flows adequate?" In: *Lab Chip* 8 (3), p. 383.

Perez-Toralla, K. et al. (2013). "New non-covalent strategies for stable surface treatment of thermoplastic chips." In: *Lab Chip* 13 (22), pp. 4409–18.

Perl, A., D. N. Reinhoudt and J. Huskens (2009). "Microcontact Printing: Limitations and Achievements". In: *Adv. Mater.* 21 (22), pp. 2257–2268.

Peyman, S. A., A. Iles and N. Pamme (2009). "Mobile magnetic particles as solid-supports for rapid surface-based bioanalysis in continuous flow". In: *Lab Chip* 9 (21), p. 3110.

Philippova, O. et al. (2011). "Magnetic polymer beads: Recent trends and developments in synthetic design and applications". In: *Eur. Polym. J.* 47 (4), pp. 542–559.

Phillips, K. P. (2002). "The Intracellular pH-regulatory HCO3-/Cl- Exchanger in the Mouse Oocyte Is Inactivated during First Meiotic Metaphase and Reactivated after Egg Activation via the MAP Kinase Pathway". In: *Mol. Biol. Cell* 13 (11), pp. 3800–3810.

Phillips, T. W. et al. (2014). "Nanocrystal synthesis in microfluidic reactors: where next?" In: *Lab Chip.*

Pinyopummintr, T. and B. Bavister (1995). "Optimum gas atmosphere for in vitro maturation and in vitro fertilization of bovine oocytes". In: *Theriogenology* 44 (4), pp. 471–477.

Pipper, J. et al. (2007). "Catching bird flu in a droplet". In: *Nat. Med.* 13 (10), pp. 1259–1263.

Puigmartí-Luis, J. (2014). "Microfluidic platforms: a mainstream technology for the preparation of crystals." In: *Chem. Soc. Rev.* 43, pp. 2253–71.

Pumera, M. (2011). "Nanomaterials meet microfluidics". In: *Chem. Commun.* 47 (20), p. 5671.

Qin, D., Y. Xia and G. M. Whitesides (2010). "Soft lithography for micro- and nanoscale patterning". In: *Nat. Protoc.* 5 (3), pp. 491–502.

Ramadan, Q. and M. Gijs (2011). "Simultaneous sample washing and concentration using a "trapping-and-releasing" mechanism of magnetic beads on a microfluidic chip". In: *Analyst* 136 (6), p. 1157.

Reenen, A. van et al. (2014). "Integrated lab-on-chip biosensing systems based on magnetic particle actuation – a comprehensive review". In: *Lab Chip* 14 (12), p. 1966.

Regehr, K. J. et al. (2009). "Biological implications of polydimethylsiloxane-based microfluidic cell culture." In: *Lab Chip* 9 (15), pp. 2132–9.

Ren, K., J. Zhou and H. Wu (2013). "Materials for Microfluidic Chip Fabrication". In: *Acc. Chem. Res.* 46 (11), pp. 2396–2406.

Rhee, M. et al. (2011). "Synthesis of Size-Tunable Polymeric Nanoparticles Enabled by 3D Hydrodynamic Flow Focusing in Single-Layer Microchannels". In: *Adv. Mater.* 23 (12), H79–H83.

Rigat-Brugarolas, L. G. et al. (2014). "A functional microengineered model of the human splenon-on-a-chip". In: *Lab Chip* 14 (10), p. 1715.

Rizos, D. et al. (2001). "Effect of culture system on the yield and quality of bovine blastocysts as assessed by survival after vitrification". In: *Theriogenology* 56 (1), pp. 1–16.

Rodriguez-Martinez, H. (2012). "Assisted Reproductive Techniques for Cattle Breeding in Developing Countries: A Critical Appraisal of Their Value and Limitations". In: *Reprod. Domest. Anim.* 47 (SUPPL. 1), pp. 21–26.

Sabourin, D. et al. (2010). "Microfluidic DNA microarrays in PMMA chips: streamlined fabrication via simultaneous DNA immobilization and bonding activation by brief UV exposure". In: *Biomed. Microdevices* 12 (4), pp. 673–681.

Sackmann, E. K., A. L. Fulton and D. J. Beebe (2014). "The present and future role of microfluidics in biomedical research." In: *Nature* 507 (7491), pp. 181–9.

Salazar-Alvarez, G., M. Muhammed and A. A. Zagorodni (2006). "Novel flow injection synthesis of iron oxide nanoparticles with narrow size distribution". In: *Chem. Eng. Sci.* 61 (14), pp. 4625–4633.

Sasso, L. A. et al. (2012). "Automated microfluidic processing platform for multiplexed magnetic bead immunoassays". English. In: *Microfluid. Nanofluidics* 13 (4), pp. 603–612.

Saville, S. L. et al. (2013). "The effect of magnetically induced linear aggregates on proton transverse relaxation rates of aqueous suspensions of polymer coated magnetic nanoparticles". In: *Nanoscale* 5 (5), pp. 2152–2163.

Schneider, J. et al. (2017). "Molecular Fluorescence in Citric Acid-Based Carbon Dots". In: *J. Phys. Chem. C* 121 (3), pp. 2014–2022.

Sebastian Cabeza, V. et al. (2012). "Size-Controlled Flow Synthesis of Gold Nanoparticles Using a Segmented Flow Microfluidic Platform". In: *Langmuir* 28 (17), pp. 7007–7013.

Sen, A., T. Harvey and J. Clausen (2011). "A microsystem for extraction, capture and detection of E-Coli O157:H7". In: *Biomed. Microdevices* 13 (4), pp. 705–715.

Shikida, M. et al. (2006). "Development of an enzymatic reaction device using magnetic bead-cluster handling". In: *J. Micromechanics Microengineering* 16 (9), pp. 1875–1883.

Shin, J. Y. et al. (2005). "Chemical structure and physical properties of cyclic olefin copolymers (IUPAC Technical Report)". In: *Pure Appl. Chem.* 77 (5).

Siegel, J. et al. (2011). "Properties of gold nanostructures sputtered on glass". In: *Nanoscale Res. Lett.* 6 (1), p. 96.

Simmons, M. et al. (2013). "The Preparation of Magnetic Iron Oxide Nanoparticles in Microreactors". In: *J. Flow Chem.* 3 (1), pp. 7–10.

Sista, R. S. et al. (2008). "Heterogeneous immunoassays using magnetic beads on a digital microfluidic platform". In: *Lab Chip* 8 (12), p. 2188.

Sollier, E. et al. (2011). "Rapid prototyping polymers for microfluidic devices and high pressure injections." In: *Lab Chip* 11 (22), pp. 3752–65.

Song, Y. et al. (2015). "Investigation from chemical structure to photoluminescent mechanism: a type of carbon dots from the pyrolysis of citric acid and an amine". In: *J. Mater. Chem. C* 3 (23), pp. 5976–5984.

Sperling, R. A. and W. J. Parak (2010). "Surface modification, functionalization and bioconjugation of colloidal inorganic nanoparticles". In: *Philos. Trans. R. Soc. A Math. Phys. Eng. Sci.* 368 (1915), pp. 1333–1383.

Stankiewicz, A. I. and J. A. Moulijn (2000). "Process intensification: Transforming chemical engineering". In: *Chem. Eng. Prog.* 96 (1), pp. 22–34.

Steigert, J. et al. (2007). "Rapid prototyping of microfluidic chips in COC". In: *J. Micromechanics Microengineering* 17 (2), pp. 333–341.

Stone, H. A. (2007). "Introduction to Fluid Dynamics for Microfluidic Flows". In: *C. Biotechnol.* Ed. by H. Lee, R. M. Westervelt and D. Ham. Boston, MA: Springer US, pp. 5–30.

Strnad, Z. (1986). *Glass-ceramic Materials: Liquid Phase Separation, Nucle-ation, and Crystallization in Glasses.* Amsterdam: Elsevier.

Suarez, W. T. et al. (2010). "A compact miniaturized continuous flow system for the determination of urea content in milk". In: *Anal. Bioanal. Chem.* 398 (3), pp. 1525–1533.

Suh, R. S. et al. (2006). "IVF within microfluidic channels requires lower total numbers and lower concentrations of sperm." In: *Hum. Reprod.* 21 (2), pp. 477–83.

Swain, J. E., D. Lai, et al. (2013). "Thinking big by thinking small: application of microfluidic technology to improve ART." In: *Lab Chip* 13 (7), pp. 1213–24.

Swain, J. E. and G. D. Smith (2011). "Advances in embryo culture platforms: novel approaches to improve preimplantation embryo development through modifications of the microenvironment." In: *Hum. Reprod. Update* 17 (4), pp. 541–57.

Tarn, M. D. (2011). "Continuous Flow Processes on Single Magnetic and Dia-magnetic Particles in Microfluidic Devices". PhD thesis. University of Hull.

Tartaj, P. et al. (2006). "Synthesis, Properties and Biomedical Applications of Magnetic Nanoparticles". In: pp. 403–482.

Temiz, Y. et al. (2015). "Lab-on-a-chip devices: How to close and plug the lab?" In: *Microelectron. Eng.* 132, pp. 156–175.

Terry, S., J. Jerman and J. Angell (1979). "A gas chromatographic air analyzer fabricated on a silicon wafer". In: *IEEE Trans. Electron Devices* 26 (12), pp. 1880–1886.

Toepke, M. W. and D. J. Beebe (2006). "PDMS absorption of small molecules and consequences in microfluidic applications". In: *Lab Chip* 6 (12), p. 1484.

Toumey, C. (2009). "Plenty of room, plenty of history". In: *Nat. Nanotechnol.* 4 (12), pp. 783–784.

Trachsel, F., C. Hutter and P. Von Rohr (2008). "Transparent silicon/glass microreactor for high-pressure and high-temperature reactions". In: *Chem. Eng. J.* 135, S309–S316.

Tsao, C.-W. (2016). "Polymer Microfluidics: Simple, Low-Cost Fabrication Process Bridging Academic Lab Research to Commercialized Production". In: *Micromachines* 7 (12), p. 225.

Tsao, C.-W. and D. L. DeVoe (2009). "Bonding of thermoplastic polymer microfluidics". In: *Microfluid. Nanofluidics* 6 (1), pp. 1–16.

Unger, M. A. et al. (2000). "Monolithic Microfabricated Valves and Pumps by Multilayer Soft Lithography". In: *Science* 288 (5463), pp. 113–116.

Vasudev, A. et al. (2013). "Prospects of low temperature co-fired ceramic (LTCC) based microfluidic systems for point-of-care biosensing and envi-ronmental sensing". In: *Microfluid. Nanofluidics* 14 (3-4), pp. 683–702.

Vayssieres, L. et al. (1998). "Size Tailoring of Magnetite Particles Formed by Aqueous Precipitation: An Example of Thermodynamic Stability of Nanometric Oxide Particles". In: *J. Colloid Interface Sci.* 205 (2), pp. 205–212.

Verbarg, J. et al. (2012). "Spinning magnetic trap for automated microfluidic assay systems". In: *Lab Chip* 12 (10), p. 1793.

Vojtíšek, M., A. Iles and N. Pamme (2010). "Rapid, multistep on-chip DNA hybridisation in continuous flow on magnetic particles". In: *Biosens. Bioelectron.* 25 (9), pp. 2172–2176.

Wahajuddin and Arora (2012). "Superparamagnetic iron oxide nanoparticles: magnetic nanoplatforms as drug carriers". In: *Int. J. Nanomedicine*, p. 3445.

Walsh, D. I. et al. (2017). "Enabling Microfluidics: from Clean Rooms to Makerspaces". In: *Trends Biotechnol.*

Walters, E. M., D. J. Beebe and M. B. Wheeler (2001). "In vitro maturation of pig oocytes in polydimethylsiloxane (PDMS) and silicon microfluidic devices". In: *Theriogenology* 55 (1), p. 497.

Wang, C., Z. Xu and C. Zhang (2015). "Polyethyleneimine-Functionalized Fluorescent Carbon Dots: Water Stability, pH Sensing, and Cellular Imaging". In: *ChemNanoMat* 1 (2), pp. 122–127.

Wang, J. et al. (2015). "High Performance Photoluminescent Carbon Dots for In Vitro and In Vivo Bioimaging: Effect of Nitrogen Doping Ratios". In: *Langmuir* 31 (29), pp. 8063–8073.

Wang, Y. and A. Hu (2014). "Carbon quantum dots: synthesis, properties and applications". In: *J. Mater. Chem. C* 2 (34), p. 6921.

Whitesides, G. M. (2006). "The origins and the future of microfluidics". In: *Nature* 442 (7101), pp. 368–373.

Whitesides, G. M. and A. D. Stroock (2001). "Flexible Methods for Microfluidics". In: *Phys. Today* 54 (6), pp. 42–48.

Wich Lab (2017). *Scale comparison: from nano to macro.* http://www.wichlab.com/research/, last accessed April 16th 2017.

Wirth, T., ed. (2013). *Microreactors in Organic Chemistry and Catalysis.* Weinheim, Germany: Wiley-VCH Verlag GmbH & Co. KGaA.

Xia, Y., J. Si and Z. Li (2016). "Fabrication techniques for microfluidic paper-based analytical devices and their applications for biological testing: A review". In: *Biosens. Bioelectron.* 77, pp. 774–789.

Xia, Y. and G. M. Whitesides (1998). "Soft Lithography". In: *Annu. Rev. Mater. Sci.* 28 (1), pp. 153–184.

Xiao, Q. et al. (2017). "Microwave-assisted one-pot synthesis of highly luminescent N-doped carbon dots for cellular imaging and multi-ion probing". In: *Microchim. Acta.*

Xing, R. et al. (2011). "Superparamagnetic magnetite nanocrystal clusters as potential magnetic carriers for the delivery of platinum anticancer drugs". In: *J. Mater. Chem.* 21 (30), p. 11142.

Xu, Q. et al. (2016). "Heteroatom-doped carbon dots: synthesis, characterization, properties, photoluminescence mechanism and biological applications". In: *J. Mater. Chem. B* 4 (45), pp. 7204–7219.

Yamazaki, M. (2004). "Industrialization and application development of cyclo-olefin polymer". In: *J. Mol. Catal. A Chem.* 213 (1), pp. 81–87.

Yeap, S. P. et al. (2012). "Electrosteric Stabilization and Its Role in Cooperative Magnetophoresis of Colloidal Magnetic Nanoparticles". In: *Langmuir* 28 (42), pp. 14878–14891.

Yetisen, A. K., M. S. Akram and C. R. Lowe (2013). "Paper-based microfluidic point-of-care diagnostic devices". In: *Lab Chip* 13 (12), p. 2210.

Ymbern, O. (2016). "Development of centrifugal microfluidic platforms based on polymer microfabrication technology". PhD thesis. Universitat Autònoma de Barcelona.

Ymbern, O., M. Berenguel-Alonso, et al. (2015). "Versatile Lock and Key Assembly for Optical Measurements with Microfluidic Platforms and Cartridges". In: *Anal. Chem.* 87 (3), pp. 1503–1508.

Ymbern, O., N. Sández, et al. (2014). "Gas diffusion as a new fluidic unit operation for centrifugal microfluidic platforms." In: *Lab Chip* 14 (5), pp. 1014–22.

Young, E. W. K. et al. (2011). "Rapid Prototyping of Arrayed Microfluidic Systems in Polystyrene for Cell-Based Assays". In: *Anal. Chem.* 83 (4), pp. 1408–1417.

Yu, M. K. et al. (2008). "Drug-Loaded Superparamagnetic Iron Oxide Nanoparticles for Combined Cancer Imaging and Therapy In Vivo". In: *Angew. Chemie Int. Ed.* 47 (29), pp. 5362–5365.

Yuan, X. et al. (2014). "Cellular distribution and cytotoxicity of graphene quantum dots with different functional groups". In: *Nanoscale Res. Lett.* 9 (1), p. 108.

Zeng, S. et al. (2014). "Nanomaterials enhanced surface plasmon resonance for biological and chemical sensing applications". In: *Chem. Soc. Rev.* 43 (10), p. 3426.

Zeringue, H. C., D. J. Beebe and M. B. Wheeler (2001). "Removal of Cumulus from Mammalian Zygotes using Microfluidic Techniques". English. In: *Biomed. Microdevices* 3 (3), pp. 219–224.

Zhang, L. et al. (1995). "Cumulus cell function during bovine oocyte maturation, fertilization, and embryo development in vitro". In: *Mol. Reprod. Dev.* 40 (3), pp. 338–344.

Zhou, J., A. V. Ellis and N. H. Voelcker (2010). "Recent developments in PDMS surface modification for microfluidic devices". In: *Electrophoresis* 31 (1), pp. 2–16.

Zhu, S., Q. Meng, et al. (2013). "Highly Photoluminescent Carbon Dots for Multicolor Patterning, Sensors, and Bioimaging". In: *Angew. Chemie* 125 (14), pp. 4045–4049.

Zhu, S., Y. Song, et al. (2015). "The photoluminescence mechanism in carbon dots (graphene quantum dots, carbon nanodots, and polymer dots): current state and future perspective". In: *Nano Res.* 8 (2), pp. 355–381.

Ziółkowska, K., R. Kwapiszewski and Z. Brzózka (2011). "Microfluidic devices as tools for mimicking the in vivo environment". In: *New J. Chem.* 35 (5), p. 979.

Appendix A

Publications

The work presented in this thesis contributed to the publication of the following articles in peer-reviewed journals:

1. Berenguel-Alonso, M. et al. (2014). "Magnetic actuator for the control and mixing of magnetic bead-based reactions on-chip". In: *Anal. Bioanal. Chem.* 406.26, pp. 6607–16.

2. Ymbern, O. et al. (2015). "Versatile Lock and Key Assembly for Optical Measurements with Microfluidic Platforms and Cartridges". In: *Anal. Chem.* 87.3, pp. 1503–1508 (part of the Doctoral thesis of Oriol Ymbern).

3. Gómez-de Pedro, S. et al. (2017). "Automatic microfluidic system to perform multi-step magneto-biochemical assays". In: *Sensors Actuators B: Chem.* 245, pp. 477–483 (part of the Doctoral thesis of Sara Gómez-de Pedro).

4. Berenguel-Alonso, M. et al. (2017). "Rapid Prototyping of a Cyclic Olefin Copolymer Microfluidic Device for Automated Oocyte Culturing". In: *SLAS Technol.* DOI: 10.1177/2472630316684625.

Magnetic actuator for the control and mixing of magnetic bead-based reactions on-chip

Miguel Berenguel-Alonso, Xavier Granados, Jordi Faraudo, Julián Alonso-Chamarro and Mar Puyol.

Analytical and Bioanalytical Chemistry 2014, 406 (26), 6607–6616.

RESEARCH PAPER

Magnetic actuator for the control and mixing of magnetic bead-based reactions *on-chip*

**Miguel Berenguel-Alonso · Xavier Granados ·
Jordi Faraudo · Julián Alonso-Chamarro · Mar Puyol**

Abstract While magnetic bead (MB)-based bioassays have been implemented in integrated devices, their handling *on-chip* is normally either not optimal—i.e. only trapping is achieved, with aggregation of the beads—or requires complex actuator systems. Herein, we describe a simple and low-cost magnetic actuator to trap and move MBs within a microfluidic chamber in order to enhance the mixing of a MB-based reaction. The magnetic actuator consists of a CD-shaped plastic unit with an arrangement of embedded magnets which, when rotating, generate the mixing. The magnetic actuator has been used to enhance the amplification reaction of an enzyme-linked fluorescence immunoassay to detect *Escherichia coli* O157:H7 whole cells, an enterohemorrhagic strain, which have caused several outbreaks in food and water samples. A 2.7-fold sensitivity enhancement was attained with a detection limit of 603 colony-forming units (CFU) /mL, when employing the magnetic actuator.

Keywords Magnetic beads · Magnetic actuator · Lab on a chip · Magnetic mixing · Immunoassay

Introduction

The rapid, low-cost and in situ determination of biologically and environmentally important analytes has long been one of

M. Berenguel-Alonso · J. Alonso-Chamarro · M. Puyol (✉)
Group of Sensors and Biosensors (GSB), Department of Chemistry,
Universitat Autònoma de Barcelona, 08193 Bellaterra, Spain
e-mail: MariaDelMar.Puyol@uab.es

X. Granados · J. Faraudo
Institut de Ciència de Materials de Barcelona (ICMAB-CSIC),
Campus UAB, 08193 Bellaterra, Spain

the main targets of analytical researchers [1], leading to the rapid development of micro-Total Analysis Systems (μTAS) [2] for selected compounds such as pollutants, DNA, proteins or cells. This fact has stimulated further miniaturization and integration of biosensors in μTAS [3]. Enzyme-linked bioassays are widely used in these systems because the amplification step allows achieving low detection limits. However, the diversity and complexity of real sample matrices are a great challenge for scientists to solve each analytical problem. To overcome this, the biorecognition element can be immobilized on a surface in order to retain the analyte, while washing out the matrix. Superparamagnetic microparticles—commonly known as magnetic beads—emerged as a suitable substrate to immobilize the biorecognition elements, due to their high surface-to-volume ratio, surface tunability and easy control by means of external magnetic fields [4]. The latter property also enables the development of biosensors in which the magnetic beads (MBs) can be controlled and placed onto the surface of the transducer during the detection step [5]. MBs have been widely used for decades and are commercially available in a wide range of sizes, magnetic properties and surface functionalizations. The versatility and availability of MBs are promoting their use in lab-on-a-chip devices [6], thus enabling the automation of the assays, the reduction of the equipment required and minimizing the consumption of reagents [7].

For instance, Choi et al. developed a complete immunoassay on a microfluidic channel with enzymatically generated electrochemical detection by retaining the MBs with an electromagnet [8] and sequentially performing all the reactions involved. Several detection methods based on enzymatic signal generation have been applied in MB-based microfluidic assays, such as amperometry [9], colorimetry [10], fluorescence [11] or chemiluminesce [12]. However, the interaction between MBs and reagents within the device is limited, on the one hand, because it is mainly ruled by diffusion on a laminar

flow, and on the other hand, due to the aggregation of MBs as a result of the external magnetic field, thus hiding the biorecognition molecules of the MBs to the reagents (detailed studies of MB aggregation can be found in the bibliography [13, 14]). In this sense, a few methods to control and mix MBs *on-chip* have been proposed to enhance the rate of reactions. In these approaches, MBs become not only the support of the bioassay, but also an active on-chip mixing and transport agent.

Continuous-flow devices have been used as platforms for free-flow magnetophoresis, in which an external magnet deflects the MBs and separates them according to their size and amount of magnetic material. Pamme's group developed a system with co-flowing reagent streams and a permanent magnet on the side, demonstrating its suitability for both a sandwich immunoassay [15] and DNA hybridization [16]. The magnet deflects the trajectory of the MBs, making them cross the different streams, thus colliding and binding to sample/reagents. Other continuous-flow devices have been proposed, in which MBs are deflected by a magnet towards different streams in order to perform a reaction or to be washed [17–19]. More complex systems of magnets have been used to control the MBs in continuous flow. For instance, the actuator proposed by Ramadan and Gijs [20] creates areas along a microfluidic channel that sequentially trap and release MBs. Despite being effective, this system is rather complex and requires a long microfluidic channel. Another example is the magnetic trap developed by Verbarg et al. [21] for a microflow cytometer, which consists of radially arranged magnets on a rotating support. Depending on the rotation direction, magnets trap—counteracting the liquid flow—or release the MBs. However, continuous-flow systems may not be suitable for assays in which an amplification step is required, as they are limited by the flow rate. Furthermore, a continuous-flow operation requires relatively high consumption of reagents.

Unlike continuous-flow systems, stop-flow approaches can tune the incubation time according to the assay needs, and the reaction volume is defined by the geometry of the device. Taking advantage of this, Herrmann et al. developed a magnetic actuator consisting of a mobile magnet [22], in order to move MBs from one end to the other end of a reaction chamber during the amplification step of an immunoassay, thus enhancing the substrate exploitation rate. A further development of their polydimethylsiloxane (PDMS) microfluidic device enabled both the formation of the immunocomplex and the enzymatic reaction to be carried out on-chip [23, 24]. The problem of nonspecific adsorption was avoided by means of a double network of chambers connected through pneumatic valves. However, difficulties to move the magnet linearly and at the desired velocity can be foreseen. On the other hand, small hydrophobic molecules from the solution can be absorbed onto PDMS [25, 26].

Based on the above considerations, in this paper, we present a novel, compact and simple magnetic actuator that efficiently moves MBs within a microfluidic structure (microchannel or microchamber). It consists of a rotating unit (same size of a CD) that is placed just under the microfluidic device, which contains a set of magnets circularly arranged and eccentric to the rotation axis. The rotation of the unit triggers the movement of the MBs within the microfluidic structure. Different arrangements of magnets are studied by means of the finite element modeling (FEM) software COMSOL Multiphysics, in order to find the optimal movement of the MBs. The simplicity and the design of the actuator, consisting only of a rotating unit and a DC motor, together with its low cost, would enable its use in a portable platform. Furthermore, the design of the magnetic actuator takes its application to parallel or multiplex analyses and/or centrifugal microfluidics into consideration.

The actuator is used in a stop-flow enzyme-linked fluorescence immunoassay for the detection of *Escherichia coli* O157:H7 whole cells. Only the amplification step (enzymatic reaction and the fluorescence detection) is performed on-chip, while the immunocomplex formation is carried out *off-chip*, in order to evaluate the improvement provided by the actuator. Further research will address the integration of the whole immunoassay on-chip. *E. coli* O157:H7 is a pathogenic strain, which may produce severe illness, and has caused several outbreaks not only in foodstuffs [27, 28], but also in water [29]. The MBs used in this study are commercially available and can be purchased with a great variety of antibody surface functionalizations, making the magnetic actuator useful for a wide range of assays with off-the-shelf reagents.

Experimental

Chemicals and materials

Dynabeads anti-*E. coli* O157 (diameter 2.8 μm, 5 mg/mL, catalog no. 71003) were purchased from Dynal Biotech (Oslo, Norway). The Phosphatase-labeled Anti-*E. coli* O157:H7 Antibody (0.1 mg, lyophilized, catalog no. 05-95-90) was obtained from KPL (MD, USA). Chemicals used to prepare the different buffer solutions including Tris-buffered saline (TBS) tablets, TBS-Tween 20, casein blocking buffer 10× (B6429), potassium chloride (KCl), diethylamine, magnesium chloride hexahydrate (MgCl$_2$·6H$_2$O), sodium chloride (NaCl) and 4-methylumbelliferyl phosphate (4-MUP) were purchased from Sigma-Aldrich (Barcelona, Spain). Tryptone and yeast extract were obtained from Pronadisa (Barcelona, Spain).

The Neodymium Iron Boron (NdFeB) block magnets (15 mm long, 2 mm wide and 8 mm thick) magnetized through thickness grade N50, and the cylinder magnet (radius 15 mm and 5 mm thick) grade N38 were purchased from Chen

Yang Technologies GmbH (Finsing, Germany). Cyclic Olefin Co-polymer (COC) sheets and films were obtained from TOPAS Advance Polymers GmbH (KY, USA) in different grades and thicknesses. Finally, poly (methyl methacrylate) (PMMA) sheets were purchased from Plásticos Ferplast (Terrassa, Spain).

Microfluidic device

The microfluidic device consists of five COC layers, which were sealed by the temperature diffusion bonding technique, as seen elsewhere [30]. COC was used due to its adequate optical properties and the diversity of available polymerization grades, with different glass transition temperatures (T_g), which enable using some sheets as sealing layers with minimal influence on the obtained microfluidic patterns after lamination. It was designed using computer-aided design (CAD) software. First, the middle layer of TOPAS 5013 (T_g=130 °C) was laminated between two films of TOPAS 8007 (T_g= 75 °C), which acted later as glue. Second, the different microfluidic elements were machined onto this layer and onto two more TOPAS 5013 sheets, which acted as top and bottom layers, by using a computer numerical control (CNC) micromilling machine Protomat C100/HF (LPKF Laser & Electronics, Garbsen, Germany). Finally, the three layers were aligned and sealed at 100 °C under a pressure of 6 bar.

Magnetic actuator

The magnetic actuator consists of a set of permanent magnets embedded in a CD-shaped PMMA rotor, fabricated with a CNC micromilling machine, attached to a stepper motor Maxon EC-I which provided the rotation movement (from 1 to 20 rpm) with a digital positioning controller EPOS2 24/5 (Maxon, Sachseln, Switzerland). Magnets were positioned at different radii from the center of the rotor forming a circumference, and the microfluidic device was placed just above. The rotation induces the movement of the MBs within the reaction chamber of the microfluidic device, as they follow the magnets.

Optical system

Fluorescence was measured using an in-house built detection system (Electronic Supplementary Material (ESM), Fig. S1) developed in collaboration with the Group of Photonic Technologies (GTF, University of Zaragoza, Spain), which basically consisted of a modulated light-emitting diode (LED) and a PIN Hamamatsu S1337-66BR large active area photodiode, integrated in a printed circuit board (PCB) [31]. The LED XSL-365-5E from Roithner Lasertechnik (Vienna, Austria) had its emission peak at 365 nm and was tilted 45° with respect to the plane of the microfluidic device, in order to reduce interferences of the light source to the detector. The LED was modulated and controlled by a Data Acquisition Card (DAQ, NI USB-6211, National Instruments, Madrid, Spain), which also captured the detected signal and transferred it to a computer in order to process it. Both DAQ and PCB were powered by the computer through a USB connector. An emission bandpass filter MF460-60 from Thorlabs (Munich, Germany) was used to prevent any excitation light reaching the detector. The PCB was embedded in a PMMA structure, which also accommodated the optical filter. This structure features an insertion port for the microfluidic chip—as if it were a cartridge—with complementary shape. This insertion mechanism avoids alignment errors, and thus fluorescence readouts were performed rapidly and reliably.

Bacteria and culture conditions

E. coli O157:H7 DSM number 17076 were obtained from DSMZ (German Collection of Microorganisms and Cell Cultures, Leibniz) and were cultured in lysogeny broth (LB) at 37 °C for 18 to 24 h with shaking at 160 rpm. Cells were pelleted by centrifugation (10,000*g*, 8 min), washed twice with TBS, and resuspended by gently vortexing in TBS. A portion of this bacterial solution was serially diluted and plated on LB agar in triplicate. The plates were incubated for 24 h at 37 °C, and the resultant colonies were enumerated in order to back calculate the bacterial culture concentration.

The rest of the bacterial solution was divided in aliquots of 1 mL in Eppendorf tubes. The tubes were centrifuged in order to pellet the bacteria; the supernatant was discarded and replaced by 50 μL of 33 % glycerol solution, and finally the Eppendorf tubes were stored at −20 °C until needed [32]. These ready-to-use samples enabled the daily preparation of fresh bacteria cultures by dilution with TBS.

Off-chip formation of the immunocomplex

Ten microlitres of Dynabeads anti-*E. coli* O157 was placed in a 1.5-mL Eppendorf tube and rocked in TBS-Tween 20 (TBST, in millimolar: 140 NaCl, 20 Tris, 0.1 % Tween 20, pH 7.6) with casein blocking buffer (diluted 1/10 in the TBST buffer) for 10 min (TBST-Casein), using a Thermomixer (Eppendorf, Hamburg, Germany) at 1,000 rpm. Then, the tubes were placed under the influence of a magnet for 2 min to trap the MBs, and the supernatant was discarded; 500 μL of the *E. coli* diluted sample was added and incubated for 10 min under the same rocking conditions as before. The supernatant was discarded, and the MBs were washed twice with TBST-Casein. Then, 200 μL of 1/100 diluted Phosphatase-labeled Anti-*E. coli* O157:H7 Antibody was added and incubated with rocking for 30 min. Finally, the MBs were washed twice with TBST-Casein and resuspended in 100 μL of diethanolamine (DEA) buffer (in millimolar: 100

diethanolamine, 50 KCl, 1 MgCl$_2$, pH 9.6). All reactions were carried out at room temperature.

On-chip detection

The immunocomplex was injected into the microfluidic chip and retained by a magnet in the reaction chamber. Then, 38 µL of a solution 1 mM of 4-MUP, prepared in DEA buffer, was injected and reacted for 10 min at room temperature (with or without magnetic actuation, depending on the experiment). The resulting solution containing 4-methylumbelliferone (4-MU) was pushed to the detection chamber, while the magnets retained the MBs in the reaction chamber. The fluorescence of 4-MU was measured on-chip by inserting the device into the port of the optical system.

Results and discussion

Microfluidic design

The microfluidic device was fabricated on COC, due to its high chemical resistance, low water absorption, biocompatibility and good optical transparency in the near-UV and visible range [33]. Furthermore, several machining techniques are available, and its fabrication can be easily scaled from prototyping to mass production, severely reducing the cost per device. The microfluidic device (see Fig. 1) consists of two main elements, namely the reaction and the detection chambers. The former is the reactor, where MBs are retained and controlled by means of the magnetic actuator, and reacted with the enzymatic substrate. Its dimensions are 2 mm wide, 12 mm long and 1 mm high, featuring a volume of 24 µL. When placed on top of the magnetic actuator, the reaction chamber is positioned just above the magnets. The latter is the detection chamber, where the fluorescence measurements are
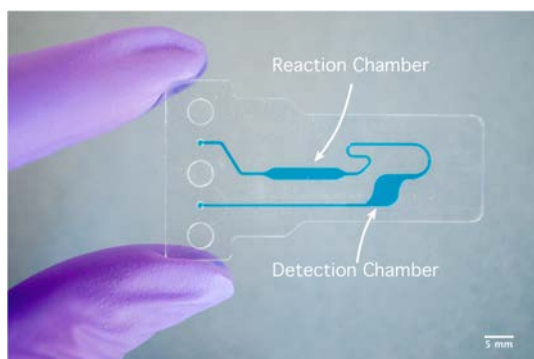
Fig. 1 COC microfluidic chip for the implementation of magnetic bead-based immunoassays

carried out, and its volume is approximately the same as the reaction chamber. The shape of the microfluidic device is complementary to the insertion port of the detection system, thus enabling the alignment of the detection chamber with the optical components.
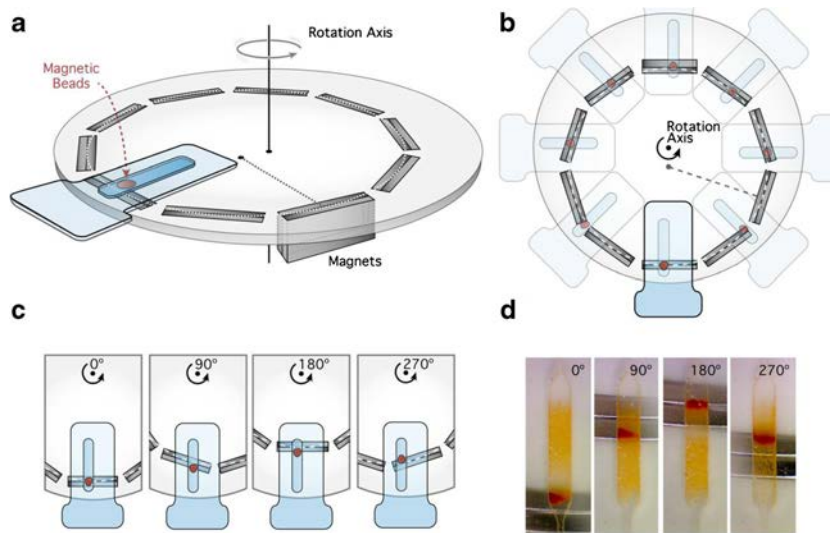
Design of the magnetic actuator

The magnetic actuator is placed just under the microfluidic device and consists of a rotating CD-shaped unit containing 20 slots for magnets (or magnet blocks) at different radii, forming an eccentric circumference (see Fig. 2a, b). When rotating, the magnets pass sequentially under the reaction chamber (Fig. 2c), where they induce the movement of the MBs. The positions of the inner and outermost slots coincide with the two extremes of the reaction chamber, so that the MBs move back and forth on each revolution. An image sequence of the movement of the MBs is shown in Fig. 2d. The size and weight of the actuator is similar to that of a CD player, which makes it suitable for integration in a portable system. Its size and circular design would enable several reactions to be carried out in parallel—either in different microfluidic devices or in a single one with different microfluidic units—as well as the use of centrifugal microfluidic devices. Furthermore, this actuator does not require relatively complex mechanical systems to work, as for instance other actuators consisting of magnets moving linearly [22], which would also have issues to control the movement of the MBs due to the deceleration and acceleration in the opposite direction to move the MBs back and forth.

The magnetic properties of the MBs used in the simulations were retrieved from a previous detailed characterization study [34]. The particles herein employed have a strong superparamagnetic response, with zero magnetization in the absence of a magnetic field. For moderate fields of 0.1 T, the magnetization is very high (about 8 Am^2/kg) and above 1 T, the magnetic response saturates at 10.8 Am^2/kg. Therefore, maximum magnetic response of the particles can be obtained with the fields generated by NdFeB magnets. Due to the acquired magnetization, particles in suspension can interact with each other through anisotropic magnetic dipole-dipole interactions. If this interaction is strong enough, the magnetophoretic motion can become a cooperative motion involving a collective, concerted displacement of a large number of particles of the system [35], which will improve the movement of the MBs and, hence, the mixing of a reaction inside the chamber.

The strength of the particle-particle magnetic interaction is characterized by the magnetic coupling parameter Γ, which is dimensionless and involves the radius of a particle, its saturation magnetization and the thermal energy [36]. Typical values of Γ for composite superparamagnetic particles (including commercial beads) are between 10^2 and 10^3. Using the

diameter of the particles provided by the manufacturer, we estimate a value $\Gamma \approx 7 \times 10^4$ for the particles employed. Therefore, magnetic particle-particle interactions are predicted to be particularly strong between Dynabeads particles, provided that they are near saturation magnetization (i.e. under magnetic fields above 0.1 T). The possibility of a cooperative motion between particles also depends on the concentration of the suspension. In order to obtain cooperative motion, the theory requires that the aggregation number N^*, given by Eq. 1 [36],

$$N^* = \sqrt{\phi \exp(\Gamma - 1)} \qquad (1)$$

where ϕ is the volume fraction, has to be much larger than 1. In general, the possibility of cooperative motion ($N^* > 1$) requires a concentration larger than a threshold, which depends on the value of Γ. According to Eq. 1, and taking into account the large value of Γ obtained for our particles (note the exponential dependence in Γ), cooperative motion will be always obtained provided that the particles are under magnetic fields above 0.1 T. Therefore, a critical aspect in the design of the device is to ensure that all the particles are under the action of a large enough magnetic field. This aspect becomes more important as one uses low concentrations or smaller particles. This is a known issue, for example, in the use of most commercial batch magnetic separators, in which significant regions of the sample are under low magnetic fields, with the subsequent loss of particles when working at low concentrations [37].

At this point, it is important to recall that the magnetophoretic motion depends both on the magnetization of the particles and on the gradient of the magnetic field [35]. A uniform magnetic field does not generate any motion; it only magnetizes the particles or orients them along the field if some anisotropy is present. In nonuniform magnetic fields, the magnetization of the particles creates a force F_m over their dipolar magnetic moment m, as given by Eq. 2 [35]:

$$\overrightarrow{F}_m = \overrightarrow{\nabla}\left(\overrightarrow{m} \cdot \overrightarrow{B}\right) \qquad (2)$$

where B is the local value of the magnetic field. Therefore, one has to design a system containing large enough magnetic fields (of the order of 0.1 T or larger), in order to maximize the magnetization of the particle (and consequently the magnetic dipole), but also large spatial magnetic gradient of the magnetic field in the adequate direction (at least of the order of 10–10^2 T/m) to obtain the desired motion according to Eq. 2.

Taking into account the above considerations, three different configurations, regarding the magnets used in each slot, were selected for the study on the basis of the following criteria: simplicity for their integration in the rotating unit, dimensions of the magnets for the accurate movement of the MBs and expected magnetic field strength. Figure 3 shows the three configurations: (a) single magnet; (b) two magnets antiferromagnetic-like coupled, in order to enhance the magnetic gradient; and (c) the same magnet couple including a static third magnet for creating a bias magnetizing field, which produces an out-of-plane magnetization. For each configuration, we performed COMSOL simulations in which we calculated the profile of the magnetic field generated by the magnets and the resulting magnetic force over the MBs. For the calculations, we employed a constant magnetization of 9.6×10^5 A/m for the magnets (as usual for NdFeB magnets) and the bibliographic characterization data of the MBs [34].

The simulation setup consisted of a single magnetic block (we neglected the interactions between magnets of different slots) and a set of 27 superparamagnetic particles homogeneously distributed in the channel, where the reaction should occur, in order to see the distribution of the forces generated upon them. The distance between the microfluidic chamber and the magnet(s) is defined by the thickness of the COC sealing layers. The distance between the magnet couple (configurations b and c, Fig. 3) was established arbitrarily for the setup of the simulations. The chamber channel is represented in the pictures as the two parallel, continuous lines confining the set of particles. Magnetization and force are represented by black and white arrows, respectively. It is worth noticing that magnetic flux density and magnetization are parallel.

As a general trend, we can observe in Fig. 3 that the magnitude of the flux density of the field is larger for the couple of magnets (Fig. 3b and c than for the single magnet (Fig. 3a). This is due to the overlapping of the stray field with the flux in the poles. More relevant, however, is the increase of the gradient of the magnetic field just in between both magnets, when they are coupled. These effects, namely the increase of the field and the increase of magnetic gradient, determine a substantial increase of the force over the MBs. Therefore, the single magnet configuration (Fig. 3a) was discarded as it is outperformed by the configurations containing a magnet couple (Fig. 3b and c).

Increasing the magnetization of the MBs would also increase the magnetic force. For this reason, the arrangement of magnets in Fig. 3c was proposed, since the static magnet was expected to create a larger and nearly homogeneous bias magnetic field, not disturbing the high gradient achieved with the magnet couple. Nevertheless, it is important to note that we could only take advantage of a larger bias field if the magnetization of the MBs did not saturate. In this respect, the magnetic configurations shown in Fig. 3b and c show a magnetic field around the MBs larger than the saturation threshold of 0.1 T. Accordingly, configuration Fig. 2b was chosen as optimal because of its magnetic characteristics (saturation of the MBs magnetization, high magnetic gradient) and the simpler, more cost-effective setup (requires less magnets) compared to configuration c.

Using configuration b, experimental performed at a concentration of 2 mg/mL (volume fraction 1.43×10^{-3}) clearly showed a collective, concerted motion of the particles along the reaction chamber. This collective motion involves a very large number of particles (arranged in fibrous structures following the magnetic field), which could be also observed with naked eye, as in previous cooperative magnetophoresis experiments [35]. A video of this motion is displayed in ESM 2. Adhesion of MBs to the walls of the device can be observed, but this issue could be addressed by modifying the surface of the microchannels to minimize adsorption [38] and by optimizing the movement velocity of the magnets.
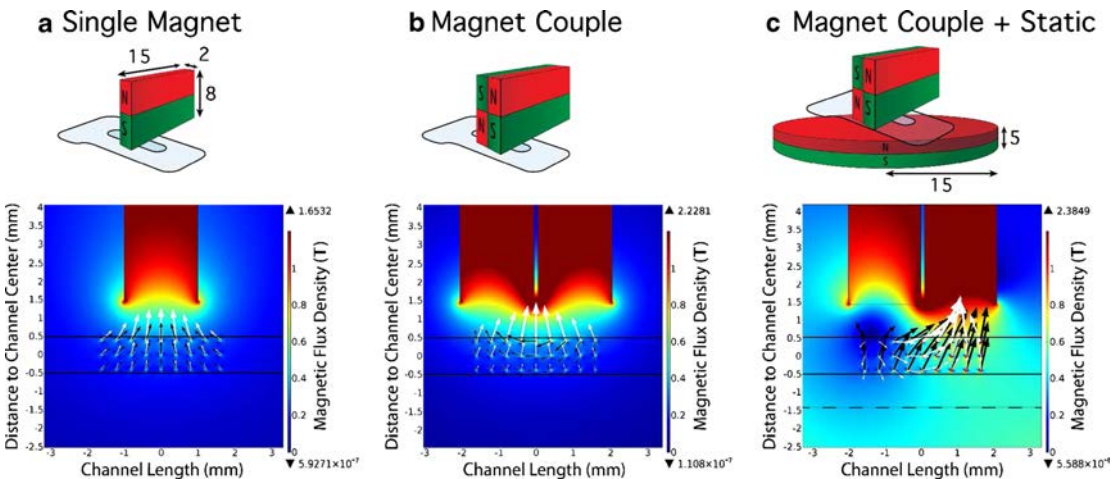
Fig. 3 *Top*: sketches of the three configurations of magnets selected for consideration, with the microfluidic device to clarify their relative positions. *Bottom*: corresponding calculation of the field (*color map*), the magnetization of the particles (*black arrows*) and the acting force (*white arrows*). The different configurations are **a** single magnet, **b** antiferromagnetic coupled pair and **c** the same magnet pair including a third magnet for creating a bias magnetizing field. The *color map* represents the local magnetic flux density for a stationary distribution of magnetizable particles, in Tesla. In order to get a better image of the force and magnetization distributions; *arrows* in the different pictures are not in the same scale. The continuous *horizontal lines* confining the MBs represent the microfluidic chamber, and the *dashed line* in configuration **c** represents the static magnet

Immunoassay and detection

The formation of the immunocomplex was carried out off-chip and subsequently injected into the microfluidic device to carry out the detection, i.e. the enzymatic reaction and the optical measurement. In this way, we focused on evaluating the enhancement provided by the magnetic actuator for a MB-based reaction on-chip, while avoiding optimization of several parameters of a microfluidic immunoassay. A typical sandwich immunoassay was performed using MBs as support material for the formation of the immunocomplex (see Fig. 4). The reactions for the formation of the immunocomplex were carried out sequentially and washed twice between each reaction.

The enzymatic reaction consisted of the dephosphorylation of the 4-MUP catalyzed by the alkaline phosphatase, to obtain the fluorescent product 4-MU. Considering the conversion rate of the reaction as constant and the time of incubation fixed, the signal intensity depends only on the amount of alkaline phosphatase-labeled antibodies present, which is proportional to the number of *E. coli* O157:H7 captured by the MBs.
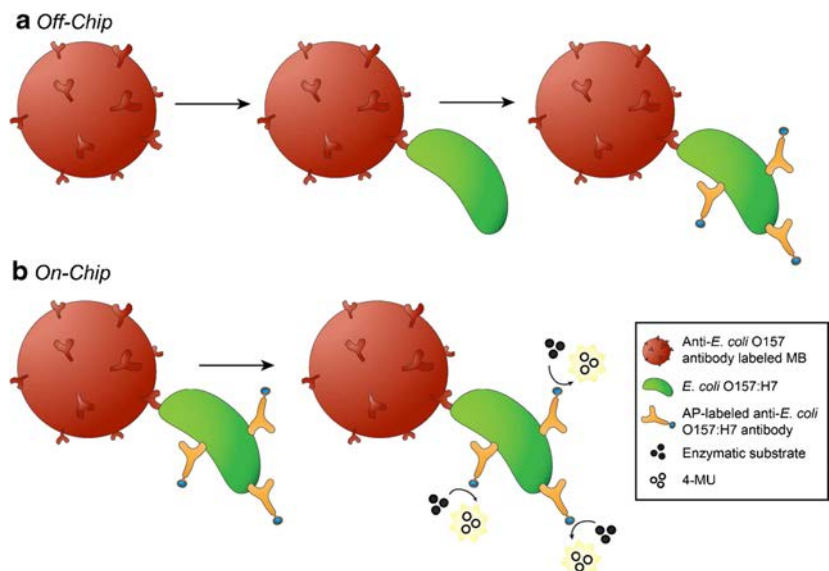
The movement of MBs can be tuned by increasing or decreasing the rotation speed of the magnetic actuator. One turn of the CD-shaped actuator is translated to one cycle of movement of the MBs, i.e. from one end to the other end of the reaction chamber and back to the starting point. The movement increases the effective surface area of the MBs exposed to the substrate, because it creates a loose cloud of MBs following the magnets. Moreover, the movement of the MBs makes the substrate from all around the reaction chamber

available to the enzyme (not only the substrate molecules directly next to the MB capture spot), homogenizing the concentration of the enzymatic product in the reaction chamber. These two combined effects lead to enhance the signal of the assay. The optimal movement velocity was found to be 1.7 mm/s (see Fig. 5). However, the signal enhancement decreased at higher velocities, due to the fact that MBs could not completely follow the magnets (i.e. the movement cycle was not completed) since they move too fast, and therefore, MBs were not exposed to the whole of the substrate. It is also worth noticing that all the studied movement velocities provided a signal enhancement compared to the system that only captures the MBs (0 mm/s).

At the same time, the relative standard deviation (RSD) of the signals decreased as the velocity increased (Fig. 5), even when the velocities were higher than 1.7 mm/s, where a signal decrease was also observed. The lower level of MB aggregation achieved due to the magnetic actuation could cause this decrease. However, the RSD values are not in complete agreement with those found in Fig. 6. Therefore, further reproducibility studies should be carried out in order to establish a relationship between RSD and linear movement velocity, because other factors must be also taken into account, as for instance the irreproducibility of the manual off-chip procedures (replicates were obtained from whole new assays).

To evaluate the performance of the magnetic actuator in comparison to systems that are only able to capture the MBs, three calibration experiments were performed (Fig. 6): (1) at 0 mm/s, i.e. only capturing the MBs; (2) at 1.7 mm/s, the higher signal enhancement; and (3) at 3.3 mm/s. The

Fig. 4 Schematic representation of the enzyme-linked fluorescence immunoassay performed. **a** The formation of the immunocomplex is carried out off-chip, washing the MBs twice after each reaction. The MBs are reacted firstly with *E. coli* O157:H7 and secondly with the alkaline phosphatase-labeled anti-*E. coli* O157:H7 antibody. **b** The immunocomplex is injected in the microfluidic chip to carry out the enzymatic reaction and the fluorescence detection on-chip
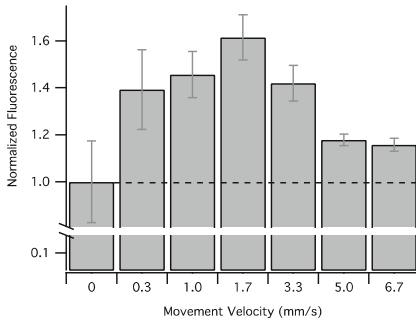
Fig. 5 Signal obtained at different movement velocities of the MBs, which are tuned by increasing or decreasing the rotation speed of the magnetic actuator. The concentration of MBs was 2 mg/mL and the *E. coli* O157:H7 sample contained 2×10^4 CFU/mL. The *dashed line* indicates the normalized signal obtained at 0 mm/s, for a better comparison with the other columns. The *error bars* show the RSD for $n=3$

calibration curve obtained at 1.7 mm/s, the optimal velocity, showed a 2.7-fold enhancement of the sensitivity (defined as the slope of the calibration curve) with respect to the 0 mm/s curve, while the one obtained at a velocity of 3.3 mm/s showed only 1.7-fold enhancement. These experimental results are in accordance to the previous optimization of the MB movement velocity. The linearity of the three calibration curves over this concentration range was good, with values of 0.997, 0.996 and 0.998 for the curves 0, 1.7 and 3.3 mm/s, respectively. The detection (LOD) for *E. coli* O157:H7 at 1.7 mm/s was calculated to be 603 colony-forming units (CFU/mL ($n=12$), whereas it was higher, 2,101 CFU/mL ($n=3$), for the system when no actuation was performed. Quantification limit (LOQ) was 1,470 CFU/mL ($n=12$) at 1.7 mm/s. LOD and LOQ were calculated as the concentration that yields a signal three or ten times the standard deviation of the blank, respectively.
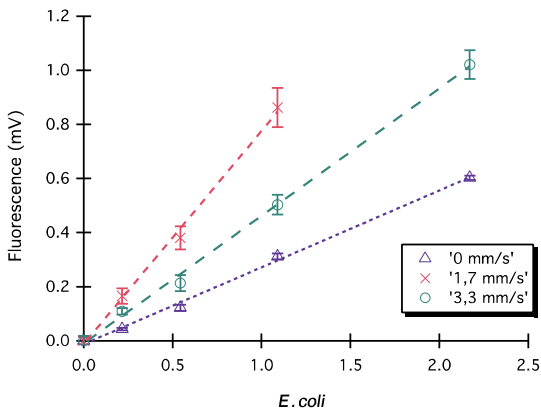
Fig. 6 Calibration curves for the detection of *E. coli* O157:H7 at different movement velocities. The *error bars* show the standard deviation for $n=3$

An even higher enhancement of the enzymatic reaction performance could be achieved by decreasing the height of the reaction chamber because we observed that MBs moved only on the lower section (i.e. as close as possible to the magnets) of the chamber (total height of 1 mm). The decrease of the chamber height would enable the particles to directly interact with the total volume of the solution in the reaction chamber. However, the height of the reaction chamber was chosen so that both reaction and detection chambers would have similar volumes, considering that the latter was previously optimized to have an optical path of 1 mm in order to be used with the optical detection system. This issue will be addressed in further studies.

This study demonstrates that the magnetic actuator herein proposed provides an enhancement of the reaction kinetics. Integrating all the reactions of the immunoassay on-chip as well as the washing steps would entail several challenges to be met, such as nonspecific adsorption. However, the kinetics of each reaction would be enhanced with the actuator, in comparison to a system only able to trap the MBs. Reactions between the MBs and big entities, such as whole cells, less prone to diffusion, would be expected to benefit even more from the mixing provided by the magnetic actuator.

Conclusions

A novel magnetic mixing actuator for MB-based reactions in microfluidic systems has been developed. Its design is simple and compact (comparable to a CD player), featuring magnet couples embedded on a rotating structure, circularly arranged and eccentric to the rotation axis. The design of this magnetic actuator enables its application to parallel analyses, centrifugal microfluidics, etc. We have also fabricated a COC microfluidic device to carry out the enzymatic reaction and detection of a MB-based immunoassay. In this first development step of the magnetic actuator, the immunocomplex was formed off-chip and subsequently injected into the microfluidic device, where the MBs were used as an active agent to produce the mixing with the enzymatic substrate. In this way, we focused our efforts on the development of the actuator and its performance to improve an enzymatic reaction.

The use of the magnetic actuator demonstrated an enhancement of the enzymatic reaction at all the rotational speeds tested compared to a system only able to trap the MBs, which is the most common case scenario. The optimal movement velocity of MBs was found to be 1.7 mm/s. Calibration curves for *E. coli* O157:H7 whole cells were performed, showing a sensitivity enhancement of 2.7-fold at 1.7 mm/s with respect to the assay without mixing. The LOD achieved at this movement velocity was 603 CFU/mL, in contrast to the LOD

obtained without actuation, 2,101 CFU/mL, under the same conditions. The MBs used in this study are commercially available and can be purchased already functionalized with a variety of antibodies, hence making the use of the magnetic actuator directly applicable to other reactions.

The use of the magnetic actuator would facilitate the handling of the MBs, thus enabling an easier transition from the off-chip manual procedures to automated on-chip protocols. This would entail the characteristic advantages of lab-on-a-chip systems such as automation, lower consumption of reagents, portability, etc.

Current efforts focus on the optimization of the microfluidic device for the formation of the immunocomplex on-chip and automation of the whole immunoassay. This integration may highlight the enhancement provided by the magnetic actuator because the interactions between MBs and whole cells are not controlled by diffusion, unlike between small molecules, since their motion is very limited due to their large size [4]. Therefore, the collisions and binding events in stopped flow strongly depend on the movement of the MBs. The design of the microfluidic device could also be adapted to perform parallel or multiplex assays with the same actuator, by simply replicating the current design in a circular microfluidic platform.

References

1. Kovarik ML, Ornoff DM, Melvin AT, Dobes NC, Wang Y, Dickinson AJ, Gach PC, Shah PK, Allbritton NL (2012) Micro total analysis systems: fundamental advances and applications in the laboratory, clinic, and field. Anal Chem 85(2):451–472
2. Arora A, Simone G, Salieb-Beugelaar GB, Kim JT, Manz A (2010) Latest developments in micro total analysis systems. Anal Chem 82(12):4830–4847
3. Alegret S (2003) Integrated analytical systems, vol XXXIX. Comprehensive Analytical Chemistry. Elsevier, Amsterdam
4. Gehring AG, Tu S-I (2011) High-throughput biosensors for multiplexed food-borne pathogen detection. Annu Rev Anal Chem 4(1):151–172
5. Liébana S, Lermo A, Campoy S, Cortés MP, Alegret S, Pividori MI (2009) Rapid detection of Salmonella in milk by electrochemical magneto-immunosensing. Biosens Bioelectron 25(2):510–513
6. van Reenen A, de Jong AM, den Toonder JMJ, Prins MWJ (2014) Integrated lab-on-chip biosensing systems based on magnetic particle actuation—a comprehensive review. Lab Chip 14(12):1966–1986
7. Gijs MAM, Lacharme F, Lehmann U (2010) Microfluidic applications of magnetic particles for biological analysis and catalysis. Chem Rev 110(3):1518–1563
8. Choi J-W, Oh KW, Thomas JH, Heineman WR, Halsall HB, Nevin JH, Helmicki AJ, Henderson HT, Ahn CH (2002) An integrated microfluidic biochemical detection system for protein analysis with magnetic bead-based sampling capabilities. Lab Chip 2(1):27–30
9. Laczka O, Maesa J-M, Godino N, del Campo J, Fougt-Hansen M, Kutter JP, Snakenborg D, Muñoz-Pascual F-X, Baldrich E (2011) Improved bacteria detection by coupling magneto-immunocapture and amperometry at flow-channel microband electrodes. Biosens Bioelectron 26(8):3633–3640
10. Shikida M, Takayanagi K, Honda H, Ito H, Sato K (2006) Development of an enzymatic reaction device using magnetic bead-cluster handling. J Micromech Microeng 16(9):1875
11. Sen A, Harvey T, Clausen J (2011) A microsystem for extraction, capture and detection of E-Coli O157:H7. Biomed Microdevices 13(4):705–715
12. Sista RS, Eckhardt AE, Srinivasan V, Pollack MG, Palanki S, Pamula VK (2008) Heterogeneous immunoassays using magnetic beads on a digital microfluidic platform. Lab Chip 8(12):2188–2196
13. Saville SL, Woodward RC, House MJ, Tokarev A, Hammers J, Qi B, Shaw J, Saunders M, Varsani RR, St Pierre TG, Mefford OT (2013) The effect of magnetically induced linear aggregates on proton transverse relaxation rates of aqueous suspensions of polymer coated magnetic nanoparticles. Nanoscale 5(5):2152–2163
14. Yeap SP, Ahmad AL, Ooi BS, Lim J (2012) Electrosteric stabilization and its role in cooperative magnetophoresis of colloidal magnetic nanoparticles. Langmuir 28(42):14878–14891
15. Peyman SA, Iles A, Pamme N (2009) Mobile magnetic particles as solid-supports for rapid surface-based bioanalysis in continuous flow. Lab Chip 9(21):3110–3117
16. Vojtíšek M, Iles A, Pamme N (2010) Rapid, multistep on-chip DNA hybridisation in continuous flow on magnetic particles. Biosens Bioelectron 25(9):2172–2176
17. Karle M, Miwa J, Czilwik G, Auwarter V, Roth G, Zengerle R, von Stetten F (2010) Continuous microfluidic DNA extraction using phase-transfer magnetophoresis. Lab Chip 10(23):3284–3290
18. Sasso L, Johnston I, Zheng M, Gupte R, Ündar A, Zahn J (2012) Automated microfluidic processing platform for multiplexed magnetic bead immunoassays. Microfluid Nanofluid 13(4):603–612
19. Lai JJ, Nelson KE, Nash MA, Hoffman AS, Yager P, Stayton PS (2009) Dynamic bioprocessing and microfluidic transport control with smart magnetic nanoparticles in laminar-flow devices. Lab Chip 9(14):1997–2002
20. Ramadan Q, Gijs MAM (2011) Simultaneous sample washing and concentration using a "trapping-and-releasing" mechanism of magnetic beads on a microfluidic chip. Analyst 136(6):1157–1166
21. Verbarg J, Kamgar-Parsi K, Shields AR, Howell PB, Ligler FS (2012) Spinning magnetic trap for automated microfluidic assay systems. Lab Chip
22. Herrmann M, Veres T, Tabrizian M (2006) Enzymatically-generated fluorescent detection in micro-channels with internal magnetic mixing for the development of parallel microfluidic ELISA. Lab Chip 6(4):555
23. Herrmann M, Roy E, Veres T, Tabrizian M (2007) Microfluidic ELISA on non-passivated PDMS chip using magnetic bead transfer inside dual networks of channels. Lab Chip 7(11):1546
24. Herrmann M, Veres T, Tabrizian M (2008) Quantification of low-picomolar concentrations of TNF-α in serum using the dual-network microfluidic ELISA platform. Anal Chem 80(13):5160–5167
25. Toepke MW, Beebe DJ (2006) PDMS absorption of small molecules and consequences in microfluidic applications. Lab Chip 6(12):1484–1486
26. Mukhopadhyay R (2007) When PDMS isn't the best. Anal Chem 79(9):3248–3253
27. Feng P (1995) Escherichia coli serotype O157:H7: novel vehicles of infection and emergence of phenotypic variants. Emerging Infect Dis 1(2):47–52

28. Centers for Disease Control and Prevention () Reports of Selected E. coli Outbreak Investigations. http://www.cdc.gov/ecoli/outbreaks.html. Accessed 11 Dec 2013

29. Keene WE, McAnulty JM, Hoesly FC, Williams LP, Hedberg K, Oxman GL, Barrett TJ, Pfaller MA, Fleming DW (1994) A swimming-associated outbreak of hemorrhagic colitis caused by Escherichia coli O157:H7 and Shigella Sonnei. New Engl J Med 331(9):579–584

30. Ymbern O, Sandez N, Calvo-Lopez A, Puyol M, Alonso-Chamarro J (2014) Gas diffusion as a new fluidic unit operation for centrifugal microfluidic platforms. Lab Chip 14(5):1014–1022

31. Gomez-de Pedro S, Puyol M, Izquierdo D, Salinas I, de la Fuente JM, Alonso-Chamarro J (2012) A ceramic microreactor for the synthesis of water soluble CdS and CdS/ZnS nanocrystals with on-line optical characterization. Nanoscale 4(4):1328–1335

32. Baldrich E, Vigués N, Mas J, Muñoz FX (2008) Sensing bacteria but treating them well: determination of optimal incubation and storage conditions. Anal Biochem 383(1):68–75

33. Nunes P, Ohlsson P, Ordeig O, Kutter J (2010) Cyclic olefin polymers: emerging materials for lab-on-a-chip applications. Microfluid Nanofluid 9(2–3):145–161

34. Fonnum G, Johansson C, Molteberg A, Mørup S, Aksnes E (2005) Characterisation of Dynabeads® by magnetization measurements and Mössbauer spectroscopy. J Magn Magn Mater 293(1):41–47

35. De Las Cuevas G, Faraudo J, Camacho J (2008) Low-gradient magnetophoresis through field-induced reversible aggregation. J Phys Chem C 112(4):945–950

36. Faraudo J, Andreu JS, Camacho J (2013) Understanding diluted dispersions of superparamagnetic particles under strong magnetic fields: a review of concepts, theory and simulations. Soft Matter 9(29):6654–6664

37. Andreu JS, Barbero P, Camacho J, Faraudo J (2012) Simulation of magnetophoretic separation processes in dispersions of superparamagnetic nanoparticles in the noncooperative regime. J Nanomater 2012:10

38. Perez-Toralla K, Champ J, Mohamadi MR, Braun O, Malaquin L, Viovy J-L, Descroix S (2013) New non-covalent strategies for stable surface treatment of thermoplastic chips. Lab Chip 13(22):4409–4418

Versatile Lock and Key Assembly for Optical Measurements with Microfluidic Platforms and Cartridges

Oriol Ymbern, Miguel Berenguel-Alonso, Antonio Calvo-López, Sara Gómez-de Pedro, David Izquierdo and Julián Alonso-Chamarro.

167

Versatile Lock and Key Assembly for Optical Measurements with Microfluidic Platforms and Cartridges

Oriol Ymbern,[†] Miguel Berenguel-Alonso,[†] Antonio Calvo-López,[†] Sara Gómez-de Pedro,[†] David Izquierdo,[‡] and Julián Alonso-Chamarro*,[†]

[†]Sensors & Biosensors Group, Department of Chemistry, Universitat Autònoma de Barcelona, Edifici Cn, 08193 Bellaterra, Catalonia, Spain

[‡]Centro Universitario de la Defensa, Academia General Militar, Carretera de Huesca, s/n, 50090 Zaragoza, Spain

Ⓢ Supporting Information

ABSTRACT: A novel and versatile optical reader for microfluidic platforms is presented. The reader includes a modular insertion port based on the lock and key concept for reproducible alignment with a miniaturized optical detection system comprising an interchangeable light emitting diode (LED) and a photodiode. The modular nature of the insertion port allows the use of microfluidic platforms in variable shapes and fluidic configurations. Three different analytical methodologies based on absorbance or fluorescence measurements were used to demonstrate the flexibility and reproducibility of the proposed experimental setup.
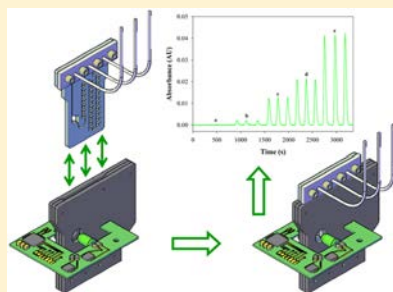
The miniaturization of (bio)analytical systems has substantial advantages[1,2] such as reduced sample and reagent consumption, response times, and costs, in addition to increased automation, reliability, and portability. The increasing trend toward miniaturization in this field has led to the development of microfluidic platforms affording integration and simplified automation of the whole analytical process. These miniaturized systems typically use optical detection methods[3,4] (particularly those based on absorbance or fluorescence measurements).[3,5−7] The growing progress in microelectronic, optoelectronic, and telecommunication technologies has enabled the development of improved small optical components meeting the requirements for incorporation into low-cost instruments.[3,8] Among others, such advances have facilitated the development of compact, robust, inexpensive equipment based on miniaturized analytical systems using light emitting diodes (LEDs) or LED lasers as light sources and photodiodes as sensitive detectors.[3,5,8]

A number of compact, monolithic analytical systems of this type have been reported[9−13] that are more than acceptable in regards to miniaturization, integration, and portability and have enabled convenient online, in situ, and field measurements. In fact, these systems perform quite well and provide adequate sensitivity and good precision. However, these miniaturized detection systems are specially designed for use at a single operating wavelength in a specific platform configuration and are thus scarcely versatile. In fact, altering the associated microfluidic design usually requires complete rearrangement of the optical components. Integrating LEDs of different wavelengths can increase versatility,[14] albeit at the expense of

increased complexity. Developing a customizable optical detection system capable of operating and at variable wavelength in different microfluidic manifolds would dispense with the need to redesign the whole detection system for each particular application.

This technical note reports a simple, versatile, inexpensive portable optical detection system for the readout of microfluidic platforms called "Optical Lock and Key Reader". The proposed system has several advantages such as the ability to operate under ambient light conditions, perform fluorescence and absorbance measurements, use different LEDs, interchange microfluidic platforms of variable shape and size, and precisely align the detection flow cell across the optical beam. A modular insertion port similar to a cuvette holder[15−17] or a cartridge reader[18] allows microfluidic platforms to be easily assembled and precisely aligned, thereby increasing the robustness of the ensuing measurements. Also, LEDs can be used in two different positions for absorbance and fluorescence measurements and be easily exchanged via a "plug and play" type mechanism. The operational principle of the proposed system presented in this work was validated by using various analytical methodologies. However, the system can be used for other, more complex analytical purposes (e.g., enzyme linked fluorescence immunoassay[19]) by adapting the proposed methodology to the microfluidic system of the platform concerned.
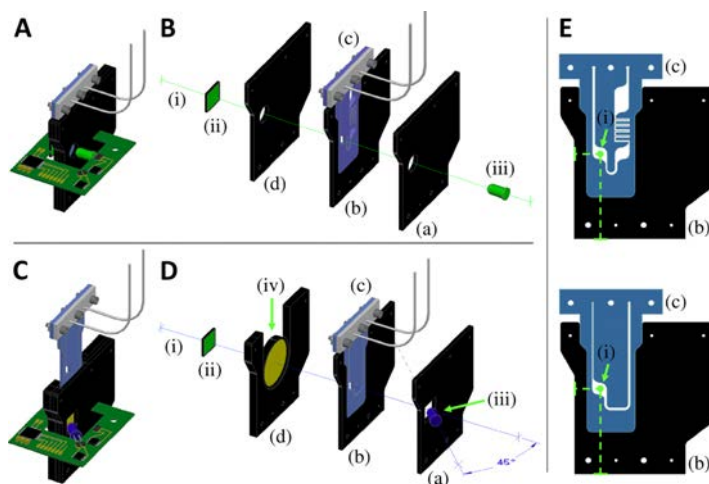
Figure 1. Schematic depiction of the lock and key concept. (A) Microfluidic platform inserted into a complementary "lock" structure. (B) Elements of the absorbance configuration as aligned with the (i) optical beam, (ii) photodiode, and (iii) LED. (a) Front mask, (b) lock piece of insertion port, (c) microfluidic platform, (d) back mask. (C) Platform upon insertion. (D) Elements of the fluorescence configuration: (ii) photodiode, (iii) LED aligned and tilted 45° with respect to (i), (iv) filter, (a) front mask, (b) lock piece, (c) microfluidic platform, (d) filter support. (E) Front view of the elements of the lock and key model. The "lock" piece (b) can be fitted with multiple platforms or cartridges (c) containing various microfluidic manifolds, but the flow cell is always perfectly aligned through the optical beam (i).

■ EXPERIMENTAL SECTION

Chemicals and Materials. All solutions used were prepared in double distilled water. 4-Methylumbelliferone (4-MU), potassium chloride (KCl), magnesium chloride hexahydrate ($MgCl_2 \cdot 6H_2O$), diethylamine, sulfanilamide (SAM), and N-α-naphthylethylenediamine (NED) were all purchased from Sigma-Aldrich (Barcelona, Spain). Sodium nitrite ($NaNO_2$) and orthophosphoric acid (H_3PO_4, 85%) were supplied by Panreac Química, S.A.U. (Barcelona, Spain). NitriVer 3 reagent was purchased from Hach Lange (Düsseldorf, Germany).

The colorimetric reagent used to determine nitrite ion in the continuous flow mode was a 1:15 NED/SAM mixture (3.9×10^{-3} M/5.8×10^{-2} M) in 1.4 M H_3PO_4 that remained stable for 2 weeks if stored refrigerated. Nitrite was determined in the batch mode by placing an amount of 2−5 mg of NitriVer 3 solid reagent in a special chamber of the microfluidic cartridge that was then sealed with Greiner EASYseal microplate sealer from Greiner Bio One (Wemmel, Belgium). Nitrite solutions were prepared on a daily basis by dilution in deaerated water of an appropriate volume of a stock solution containing 1000 mg L^{-1} of NO_2^-. Fluorescence determinations in the continuous flow mode were done by using 4-MU standard solutions prepared in DEA buffer (100 mM diethanolamine, 50 mM KCl, and 1 mM $MgCl_2$).

Cyclic Olefin Copolymer (COC) sheets and films in different grades and thicknesses were purchased from TOPAS Advanced Polymers GmbH (Florence, KY), and poly(methyl methacrylate) (PMMA) sheets were supplied by Plásticos Ferplast (Terrassa, Spain).

Microfluidic Platforms. The platforms were fabricated as described elsewhere.[20,21] The microfluidic systems of the different platforms or cartridges were designed by using Computer-Aided Design (CAD) software and machined onto three different layers of COC substrate on a Protomat C100/HF Computer Numerical Control (CNC) micromilling

machine from LPKF Laser & Electronics (Garbsen, Germany). Substrate layers were laminated and the platform microfluidic system sealed by using the temperature diffusion bonding technique,[20,21] which involves cross-linking polymer chains on layer surfaces under specific pressure and temperature conditions. The availability of COC in different grades[22] with also different glass transition temperatures (Tg) allowed platforms to be sealed with no deformation or minimal influence on the microfluidic system structure. COC grade 5013 was used for this purpose on the grounds of its good optical properties.[22] The central layer of TOPAS 5013 (Tg = 130 °C) was previously laminated on both sides with TOPAS 8007 film, which acted as a sealing agent by effect of its low Tg value (75 °C). The three layers were aligned and the microfluidic platform was sealed at 100 °C under a pressure of 6 bar.

For continuous flow injection, the microfluidic platform was connected with 0.8 mm internal diameter Teflon tubing (Scharlab, S.L., Cambridge, England) to an external peristaltic pump (Minipuls 3, Gilson, Wisconsin) fitted with Tygon tubing of 1.14 mm i.d. from Ismatec (Wertheim, Germany). A six-port injection valve from Hamilton MVP (Reno, NV) was used to inject standard solutions.

Optical Lock and Key Reader. A miniaturized optical detection system, described elsewhere,[23] was embedded in the proposed Optical Lock and Key Reader. It consisted of an interchangeable LED and a photodetector (viz., a PIN Hamamatsu S1337-66BR large active area photodiode) mounted and integrated on a printed circuit board (PCB). The LED was modulated by a sine wave signal generated by a data acquisition card (DAQ) (NI USB-6211, National Instruments, Madrid, Spain) and certain parameters (frequency and amplitude) can be changed in each measurement if necessary. The sampling frequency used to generate the modulation signal and digitalize the detected ones was adjusted

to 128 times the modulation frequency to avoid problems in synchronizing signals in the DAQ. Then, the DAQ transferred the modulation signals and each detected signal from the PCB to a computer, where they were processed with several lock-in amplifiers digitally implemented in a C sharp (C#) software application. Lock-in amplification facilitated processing of raw data, increased the signal-to-noise ratio, and afforded operation in ambient light without interferences.[21,23] The whole assembly was powered by the computer.

A B5-433-B525 LED from Roithner Lasertechnik (Vienna, Austria) with an emission peak at 525 nm was used for nitrite ion absorbance measurements because it matched the absorption maximum for the azo compound formed in the Griess reaction (540 nm). The LED was mounted in front of the photodetector (Figure 1A,B), leaving the optical flow cell of the polymeric microfluidic platforms between both components. Fluorescence measurements were made with an XSL-365-5E LED from Roithner Lasertechnik (Vienna, Austria) with an emission peak at 365 nm coinciding with the excitation wavelength of 4-MU.[24] The excitation LED was tilted by 45° from the normal to the optical flow cell in order to minimize interferences in the detector (Figure 1C,D). An MF460-60 band-pass emission filter from Thorlabs (Munich, Germany) was used to prevent excitation light from reaching the detector, and the maximum fluorescence emission of 4-MU peaks at 445 nm.[24] In both cases, the LED was mounted into a socket connector on the surface of the PCB that fitted the LED leg pins together.

The PCB was embedded in a customized PMMA structure (Figure 2A) that additionally accommodated the lock and key insertion port for the microfluidic platform and the optical filter

Figure 2. (A) Photograph of the Optical Lock and Key Reader during the reading process showing the microfluidic platform inserted in the insertion port. (B) Schematic depiction of the insertion port. The "lock" piece (b) can be designed, when required, to hold variably sized and shaped microfluidic platforms or cartridges. In some configurations, the dimensions X' and Y' can be modified. The X and Y dimensions remain constant with respect to the center of the optical beam (i). (C and D) Schematic depiction of "key" microfluidic platforms (c) and "lock" pieces (b) with a complementary shape of the insertion port.

when required. The structure was designed by using CAD software and fabricated on the CNC milling machine.
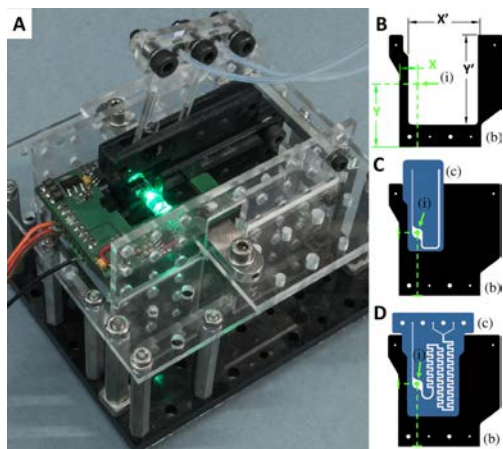
RESULTS AND DISCUSSION

Design of the Optical Lock and Key Reader. The reader consists of two essential components, namely, (a) a miniaturized optical detection system including a PCB, an optical filter, required for fluorescence measurements, and a DAQ and (b) an insertion port for the microfluidic platforms and a support structure for embedding the PCB.

The most salient advantages of the optical detection system are its good performance and the ability to operate under ambient light conditions. Moreover, the use of a lock-in amplification via computer software and a DAQ is a low cost solution to reduce noise instead of a commercial lock-in amplifier. The versatility of the proposed system can also be increased by using exchangeable LEDs to monitor a wide range of analytical processes. Also, the LED can be positioned at two different angles with respect to the optical beam (Figure 1), namely, normal to the flow cell for absorption measurements and tilted 45° for fluorescence measurements. In the latter, the design of the insertion port allows an optical filter to be fitted between the optical detection flow cell and the detector (see Figure 1) in order to suppress reflected light from the excitation LED. The versatility of the proposed system allows it to be further modified to improve the quality of the optics and their sensitivity to some extent.[3,5,8] Also, collimation, focusing and the use of apertures or light baffles is possible, albeit at the expense of greater instrumental complexity.

One major advantage of the reader is that the microfluidic platform can be accurately, reproducibly positioned for correct alignment of the optical detection flow cell along the optical beam. This is a result of the insertion port having a lock and key design (Figure 1E). Thus, microfluidic platforms, the "key", and the insertion port, the "lock", have complementary shapes so that the former can fit exactly into the latter. An offset of 100 μm is used to make the insertion port wider than the microfluidic platform in order to avoid friction and facilitate the insertion and ejection. The system affords exact alignment and hence repeatable insertion of platforms for accurate optical readings. The results thus obtained are described in detail under Alignment Repeatability of the Optical Lock and Key Reader.

The microfluidic platforms can accommodate microfluidic patterns of variable complexity; however, the detection flow cell is always placed in the same relative position (Figure 1E). If needed, the size and geometric shape of the microfluidic platform can be modified for fitting to more complex microfluidic manifold configurations. In this situation, the modular design of the insertion port facilitates replacement of the "lock" structure or piece (see Figure 2). The essential requirement to be met in designing the microfluidic platform and the complementarily shaped insertion port is that the optical detection flow cell should be placed at the center of the optical beam (X and Y in Figure 2B), dimensions X' and Y' can be altered to fit different platform configurations. If necessary, an additional dimension Z' can be introduced by increasing the thickness of the lock piece. This flexibility makes the Optical Lock and Key Reader a versatile tool for optical measurements on a wide variety of microfluidic platforms specially designed for specific analytical methodologies. Also, measurements can be performed in the continuous flow or batch mode, which

increases the potential of the Optical Lock and Key Reader even further.

Analytical Validation of the Optical Lock and Key Reader. The performance of the proposed reader was validated by using it to implement various analytical methodologies based on absorbance or fluorescence measurements. We used 4-methylumbelliferone (4-MU) as the analyte for fluorescence measurements and nitrite ion (NO_2^-) as the analyte for absorbance measurements. Three different microfluidic systems were constructed for use in the batch or continuous flow mode. Batch absorbance measurements were made by loading the platform at the reader insertion port after the end of the indicator reaction. However, the continuous flow mode was preferred for optimal monitoring of the dynamic process by making repeated optical measurements of absorbance or fluorescence intensity. In addition, using the continuous flow injection technique afforded peak height measurements and hence obtaining the desired analytical information while monitoring baseline stability in a simple, expeditious manner.

Fluorescence Tests. The performance of the Optical Lock and Key Reader in fluorimetric measurements was assessed with 4-methylumbelliferone (4-MU), which is a widely used standard for fluorimetric determination of enzyme activities.[24] The reagent was used in DEA buffer (pH 7.0−10.5) in order to operate under the conditions of maximum quantum yield and emission intensity.[24]

Fluorimetric Measurements in the Continuous Flow Mode. A simple microfluidic platform consisting of an inlet, a microfluidic channel, an optical detection flow cell, and an outlet (Figure 3B) was constructed for this purpose. The
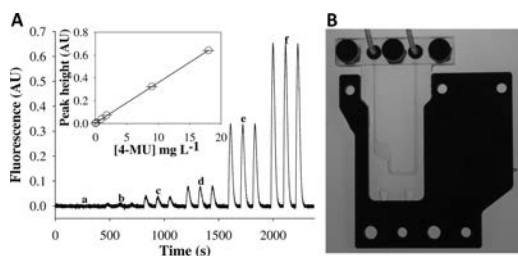
Figure 3. (A) Signal recording obtained from the fluorescence measurements made with the Optical Lock and Key Reader. All solutions [(a) 0 mg L^{-1}, (b) 0.2 mg L^{-1}, (c) 0.9 mg L^{-1}, (d) 1.8 mg L^{-1}, (e) 9 mg L^{-1}, and (f) 18 mg L^{-1}] were injected in triplicate. The inset shows the linear response of fluorescence intensity to the 4-MU concentration. (B) Image of the microfluidic platform for fluorescence measurements and the lock piece.

platform was fabricated as described above and met the specific requirements for fitting into the lock insertion port. The DEA carrier solution, where the 4-MU standard solutions were injected, was pumped into the microfluidic device through the inlet. The injected volume was 100 μL and the overall flow rate 800 μL min^{-1}. A fluorescence signal was continuously recorded by keeping the microfluidic platform inserted in the reader.

Figure 3A shows the calibration curve obtained, which fitted the equation $F = 0.0354 [4\text{-MU}] + 0.0034$ with a coefficient of determination $r^2 = 0.9998$. The curve was linear over the 4-MU concentration range 0.8−18 mg L^{-1}, and the limit of detection (LOD) obtained was 0.2 mg L^{-1}. Repeatability was assessed from repeated injections ($n = 9$) of a 9 mg L^{-1} of 4-MU

solution. A relative standard deviation (RSD) of 1.62% was obtained.

Absorbance Tests. Nitrite ion (NO_2^-) was determined colorimetrically using the Griess reaction. This reducing agent is widely used by the food production industry to prevent bacterial growth.[25] The Griess reaction involves the formation of a diazonium salt between sulfanilamide (SAM) and nitrite ion that subsequently forms a red azo compound with the azo dye NED in an aqueous acid medium.[25]

Colorimetric Measurements in the Continuous Flow Mode. The continuous flow determination of nitrite ion was performed in a microfluidic system consisting of two inlets, a two-dimensional meander micromixer, an optical flow cell, and one outlet (Figure 4B). As before, the platform was constructed
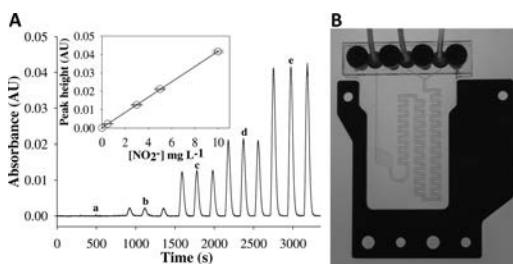
Figure 4. Signal recording obtained from nitrite ion measurements in the continuous flow mode. All solutions [(a) 0 mg L^{-1}, (b) 0.5 mg L^{-1}, (c) 3 mg L^{-1}, (d) 5 mg L^{-1}, (e) 10 mg L^{-1})] were injected in triplicate. The inset shows the linear calibration curve obtained. (B) Image of the microfluidic platform and the lock piece with a complementary shape of the insertion port.

in accordance with the above-described specifications. The two inlets were used to deliver nitrite ion standards of variable concentration, or water as a carrier, and the Griess reagent. The two solutions were mixed at a merging point and the micromixer before reaching the optical flow cell for continuous recording of the absorbance. The injected volume was 100 μL and the overall flow rate 500 μL min^{-1}.

Figure 4A shows the calibration curve obtained, which fitted the equation $A = 0.0042 [NO_2^-] + 0.0001$ with $r^2 = 0.9996$. The linear range was 0.5−10 mg L^{-1} and the LOD 0.1 mg L^{-1}. An RSD less than 1% was calculated from repeated injections ($n = 5$) of a 5 NO$_2^-$ mg L^{-1} solution.

Colorimetric Measurements in the Batch Mode. The microfluidic platform for determining NO$_2^-$ in the batch mode was constructed in a disposable microfluidic cartridge configuration. The microfluidic system included an inlet, a reagent storage chamber, an optical detection flow cell, an outlet, and a simple microfluidic channel connecting all elements (Figures 5B,C). The analytical procedure started with deposition of NitriVer 3 in the reagent storage chamber, which was then sealed with an adhesive foil for microplates. Next, 120 μL of a nitrite ion standard solution at an appropriate concentration was loaded in the microfluidic cartridge to dissolve the preloaded solid reagent and form the colored product to be measured at the optical detection flow cell. After the reaction product was obtained, the microfluidic cartridge was inserted and ejected in triplicate in the Optical Lock and Key Reader for measurement (3 s per replicate).

Eight different nitrite concentrations were measured to construct the calibration curve of Figure 5A. The above-
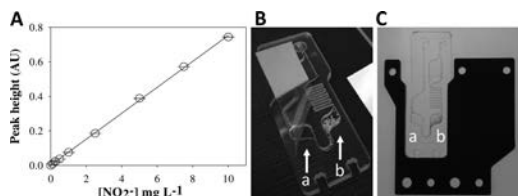
Figure 5. (A) Calibration curve for the determination of nitrite ion in the batch mode. All solutions (0.1, 0.25, 0.5, 1, 2.5, 5, 7.5, and 10 mg L^{-1} of NO$_2^-$) were measured in triplicate. (B and C) Images of the microfluidic cartridge and the lock piece for batch absorbance measurements showing (a) the optical flow cell and (b) the reagent storage chamber.

described overall procedure was followed to measure each individual nitrite ion standard solution in triplicate. A linear response was thus obtained over the concentration range 0.1–10 mg L^{-1} that fitted the equation $A = 0.0751[NO_2^-] + 0.0015$ with $r^2 = 0.9995$. The calculated limit of quantitation (LOQ) and detection (LOD) for nitrite ion was 0.05 and 0.002 mg L^{-1}, respectively. Repeatability was assessed by repeating the whole analytical process 9 times with a standard solution containing 2.5 mg L^{-1} of NO$_2^-$ and calculated to be 3% as RSD ($n = 9$).

The results were compared between the continuous flow and batch modes. The path length of the microfluidic platform was 1 mm in both modes. The differences in LOD can be ascribed to differences in reaction time and dilution factor between the two modes. The latter depends on sample injection volume, flow rate, and microfluidic manifold used. Obviously, a better LOD was obtained in the batch mode. The sample is not diluted while mixing with NitriVer 3 solid reagent and the cartridge is read when reaction time is attained. On contrast, the transient signal obtained in the continuous flow mode is affected by sample volume injected and dilution suffered by the sample in the micromixer, both chemical and hydrodynamic variables.

Alignment Repeatability of the Optical Lock and Key Reader. As stated under Design of the Optical Lock and Key Reader, we assessed the influence on measurement reproducibility of the insertion/ejection procedure of the microfluidic platform into/from the insertion port. A cartridge was loaded with a 2.5 mg L^{-1} NO$_2^-$ standard solution as described under Colorimetric Measurements in the Batch Mode. Once the resulting colored product was formed, the cartridge was successively inserted and ejected 9 times. Absorbance measurements were found to be subject to an RSD less than 1% ($n = 9$). On the basis of these results, it can be affirmed that the insertion port permits a reproducible alignment with the flow cell and the optical beam.

The overall results testify to the analytical viability and versatility of the Optical Lock and Key Reader in terms of linear ranges and detection limits. Also, the low RSD values obtained confirm the reproducibility of both the optical measurement process and the insertion/ejection procedure. Furthermore, the reader can be adapted to more complex analytical procedures when needed, as it has been demonstrated.[19]

CONCLUSIONS

The proposed Optical Lock and Key Reader is a simple, robust, versatile, inexpensive system for batch or continuous absorbance and fluorescence measurements on microfluidic

devices. Alignment problems are minimized by using a modular insertion port to facilitate rearrangement of the system with multiple microfluidic platforms. In this way, the usefulness of the system is not limited to a single optical detection setup with exchangeable LEDs; rather, the reader is open to further modification and integration of supplementary optical components with a view to expanding the range of analytical procedures amenable to implementation on these microfluidic platforms.

ASSOCIATED CONTENT

Ⓢ Supporting Information

Figure S1 and movie file with an animated sequence of schematic illustrations showing the modular configuration of the Optical Lock and Key Reader for microfluidic platforms and cartridges. This material is available free of charge via the Internet at http://pubs.acs.org.

AUTHOR INFORMATION

Corresponding Author

*E-mail: julian.alonso@uab.cat. Fax: +34 935812149. Phone: +34 935812477.

Author Contributions

The manuscript was written and its final version approved by all authors. Also, all authors contributed equally to the work reported herein.

Notes

The authors declare no competing financial interest.

ACKNOWLEDGMENTS

REFERENCES

(1) Manz, A.; Eijkel, J. C. T. *Pure Appl. Chem.* **2001**, *73* (10), 1555–1561.
(2) de Mello, A. J. *Nature* **2006**, *442*, 394–402.
(3) Mogensen, K. B.; Kutter, J. P. *Electrophoresis* **2009**, *30*, S92–S100.
(4) Baker, C. A.; Duong, C. T.; Grimley, A.; Roper, M. G. *Bioanalysis* **2009**, *1* (5), 967–975.
(5) Kuswandi, B.; Nuriman; Huskens, J.; Verboom, W. *Anal. Chim. Acta* **2007**, *601*, 141–155.
(6) Myers, F. B.; Lee, L. P. *Lab Chip* **2008**, *8*, 2015–2031.
(7) Szczypiński, R.; Mik, Ł.; Kruk, J.; Baszczyk, M.; Dorosz, P.; Głab, S.; Pijanowsk, D. G.; Kucewicz, W. *Przegl. Elektrotech.* **2012**, *10b/2012*, 88–91.
(8) Kulmala, S.; Suomi, J. *Anal. Chim. Acta* **2003**, *500*, 21–69.
(9) Dasgupta, P. K.; Eom, I.; Morris, K. J.; Li, J. *Anal. Chim. Acta* **2003**, *500*, 337–364.
(10) de Lima, K. M. G. *Microchem. J.* **2012**, *103*, 62–67.
(11) Fonseca, A.; Raimundo, I. M., Jr. *Anal. Chim. Acta* **2007**, *596*, 66–72.
(12) Yang, F.; Pan, J.; Zhang, T.; Fang, Q. *Talanta* **2009**, *78*, 1155–1158.
(13) Ramírez-García, S.; Baeza, M.; O'Toole, M.; Wu, Y.; Lalor, J.; Wallace, G. G.; Diamond, D. *Talanta* **2008**, *77*, 463–467.

172

(14) da Rocha, Z. M.; Martinez-Cisneros, C. S.; Seabra, A. C.; Valdés, F.; Gongora-Rubio, M. R.; Alonso-Chamarro, J. *Lab Chip* **2012**, *12*, 109−117.

(15) Aline, Inc. http://www.alineinc.com/products/ (accessed October 14, 2014).

(16) Avid Nano. http://www.avidnano.com/knowledge/technology/ (accessed October 14, 2014).

(17) Hou, H. H.; Yang, R. J.; Fu, L. M.; Tsai, C. H.; Lin, C. F.; Tai, C. H. Disposable Glucose Concentration Detection Microfluidic Chip Fabricated by CO_2 Laser Ablation. In *ICABE Conference Advances in Biomedical Engineering*, 2011; Vol. *1−2*, pp 503−506.

(18) Glynn, M. T.; Kinahan, D. J.; Ducrée, J. *Lab Chip* **2013**, *13*, 2731−2748.

(19) Berenguel-Alonso, M.; Granados, X.; Faraudo, J.; Alonso-Chamarro, J.; Puyol, M. *Anal. Bioanal.Chem.* **2014**, *406* (26), 6607−6616.

(20) Steigert, J.; Haeberle, S.; Brenner, T.; Müller, C.; Steinert, C. P.; Koltay, P.; Gottschlich, N.; Reinecke, H.; Rühe, J.; Zengerle, R.; Ducrée, J. *J. Micromech. Microeng.* **2007**, *17*, 333−341.

(21) Ymbern, O.; Sández, N.; Calvo-López, A.; Puyol, M.; Alonso-Chamarro, J. *Lab Chip* **2014**, *14*, 1014−1022.

(22) TOPAS Advanced Polymers. http://www.topas.com/ (accessed October 14, 2014).

(23) Gómez-de Pedro, S.; Puyol, M.; Izquierdo, D.; Salinas, I.; de la Fuente, J. M.; Alonso-Chamarro, J. *Nanoscale* **2012**, *4*, 1328−1335.

(24) Zhi, H.; Wang, J.; Wang, S.; Wei, Y. *J. Spectrosc.* **2013**, 147128.

(25) Xi, Y.; Templeton, E. J.; Salin, E. D. *Talanta* **2010**, *82*, 1612−1615.

173

Automatic microfluidic system to perform multi-step magneto-biochemical assays

Sara Gómez-de Pedro, Miguel Berenguel-Alonso, Pedro Couceiro, Julián Alonso-Chamarro and Mar Puyol.

Automatic microfluidic system to perform multi-step magneto-biochemical assays

CrossMark

S. Gómez-de Pedro, M. Berenguel-Alonso, P. Couceiro, J. Alonso-Chamarro, M. Puyol*

Sensors & Biosensors Group, Department of Chemistry, Autonomous University of Barcelona, Edifici Cn, 08193 Bellaterra, Catalonia, Spain

A R T I C L E   I N F O

A B S T R A C T

A simple and automatic microfluidic system to perform a multistep colorimetric magnetic bead-based enzyme-linked oligonucleotide sandwich assay in a short analysis time is reported. As a proof of concept of the advantages of miniaturizing and automating bio-chemical assays, the determination of an *Escherichia coli* oligonucleotide has been addressed. Moreover, the use of magnetic beads allows simplification of the required cleaning steps as well as the application of an active mixing strategy, based on magnetic beads manipulation by a magnetic actuator, which enhances the reagents mixture inside the microsystem. The presented microsystem allows reducing the analysis time to less than thirty minutes with a detection limit in the nanomolar range. Moreover, the different elements employed for the set-up are based on low cost components, which also minimizes the total costs of the proposed approach.

© 2017 Elsevier B.V. All rights reserved.

1. Introduction

The use of hybridization methods in biochemical, clinical and forensic diagnosis [1–4] as well as in the identification of food-borne or environmental pathogens [5] has demonstrated many advantages regarding other bioanalytical methods, since they depend on the recognition of unique gene sequences of specific strains of organisms [6]. Compared to immunological methods, they are faster and show higher specificity, sensitivity and lower cross-reactivity [7–9]. Polymerase chain reaction (PCR) [10–12] and microarray-based DNA chips [13] are the gene sequence-based methods currently used to detect specific strains of indicator bacteria in water. The first ones present many advantages over traditional detection methods, such as sensitivity and speed. However, they still involve expensive and complicated protocols, which must be performed by skilled personnel [14]. On the other hand, microarray-based DNA chips have demonstrated high-throughput and DNA multiplexing analysis, but they are limited by their high cost and reproducibility [15]. Moreover, these methods normally require several hours to perform the entire analysis because the immobilization of the target by the capture probe is an unfavourable process, largely limited by diffusion [16].

Microfluidic systems can overcome these limitations while allowing automation of the entire bioassay [17]. Since channel distances are on the micrometer range, the use of such devices shortens diffusion distances, improving mass transport, and therefore, considerably reducing hybridization time [18]. In addition, miniaturization and microfluidics entail some well known benefits such as the use of smaller chemicals amounts (which is of special importance when expensive reagents are required) which leads to lower waste generation, while reduction the power consumption. For this reasons, several microfluidic approaches have been proposed. Microfluidic diffusion based platforms, where the biological material is immobilized into the microchannel walls [19,20], present improved selectivity but the incubation times are still controlled by slow diffusion processes. Continuous flow microfluidic devices can overcome this limitation using mixing strategies, such the use of microfluidic meanders in continuous flow [21,22], or the use of microvalves and micropumps in sequenced flow to increase chaotic advection [23]. However, continuous flow microsystems originate an excessive intake of expensive bioreagents. In order to solve this limitations, super-paramagnetic microparticles and magnetic beads (MBs), modified with biologic material [24,25], have been used as mobile substrates in microfluidic systems. The magnetic core of these particles allow their easy manipulation using external magnetic fields, while enhancing the assay's sensitivity and detection limit due to their large surface-to-volume ratio [26].

Herein, we report a simple, low cost and automatic microfluidic system for the specific determination of oligonucleotides [27,28] in

* Corresponding author.
 E-mail address: mariadelmar.puyol@uab.cat (M. Puyol).

176

a short analysis time by using a colorimetric magnetic bead-based enzyme-linked oligonucleotide sandwich assay. The determination of an *Escherichia coli* (*E. coli*) DNA oligonucleotide was chosen, since *E. coli* is used as indicator of water quality in routine analysis [29]. The proposed approach uses MBs as active agents for the control and transport of reagents during the oligonucleotide incubations and enzymatic reaction stages, as well as retention structures for the required cleaning steps of the assay. MBs are manipulated inside the microfluidic system by controlling the rotational speed of an integrated external magnetic actuator [30]. Furthermore, the different stages of the assay have been automated, which improves the reproducibility of the system.

2. Materials and methods

2.1. DNA oligonucleotides and chemicals

Carboxylic acid modified MBs (2.8 μm diameter, 2×10^9 beads mL^{-1}) (Dynabeads® M-270 Carboxylic Acid) were purchased from Invitrogen Dynal AS (Oslo, Norway). All ssDNA sequences from *E. coli* were provided deprotected and desalted (HPLC purification) from Sigma-Aldrich (Madrid, Spain). Three different probe sequences were acquired: capture (5′-CCGCAGCAGGGAGGCAAACA-(CH$_2$)$_7$-NH$_2$-3′), target (5′- TGTTTGCCTCCCTGCTGCCGGTTTTTCACCGA AGTTCATGCCAGTCCAGCGTTTTTGCAGCAGAAAAGCCGCC-GACTTCGGTTTGCGGTCGCGGGTGAAGATCCCCTTCTTGTTA CCGCCAACGCGCAATATGCCTTGCGAGGTCGCAAA ATCGGCGAAATTCCATA-3′) and probe (5′-biotin-TATGGAATTTCGCCGATTTT-3′). Capture and probe sequences were complementary to the beginning and end of the target sequence, respectively. Streptavidin- β-galactosidase conjugate (lyophilized powder), o-nitrophenyl β-D-galactopyranoside (ONPG), *N*-hydroxysulfosuccinimide (Sulfo-NHS), 1-ethyl-3-[3-dimethylaminopropyl]carbodiimide (EDC), bovine serum albumin (BSA), potassium chloride (KCl), magnesium sulphate (MgSO$_4$), sodium phosphate dibasic (Na$_2$HPO$_4$), sodium phosphate monobasic (NaH$_2$PO$_4$) as well as 2-(*N*-morpholino)ethanesulfonic acid (MES), tris(hydroxymethyl)aminomethane (Tris), phosphate buffered saline (PBS) with Tween® 20 (P3563), saline-sodium citrate (SSC) buffer 20x (S6639) and casein blocking buffer 10x (B6429) were also purchased from Sigma-Aldrich. Milli-Q water (18.2 MΩ cm) was used in all solutions.

2.2. Sample and buffer preparation

Buffer solutions of MES (25 mM at pH 5.0), Tris (50 mM at pH 7.4) and PBS (0.01 M with Tween® 20 and 2% BSA at pH 7.4) were prepared for the functionalization of MBs. A 5x SSC buffer solution (750 mM NaCl and 75 mM sodium citrate solution at pH 7) was used as hybridization buffer. Z-buffer solution, used as amplification buffer in the enzymatic reaction, consisted on 100 mM PO$_4$³⁻, 20 mM KCl and 1 mM MgSO$_4$ at pH 7.0. A 1x casein blocking buffer solution was prepared for the microfluidic platform conditioning.

The different lyophilized oligonucleotides were re-suspended in sterile water and frozen at −20 °C in 100 μL aliquots of 100 μM concentration until further use. The required target and probe oligonucleotide solutions were obtained by dilution using 5x SSC buffer. For the probe, a final concentration of 200 nM was prepared, while 10, 20, 30, 40 and 50 nM solutions were prepared for the target oligonucleotide. The capture sequence solution used had the same concentration as the solutions stored in the freezer.

A 1.5 μg μL^{-1} streptavidin-β-galactosidase conjugate solution was prepared in z-buffer, and the substrate (ONPG) was used in a 30 mM concentration.

2.3. Functionalization of microbeads

Conjugation of the MBs with the capture probe was performed prior to the DNA assay. The immobilization of the DNA probe onto the surface of the particles was carried out by a procedure recommended by Invitrogen Dynal. It consists on the activation of the carboxylic acid-beads with a carbodiimide followed by covalently coupling the amine of the capture oligonucleotide, resulting in a stable amide bond between the bead and the capture.

First, 100 μL (3 mg) of carboxylic acid-MBs solution were placed in a 1.5 mL Eppendorf tube. Then, the supernatant was pipetted off from the Eppendorf while trapping the beads with a magnet, and after that, 100 μL of a 25 mM MES buffer solution at pH 5.0 were added. The re-suspended particles were placed in a Thermomixer (Eppendorf, Hamburg, Germany) and rocked for 5 min at 850 rpm. This washing process was carried out by triplicate. Later, 21 μL of a 100 μM (2.1 nmols) capture oligonucleotide solution were added to the cleaned and dried MBs and brought to a final volume of 100 μL with MES solution. The mixture was incubated in the Thermomixer during 30 min under the same rocking conditions as before to immobilize the DNA probe on the surface of the paramagnetic beads by electrostatic interactions. Then, 3 mg of EDC recently weighted and 9 mg of sulfo-NHS were added to the incubated solution and rocked again during 12 h to ensure the complete formation of the amide. The supernatant was removed again, and 100 μL of 50 mM Tris solution at pH 7.4 were added to the Eppendorf. The solution was rocked for 10 min in order to block the remaining carboxylic acid groups of MBs. Once discarded the excess of Tris, a PBS blocking buffer (0.01 M of PBS with Tween® 20 solution and 2% BSA) was used to clean the conjugated MBs (in triplicate). Finally, the capture-functionalized beads were re-suspended in SSC buffer and washed again in triplicate. All procedure was carried out at room temperature. The obtained capture probe functionalized MBs (MBs-capture) were stored at 4 °C until their use.

2.4. Microfluidic platform

The microfluidic platform was designed using Computer-Aided Design (CAD) software. Cyclic Olefin Co-polymer (COC) grade 5013 (TOPAS Advance Polymers GmbH, KY, US) was used as the substrate material. The device consisted of three COC layers: a top lid, containing the different inlets and the outlet; the middle layer, containing the main fluidic elements of the device, such as the chambers and channels, and the bottom lid, which only had a structural function. The different microfluidic elements were machined onto the three different layers using a Computer Numerical Control (CNC) micromilling machine Protomat C100/HF (LPKF Laser & Electronics, Garbsen, Germany). The device was sealed by thermal bonding, at 100 °C and 6 bar, as described elsewhere [31].

2.5. Microsystem set-up

A scheme of the entire set-up is shown in Fig. 1A. It is composed of a fluidic injection system, a microfluidic platform, a magnetic actuator and a miniaturized optical system. The fluidic injection system consisted of a set of seven syringe pumps (540060 TSE systems, Bad Homburg Germany) where 1, 2 or 10 mL syringes (Hamilton series GASTIGHT 1000 TLL, Bonaduz, GR, Switzerland) where mounted. The syringes were connected to the polymeric microfluidic platform by polytetrafluoroethylene (PTFE) tubes (i.d. 0.9 mm). The syringe pumps where computer controlled allowing the use of continuous or stop flow modes for each solution or suspension (MBs-capture, target, probe, enzyme, substrate and buffers). Additionally, a three-way valve and a T-shape connector were also used to select the proper buffer solution.
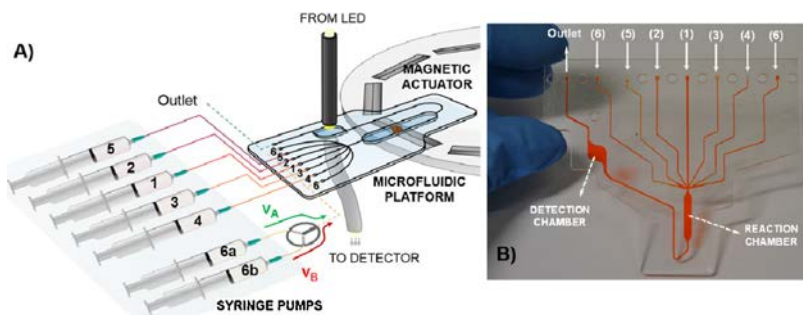
Fig. 1. (A) Scheme of the experimental set-up, where the microfluidic platform, magnetic actuator, optical components and flow managing system are depicted. (B) Photograph of the microfluidic platform, where the seven different inlets, the reaction chamber, the optical detection chamber and the outlet are tagged. Syringe reagents: 1: MBs-Capture; 2: Target; 3: Probe-Biotin; 4: Streptavidin-Enzyme; 5: ONPG; 6a: SSC buffer and 6b: z-buffer.

The magnetic actuator used is described elsewhere [30]. Briefly, it consists of a rotating unit, where a set of neodymium iron boron block magnets grade N50 (Chen Yang Technologies GmbH, Finsing, Germany) are placed eccentrically to the rotation axis. The rotational movement is provided by a D. C. geared motor from Crouzet (Farnell, Barcelona, Spain). When the microfluidic device is mounted on top of the actuator (fixed to a support), the reaction chamber is positioned on top of the magnets, under the influence of their magnetic field. The position of the inner and outermost magnets coincides with both extreme positions of the reaction chamber, so that when the magnetic actuator rotates, the MBs are dragged back and forth. In this way, an average linear velocity of the MBs can be calculated.

The miniaturized optical system employed for the on-line absorbance measurements [32] consists of a 420 nm Light Emitting Diode (LED) (LED420-33 Roithner Lasertechnik, Vienna, Austria) and a photodetector (PIN Hamamatsu S1337-66BR) mounted in a Printed Circuit Board (PCB). The LED is modulated by a Data Acquisition Card (DAQ), which transfers the detected signal from the PCB to a computer, where it is processed. Data acquisition is also computer controlled. Two optical fibres (1 mm of diameter) are used in order to bring light from the emitting source to the microfluidic platform and to collect the transmitted light to the detector. Both fibres are fixed on the top and bottom of the optical detection chamber of the microfluidic system by means of a PMMA connection adaptor.

3. Results and discussion

3.1. Microfluidic platform design

From the variety of materials substrates that can be employed to fabricate the microfluidic platform, COC was selected because of its high transparency in the UV–vis region and because it involves a simple fabrication procedure based on a multilayer approach. Various COC grades are commercially available, differing essentially in their heat deflection temperature, which is determined by the ratio of the co-monomers. COC grades with lower heat deflection temperature can be used as sealing layers during the bonding process. This is a great advantage of COC in front of other thermoplastic materials, as it avoids the occlusion of the microfluidic structures when using thermal bonding processes or glues to seal the microfluidic devices, while assuring a perfect sealing. On the other hand, COC shows low water absorption and biological compatibility, which make it an ideal substrate for bioanalytical applications.

The microfluidic platform is composed of seven different inlets, which converge in a reaction chamber. Five of the inlets (**1–5** inlets in Fig. 1) are used to feed the chamber with the different necessary

reagents: MBs-capture, target, probe, enzyme and substrate solutions. Only the MBs-capture solution must be inserted through a straight channel to avoid the possible deposition of the beads in corners or irregularities on the walls (inlet **1** in Fig. 1B). Inlets 6 (Fig. 1) are used for the buffer solutions insertion, and are located on opposite sides to ensure the correct cleaning of the reaction chamber before starting a new reaction step. The reaction chamber of 25 μL (2 mm wide, 12 mm long and 1 mm high) is therefore employed for the incubation, cleaning and amplification steps, while the magnetic actuator located directly below it automatically activates the motion or retains the MBs inside the chamber depending on the required process step [30]. At the outlet of the reaction chamber, an optical detection chamber of 25 μL is designed to match the optical fibres core to correctly perform the absorption measurements. A picture of the entire microfluidic platform is shown in Fig. 1B.

3.2. Assay procedure

A sequential approach was used to carry out the magnetic bead-based enzyme-linked oligonucleotide sandwich assay. Three different stages were required, each consisting on an incubation and a washing step. A final amplification stage was also required to obtain the colorimetric compound.

The determination of *uid* gene was employed to perform the assay, since it is commonly used in diagnostic methods for *E. coli* DNA detection. Concretely, a 166-bp structural fragment of the *uid A* gene was used, located at the carboxyl coding region, which has been reported to be unique and conserved in general *E. coli* [27,28]. Complementary fragments of 20-bp were used to selectively identify the beginning and end of the gene fragment. All sequences are described below, where both complementary regions have been underlined.

Capture *E. coli DNA*: 5′-<u>CCGCAGCAGGGAGGCAAACA</u>-(CH2)7-NH2-3′

Target *E. coli DNA*: 5′-<u>TGTTTGCCTCCCTGCTGCGG</u>TTTTTCACCGAAGTTCATGCCAGTCCAGCGTTTTTGCAGCAGAAAAGCCGCCGACTTCGGTTTGCGGTCGCGGGTGAAGATC-CCCTTCTTGTTACCGCCAACGCGCAATATGCCTTGCGAGGTCGC<u>AAAATCGGCGAAATTCCATA</u>-3′

Probe *E. coli DNA*: 5′-biotin-<u>TATGGAATTTCGCCGATTTT</u>-3′

As it can be observed, capture oligonucleotide was provided with an aliphatic chain spacer bearing a final primary amine in order to form an amide with the carboxylic acid of the MBs. The probe was provided functionalized with biotin in order to bind the enzyme, which bears a streptavidin protein, by means of the well-known and strong non-covalent interaction of both compounds.

Once the three oligonucleotide sequences are hybridized and conjugated to the enzyme, the colorimetric enzymatic reaction
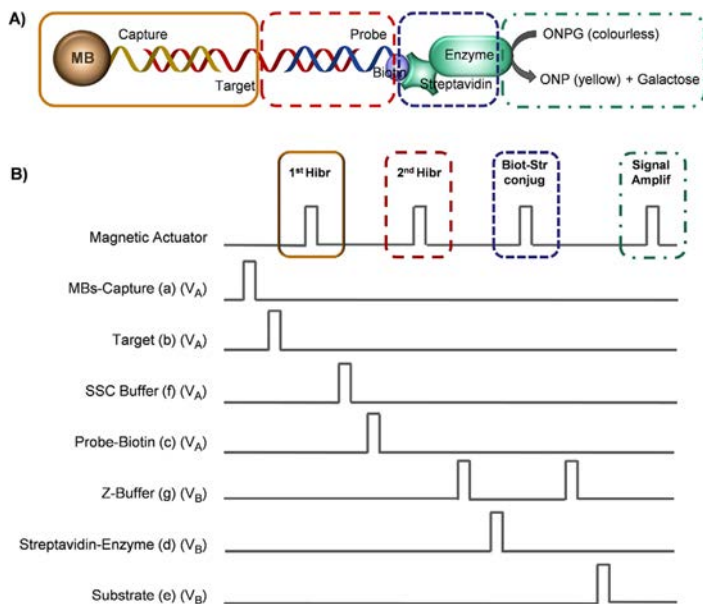
Fig. 2. (A) Schematic representation of the complete assay. (B) Diagram of the different status of the syringes and the magnetic actuator in an *E. coli* oligonucleotide assay. Each change of state in the signal involves the on/off of the different syringe pumps (MBs-capture, Target, Probe-Biotin, Streptavidin-Enzyme, Substrate, SSC buffer or Z-buffer) or the magnetic actuator, respectively (high level: on/working; low level: off/stopped). The position of the three-way valve is also specified (v_A/v_B). The different reactions carried out along the assay (hybridizations, biotin-streptavidin conjugate formation, and enzymatic reaction) have been highlighted with frames. (For interpretation of the references to color in the text, the reader is referred to the web version of this article.)

is carried out, where ONPG is hydrolyzed to galactose and o-nitrophenol (ONP), which can be monitored at 420 nm [33]. Thus, the presence of ONP at the end of the assay entails the formation of the whole complex and the concentration of the target oligonucleotide is determined.

Fig. 2 shows a schematic representation of the whole assay, and a diagram status of the different components (syringes and the magnetic actuator). **1–6** numerations in Fig. 1 are referred to inlet channels of the microfluidic platform. The whole microfluidic system is rinsed with casein blocking buffer solution for 10–15 min to remove air as well as to minimize unspecific adsorptions of reagents and particles to the walls of the polymeric platform. The microfluidic system is then filled with the hybridization buffer (SSC buffer). A 0.09 μg μL^{-1} of the MBs-capture solution is firstly prepared and pumped to the microfluidic system at 80 μL min^{-1} through inlet **1**. The magnetic actuator, maintained in stop mode, ensures the retention of all MB in the reaction chamber. 50 μL of the target oligonucleotide solution are pumped through inlet **2** at 30 μL min^{-1} in a concentration covering the range of 10–50 nM. This sample volume ensures the filling of the reaction chamber (25 μL). Then, the magnetic actuator is switched on, so the magnets begin to move and keep on during certain time (from 1 to 20 min), ensuring the mixture of the target and capture probe solutions through the movement of MBs along the whole chamber (first hybridization – black frames in Fig. 2). Cleaning is then performed with SSC buffer, which is inserted through inlets **6** at 50 μL min^{-1}. As it can be seen (Fig. 2B), all the required cleaning steps are carried out with the magnetic actuator in stop mode. Next step is the injection of 50 μL of the 200 nM Probe-Biotin solution through inlet **3** at 30 μL min^{-1}. The magnetic actuator is again activated to promote the second hybridization of oligonucleotides (blue frames in Fig. 2).

The three-way valve is set to position **v**$_B$ and the reaction chamber is cleaned and conditioned with z-buffer, through inlets **6**, since the use of β-galactosidase is preferred in this buffer solution [33].

After that, 50 μL of a 1.5 μg μL^{-1} streptavidin-β-galactosidase conjugate solution (**d**) are pumped at 30 μL min^{-1} through inlet **4**, and the magnetic actuator is activated to run the last incubation reaction, where probe oligonucleotide is linked to the enzyme through the streptavidin-biotin complex (green frames in Fig. 2).

Once the excess of the enzyme is removed from the reaction chamber with z-buffer, 100 μL of a 30 mM ONPG solution are injected at 100 μL min^{-1} through inlet **5**. The MBs-oligonucleotides-enzyme conjugate is mixed with the substrate solution using the magnetic actuator (orange frames in Fig. 2) until a reliable signal of product (ONP) (from 1 to 15 min) is obtained. The read out is done in a separate chamber (detection chamber) to avoid light dispersion from the MBs colloidal suspension. Once the amplification reaction is performed, the substrate solution is continuously injected in order to fill the detection chamber with the generated coloured product. Since the optical system is continuously reading light absorption, a transitory signal is obtained and the maximum peak intensity is proportional to the concentration of the generated substrate, and consequently the target. Simultaneously, the reaction chamber is regenerated with fresh substrate solution, so a new amplification reaction can be performed in order to obtain a replicate of the measurement. In this work, three replicates were done for each assay and the absorbance of the ONPG solution was used as the baseline signal and as the blank signal.

3.3. Process optimization for the automatic multistep DNA assay

Experimental conditions, such as the concentration of MBs, the amplification time, the rotational speed of the magnetic actuator and the incubation time, were optimized in order to minimize the total analysis time while maintaining maximum sensitivity. All assays were performed at room temperature in triplicate using a 20 nM target solution. Blank signal was obtained in the absence of target oligonucleotide, also in triplicate.
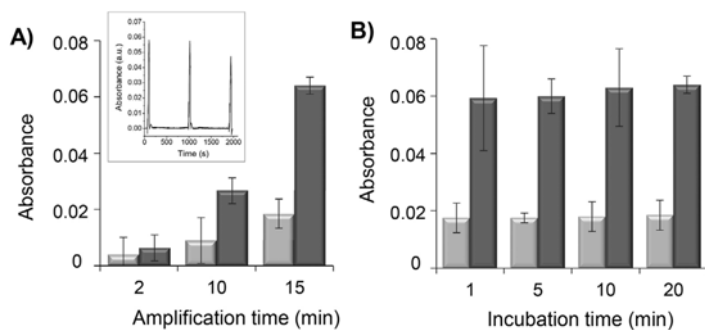
Fig. 3. Signals obtained for the different experiments performed in the process optimization (n = 3) (light bars: blank signal, dark bars: target signal). MBs linear velocity of 3.3 mm s^{-1}. Reagents concentrations: 20 nM target, 200 nM probe, 1.5 μg/μL enzyme, 30 mM ONPG and 5.4 μg μL^{-1} MBs. (A) Amplification time. Inner box: Example of a data logging triplicate for the assays performed with 15 min amplification time. (B) Incubation time of the assay.
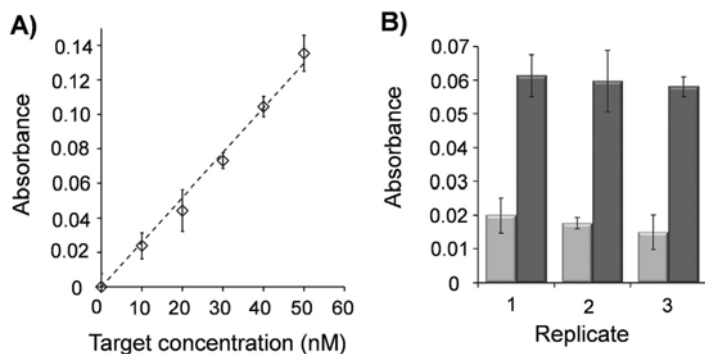
Fig. 4. (A) Calibration curve of target oligonucleotides of *E. coli*. (B) Reproducibility of the method for three different assays of a 20 nM *E. coli* DNA solution (light bars: blank signal, dark bars: target signal).

Two different concentrations of the capture functionalized beads (MBs) were tested. Volumes of 1000 or 1500 μL of a 0.09 μg μL^{-1} MBs solution were pumped through the 25 μL reaction chamber, where the MBs were retained. Thus, concentrations of 3.6 μg μL^{-1} or 5.4 μg μL^{-1} of MBs and 2.6 or 3.9 μM of capture probe where obtained, respectively. With the lowest MBs concentration and at the fixed MBs linear velocity of 3.3 mm s^{-1}, they were not able to move through the entire length of the reaction chamber because of the worse cooperative motion of the magnetic particles at low concentration. As a less reagent mixture and consequently lower sensitivity were expected, this option was discarded. Conversely, MBs moved as a loose cloud all through the reaction chamber when the highest concentration was tested, assuring an enhanced mixture of the solutions contained. Therefore, a 5.4 μg μL^{-1} of MBs were used for the subsequent parameters optimization.

In order to study the influence of the enzymatic reaction amplification time on absorbance signal, assays were performed at a MBs linear velocity of 3.3 mm s^{-1} and reaction times of 20 min for each incubation steps were used, in order to ensure complete hybridization of all target oligonucleotides and the formation of the avidin-streptavidin complex. The longest amplification time tested (2, 10 and 15 min) provided the highest absorbance signal, as well as the lowest relative standard deviation (RSD), as expected (Fig. 3A). For this reason, 15 min of amplification times was used in further experiments.

The magnetic actuator rotational speed influence on the absorbance signal was also studied, since this parameter is clearly related to the efficiency of the reagents mixture and therefore to the achieved sensitivity and reproducibility [28]. MBs linear velocities of 3.3, 5.0 and 6.7 mm s^{-1} were tested using a 5.4 μg μL^{-1} MBs concentration and leaving the assays for 15 min of amplification time and 20 min of incubation times. A clear improvement of the signal, with a minimum RSD, was observed at the lowest speed tested because at higher velocities MBs could not completely follow the magnets moving too fast (i.e. the movement cycle was not completed) and therefore, MBs were not exposed to the whole of the solution.

Finally, four different incubation times (1, 5, 10 and 20 min) were tested. This parameter is of major interest, since three different incubations are required in the performed assay and its reduction could noticeably decrease the total analysis time. As it can be seen in Fig. 3B the absorbance signal obtained does not significantly increased for incubation times higher than 1 min. This is probably a consequence of the enhanced mixing obtained by the active mixing strategy adopted. The MBs motion allowed a significant reduction of the incubation times required, which at the end entailed to perform the entire assay in less than one hour. Moreover, taking into account that the necessary pre-treatment step with casein for blocking unspecific adsorptions and that the initial loading of the chip with the MBs can be performed previous to the assay, the estimated time to perform the measurement is less than 30 min.

3.4. Sensitivity of the procedure for DNA hybridization analysis

Sensitivity and detection limit of the proposed approach were calculated from the calibration curves. 10, 20, 30, 40 and 50 nM solutions of the target were tested at room temperature using the following solutions: 20 nM of the target, 200 nM of the probe, 1.5 µg/µL of the enzyme and 30 mM of the ONPG, and at the optimized parameters (5.4 µg µL^{-1} of MBs, 3.3 mm s^{-1} of MBs linear velocity, 15 min of amplification time and 1 min for each incubation). Fig. 4A shows the observed linear response (R^2 = 0.991), where a sensitivity of 0.0026 a.u. nM^{-1}, calculated as the slope of the linear fitting, was attained. The obtained limit of detection, calculated as three times the standard deviation of the blank signal, was 1 nM. Other analytical systems already described in the literature show better sensitivity in terms of limit of detection but, on the other hand, they use expensive instrumentation or require pre-enrichment steps, which not only considerably enlarges the total analysis time. They also require of qualified personnel, increasing also the cost of the assay [34–37]. Reproducibility was also evaluated performing three different complete assays with a 20 nM *E. coli* DNA solution, obtaining a relative standard deviation of 4.1% (n = 3) (Fig. 4B).

4. Conclusions

A simple, cheap and automatic microfluidic system to perform multi-step magnetic bead-based enzyme-linked oligonucleotide sandwich assays is presented. The microsystem was applied to the analysis of an *E. coli* oligonucleotide, optically determined through the enzymatic reaction of β-galactosidase, which generates a coloured product that absorbs at 420 nm. A detection limit of 1.1 nM with an analysis time of less than hour, including the pre-treatment of the device (approximately half an hour per sample and only one minute of incubation time), was attained. Since the different stages of the assay are automated, no significant variations between assays were obtained. Moreover, the different elements of the set-up are based on low cost components, which minimize the total costs of the system. The remarkable advantage of the proposed approach is a short total analysis time with suitable repeatability, good robustness and relatively high sensitivity. This is a consequence of merging the advantages of using MBs as solid substrates to enhance sensitivity and simplify the assay operation with the easy automation of the process in a microfluidic system, which enables to control easily the mixing of the reagents. In this way, a rapid and reproducible hybridization analysis can be performed, being thus a useful alternative to other proposed methods for pathogens determination in water.

References

[1] P. Yáñez-Sedeño, I. Agüí, R. Villalonga, J.M. Pingarrón, Biosensors in forensic analysis. A review, Anal. Chim. Acta 823 (2014) 1–19.
[2] P. Phoompoung, M. Chayakulkeeree, Recent progress in the diagnosis of pathogenic Candida species in blood culture, Mycopathologia 181 (2016) 363–369.
[3] B.R. Maharana, A.K. Tewari, B.C. Saravanan, N.R. Sudhakar, Important hemoprotozoan diseases of livestock: challenges in current diagnostics and therapeutics: an update, Vet. World 9 (2016) 487–495.
[4] L.X. Wang, C.J. Ji, Advances in quantitative bioanalysis of oligonucleotide biomarkers and therapeutics, Bioanalysis 8 (2016) 143–155.

[5] V. Mancini, S. Murolo, G. Romanazzi, Diagnostic methods for detecting fungal pathogens on vegetable seeds, Plant Pathol. 65 (2016) 691–703.
[6] J. Weile, C. Knabbe, Current applications and future trends of molecular diagnostics in clinical bacteriology, Anal. Bioanal. Chem. 394 (2009) 731–742.
[7] A.-L. Välimaa, A. Tilsala-Timisjärvi, E. Virtanen, Rapid detection and identification methods for Listeria monocytogenes in the food chain—a review, Food Control 55 (2015) 103–114.
[8] R. Girones, M.A. Ferrus, J.L. Alonso, J. Rodriguez-Manzano, B. Calgua, A. Correa Ade, A. Hundesa, A. Carratala, S. Bofill-Mas, Molecular detection of pathogens in water—the pros and cons of molecular techniques, Water Res. 44 (2010) 4325–4339.
[9] F.Y. Ramírez-Castillo, A. Loera-Muro, M. Jacques, P. Garneau, F.J. Avelar-González, J. Harel, A.L. Guerrero-Barrera, Waterborne pathogens: detection methods and challenges, Pathogens 4 (2015) 307–334.
[10] I.F. Lei, P. Roffey, C. Blanchard, K.J. Gu, Development of a multiplex PCR method for the detection of six common foodborne pathogens, Food Drug Anal. 16 (2008) 37–43.
[11] M. Pedrero, S. Campuzano, J.M. Pingarron, Electrochemical genosensors based on PCR strategies for microorganisms detection and quantification, Anal. Methods 3 (2011) 780–789.
[12] S. Ishii, T. Segawa, S. Okabe, Simultaneous quantification of multiple food- and waterborne pathogens by use of microfluidic quantitative PCR, Appl. Environ. Microbiol. 79 (2013) 2891–2898.
[13] H.J. Kim, S.H. Park, T.H. Lee, B.H. Nahm, Y.R. Kim, H.Y. Kim, Microarray detection of food-borne pathogens using specific probes prepared by comparative genomics, Biosens. Bioelectron. 24 (2008) 238–246.
[14] V. Velusamy, K. Arshak, O. Korostynska, K. Oliwa, C. Adley, An overview of foodborne pathogen detection: in the perspective of biosensors, Biotechnol. Adv. 28 (2010) 232–254.
[15] C.R. Hsiao, C.H. Chen, Characterization of DNA chips by nanogold staining, Anal. Biochem. 389 (2009) 118–123.
[16] J.B. Rampal, Microarrays: volume 2, in: Applications and Data Analysis (Methods in Molecular Biology), 2nd ed., Humana Press, 2007.
[17] M.K. Araz, A.M. Tentori, A.E. Herr, Microfluidic multiplexing in bioanalyses, Jala 18 (2013) 350–366.
[18] O.Y.F. Henry, C.K. O'Sullivan, Rapid DNA hybridization in microfluidics, Trends Anal. Chem. 33 (2012) 9–22.
[19] H. Ben-Yoav, P.H. Dykstra, W.E. Bentley, R. Ghodssi, A microfluidic-based electrochemical biochip for label-free diffusion-restricted DNA hybridization analysis, Biosens. Bioelectron. 38 (2012) 114–120.
[20] M. Mirasoli, F. Bonvicini, I.S. Dolci, M. Zangheri, G. Gallinella, A. Roda, Portable chemiluminescence multiplex biosensor for quantitative detection of three B19 DNA genotypes, Anal. Bioanal. Chem. 405 (2013) 1139–1143.
[21] R.D. Sochol, B.P. Casavant, M.E. Dueck, L.P. Lee, L.J. Lin, A dynamic bead-based microarray for parallel DNA detection, Micromech. Microeng. 21 (2011) 054019.
[22] L. Chen, S. Lee, M. Lee, C. Lim, J. Choo, J.Y. Park, S. Lee, S.-W. Joo, K.-H. Lee, Y.-W. Choi, DNA hybridization detection in a microfluidic channel using two fluorescently labelled nucleic acid probes, Biosens. Bioelectron. 23 (2008) 1878–1882.
[23] S. Huang, C. Li, B. Lin, J. Qin, rname>DNA hybridization detection in a microfluidic channel using two fluorescently labelled nucleic acid probes, Biosens. Bioelectron. 23 (2008) 1878–1882.
[23] S. Huang, C. Li, B. Lin, J. Qin, Microvalve and micropump controlled shuttle flow microfluidic device for rapid DNA hybridization, Lab Chip 10 (2010) 2925.
[24] H. Li, Z. He, and chemiluminescent imaging detection, Analyst 134 (2009) 800–804.
[25] H. Zhang, L. Liu, C.-W. Li, H. Fub, Y. Chen, M. Yang, Multienzyme-nanoparticles amplification for sensitive virus genotyping in microfluidic microbeads array using Au nanoparticle probes and quantum dots as labels, Biosens. Bioelectron. 29 (2011) 89–96.
[26] S. Senapati, A.R. Mahon, J. Gordon, C. Nowak, S. Sengupta, T.H.Q. Powell, J. Feder, D.M. Lodge, H. Chang, Rapid on-chip genetic detection microfluidic platform for real world applications, Biomicrofluidics 3 (2009) 022407.
[27] S. Iqbal, J. Robinson, D. Deere, J.R. Saunders, C. Edwards, J. Porter, Efficiency of the polymerase chain reaction amplification of the uid gene for detection of Escherichia coli in contaminated water, Lett. Appl. Microbiol. 24 (1997) 498–502.
[28] H. Sun, T.S. Choy, D.R. Zhu, W.C. Yam, Y.S. Fung, Nano-silver-modified PQC/DNA biosensor for detecting E. coli in environmental water, Biosens. Bioelectron. 24 (2009) 1405–1410.
[29] World Health Organization, Guideline for Drinking-water Quality, fourth edition, WHO, 2011.
[30] M. Berenguel-Alonso, E. Granados, J. Faraudo, J. Alonso-Chamarro, M. Puyol, Magnetic actuator for the control and mixing of magnetic bead-based reactions on-chip, Anal. Bioanal. Chem. 406 (2014) 6607–6616.
[31] O. Ymbern, N. Sández, A. Calvo-López, M. Puyol, J. Alonso-Chamarro, Gas diffusion as a new fluidic unit operation for centrifugal microfluidic platforms, Lab Chip 14 (2014) 1014–1022.
[32] S. Gomez-de Pedro, M. Puyol, D. Izquierdo, I. Salinas, J.M. de la Fuente, J. Alonso-Chamarro, A ceramic microreactor for the synthesis of water-soluble CdS and CdS/ZnS nanocrystals with on-line optical characterization, Nanoscale 4 (2012) 1328–1335.

[33] M. Baeza, C. López, A. Alonso, J. López-Santín, G. Álvaro, Ceramic microsystem incorporating a microreactor with immobilized biocatalyst for enzymatic spectrophotometric assays, Anal. Chem. 82 (2010) 1006–1011.
[34] A.F. Maheux, L. Bissonnette, M. Boissinot, J.-L.T. Bernier, V. Huppé, F.J. Picard, E. Bérubé, M.G. Bergeron, Rapid concentration and molecular enrichment approach for sensitive detection of Escherichia coli and Shigella species in potable water samples, Appl. Environ. Microbiol. 77 (2011) 6199–6207.
[35] G.-Y. Kim, A. Son, Development and characterization of a magnetic bead-quantum dot nanoparticles based assay capable of Escherichia coli O157:H7 quantification, Anal. Chim. Acta 677 (2010) 90–96.
[36] D.-Y. Lee, H. Lauder, H. Cruwys, P. Falletta, L.A. Beaudette, Development and application of an oligonucleotide microarray and real-time quantitative PCR for detection of wastewater bacterial pathogens, Sci. Total Environ. 398 (2008) 203–211.
[37] A.M. Ibekwe, P.M. Watt, C.M. Grieve, V.K. Sharma, S.R. Lyons, Multiplex fluorogenic real-time PCR for detection and quantification of Escherichia coli O157:H7 in dairy wastewater wetlands, Appl. Environ. Microbiol. 68 (2002) 4853–4862.

Biographies

Sara Gómez-de Pedro obtained her Ph.D. in analytical chemistry in 2014 at the Autonomous University of Barcelona. Her research in the Sensors and Biosensors group was focused on the development of (bio)analytical microsystems based on the use of nanoparticles for environmental applications. She is currently working for Medcom Advance S. A. as Senior Research Officer. Her research interests include the development of microfluidic devices for biomedicine, chemical biology and environmental monitoring.

Miguel Berenguel-Alonso received his MSc at the Group of Sensors and Biosensors of the Universitat Autònoma de Barcelona in 2011. He is currently a PhD researcher in the same group under the supervision of Dr. Mar Puyol. His research interests range from the development of microfluidic systems for the synthesis of nanoparticles and their use in (bio)analytical applications, to cell culture *on-chip*.

Pedro Couceiro obtained his Ph.D. in analytical chemistry in 2016 at the Autonomous University of Barcelona. His research in the Sensors and Biosensors group was focused on the development of a microfluidic Free Flow Electrophoresis device based on Low Temperature Co-Fired Ceramics Technology. He is currently a Post-Doc researcher in the Sensors and Biosensors group and his research interests include continuous synthesis and separation processes for process intensification using microfluidic platforms.

Julian Alonso Chamarro received his BSc in chemistry in 1981 and his PhD in Analytical Chemistry in 1987 at the Autonomous University of Barcelona. He is Professor of Analytical Chemistry at the same university. He has co-authored more than 120 research papers on (Bio)Chemical Sensors and Automated Flow Systems and is author of different patents about sensors and analytical instrumentation for environmental monitoring. His research interests include the design and fabrication of microsystems for chemical analysis (μTAS) based on LTCC, polymer and IC technologies, microfluidic platforms for the synthesis of nanomaterials and optical and electrochemical microsensors. Most of these developments were applied in the environmental and industrial control fields. Other research interest area is the synthesis of ionophores and dyes for chemical sensing.

Mar Puyol obtained her BSc degree in Chemistry in 1996 from the Autonomous University of Barcelona. She obtained her MSc degree in Analytical Chemistry from the same University in 1998, and she completed her PhD in Analytical Chemistry about Integrated Waveguide Absorbance Optochemical Sensors based on the silicon technology in 2002. She was employed in the Applied Physics Department of the Universidad de Zaragoza until 2006 as a researcher. She is actually Lecturer in the Autonomous University of Barcelona. Her research interests include the study and characterization of new chromo(fluoro)ionophores and its integration as recognition elements in miniaturized otochemical sensors. She is also working on the development of microsystems for chemical analysis (μTAS) based on LTCC, polymer and IC technologies and on the design and fabrication of microfluidic platforms for the synthesis of nanomaterials and for the development of (bio)chemical miniaturized analyzers based on the use of nanostructured materials.

Rapid Prototyping of a Cyclic Olefin Copolymer Microfluidic Device for Automated Oocyte Culturing

Miguel Berenguel-Alonso, Maria Sabés-Alsina Roser Morató, Oriol Ymbern, Laura Rodríguez-Vázquez, Oriol Talló-Parra, Julián Alonso-Chamarro, Mar Puyol and Manel López-Béjar.

Rapid Prototyping of a Cyclic Olefin Copolymer Microfluidic Device for Automated Oocyte Culturing

**Miguel Berenguel-Alonso[1]*, Maria Sabés-Alsina[2]*, Roser Morató[3],
Oriol Ymbern[1], Laura Rodríguez-Vázquez[2], Oriol Talló-Parra[2],
Julián Alonso-Chamarro[1], Mar Puyol[1], and Manel López-Béjar[2]**

Abstract

Assisted reproductive technology (ART) can benefit from the features of microfluidic technologies, such as the automation of time-consuming labor-intensive procedures, the possibility to mimic in vivo environments, and the miniaturization of the required equipment. To date, most of the proposed approaches are based on polydimethylsiloxane (PDMS) as platform substrate material due to its widespread use in academia, despite certain disadvantages, such as the elevated cost of mass production. Herein, we present a rapid fabrication process for a cyclic olefin copolymer (COC) monolithic microfluidic device combining hot embossing—using a low-temperature cofired ceramic (LTCC) master—and micromilling. The microfluidic device was suitable for trapping and maturation of bovine oocytes, which were further studied to determine their ability to be fertilized. Furthermore, another COC microfluidic device was fabricated to store sperm and assess its quality parameters over time. The study herein presented demonstrates a good biocompatibility of the COC when working with gametes, and it exhibits certain advantages, such as the nonabsorption of small molecules, gas impermeability, and low fabrication costs, all at the prototyping and mass production scale, thus taking a step further toward fully automated microfluidic devices in ART.

Introduction

Assisted reproductive technologies (ARTs) have enabled millions of people in the world to have children who otherwise would not have been able to do so. The application of ART in animals, mainly by artificial insemination (AI), had a great impact in the improvement of the efficiency of animal production. Reproductive biotechnologies are intended to be used routinely to shorten generational intervals and to propagate genetic material among breeding animal populations.[1] To achieve this goal, reproductive technologies have been developed over the years, for instance, AI, embryo transfer, in vitro fertilization (IVF), and in vitro embryo production, as well as multiplication techniques (cloning) for the application of transgenesis.[1]

Despite the remarkable progress made and the punctual relevance of some of the above-mentioned technologies, the efficiency of the processes is usually very low, with the exception of AI in cattle. Furthermore, ARTs such as oocyte maturation or IVF require labor-intensive, time-consuming procedures (including frequent pipetting of oocytes to be washed, media changes, etc., which have not significantly evolved since their establishment) and some critical steps that only highly specialized personnel are able to perform.

Microfluidics has emerged as a new tool for ART that could potentially solve these problems by automating the handling and preparation procedures,[2] thus minimizing the errors associated with manual operation and reducing manipulation stress on the cells. Microfluidics can also

[1]Group of Sensors and Biosensors, Chemistry Department, Universitat Autònoma de Barcelona, Bellaterra, Spain
[2]Department of Animal Health and Anatomy, Universitat Autònoma de Barcelona, Bellaterra, Spain
[3]Biotechnology of Animal and Human Reproduction (TechnoSperm), Department of Biology, Institute of Food and Agricultural Technology, University of Girona, Girona, Spain
*Miguel Berenguel-Alonso and Maria Sabés-Alsina contributed equally to this work.

Corresponding Author:
Mar Puyol, Group of Sensors and Biosensors, Chemistry Department, Universitat Autònoma de Barcelona, Bellaterra, 08193, Spain.
Email: mariadelmar.puyol@uab.es

provide environments that mimic in vivo conditions since fabrication technologies enable the design of structures resembling biological environments,[3–6] including those related to ART.[7] Furthermore, other inherent advantages of microfluidics, such as the low volumes required, the precise control of fluids, or the miniaturization and integration of different elements in portable devices, would also benefit ART.

The vast majority of microfluidic systems used in ART are made of polydimethylsiloxane (PDMS), a transparent and gas-permeable elastomer. This is the consequence of its widespread use in academia, which is due to several factors: cheap, rapid, easy prototyping, optical transparency, easy surface modification, elasticity, etc.[8] The latter also provides the grounds for the integration of actuation systems, such as pumping or valving. ART applications of PDMS devices range from sperm separation[9] to oocyte fertilization[10] or embryo culture,[11] among others. A comprehensive review of microfluidic systems applied in ART can be found in Swain et al.[12]

However, certain limitations of PDMS have encouraged the use of other materials in microfluidics, such as thermoplastics.[13] Among these, polystyrene (PS) and cyclic olefin copolymers (COCs) have emerged as alternatives for the production of microfluidic devices for biological applications, overcoming the limitations of PDMS. On the one hand, PS has been the choice material for disposable cell culture labware since the 1960s, and recently has been used as a substrate material to produce microfluidic devices,[14] thus bringing together state-of-the-art microfluidics technology and a well-known material for biologists. However, the fabrication process is still challenging, mostly due to bonding issues.[15]

On the other hand, COCs are a relatively new group of polymers with very promising properties for microfluidic applications,[16] such as chemical resistance (higher than most thermoplastics), excellent optical transparency (even in the near-ultraviolet [UV] region), low water absorption, and biological compatibility.[17,18] Furthermore, COC has obtained the *USP Class VI* qualification[19] and is approved for use in medical devices. COC is a copolymer consisting of ethylene and norbornene, which offers several grade variations in terms of glass transition temperatures (T_g), ranging from 70 to 155 °C.[20] This is a big advantage in front of other thermoplastics, as it allows the bonding of different layers without channel deformation using grades with low T_g as sealants,[21] and avoiding processes like solvent bonding, which are potentially harmful for biology applications. COC also enables surface modification,[22] which can be useful for avoiding protein adsorption, for instance, in bioanalytical applications. Several fabrication techniques are available for the production of COC microfluidic devices, such as micromilling, hot embossing, and injection molding. The last two techniques enable the fabrication of the required microstructures to trap

oocytes. However, the fabrication of the master is usually expensive and requires relatively complex manufacturing processes, such as photolithography.

Herein, we developed a new fabrication methodology combining computer numerically controlled (CNC) micromilling and hot embossing using low-temperature cofired ceramic (LTCC) masters, which enables fast prototyping, as well as the fabrication of microfluidic features in the 50–100 μm range. Furthermore, we studied for the first time the suitability of a COC monolithic microfluidic device for an ART application. We studied bovine oocyte maturation and sperm characteristics during the culture in a COC microfluidic device. We investigated whether oocytes maintain the same rates of in vitro maturation and their ability to be fertilized. We also evaluated spermatozoa-relevant parameters, such as viability, motility, and membrane integrity, after culture in the microfluidic device. This is, to the best of our knowledge, the first COC monolithic microfluidic device dedicated to an ART application, and from the obtained results, we can demonstrate the great potential of COC as a substrate material due to its biocompatibility and simple fabrication processes, at both the prototyping and mass production scales.

Materials and Methods

Reagents

All reagents were purchased from Sigma Chemical Co. (St. Louis, MO) unless otherwise stated. Plastic dishes, four-well plates, and tubes were obtained from Nunc (Roskilde, Denmark).

Fabrication of Microfluidic Devices

Two different microfluidic devices were fabricated on COC to separately study the maturation of oocytes and sperm storage. COC was obtained from TOPAS Advance Polymers GmbH (Florence, KY). TOPAS 5013 sheets (T_g 134 °C) were used in this study for the machining of microchannels, while 25 μm thick TOPAS 8007 foils (T_g 78 °C) were used as sealing substrate between layers using a temperature diffusion bonding technique, as described elsewhere.[23]

Sperm Storage Microfluidic Device. The fabrication procedure of this device is based on a procedure previously reported in our research group.[24] Briefly, the device consists of three layers of TOPAS 5013 1 mm thick. The top and bottom layers were laminated with a 25 μm TOPAS 8007 (which acted later as glue to seal the device)[23] in a uniaxial hydraulic press (Talleres Francisco Camp, Granollers, Spain). The COC layers were machined using a micromilling CNC machine: Protomat S63 (LPKF Laser & Electronics, Garbsen, Germany). The fluidic channel was milled in the
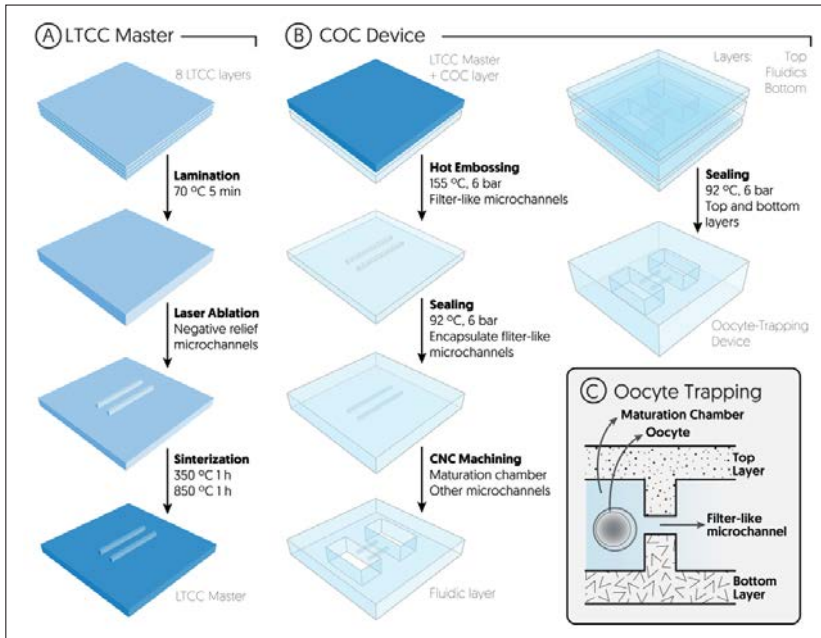
Figure 1. Schematic representation (not to scale) of the oocyte-trapping microfluidic device fabrication and working principle of the entrapment. (**A**) Fabrication of the LTCC master. (**B**) Fabrication of the COC oocyte-trapping microfluidic device, by means of hot embossing the smallest features (i.e., the filter-like microchannels) and micromilling the maturation chamber and the rest of the channels. The device is then sealed by means of a thermocompression process. (**C**) Cross section view of the device showcasing the oocyte-trapping principle, which is based on a channel constriction where the oocytes do not fit—the oocytes are trapped in a filter-like structure.

middle layer, by cutting the COC through. The top layer was drilled to create the inlets. Then, the three layers were aligned and laminated at 100 °C under a pressure of 6 bars. This approach prevents any surface roughness created by the milling machine when creating a bas-relief channel.

Oocyte-Trapping Microfluidic Device. The oocyte-trapping microfluidic device was fabricated using a combination of hot embossing and micromilling. The microchannels that retain the oocytes were fabricated by means of a hot embossing technique in order to obtain a "filter-like" structure with the appropriate dimensions to trap the oocytes—micromilling is not suitable for such dimensions—while the bigger features were machined using the CNC micromilling machine. **Figure 1** shows a schematic representation of the fabrication process.

First, a master was built using LTCC 951PX, 254 μm thick, from Dupont (Berlin, Germany). Eight LTCC layers were thermolaminated together in a uniaxial hydraulic press. Then, the ceramic block was etched by means of a Protolaser 200, from LPKF (Garbsen, Germany), and sintered in a programmable box furnace from Carbolite (CBCWF11/23P16, Afora, Spain). The master was designed to have four negative images of microchannels, in order to create a filter-like structure in the microfluidic device.

Second, the LTCC master was used to fabricate the oocyte-trapping microfluidic device. A 500 μm thick layer of TOPAS 5013 was embossed with the master at 155 °C

and 6 bars, thus obtaining four microchannels in the COC. Another 500 μm COC layer (previously laminated with a 25 μm thick TOPAS 8007 foil) was laminated with the replica, at 92 °C and 6 bars, to seal the microchannels and obtain the filter-like structure. The rest of the fluidic structures, namely, the maturation chamber and the inlet/outlet channels, were machined cutting through the whole COC block using the micromilling machine.

The COC block with the microfluidic structures was thermally laminated between two more layers of COC (top and bottom layers), thus obtaining the sealed microfluidic device. Both top and bottom layers had been prelaminated with a film of TOPAS 8007, which acted as gluing layer, as described elsewhere.[23] Inlet/outlet vias were drilled using the CNC micromilling machine.

Experimental Design and Setups

In order to evaluate the suitability and biocompatibility of COC as a substrate material for microfluidic devices used in ART, we designed two different microfluidic devices, one for sperm storage and another one for oocyte maturation. Three different sets of experiments were carried out.

First, bovine oocytes were randomly distributed between the microfluidic device and a four-well culture dish, and matured for 24 h. Maturation rates were analyzed following nuclear and cytoplasmic maturation (chromosome and cortical granule distribution, respectively) by means of
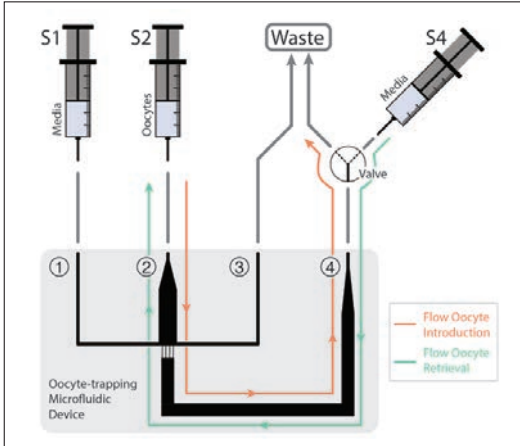
Figure 2. Schematic representation of the experimental setup for the oocyte maturation experiments *on-chip*. The oocyte-trapping microfluidic device consisted of four inlet/outlet ports. Ports 1 and 3 were simply used to fill the device with media and remove any air bubbles trapped next to the filter-like channels. Ports 2 and 4 were used for the oocyte injection/retrieval.

staining. Second, sperm viability, acrosome abnormalities, and motility were assessed at 3, 6, 12, and 24 h in three different units, namely, the sperm storage microfluidic device, a four-well culture dish, and a 1.5 mL Eppendorf tube. Finally, bovine oocytes were matured either in the microfluidic device or in a four-well culture dish, and subsequently fertilized in vitro in four-well dishes to evaluate penetration rates. All the experiments were conducted in triplicate.

In order to carry out these sets of experiments, two different setups were designed. On the one hand, the experiments involving the sperm storage microfluidic device were carried out by simply using a pipette to inject or retrieve the sperm samples into or from the device.

On the other hand, the experiments involving the oocyte-trapping microfluidic device were carried out in a setup schematically depicted in **Figure 2**. Inlet 1 was connected to a syringe pump (540060, TSE Systems, Bad Homburg, Germany) in combination with a 2.5 mL gastight glass syringe from Hamilton (Bonaduz, Switzerland) by means of polytetrafluoroethylene (PTFE, i.d. 0.8 mm) tubing. This syringe (S1) contained the maturation medium to fill the microfluidic channels. Inlet 2 contained a short fragment of flexible Tygon tube, which was used as an injection port for the polished glass capillary syringe (S2) containing the oocytes. Once the capillary was inserted in the injection port, the syringe was set on a pump in order to inject the oocytes into the microfluidic device. Port 3 was used as an auxiliary waste outlet during the process of filling the device with media in order to remove any air bubbles, and then was capped with a stopper for the rest of the

experiment. Port 4 was linked to a three-way valve (161T031, NResearch, Northboro, MA) connecting the oocyte-trapping microfluidic device to either the waste (during oocyte loading) or a syringe (S4) with media (during oocyte collection after the experiment).

Bovine Oocyte Collection and In Vitro Maturation

Bovine ovaries were collected from recent culled dairy heifers at local slaughterhouses and immediately transported to the laboratory. They were then washed three times in warm saline solution (38 °C). Subsequently, follicles with a diameter of 2–6 mm were aspirated using an 18-gauge needle. Only unexpanded cumulus–oocyte complexes surrounded by five or more cumulus cell layers and with homogeneous cytoplasm were matured in vitro and cultured at 38.5 °C in a humidified atmosphere of 5% of CO_2 for 24 h. The maturation medium contained TCM-199 medium supplemented with 10% (v/v) fetal calf serum, 10 ng/mL epidermal growth factor, and 50 μg/mL gentamycin.[25]

Assessment of Sperm Parameters

Commercial frozen bull semen of proven fertility was used. Semen straws were thawed in a water bath at 38.5 °C for 30 s, and then spermatozoa were immediately centrifuged at room temperature in a top-layer solution of a discontinuous gradient (BoviPure, Nidacon International AB, Göthenborg, Sweden) for 10 min and 100*g*. The supernatant was removed, and the pellet was resuspended in 3 mL of BoviPure wash solution and centrifuged again for 5 min at 100*g*. The sperm concentration of the pellet was determined using a hemocytometer chamber (Neubauer chamber) and adjusted to a final concentration of 1×10^6 spz/mL with fertilization medium (Tyrode's medium supplemented with 25 mM sodium bicarbonate, 22 mM sodium lactate, 1 mM sodium pyruvate, 6 mg/mL fatty acid–free bovine serum albumin [BSA], and 10 mg/mL heparin sodium salt [Calbiochem, Darmstadt, Germany]), and cultured at 38.5 °C in a humidified atmosphere of 5% of CO_2 for 24 h.

The sperm cells' viability and acrosome abnormalities were assessed by the nigrosine–eosin stain method.[26] Ten microliters of sperm sample and 10 μL of the dye solution were mixed and smeared onto a glass slide and allowed to air-dry. Then, the slide was covered with mounting medium and a cover glass. Slides were analyzed using an optical microscope (Motic BA210, Barcelona, Spain) at 1000× magnification under immersion oil. As many as 200 cells were counted on each slide, and the percentages of sperm viability and spermatozoa with acrosome abnormalities were calculated.

The motility characteristics of the frozen–thawed spermatozoa were determined using a computer-assisted sperm

analysis (CASA) system (Integrated Sperm Analysis System V1.2; Proiser SL, Valencia, Spain). The CASA system is based on the analysis of 25 consecutive digital images taken from a single field at 100× magnification in a dark background in a time lapse of 1 s. A sample drop of 5 μL was placed on a prewarmed slide and viewed in a phase contrast microscope equipped with a warmer stage at 37 °C. At least five separate fields were taken of each sample, and a minimum of 200 cells per sample were examined. The motility descriptors obtained after CASA were progressive motility (percentage of spermatozoa that showed an average path velocity [VAP] above 50 μm/s and 70% of straightness coefficient) and total motility (percentage of spermatozoa that showed a VAP above 10 μm/s).

Oocytes and Sperm Handling On-Chip

The microfluidic devices were washed with 70% ethanol and rinsed twice with Milli-Q water. After drying, they were exposed to UV light for 30 min for sterilization. Prior to introduction of either oocytes or sperm, the microfluidic devices were respectively filled in with maturation or fertilization medium equilibrated at 38.5 °C in a 5% CO_2 incubator.

Oocytes were loaded into the microfluidic device through a flexible Tygon tube (Port 2, **Fig. 2**), which acted as an injection port, where the tip of the polished glass capillary syringe (S2) was inserted. Then, the syringe was coupled to a pump and a flow rate of 50 μL/min was applied until the oocytes reached the maturation chamber. To achieve that, Port 3 was capped and therefore the flow was directed from Port 2 to Port 4 through the filter-like microchannels, and then into the waste (**Fig. 2**). The oocytes were thus retained in the filter-like structure since their size is bigger than the microchannel dimensions. In order to retrieve the oocytes after the maturation experiments, the flow direction was inverted: the syringe in Port 2 was unplugged—leaving only a small fragment of tube—and the valve in Port 4 was switched, connecting the device to the syringe (S4). Then, a 50 μL/min flow rate was applied in the direction from Port 4 toward Port 2 (**Fig. 2**). Oocytes were thus collected in four-well plates.

Sperm samples were injected into the sperm storage microfluidic device directly with a pipette. Immediately after injection, both inlet and outlet were sealed using an adhesive film AB-1170 from Thermo Scientific (Schwerte, Germany), and the microfluidic device was incubated at 38.5 °C for the corresponding period of time. After the incubation, the film was removed and the sperm sample was collected with a pipette. The sperm samples were then analyzed to assess sperm quality parameters after exposure to the COC.

In Vitro Fertilization

After maturation, the cumulus–oocyte complexes were washed twice in phosphate-buffered saline (PBS) solution

and then transferred to fertilization medium. Frozen–thawed bull spermatozoa were counted in a Neubauer chamber and diluted in an appropriate volume of fertilization medium to give a final concentration of 10^6 spermatozoa/mL. All cumulus–oocyte complexes were coincubated with spermatozoa for 20 h at 38.5 °C in fertilization medium in a humidified 5% CO_2 incubator.

Oocyte Evaluation and Classification

After 24 h of in vitro maturation, oocytes were totally denuded of cumulus cells by gentle pipetting in PBS. In order to evaluate nuclear stage and cortical granule distribution after in vitro maturation, oocyte samples were fixed in a solution of 4% (w/v) of formaldehyde and PBS at 38.5 °C for 30 min and permeabilized in Triton X-100 2.5% (v/v) in PBS for 15 min. Then, oocytes were immunostained for cortical granule detection with fluorescein isothiocyanate–labeled *Lens culinaris agglutinin* (FITC-LCA). Fixed and stained oocytes were mounted on poly-L-lysine-treated coverslips fitted with a self-adhesive reinforcement ring in a 3 μL drop of Vectashield containing 125 ng/mL 4′,6-diamidino-2-phenylindole (DAPI) (Vectorlabs, Burlingame, CA) for chromosome detection and flattened with a coverslip. The preparation was sealed with nail varnish and stored at 4 °C protected from light. Chromosomes and the cortical granule status of each oocyte were assessed under an epifluorescent microscope (Nikon Eclipse TE 2000S) and a laser confocal microscope (Leica TCS SP2). Oocyte images were recorded in a computer.

Cultured oocytes were checked to have reached the metaphase II (MII) stage. Oocytes that reached the MII stage after maturation were classified into two categories: (1) normal MII, uniform alignment of the chromosomes on the spindle, and (2) anomalous MII, nuclear content changed into chromatin-like structure forming condensed aggregates, forming aberrantly distributed chromosomes or the absence of chromosomes.

Translocation of cortical granules to the oolema was used as an indicator of cytoplasmic maturation.[27] The criteria used to define the cortical granule distribution of oocytes was classified into two categories: (1) normal cytoplasmic maturation, cortical granules were distributed adjacent to the plasma membrane and positioned such that they formed a continuous layer, and (2) anomalous cytoplasmic maturation, cortical granules appeared aggregated in clusters, or cortical granules were distributed in the cortical area (not limited to the vicinity of the plasma membrane), or there was an absence of cortical granules.

Evaluation of Sperm Penetration

At 20 h postinsemination, the presumptive zygotes were pipetted to remove excess sperm and cumulus cells, washed three times in PBS, fixed in 4% (v/v) paraformaldehyde in

PBS at 38.5 °C for 30 min, stained with Vectashield containing DAPI, and mounted on glass slides. The number of pronuclei was assessed under an epifluorescence microscope (Axioscop 40FL, Carl Zeiss, Göttingen, Germany). Once stained, slides were examined and parameters including penetration, monospermic penetration, male pronucleus formation, and polyspermic penetration were recorded. Penetration was determined by the presence of one or more swollen sperm heads and/or male pronuclei. The presence of three or more pronuclei was designated as polyspermic.

Statistical Analysis

All statistical analyses were performed using the R program (version 2.15.0; R Development Core Team, 2009). Data of *on-chip* oocyte maturation were analyzed using contingency tables and Pearson's chi-squared statistical test. The analysis of differences among the different tested devices for sperm viability and motility parameters was carried out using the Kruskal–Wallis test. All data are expressed as mean ± SD. In all cases, differences between groups with $p < 0.05$ were considered significant.

Results and Discussion

Microfluidic Design and Fabrication

Two different microfluidic devices were designed in order to study the oocytes and the sperm samples independently. The microfluidic device for sperm consisted of a simple channel to store the sperm for different periods of time and then compare the quality of the samples with the control experiments. Four independent microfluidic units were fabricated on the same substrate to study the sperm samples at 3, 6, 12, and 24 h, respectively. The dimensions of the channel were chosen to fit the required volume for the motility and viability tests, plus excess in case it might be needed (total volume ca. 90 μL). **Figure 3** shows the microfluidic device used in the study of the sperm samples.

The oocyte-trapping microfluidic device consisted of a maturation chamber with a filter-like structure to trap the oocytes and four inlet/outlet ports (**Fig. 4**). Ports 1 and 3 were used to fill the entire device with the maturation medium and remove any air bubble prior to oocyte introduction, and then they were not used anymore during the experiments. Ports 2 and 4 were used to inject/retrieve the oocytes into/from the device by applying a flow rate in one or another direction. The features of the oocyte microfluidic device were more challenging than those of the sperm microfluidic device, from the fabrication perspective. Microfluidic channels with a smaller size than the oocyte diameter were required to trap them, and common micromilling equipment, usually employed for thermoplastics, is
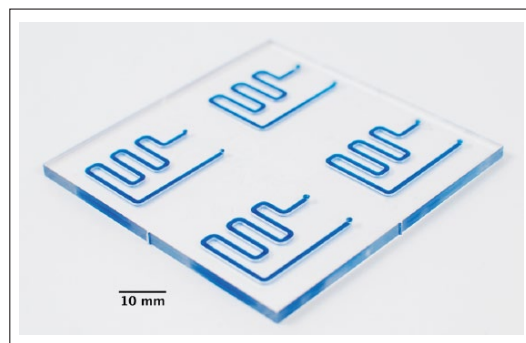

Figure 3. Microfluidic device for sperm storage. The device features four independent fluidic units to analyze a sample at different times. For clarity purposes, the channels were filled with blue dye.

not able to achieve such dimensions.[28] Therefore, filter-like channels were hot embossed on the COC plates.

Several materials can be found in the literature for the fabrication of masters, for example, micromilled brass,[29] photolithographically patterned silicon,[30] or epoxy.[18] However, the fabrication of these type of masters requires time-consuming and expensive processes. Therefore, the master used in this work was fabricated using LTCC technology, due to its simple and fast iteration from design to prototype (around 6 h) in an inexpensive way.[31] Furthermore, no clean room facilities were required for its fabrication. Several COC replicas were fabricated without noticeable degradation of the master. The simple prototyping enabled by the LTCC technology enhances the optimization process of the master features required by the desired application.

The different layers of COC were laminated together using the thermal diffusion bonding technique. TOPAS 8007 foils, 25 μm thick, were used as a "gluing" layer. The lower T_g of this substrate enables the lamination of the layers with minimal deformation. In this case, this is particularly important in order to avoid occlusion due to the reduced dimensions of the filter-like microchannels. The availability of a number of COC grades with different thermal properties is one of its assets in front of other thermoplastics like PS for several reasons: the fabrication process becomes simpler, smaller features can be implemented in monolithic devices, and surface modification/activation or solvents are not required for bonding. The latter fact is very important in biological applications, since solvents and other reagents used for surface modification could potentially harm cells.

The filter-like microchannels obtained after sealing the microfluidic device had a trapezoidal shape, with dimensions of approximately 100 and 50 μm, respectively, for the bases, and 55 μm high (**Fig. 4C**). The oocyte-trapping microfluidic device enabled the injection, maturation, and removal of the oocytes (**Fig. 5**).
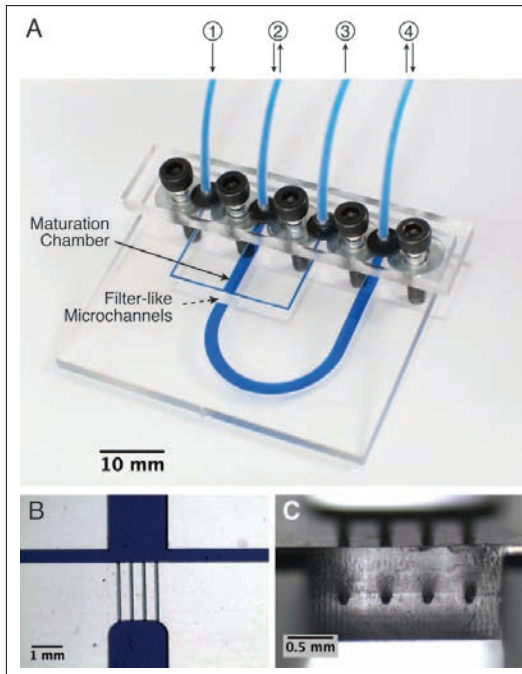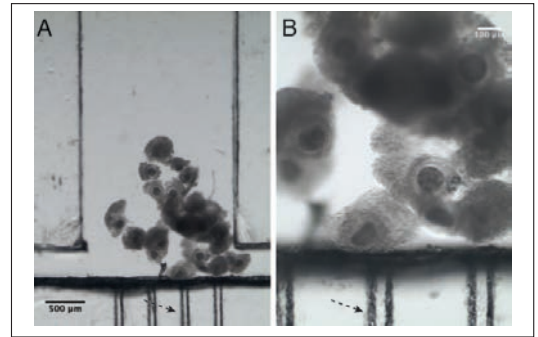
Figure 4. (**A**) Oocyte-trapping microfluidic device. The dashed arrow indicates the position of the capillary channels that act as a filter for oocytes. For clarity purposes, the channels were filled with blue dye. (**B**) Microscope close-up of the oocyte-trapping region. (**C**) Cross section view of the oocyte-trapping microchannels embossed using the LTCC master.

On-Chip Oocyte Maturation

The oocytes were injected into the microfluidic device at an optimal flow rate of 50 μL/min (experimentally determined). Using smaller flow rates would involve longer times for oocyte loading/retrieval. No oocyte deformation was observed using this flow rate. Higher flow rates would cause deformation and/or denudation of the oocytes in the filter-like channels (channel constriction). Other studies in the literature take advantage of this phenomenon for cumulus removal.[32] However, we were not interested in it due to the important role of cumulus cells in oocyte maturation.[33] The oocytes were retained in the vicinity of the filter-like microchannels of the maturation chamber, as seen in **Figure 5**.

Figure 6A shows the results obtained from the oocytes in vitro matured into the microfluidic device compared with the four-well culture dish. **Figure 6B,C** shows examples of oocytes correctly matured. Although oocytes matured in the microfluidic device showed a low-grade cumulus cell expansion, no significant differences ($p > 0.05$) were found in the percentage of oocytes progressing to normal MII and


Figure 5. Microscope pictures of the oocytes trapped in the microfluidic device. The dashed arrow indicates the position of the capillary channels that act as a filter for oocytes. (**A**) General view of the maturation chamber and (**B**) close-up of the oocytes near the capillary channels. The shadowed areas of the capillary channel correspond to its walls, as it has a trapezoidal shape.

cytoplasmic maturation between both devices. These results are in agreement with others found in the literature,[34] in which pig oocytes matured in PDMS microchannels did not show significant differences ($p > 0.05$) in the percentage of maturation rates compared with oocytes matured in conventional 500 μL drops or in 8 μL drops (volume control). In addition, Walters et al.[34] also observed a low grade of cumulus cell expansion of the cumulus–oocyte complexes matured in the PDMS device. The molecular processes involved in cumulus cell expansion need to be evaluated to check presumptive implications on processes related to fertilization and embryo development.

The small volumes used in microfluidics may lead to a rapid depletion of factors and/or a pH shift in the surroundings of the oocytes. The pH in the microfluidic device is not buffered with the CO_2 atmosphere of the incubator because it is airtight—unlike the four-well dish—and this could cause the lower cumulus cell expansion, since oocytes appear to lack porters to regulate their intracellular pH,[35,36] which is greatly affected by CO_2 and O_2 concentrations.[37] Although this could be overcome by employing dynamic culture, that is, imparting flow and thus renewing the media, in this study we evaluated the static culture, as it can be more easily compared with the traditional four-well dish method.

Time-Dependent On-Chip Sperm Evaluation

Results obtained from the analysis of the sperm storage into the microfluidic device, a four-well culture dish, and a 1.5 mL Eppendorf tube are shown in **Table 1**. Data show the expected decrease of the percentage of viability and motility, and an increase of the percentage of acrosome abnormalities over time, with no significant differences among
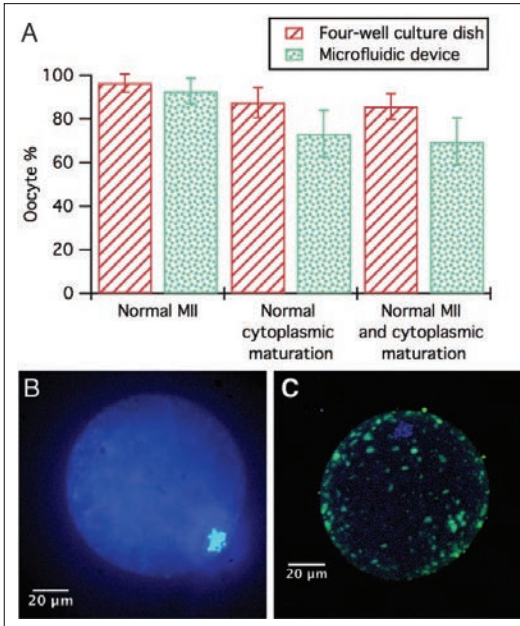
Figure 6. (**A**) Effect of different culture devices on nuclear and cytoplasmic maturation of bovine oocytes. No significant differences were detected ($p > 0.05$). (**B**) Oocyte correctly matured in vitro to the MII nuclear stage. Image obtained under an epifluorescence microscope after DAPI staining. Oocyte diameter is close to 100 μm. (**C**) Oocyte correctly matured in terms of nuclear maturation (MII stage) and cortical granule (CG) migration. Image merged from nuclear (blue fluorescence) and CG (green fluorescence) staining under confocal laser microscopy.

the three devices ($p > 0.05$). This suggests that COC is an innocuous and biocompatible material regarding sperm quality parameters, and it could be used for the development of microfluidic systems. Previous studies have tested the biocompatibility of materials such as PS (standard petri dish material), polymides, silicons, and PDMS, assessing mice embryo development and pig sperm motility parameters.[38–40] However, to the authors' best knowledge, this is the first study that has tested the biocompatibility and absence of the toxicity of COC on bovine gametes.

In Vitro Fertilization after On-Chip Oocyte Maturation

Table 2 shows the significantly higher percentages of sperm penetration observed in the four-well culture dish when compared with the microfluidic device at 18 h after IVF (61.44% vs. 35.63%, respectively; $p < 0.05$). However, in

terms of normal fertilization with male pronuclear formation, no significant differences were observed between both devices ($p > 0.05$). These data suggest that when an oocyte is penetrated by a sperm cell, fertilization is comparable and efficient in both maturation systems. Thus, the detected reduction in the fertilization rate after *on-chip* oocyte maturation seems to be a consequence of the quality of the matured oocyte rather than due to deficiencies in the process of fertilization. The oocyte maturation system adequately supported nuclear maturation but probably failed to produce oocytes with a complete cytoplasmic competency, additionally to correct cortical granule migration and maturation. Cytoplasmic maturation encompasses a wide array of metabolic and structural modifications, including events that ensure the occurrence of normal fertilization, meiotic-to-mitotic cell cycle progression, and activation of pathways required for genetic and epigenetic programs of preimplantation embryonic development.[41] Additionally, it is known that cumulus cell expansion is an important marker for oocyte maturation.[42] Indeed, in cattle, inhibition of cumulus cell expansion was shown to be independent from nuclear maturation, but essential for fertilization and subsequent cleavage and blastocyst development.[43] Thus, it might be thought that the low grade of cumulus cell expansion observed after *on-chip* maturation could also be related to a poorer maturation of the zona pellucida, necessary for a proper fertilization of the oocyte. However, and as stated before, employing a dynamic culture with the *on-chip* oocyte maturation system could help to improve the overall oocyte maturation.

The differences between the microfluidic device and the four-well culture dish can also be explained by the fact that the COC microfluidic device is airtight and does not allow the gas exchange, thus impeding the buffering of the media by the CO_2 contained inside the incubator. Similar maturation studies in PDMS microfluidic devices (gas permeable) show a significantly higher percentage of porcine embryo cleavage rates (67% vs. 49%; $p < 0.05$).[44] However, the gas permeability of PDMS implies that the microfluidic device needs to be in an incubator with controlled atmosphere. In contrast, COC microfluidic devices, in combination with a suitable heater,[45,46] would not require a control of the atmosphere, and therefore minimize the required equipment. Moreover, the problem of the depletion of factors around the oocytes and the media buffering could be overcome by using a dynamic culture, that is, renewing the media by pumping a fresh one into the maturation chamber.

Conclusions

This work describes a novel rapid prototyping process for COC microfluidic devices, combining a hot embossing step—using an LTCC master—for the smaller features required and

Table 1. Sperm Quality Parameters (Viability, Acrosome Abnormalities, and Motility Characteristics) after the Storage in Three Different Devices (Microfluidic Device, a Four-Well Culture Dish, and a 1.5 mL Eppendorf Tube) for 3, 6, 12, and 24 h.

Parameter	Time (h)	Microfluidic Device	Four-Well Culture Dish	Eppendorf Tube
Viable sperm cells (%)	3	48.3 ± 3.0	52.8 ± 3.6	50.2 ± 4.5
	6	34.7 ± 5.5	37.7 ± 10.9	39.6 ± 8.5
	12	20.5 ± 0.5	29.1 ± 5.3	27.8 ± 6.1
	24	20.0 ± 8.2	27.0 ± 4.8	22.5 ± 3.1
Acrosome abnormalities (%)	3	44.8 ± 11.6	43.5 ± 19.8	37.2 ± 2.5
	6	46.3 ± 9.8	38.2 ± 7.7	48.0 ± 6.1
	12	70.5 ± 12.2	46.2 ± 17.4	52.5 ± 4.6
	24	70.5 ± 17.8	67.5 ± 9.9	66.7 ± 2.8
Progressive motility (%)	3	18.1 ± 0.5	15.9 ± 4.9	18.2 ± 0.6
	6	17.9 ± 5.0	19.4 ± 3.2	22.4 ± 7.6
	12	6.1 ± 4.8	12.5 ± 3.1	12.8 ± 7.2
	24	1.7 ± 0.5	5.7 ± 5.8	3.0 ± 1.3
Total motility (%)	3	28.9 ± 3.4	22.3 ± 3.9	24.0 ± 2.4
	6	27.2 ± 5.0	24.1 ± 3.9	27.2 ± 6.4
	12	11.1 ± 2.8	16.0 ± 3.2	16.7 ± 8.9
	24	4.1 ± 3.1	7.2 ± 6.4	4.2 ± 1.1

Table 2. Effects of Devices on the In Vitro Fertilization Rates of In Vitro Matured Bovine Oocytes.

Device	Oocytes (n)	Total Fertilization	Normal Fertilization	Abnormal Fertilization
		Penetration (%)	Male Pronucleus Formation (%)	Polyspermic Penetration (%)
Four-well culture dish	153	61.4*	82.9	17.0
Microfluidic device	87	36.8*	78.8	21.9

*Values within a column differ significantly, $p < 0.05$.

a micromilling step for the rest of the fluidic structures. We have demonstrated that the COC microfluidic device enables the functional and automated maturation of oocytes, and that it is nontoxic for gametes. The microfluidic device allows trapping the oocytes by means of a filter-like structure and their maturation. No significant differences were observed in oocytes reaching normal MII and cytoplasmic maturation in terms of cortical granule migration, compared with the control experiments. Lower penetration rates were observed for oocytes matured in the microfluidic device, which could be related to the lower grade of cumulus cell expansion of the cumulus–oocyte complexes or an incomplete cytoplasmic maturation of the oocytes. However, this issue could be addressed by improving the factor availability and pH buffering capacity in the surroundings of the oocytes, for instance, by dynamic culture.

The properties of COC open new possible applications for microfluidic systems in ART due to the simple fabrication processes at both the prototyping and mass production scales, taking advantage of the different material grades commercially available. COC is not hindered by mass production limitations, absorption of molecules, or gas permeability, thus avoiding a strict control of the exterior atmosphere conditions, and provides simpler fabrication methods than other thermoplastics, especially regarding bonding.

Current efforts focus, on the one hand, on the development of a temperature control system to avoid the use of big, heavy, and expensive equipment such as incubators, and on the other hand, on the control of the factors and the buffering of the media in the surroundings of the oocytes. These two features would enable the construction of an independent automated microfluidic platform using COC for different ART applications.

Economy and Competitiveness, Spain). Finally, the authors want to thank A. Pujol for the photography work.

References

1. Rodriguez-Martinez, H. Assisted Reproductive Techniques for Cattle Breeding in Developing Countries: A Critical Appraisal of Their Value and Limitations. *Reprod. Domest. Anim.* **2012**, *47*, 21–26.
2. Luo, Z.; Güven, S.; Gozen, I.; et al. Deformation of a Single Mouse Oocyte in a Constricted Microfluidic Channel. *Microfluid. Nanofluidics* **2015**, *19*, 883–890.
3. Ziółkowska, K.; Kwapiszewski, R.; Brzózka, Z. Microfluidic Devices as Tools for Mimicking the In Vivo Environment. *New J. Chem.* **2011**, *35*, 979–990.
4. Beebe, D. J.; Ingber, D. E.; den Toonder, J. Organs on Chips 2013. *Lab Chip* **2013**, *13*, 3447–3448.
5. Rigat-Brugarolas, L. G.; Elizalde-Torrent, A.; Bernabeu, M.; et al. A Functional Microengineered Model of the Human Splenon-on-a-Chip. *Lab Chip* **2014**, *14*, 1715–1724.
6. Auroux, P.-A.; Iossifidis, D.; Reyes, D. R.; et al. Micro Total Analysis Systems. 2. Analytical Standard Operations and Applications. *Anal. Chem.* **2002**, *74*, 2637–2652.
7. Kim, M. S.; Bae, C. Y.; Wee, G.; et al. A Microfluidic In Vitro Cultivation System for Mechanical Stimulation of Bovine Embryos. *Electrophoresis* **2009**, *30*, 3276–3282.
8. Mukhopadhyay, R. When PDMS Isn't the Best. *Anal. Chem.* **2007**, *79*, 3248–3253.
9. Cho, B. S.; Schuster, T. G.; Zhu, X.; et al. Passively Driven Integrated Microfluidic System for Separation of Motile Sperm. *Anal. Chem.* **2003**, *75*, 1671–1675.
10. Ma, R.; Xie, L.; Han, C.; et al. In Vitro Fertilization on a Single-Oocyte Positioning System Integrated with Motile Sperm Selection and Early Embryo Development. *Anal. Chem.* **2011**, *83*, 2964–2970.
11. Esteves, T. C.; van Rossem, F.; Nordhoff, V.; et al. A Microfluidic System Supports Single Mouse Embryo Culture Leading to Full-Term Development. *RSC Adv.* **2013**, *3*, 26451–26458.

12. Swain, J. E.; Lai, D.; Takayama, S.; et al. Thinking Big by Thinking Small: Application of Microfluidic Technology to Improve ART. *Lab Chip* **2013**, *13*, 1213–1224.
13. Sackmann, E. K.; Fulton, A. L.; Beebe, D. J. The Present and Future Role of Microfluidics in Biomedical Research. *Nature* **2014**, *507*, 181–189.
14. Young, E. W. K.; Berthier, E.; Guckenberger, D. J.; et al. Rapid Prototyping of Arrayed Microfluidic Systems in Polystyrene for Cell-Based Assays. *Anal. Chem.* **2011**, *83*, 1408–1417.
15. Berthier, E.; Young, E. W. K.; Beebe, D. Engineers Are from PDMS-Land, Biologists Are from Polystyrenia. *Lab Chip* **2012**, *12*, 1224–1237.
16. Nunes, P. S.; Ohlsson, P. D.; Ordeig, O.; et al. Cyclic Olefin Polymers: Emerging Materials for Lab-on-a-Chip Applications. *Microfluid. Nanofluidics* **2010**, *9*, 145–161.
17. van Midwoud, P. M.; Janse, A.; Merema, M. T.; et al. Comparison of Biocompatibility and Adsorption Properties of Different Plastics for Advanced Microfluidic Cell and Tissue Culture Models. *Anal. Chem.* **2012**, *84*, 3938–3944.
18. Jeon, J. S.; Chung, S.; Kamm, R. D.; et al. Hot Embossing for Fabrication of a Microfluidic 3D Cell Culture Platform. *Biomed. Microdevices* **2011**, *13*, 325–333.
19. Kuo, J. S.; Chiu, D. T. Disposable Microfluidic Substrates: Transitioning from the Research Laboratory into the Clinic. *Lab Chip* **2011**, *11*, 2656–2665.
20. Tsao, C.-W.; DeVoe, D. L. Bonding of Thermoplastic Polymer Microfluidics. *Microfluid. Nanofluidics* **2008**, *6*, 1–16.
21. Jena, R. K.; Yue, C. Y.; Lam, Y. C. Micro Fabrication of Cyclic Olefin Copolymer (COC) Based Microfluidic Devices. *Microsyst. Technol.* **2011**, *18*, 159–166.
22. Jena, R. K.; Yue, C. Y. Cyclic Olefin Copolymer Based Microfluidic Devices for Biochip Applications: Ultraviolet Surface Grafting Using 2-Methacryloyloxyethyl Phosphorylcholine. *Biomicrofluidics* **2012**, *6*, 12822.
23. Steigert, J.; Haeberle, S.; Brenner, T.; et al. Rapid Prototyping of Microfluidic Chips in COC. *J. Micromech. Microeng.* **2007**, *17*, 333–341.
24. Berenguel-Alonso, M.; Granados, X.; Faraudo, J.; et al. Magnetic Actuator for the Control and Mixing of Magnetic Bead-Based Reactions On-Chip. *Anal. Bioanal. Chem.* **2014**, *406*, 6607–6616.
25. Rizos, D.; Ward, F.; Boland, M. P.; et al. Effect of Culture System on the Yield and Quality of Bovine Blastocysts as Assessed by Survival after Vitrification. *Theriogenology* **2001**, *56*, 1–16.
26. Bamba, K. Evaluation of Acrosomal Integrity of Boar Spermatozoa by Bright Field Microscopy Using an Eosin-Nigrosin Stain. *Theriogenology* **1988**, *29*, 1245–1251.
27. Damiani, P.; Fissore, R. A.; Cibelli, J. B.; et al. Evaluation of Developmental Competence, Nuclear and Ooplasmic Maturation of Calf Oocytes. *Mol. Reprod. Dev.* **1996**, *45*, 521–534.
28. Guckenberger, D. J.; de Groot, T.; Wan, A. M.-D.; et al. Micromilling: A Method for Ultra-Rapid Prototyping of Plastic Microfluidic Devices. *Lab Chip* **2015**, 2364–2378.
29. Hupert, M. L.; Guy, W. J.; Llopis, S. D.; et al. Evaluation of Micromilled Metal Mold Masters for the Replication of Microchip Electrophoresis Devices. *Microfluid. Nanofluidics* **2006**, *3*, 1–11.

30. Charest, J. L.; Eliason, M. T.; García, A. J.; et al. Combined Microscale Mechanical Topography and Chemical Patterns on Polymer Cell Culture Substrates. *Biomaterials* **2006**, *27*, 2487–2494.

31. Ibáñez-García, N.; Alonso, J.; Martínez-Cisneros, C. S.; et al. Green-Tape Ceramics. New Technological Approach for Integrating Electronics and Fluidics in Microsystems. *TrAC Trends Anal. Chem*. **2008**, *27*, 24–33.

32. Zeringue, H. C.; Beebe, D. J.; Wheeler, M. B. Removal of Cumulus from Mammalian Zygotes Using Microfluidic Techniques. *Biomed. Microdevices* **2001**, *3*, 219–224.

33. Zhang, L.; Jiang, S.; Wozniak, P. J.; et al. Cumulus Cell Function during Bovine Oocyte Maturation, Fertilization, and Embryo Development In Vitro. *Mol. Reprod. Dev*. **1995**, *40*, 338–344.

34. Walters, E. M.; Beebe, D. J.; Wheeler, M. B. In Vitro Maturation of Pig Oocytes in Polydimethylsiloxane (PDMS) and Silicon Microfluidic Devices. *Theriogenology* **2001**, *55*, 497.

35. FitzHarris, G.; Baltz, J. M. Granulosa Cells Regulate Intracellular pH of the Murine Growing Oocyte via Gap Junctions: Development of Independent Homeostasis during Oocyte Growth. *Development* **2006**, *133*, 591–599.

36. Phillips, K. P.; Petrunewich, M. A. F.; Collins, J. L.; et al. The Intracellular pH-Regulatory HCO3–/Cl– Exchanger in the Mouse Oocyte Is Inactivated during First Meiotic Metaphase and Reactivated after Egg Activation via the MAP Kinase Pathway. *Mol. Biol. Cell* **2002**, *13*, 3800–3810.

37. Pinyopummintr, T.; Bavister, B. D. Optimum Gas Atmosphere for In Vitro Maturation and In Vitro Fertilization of Bovine Oocytes. *Theriogenology* **1995**, *44*, 471–477.

38. Chan, N. G.; Raty, S.; Zeringue, H. C.; et al. Development of Microfabricated Devices for Embryo Production: Embryo Biocompatibility. *Theriogenology* **2001**, *55*, 332.

39. Clark, S. G.; Davis, J.; Beebe, D. J.; et al. Biocompatibility of Porcine Sperm Cells in Polydimethylsioloxane (PDMS). *Theriogenology* **2001**, *55*, 421.

40. Chan, N. G.; Lyman, J. T.; Choi, S. J.; et al. Development of an Embryo Transport and Analysis System: Material Biocompatibility. *Theriogenology* **1999**, *51*, 234.

41. Combelles, C. M. H. Assessment of Nuclear and Cytoplasmic Maturation in In-Vitro Matured Human Oocytes. *Hum. Reprod*. **2002**, *17*, 1006–1016.

42. Chen, L.; Wert, S. E.; Hendrix, E. M.; et al. Hyaluronic Acid Synthesis and Gap Junction Endocytosis Are Necessary for Normal Expansion of the Cumulus Mass. *Mol. Reprod. Dev*. **1990**, *26*, 236–247.

43. Gutnisky, C.; Dalvit, G. C.; Pintos, L. N.; et al. Influence of Hyaluronic Acid Synthesis and Cumulus Mucification on Bovine Oocyte In Vitro Maturation, Fertilisation and Embryo Development. *Reprod. Fertil. Dev*. **2007**, *19*, 488–497.

44. Hester, P. N.; Roseman, H. M.; Clark, S. G.; et al. Enhanced Cleavage Rates Following In Vitro Maturation of Pig Oocytes within Polydimethylsiloxane-Borosilicate Microchannels. *Theriogenology* **2002**, *57*, 723.

45. Miralles, V.; Huerre, A.; Malloggi, F.; et al. A Review of Heating and Temperature Control in Microfluidic Systems: Techniques and Applications. *Diagnostics* **2013**, *3*, 33–67.

46. Heo, Y. S.; Cabrera, L. M.; Bormann, C. L.; et al. Real Time Culture and Analysis of Embryo Metabolism Using a Microfluidic Device with Deformation Based Actuation. *Lab Chip* **2012**, *12*, 2240–2246.

Appendix B

Temperature Control Program

This program is intended to control the temperature of a heater (actuator) and maintain it at a set value. It is based on a Proportional-Integral-Derivative (PID) controller, which continuously calculates an error value —the difference between a desired *setpoint* and a measured variable (sensor input)— and applies a correction (output) to the actuator. The program was originally designed by C.S. Martínez-Cisneros to be used with a PIC4431 and adapted by M. Berenguel-Alonso to a PIC4553.

```
1  //* Al cambiar set points cambiar variables sp_zona1*//
2  //* Asignar a sp_zona1 el valor equivalente al voltaje
      correspondiente a la temperatura deseada (linea 25) */
3  //* Asignar corriente en linea 21, variable I*//
4
5  #if defined(__PCH__)
6  #include <18f4553.h>
7  #device ADC=12
8  #FUSES NOWDT, HS, PUT, NOPROTECT, BROWNOUT, NOLVP, NOCPD, NOWRT
9  //#fuses HS,NOWDT,PUT
10  //NOPROTECT
11  #use delay(clock=10000000)
12  #use rs232(baud=9600, xmit=PIN_C6, rcv=PIN_C7, ERRORS)   // Jumpers
      : 8 to 11, 7 to 12
13  #endif
14
15  #include <math.h>
16  #include <stdlib.h>
17
18  main() {
19
20      long int v1,conv_zona1=0,n;
21      float voltaje,T=0,R=0,V=0,I=0.00047,R0=100,AC=3.9083e-03,BC
      =-5.775e-07,A=0,B=0,C=0,B2=0,raiz,V2;
22      long periodo;
23      char cont=0;
24
25      float kp_zona1, ki_zona1, kd_zona1, sp_zona1=0.07570, en_zona1
      =0, en_1_zona1=0, en_2_zona1=0;
26      float k0_zona1, k1_zona1, k2_zona1, mn_zona1=0, mn_1_zona1=0;
27
28   // SETUP_ADC_PORTS(sAN0);
29   //   setup_adc(ADC_CLOCK_INTERNAL);
30
31      setup_adc_ports(ALL_ANALOG);
32      setup_adc(ADC_CLOCK_INTERNAL);
33      setup_ccp1(CCP_PWM);
34      setup_timer_2(T2_DIV_BY_16,255,1);
35
36
37      while(TRUE)
38      {
39          //Inicia lectura de sensor
40
41          set_adc_channel(0);
42          delay_us(40);
43          V=0;
44          for (n=1;n<=100;++n)
45          {
46              v1 = Read_ADC();
47              voltaje=((float)v1*5/4096);
```

196

```
48          V = V+v o l t a j e ;
49          delay_us ( 2 0 ) ;
50       }
51      V = (V/100)+0.010;
52      V2=V/ 2 3 . 7 3 2 ;
53     // V2=V2+0.03;
54      R=V2/I ;
55
56      A=BC∗R0 ;
57      B=AC∗R0 ;
58      C=R0−R;
59
60      B2=pow (B, 2 ) ;
61      r a i z=s q r t (B2−(4∗A∗C) ) ;
62      T= (−B+r a i z )/(2∗A) ;
63
64      //Termina l e c t u r a de s e n s o r e s
65
66      //Control de zona 1
67
68      kp_zona1=10;          //0.95;
69      ki_zona1=0.035;      //0.021
70      kd_zona1=0.015;      //0.01
71
72      k0_zona1 = kp_zona1 + ki_zona1∗5 + kd_zona1/5;
73      k1_zona1 = −kp_zona1−(2∗kd_zona1∗5);
74      k2_zona1 = 5∗kd_zona1 ;
75      en_zona1 = sp_zona1−V2;
76      mn_zona1 = mn_1_zona1 + k0_zona1∗en_zona1 + k1_zona1∗
    en_1_zona1 + k2_zona1∗en_2_zona1 ;
77
78      if (mn_zona1>=5)        mn_zona1=5;
79      if (mn_zona1<=0)        mn_zona1=0;
80      conv_zona1 = mn_zona1∗1023/5;
81
82      set_pwm1_duty ( conv_zona1 ) ;
83      en_1_zona1 = en_zona1 ; mn_1_zona1 = mn_zona1 ; en_2_zona1 =
    en_1_zona1 ;
84
85      //termina control zona 1
86
87      if ( cont==10){
88          p r i n t f ( " %2.5 f " ,T) ;
89          p r i n t f ( "  %2.5 f " ,V) ;
90          p r i n t f ( "  %2.5 f " ,V2) ;
91          p r i n t f ( "  %2.5 f " , mn_zona1 ) ;
92          p r i n t f ( "  %2.5 f " ,R) ;
93
94          //c1=abs ( temp1−270) ;
95
96          p r i n t f ( " \ r \n " ) ;
```

197

```
 97
 98              cont  =  0;
 99          }
100        cont=cont+1;
101        }
102 }
```

Appendix C

PCB Design and Enclosure

The circuit diagram and the final design of the Printed Circuit Board (PCB) for the temperature control system are herein attached (Figures C.1 and C.2). The diagram of the circuit was mainly developed by Dr. C.S. Martínez-Cisneros (Dept. of Materials Science and Engineering, Universidad Carlos III Madrid), and refined by our research group in collaboration with Dr. Joan Garcia and Javier Hellín (Dept. of Electronic Engineering, UAB). After the circuit was successfully tested on a breadboard (circuit prototyping system), the PCB was designed using the software *Eagle*.

The design consisted on a double sided PCB. However, problems appeared due to crosstalk, or mutual coupling, between different tracks of the circuit. Therefore, the design was iterated in collaboration with the specialized company Cidein S.L. (Barcelona, Spain). The final layout consists of a multilayer PCB with independent layers for ground (GND) and 5 V power supply.

Finally, a custom-made aluminum enclosure for the PCB was designed and fabricated in our fabrication laboratory (Figure C.3). The enclosure included all necessary connections to operate and re-program the temperature controller system.
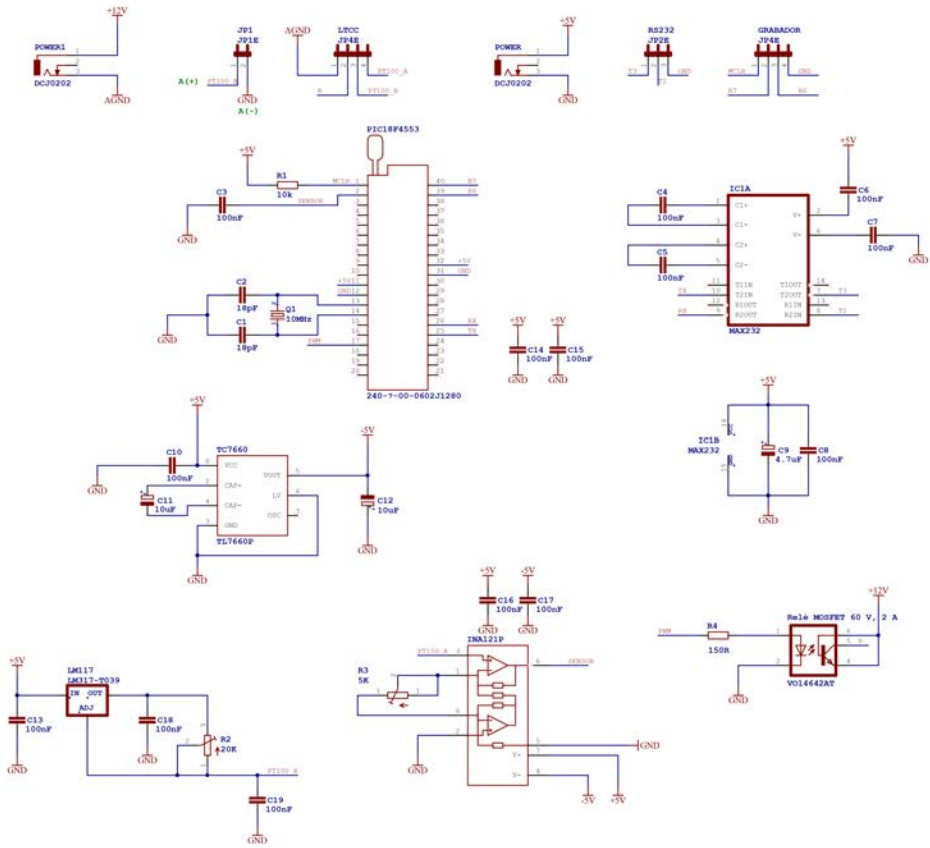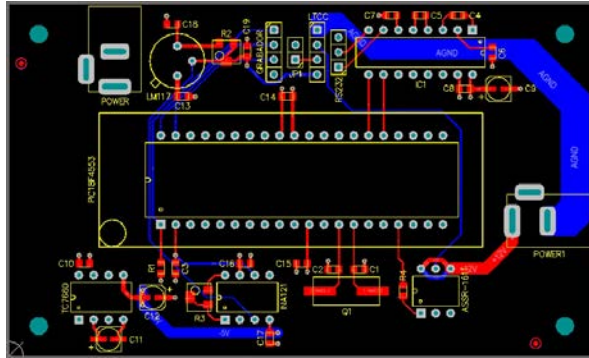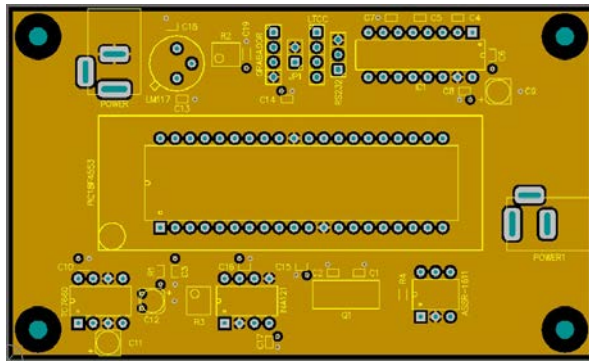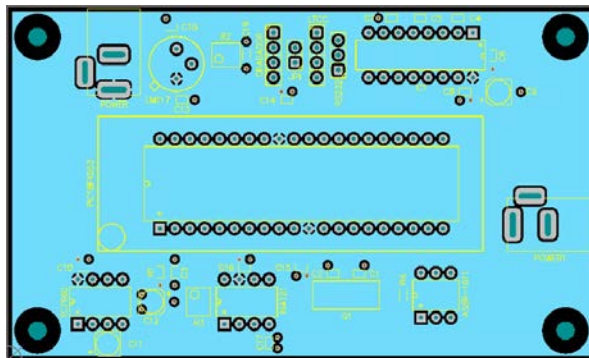
Figure C.1: Schematic diagram of the PCB microcontroller.

(a) Top and bottom layers

(b) GND layer

(c) Power layer

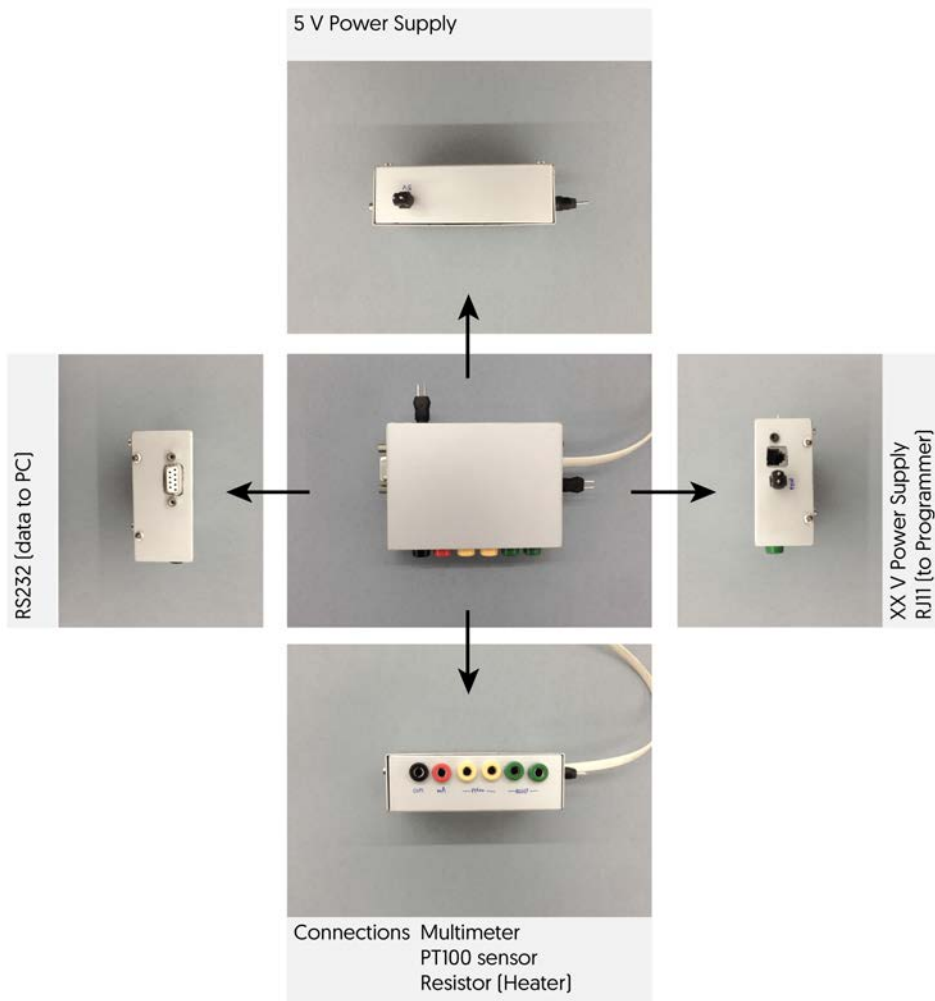Figure C.2: Design of the different layers constituting the PCB controller.

Figure C.3: Custom-made aluminum enclosure and connections for the PCB microcontroller.

Appendix D

CNC Software Tutorial Series

This tutorial series was created upon the acquisition of the Computer Numeric Control (CNC) micromilling machine Protomat S63, from LPKF Laser & Electronics (Garbsen, Germany). This micromilling machine is originally intended for PCB prototyping. Furthermore, the new software differed substantially from that of older microstructuring equipment in the group. As responsible of the new CNC micromilling machine, I developed a fabrication protocol for LOC prototyping, together with a video tutorial series (see Figure D.1). The tutorials are publicly available on Youtube:
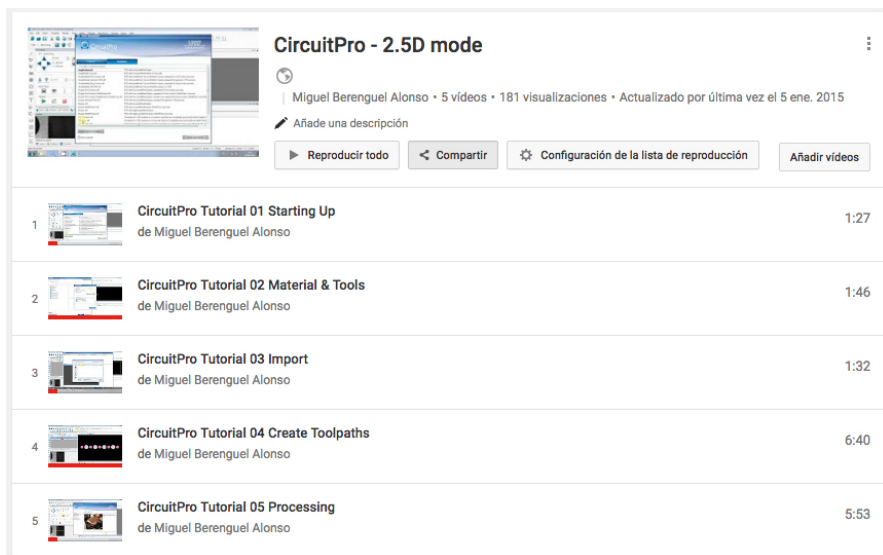
CircuitPro 2.5D-mode Tutorial Series

Figure D.1: CircuitPro 2.5D mode tutorial series on Youtube.